Photophysics of Fused Ring Electron Acceptors for Photovoltaic Applications

Sreelakshmi Chandrabose

Victoria University of Wellington

A thesis submitted for the degree of

Doctor of Philosophy in Physics

2020

dedicated to my family
"***there is no greater gift than education***"

Abstract

Organic photovoltaic cells (OPVs) have received significant interest over the last decade as they offer the potential of cheap renewable energy *via* direct photon to electron conversion of abundantly available Sun light. Compared to the inorganic equivalents, they offer lightweight, low-cost, and flexibility advantages. Conventional OPVs are typically based on blends of electron-donor materials and fullerene-based electron-acceptor materials that form bulk-heterojunctions (BHJs). But the attention has recently shifted to organic non-fullerene acceptors especially fused ring electron acceptors (FREAs) owing to their attractive properties including flexible energy levels, tunable band gap, crystallinity, and planarity. Thus the power conversion efficiency (PCE) of OPVs has recently attained a record of 16% by synthesizing FREAs with modified chemical structures.

Owing to the high crystallinity and packing orientation of acceptors, FREA based OPV systems are characterized by large and pure phases sized 20-50 nm. This is consistent with the observation that charge generation dynamics in these systems lacked the ultrafast component that characterizes most fullerene blends. To test the hypothesis that the optimal phase size can be large due to facile exciton diffusion in FREAs, a planar indacenodithiophene (IDT) based FREA, IDIC is selected as a model system to study the exciton dynamics. **Chapter 3** includes the exciton diffusion measurements in IDIC films using transient absorption spectroscopy which resolves a substantially high, quasi-activationless diffusion coefficient that exceeds that of typical organic semiconductors. The study also includes a deep insight of the key factors behind the enhanced exciton diffusion in IDIC and is shown to arise from different molecular and packing factors which enhance the long-range resonant energy transfer.

Rapid exciton diffusion in IDIC films introduced the possibility of solution-processed bilayer devices. **Chapter 4** comprises both device and photophysics of planar bilayer

devices with a PCE of 11.1% which is readily accounted for the material and device design. By pairing a mid-band gap polymer donor with a range of FREAs, it is shown that the combination of high molecular packing densities and absorption coefficients, long exciton diffusion lengths, and efficient, resonant, long-range energy transfer between donor and acceptor layers enable efficient bilayer devices. By designing new materials with these characteristics, along with orthogonal solubility for layer-by-layer deposition of clean bilayers, it is suggested that the clear connection between material design and function in the bilayer structure will accelerate the development of more efficient organic photovoltaic devices.

The molecular packing of active layer components has a crucial role in the device performance of OPV devices. Especially for FREA based OPV systems, the long-range structural order induced by end group $\pi-\pi$ stacking is considered as the critical factor for achieving high PCEs. **Chapter 5** includes a deep spectroscopic insight into the exciton and charge transport processes in a series of FREA based OPV systems having different molecular packing and ordering. Here the molecular stacking manipulation in FREAs is achieved by changing the length of alkyl side-chains so that the FREA backbone is changed from a $\pi-\pi$ stacking mode to a non-stacking mode. Transient absorption spectroscopic analysis of neat FREAs and blends reveals that exciton diffusion and intermolecular charge transfer processes do not necessarily rely on the molecular $\pi-\pi$ stacking, while close atom contact can also enable these processes. This work provides new insights into the design of advanced materials for next generation organic photovoltaics considering diverse transport channels formed by close atom interactions.

Chapter 6 discusses the advantages of ternary OPV strategy in BHJ world with a 13% efficient ternary device based on a highly efficient FREA, FOIC. The introduction of a mid-band gap small molecule donor TR into the binary blend PTB7-Th:FOIC improves the open circuit voltage (V_{OC}), short circuit current (J_{SC}), fill factor (FF), and thereby the overall device performance. Transient absorption spectroscopy reveals ultrafast resonant energy transfer from TR to PTB7-Th domains which is consistent with their intermixed morphology. Additionally, the study also includes the rapid long-range energy transfer from PTB7-Th to FOIC phases that benefits both the binary and ternary blends.

Taken together, this thesis presents a valuable and deep insight into the photophysics

of FREAs and highly efficient FREA based OPV systems using time-resolved spectroscopic techniques.

Acknowledgements

Great! This is the single word by which I can explain my overall experience in Victoria University of Wellington, New Zealand. I find myself improved a lot both personally and professionally in the last couple of years by the stimulating academic environment, I got here in Victoria. I take this precious opportunity to express my sincere and heartfelt obligations towards all of the people whom I am ineffably indebted for making me who I am today.

First, and foremost, my deep gratitude goes to my supervisor Prof. Justin M. Hodgkiss, for his continuous support, guidance, expertise, assistance, and patience throughout the process of my research and thesis writing. I greatly appreciate his endurance and consideration to all the people who work with him. It is really inspiring! I have been extremely lucky to have a supervisor like him who cared so much about my results, publications, and who responded to my questions and concerns so hastily. Thank you so much Justin, I really enjoyed as your student.

Next, I gratefully acknowledge the ultrafast laser spectroscopy group members/alumni who have been there as strong supporters throughout my voyage. My special thanks goes to Dr. Kai Chen, the mastermind of our lab for all his helps and patience in working with me. I admire his abilities and passion towards research which is a great inspiration for me. I would also like to thank Shyamal Prasad for teaching me the first lessons of transient absorption spectroscopy and data analysis. I am also grateful to Karen for all her helps, especially the proof reading of my thesis. I really enjoyed our ridiculous conversations about optics and spectroscopy. I also thank Dr. Michael B. Price for his immense support and helps in completing the bilayer OPV paper. Finally, my dear colleagues Alexandra, Isabella, Ronnie, and Silvina for contributing immensely to my personal and professional time at Victoria.

During my PhD training, I was lucky to have multiple collaborations with great

people. I feel privileged to collaborate with Prof. Xiaowei Zhan and his team from Peking University, China who provided us with the highly efficient non-fullerene acceptors and related OPV systems. Also, Prof. Jin Young Kim and group from UNIST and Prof. Han Young Woo and team from Korea University, South Korea for providing the highly performing bilayer OPV systems and valuable discussions throughout the completion of the bilayer paper.

From the bottom of my heart, I would like to express my sincere gratitude to my parents Chandrabose and Sheela and my sister Seethalakshmi with whom the most basic source of my life energy resides. I am in great debt to you for your infallible love, support, trust, and understanding of my goals and aspirations. My formal academic education is finalized by this thesis, which I am more than happy to devote to you. Moreover, I immensely appreciate my amazing friends (Shalini, Mima, Vaibhav, Parth, and Aldritt) and relatives (Reshmi Kishore and family) in New Zealand for their continuous encouragement and unconditional support throughout the research.

Most of all, I thank GOD ALMIGHTY, for constantly motivating me with his eternal love and giving me courage at each stride to step forward with confidence and self-belief.

Sreelakshmi Chandrabose

Publications

Thesis includes the works from following publications.

Chapter 2

T. Liu, L. Huo, **S. Chandrabose**, K. Chen, G. Han, F. Qi, X. Meng, D. Xie, W. Ma, and Y. Yi, *Optimized fibril network morphology by precise side-chain engineering to achieve high-performance bulk-heterojunction organic solar cells*. Advanced Materials, **2018**: p. 1707353.

Chapter 3

S. Chandrabose, K. Chen, A. J. Barker, J. J. Sutton, S. K. K. Prasad, J. Zhu, J. Zhou, K. C. Gordon, Z. Xie, X. Zhan and J. M. Hodgkiss, *High exciton diffusion coefficients in fused ring electron acceptor films.* Journal of the American Chemical Society, **2019**: p. 6922-6929.

Chapter 4

S. Chandrabose, S. Y. Park, M. B. Price, H. S. Ryu, T. H. Lee, Y. S. Shin, Z. Wu, W. Lee, K. Chen, X. Zhan, H. Y. Woo, J. Y. Kim and J. M. Hodgkiss, *High efficiency bilayer organic photovoltaic cells enabled by large extinction coefficients, high exciton diffusion lengths, and interlayer energy transfer.* submitted for publication.

Chapter 5

L. Ye, K. Weng, J. Xu, X. Du, **S. Chandrabose**, K. Chen, J. Zhou, G. Han, S. Tan, Z. Xie, Y. Yi, N. Li, F. Liu, J.M. Hodgkiss, C.J. Brabec and Y. Sun, *Unravelling the $\pi - \pi$ stacking free charge transport channels in non-fullerene acceptor based organic photovoltaics.* submitted for publication.

Chapter 6

S. Dai, **S. Chandrabose**, J. Xin, T. Li, K. Chen, P. Xue, K. Liu, K. Zhou, W. Ma, and J.M. Hodgkiss, *High-performance organic solar cells based on polymer donor/small molecule donor/non-fullerene acceptor ternary blends.* Journal of Material Chemistry A, **2019**. 7(5): p. 2268-2274.

Contents

List of Figures

List of Tables

List of Abbreviations

AFM	Atomic Force Microscopy
ALD	Atomic Layer Deposition
BHJ	Bulk-Hetero Junction
CB	Chlorobenzene
CS	Charge Separated
CT	Charge Transfer
DCM	Dichloromethane
DET	Dexter Energy Transfer
DOS	Density of States
EA	Electro-absorption
EFA	Error Factor Analysis
EQE	External Quantum Efficiency
ETL	Electron Transporting Layer
FA	Fullerene Acceptors
FF	Fill Factor
FIB	Focused Ion Beam
FREA	Fused Ring Electron Acceptor
FRET	Förster Resonance Energy Transfer
GIWAXS	Grazing-Incidence Wide Angle X-ray Scattering
GSB	Ground State Bleach
GVD	Group Velocity Dispersion
HOMO	Highest Occupied Molecular Orbital

HPLC	High Performance Liquid Chromatography
HTL	Hole Transporting Layer
IDT	Indaceno-dithiophene
IDTT	Indacenodithieno[3,2-b]thiophene
IRF	Instrument Response Function
LBL	Layer-By-Layer
LUMO	Lowest Unoccupied Molecular Orbital
MCR	Multivariate Curve Resolution
NDI	Naphthalene Diimide
NFA	Non-Fullerene Acceptors
NIR	Near Infrared
OLED	Organic Light Emitting Diode
OPA	Optical Parametric Amplification
OPV	Organic Photovoltaics
OSC	Organic Solar Cell
PCE	Power Conversion Efficiency
PDI	Perylene Diimide
PIA	Photoinduced Absorption
PL	Photoluminescence
R-SoXS	Resonant Soft X-ray Scattering
SE	Stimulated Emission
SFG	Sum Frequency Generation
SHG	Second Harmonic Generation
SMA	Small Molecule Acceptors
SRA	Stimulated Raman Amplification
SSA	Singlet-Singlet Annihilation
SVD	Singular Value Deposition
TA	Transient Absorption
TEM	Transmission Electron Microscopy

TGPL	Transient Grating Photoluminescence
TOPAS	Travelling wave optical parametric amplifier of white light continuum
TSC	Ternary Solar Cell
WLC	White Light Continuum
YAG	Yttrium Aluminum Garnet

Chapter 1

Introduction to organic photovoltaics

The Earth receives enormous energy to fulfill the yearly demand of energy in less than an hour. The energy, the Sun sends out arrives on the Earth as a mixture of light and heat. Both of these are incredibly important, but we can't use them directly to fulfill most of our energy needs. We have to convert solar energy into other forms of energy that can be used more easily, such as electricity. And that is exactly what solar cells do. This chapter introduces the basic concepts and definitions regarding **organic photovoltaic cells (OPVs)**. A clear explanation of the mechanism behind exciton diffusion and associated energy transfers is presented. Additionally, a brief literature review on OPVs based on both fullerene and non-fullerene acceptors is included where the focus is mainly on fused ring electron acceptors (FREAs), an important class of non-fullerene acceptors on which this thesis is concentrated on.

1.1 Organic photovoltaics

Organic semiconductors are materials composed of carbon and hydrogen atoms, with a few heteroatoms like nitrogen, sulfur, and oxygen which exhibit properties, usually associated with that of a semiconductor.[89] All organic semiconductors are characterized by a common structural property called conjugation - alternating single and double bonds. The carbon atoms comprising their backbone are covalently bonded by three sp^2 hybridized orbitals and an unhybridized P_z orbital.[135] The adjacent P_z orbitals overlap together to form shared orbitals that result in an extended $\pi-$ conjugated system where the electrons are delocalized. The delocalization can be extended over a whole molecule or a part of it (conjugated segment). In the ground state, electrons occupy the highest occupied molecular orbital (HOMO or $\pi-$ orbital), and on photon absorption, they get excited to the lowest unoccupied molecular orbital (LUMO or π^*- antibonding orbital) to form excitons.

Unlike the intrinsic inorganic equivalents like silicon and germanium, organic semiconductors are extrinsic whose conductivity comes from photoexcitation, injection of charges at electrodes and doping. Their absorption and emission fall in the UV-visible and near-infrared (NIR) range of the electromagnetic spectrum. On absorption of photons, instead of charges, they generate strongly bound excitons as they have highly localized electron-hole wavefunctions and low dielectric screening (dielectric constant ϵ_r $\sim$3 - 4), enhancing the Coulomb attraction between the electron and the hole. These excitons must split into polarons (electrons and holes) to allow charge transport and thereby generate current. There are mainly three varieties of organic semiconductors, molecular crystals, amorphous molecular films, and polymer films.

Organic photovoltaic cells use semiconductive organic polymers or small organic molecules to produce electricity from light. They are a promising cost-effective alternative to the conventional silicon-based solar cells as they possess lightweight, low cost, and flexibility advantages.[107] The splitting of excitons into polarons is commonly achieved by the structure of the OPV that includes an electron donor component that absorbs light and an electron acceptor component that takes electrons and transports them to the electrode. The energy difference between the LUMOs and/or HOMOs provides the driving force for the dissociation of excitons. There is an interface between the donor and the acceptor components that the excitons must reach in order to dissociate. The necessary condition for an efficient OPV is the requirement that

the excitons can diffuse across a large distance (exciton diffusion length) in their lifetime.

The simplest form of an OPV is a bilayer planar heterojunction in which the electron donor and acceptor components are sandwiched between the conductive electrodes. Since the active layer needs at least 100 nm to absorb enough light, excitons have to travel a large distance in order to reach the interface. As organic materials posses exciton diffusion length of the order of 10 nm,[135] a large fraction of excitons is unable to reach the junction. This problem is solved by the generation of bulk-heterojunctions (BHJs) which contain an intermixed composite of donors and acceptors.[186] Here, the active layer consists of a donor-acceptor blend with domain sizes of the order of nanometers that can allow the short-lived exciton to find an interface easily. Unlike bilayers, BHJs can be made very thick enough for effective light absorption without any difficult processing methods while retaining a similar level of performance.

Figure 1.1 gives a schematic of exciton generation, diffusion and charge separation in a typical bulk-heterojunction solar cell. The ground states of the majority of the organic semiconductors are characterized by a net spin-zero which are named as singlet states. When materials are illuminated with light having energy that matches with a possible electronic transition, absorption of light quanta happens which results in the promotion of an electron from S_0 or HOMO state to S_1 or LUMO state. Due to the low dielectric screening, instead of free charge carriers, strongly bound neutral excitons are produced which need to get dissociated at the donor-acceptor interfaces in order to generate photo-current. For this, excitons have to diffuse or migrate across a distance called the exciton diffusion length during their lifetime. Once they have reached the interface, they adopt a charge transfer (CT) state which plays a fundamental role in the operation of OPVs. Even after charge transfer, the resulting electron-hole pairs still experience Coulombic attraction because the donor and the acceptor phases are physically close to each other at the interfaces.[50] The binding energy of the CT state is reported to in the range of 0.1 - 0.5 eV.[50,205] The CT state will then dissociate to form charge-separated (CS) state or free charges.

OPVs are generally classified into two types according to whether their active layer constituents are either polymers or small molecules, which are different in terms of their production, purification, and device fabrication.[129] Polymer solar cells are an important branch of OPVs, which possess an active layer of a blend film comprising

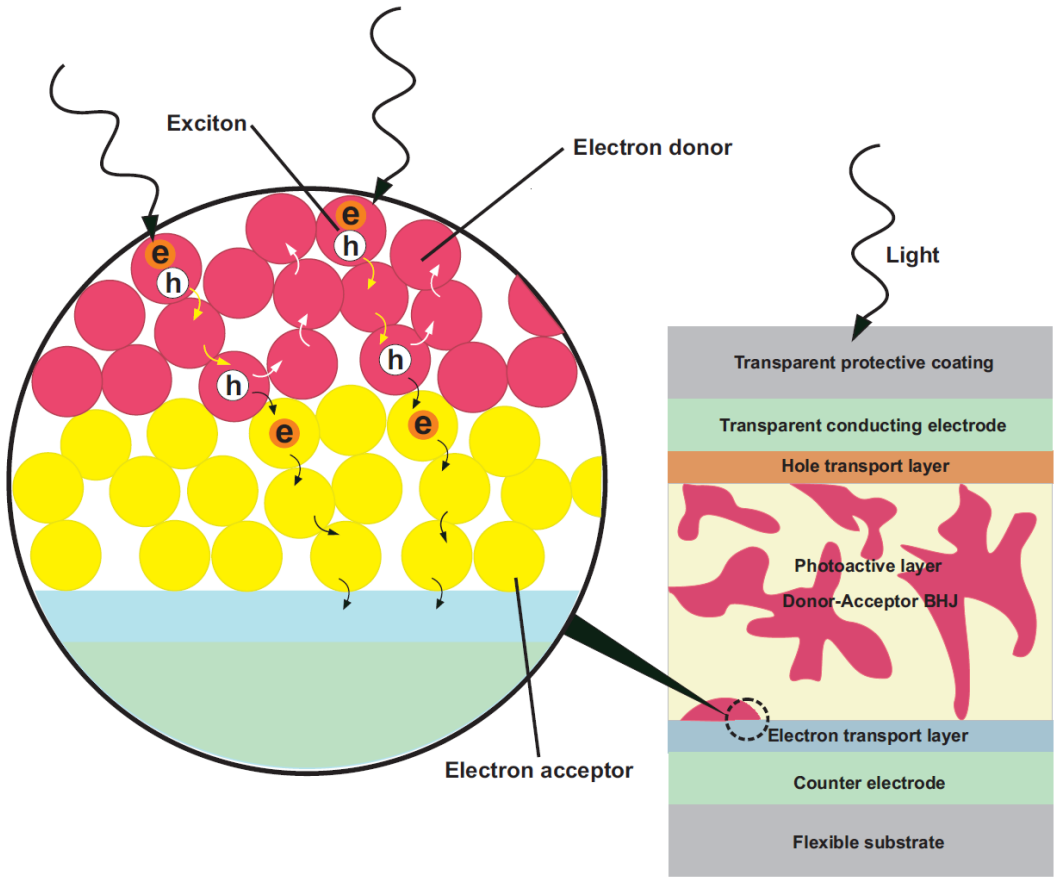

Figure 1.1: Schematic of exciton generation, diffusion, and charge separation in a bulk-heterojunction solar cell.

a conjugated polymer as the electron donor and a small molecular acceptor. Alan J. Heeger, Alan MacDiarmid, and Hideki Shirakawa received the Nobel Prize for Chemistry in 2000 for their discovery that the polymers can act as conductors due to their highly polarizable p-systems.[157] Their $\pi - \pi^*$ optical transitions are relatively strong, typically fall in the visible spectrum, and can be tuned synthetically through molecular design. Polymer solar cells are usually processed from solution in organic solvents. Small molecular solar cells based on organic small molecules are processed mainly using thermal evaporation deposition in a high vacuum environment. They are also produced from the solution process, but the film quality and crystallization is expected to be an issue.[117]

1.1.1 Fullerene based OPVs

Conventional OPVs are typically based on electron-donating polymers/small molecules and fullerene based electron acceptor materials that generate bulk-heterojunctions in

the device. Fullerene acceptors (FA) are characterized by a strong tendency to accept electrons from donor materials as they possess high electron-affinity in the range of 3.5 - 4 eV.[71] They are excellent in forming an interpenetrating nanoscale morphological network with donor materials which can effectively increase charge separation and transport in the device.[107,179] Other favorable features of fullerene acceptors include high electron mobility, 3D structure, solubility from side-chains and highly delocalized LUMO levels which can form extensive and robust charge percolation pathways.[179]

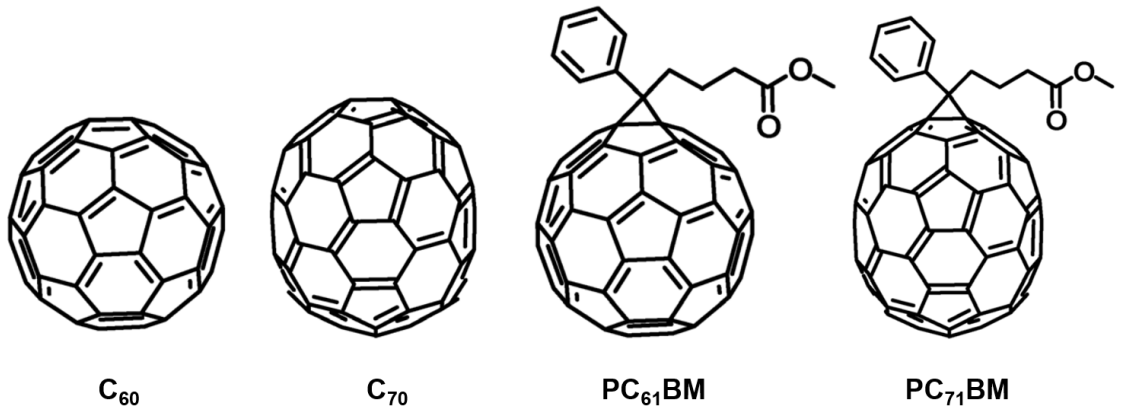

Figure 1.2: Chemical structures of pristine fullerene (C_{60}) and its derivatives, adapted from Lin *et al.*[107]

In 1992, Sariciftci *et al.* discovered that the photoexcitation of a blend of a conjugated polymer and fullerene (C_{60}) resulting in an ultrafast, highly efficient photoinduced electron transfer.[151] Later, the low performance in OPVs for pristine fullerene due to their limited solubility paved the way to the synthesis of new fullerene derivatives such as [6,6]-phenyl-C_61-butyric acid methyl ester ($PC_{61}BM$) and [6,6]-phenyl-C_71-butyric acid methyl ester ($PC_{71}BM$) which possess high solubility in aromatic solvents, easy preparation, lower-lying LUMO levels as well as higher stability than pristine C_{60}.[49] Recently, a tandem solar cell with $PC_{61}BM$ and $PC_{71}BM$ as acceptor layers reached a power conversion efficiency (PCE) of $\sim$15%.[117] **Figure 1.2** gives chemical structures of pristine fullerene and its derivatives.

But in fullerene based solar cells, donor materials make a major contribution to the photocurrents because of the very weak absorption of fullerene derivatives in the visible and near IR regions. This is due to the high symmetric nature of their chemical structures and poor synthetic flexibility. They have restricted opportunities for variation of the band gaps because of the limited number of different chemical structures

that can be easily modified by keeping the C_{60}:C_{70} core more or less intact.[23] Also their purification needs special equipment for specific processes like high-performance liquid chromatography (HPLC) which can limit their output and lead to high cost of production, thereby decreasing their practical applications.[79139] In addition to these, their lower photochemical and thermal stability, restricted tunability of electron affinities and other limitations of fullerene based solar cells have led to the development of alternative electron acceptor materials.[179]

1.1.2 Non-fullerene acceptors for OPVs

Since the fullerene based acceptors do present some challenges in terms of chemical modification to tune their band gap, much attention has been paid to non-fullerene acceptors, whose design and production were the main goals for the researchers in that field for a long time. Compared to fullerene acceptors, non-fullerene acceptors possess distinct advantages like a tunable band gap that can extend their absorption even to the NIR region, flexible energy levels those match with that of high-performance donor materials and tunable crystallinity and planarity that controls the morphology and thereby the device stability.[23] As this thesis concentrates on the photophysics of non-fullerene acceptors and their solar cells, summarizing the critical achievements in this field is considered to be essential.

Fused ring electron acceptors

Fullerene free solar cells based on fused ring electron acceptors (FREAs) have been widely investigating due to their outstanding performance. Relative to fullerene acceptors, FREAs possess flexible electronic energy levels and easily tuned absorption ranging from blue to red light, even extending to near IR region. Structurally, FREAs consist of two $\pi-$ electron-withdrawing moieties (end-capping groups) linked *via* a planar central core made up of fused rings connected to alkyl or aryl side-chains floating above or below the plane. The advantage of aromatic fused rings in the design of organic acceptors is that their extended conjugation forms effective interchain $\pi - \pi$ overlapping and thereby enhances the intermolecular charge transport.[108] The introduction of electron-withdrawing groups into $\pi-$ conjugated semiconductors can lower the LUMO energies, as the π^* energy of the electron-withdrawing group is very close to the LUMO energy of the π - conjugated semiconductor which results in an efficient mixing of the orbitals and thereby stabilization of the LUMO.[6] The side-chains are incorporated mainly for the purpose of tuning the solubility of the molecule, but as

they are usually insulating, there would be a trade-off between the solubility and conductivity of the corresponding acceptors.[178]

Recently, considerable interest has been given in the improvement of FREA based solar cells by the manipulation of the central core and the side electron-withdrawing chains. Tuning of the fused rings and the electron-withdrawing groups can effectively vary the absorption, electron affinity, and ionization energy of the material. So far, FREA based polymer solar cells have shown PCEs of up to 12-16%.[110,189] One of the FREAs that is being widely researched is Rylene diimides and its derivatives. These molecular systems are characterized by excellent thermal and oxidative stabilities, easy tuning of HOMO and LUMO energies, high electron mobility, high absorption coefficients and electron affinities comparable to those of fullerenes. These properties can be easily tuned either by the variation of the rylene core or substituents on the imide nitrogen atoms.[161,191] In 2007, Zhan *et al.* reported a PDI (Perylene diimide) based polymer acceptor, after which the OPVs of PDI or NDI (Naphthalene diimide) based FREAs have been widely attractive.[192] PDI based acceptors generally show strong absorption in the visible region with a high absorption coefficient of $\sim 10^4$ $M^{-1}cm^{-1}$.[173,176] They have high electron-accepting ability and high electron mobility of the order of 10^1 to 10^3 $cm^2V^{-1}s^{-1}$.[190] However, typical fused rings show strong aggregation which leads to the formation of large crystalline aggregate domains. Consequently, strong self-trapping of excitons occurs within these large aggregates, which can severely affect the exciton diffusion and thereby the PCE of the solar cell.[80,201]

The goal of decreasing self-aggregation in traditional fused rings resulted in the design of new FREAs based on electron donating extended fused rings such as IDT (indaceno-dithiophene) and IDTT (indacenodithieno[3,2-b]thiophene), tailored by end-capping electron-deficient groups (examples are given in **Figure 1.3**). Their highly rigid and co-planar structure can prevent rotational disorder and reduce reorganization energy, which may enhance the charge carrier mobility.[100] In contrast to Rylene based FREAs which are usually synthesized by multi-step reactions, these FREAs with an acceptor-donor-acceptor (A-D-A) structure can be easily synthesized by simple reactions. Also, their optical and electronic properties can easily be varied by changing the end-capping electron-withdrawing groups.[104] Most of the BHJ solar cells based on FREAs need additional complicated treatments for their active layers such as thermal annealing, solvent additive processing, vapor annealing, and hot spin coating to optimize their morphology. But, these treatments are not favorable in

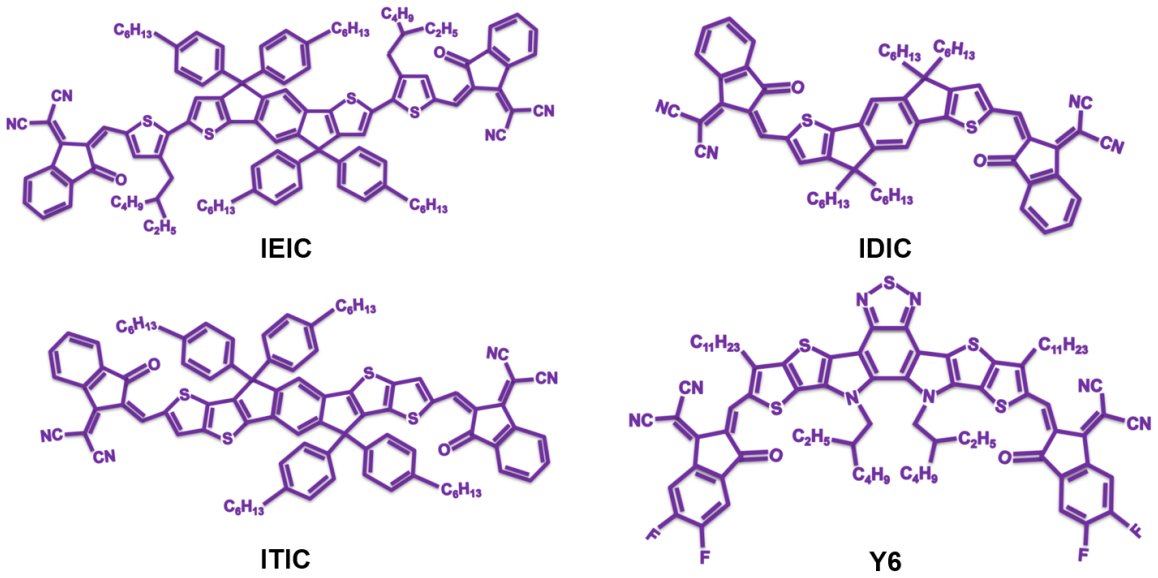

Figure 1.3: Chemical structures of highly efficient fused ring electron acceptors.

terms of their compatibility with the simple, low-cost industry-scale production of large-area solar cells. Thus, it is of great interest to develop high-performance OPVs based on as-cast films without additional treatments, which depends on the intrinsic morphological miscibility between donors and acceptors in active layers.

In 2012, Zhan and coworkers for the first time reported a novel acceptor, DC-IDT2T based on an IDT core, which when blended with a polymer donor yield a PCE of 3.93% without any post-treatment.[8] They also reported two novel A-D-A type molecules, IDT-2BM and IDTT-2BM with IDT and IDTT units as cores and strong electron-withdrawing group 2-(benzo[c][1,2,5]thiadiazol-4-ylmethylene)malanonitrile (BM) as the end-capping group. OPVs employing these acceptors achieved PSCs as high as 4.26% and 4.81%, respectively.[9] In 2015, they designed and synthesized IEIC based on indaceno[1,2-b:5,6-b′] and 2-(3-oxo-2,3-dihydroinden-1-ylidene) malononitrile (INCN) which exhibited good thermal stability, high extinction coefficients in the 500 - 750 nm region, deep LUMO energy level, and a relatively high electron mobility of 2.1 $\times$ 10^{-4} cm^2 V^{-1} s^{-1} when blended with PTB7-Th showed PCE up to 6.31%. Later, Yan and his team developed a large band gap polymer PffT2-FTAZ-2DT having complementary absorption to IEIC from 450 to 800 nm which led to a PCE of 7.3%.[102] Modifying IEIC, another efficient FREA, ITIC was then developed with rigid out-of-plane side-chains on to the fused rings, when blended with PTB7-Th yielded a PCE of 6.8%.[108] Lin and coworkers in 2016 blended ITIC with a medium gap polymer

donor J51 and demonstrated a PCE of 9.26% with a high fill factor (FF) of 69%.[52] Zhan and coworkers successfully developed ITIC-Th based on IDT core by modifying the phenyl side-chains of ITIC with thienyl side-chains. The device based on ITIC and a polymer donor PDBT-T1 exhibited a PCE of 9.6%.[109]

In 2016, the same group reported a planar IDT based FREA, IDIC whose blend with the donor polymer PTFBDT-BZS shows 11.39% of record efficiency when optimized by using DIO as the solvent additive.[111] This blend shows high IPCE in the near IR region and exhibits efficient as well as long-lived charge carrier generation when excited at 716 nm where IDIC absorbs. Later, it blended with a mid-band gap polymer based on benzodithiophene and difluorobenzotriazole units (FTAZ) to create OPVs with a power conversion efficiency of 12-13%.[110] This reflects the direct evidence for IDIC to be used as an excellent acceptor channel. We started our project "Photophysics of fused ring electron acceptors" with IDIC, which has provided a crucial breakthrough in the field of fullerene free acceptors and that makes our work unique and important. In 2017, Zhan and team designed and synthesized a series of FREAs, INIC1, INIC2, and INIC3 based on electron-rich fused-9-ring core, IBDT with 1-2 fluorine atoms connected at different positions of the end-capping moieties of the non-fluorinated counterpart INIC. The solar cell of INIC3 with the donor polymer FTAZ exhibited a PCE as high as 11.5% with a high electron mobility of 1.4×10^{-4} $cm^2V^{-1}s^{-1}$ and FF of 67%.[32] Later, they reported a fused tris(thienothiophene) (3TT) based FREA called FOIC, which when blended with two donor polymers in a ternary solar cell achieved a PCE of 13.1% in which long-range resonance energy transfer from donor to acceptor phases was confirmed.[98,99] In 2019, Yuan *et al.* reported a new class of non-fullerene acceptor Y6 that employs an electron-deficient-core-based central fused ring with a benzothiadiazole (BT) core.[189] OPVs made from Y6 and the polymer donor PBDB-T-2F delivered a record PCE of 15.7% with both conventional and inverted architecture.

1.1.3 Potential of non-fullerene OPVs

There are several factors determining the efficiency of a solar cell. The key factors include open-circuit voltage (V_{OC}), the maximum voltage available from a solar cell, short circuit current (J_{SC}), the current flowing through the cell with zero voltage and fill factor (FF) which is defined as the ratio of the maximum power from the solar cell to the product of V_{OC} and J_{SC}. In an OPV, to overcome the exciton binding energy, a large energy offset between the LUMO/HOMO energy levels is required

to provide the driving force for the charge separation. Since the driving force does not contribute to the V_{OC} of the cell, it accounts for an important part of the V_{loss} in OPVs.[195] Another crucial factor contributing to the V_{loss} is the non-radiative recombination of the charge carriers that substantially decreases the (EQE_{EL}) which is typically on the order of $10^{-6} - 10^{-8}$ for OPVs.[51] Efforts of decreasing V_{loss} and thereby increasing V_{OC} usually result in the reduction of J_{SC} and FF. This results in a trade-off between V_{OC} and J_{SC}/FF which has been a major issue for a long time. But there are several non-fullerene based OPVs reported with small V_{loss} without affecting J_{SC}/FF and thereby achieved V_{OC} of >1.1 eV. The main reason behind this is the large extinction coefficients of non-fullerene acceptors compared to that of the fullerene counterparts that increases the light-harvesting efficiency which favors J_{SC} without affecting V_{OC}. For instance, Liu *et al.* in 2016, reported an organic photovoltaic cell based on a non-fullerene acceptor, P3TEA:SF-PDI_2 with a negligible driving force of 0.05 eV, achieved an efficiency of 9.5%.[51] With such a small driving force, the blend cells still exhibited ultrafast charge generation with a characteristic exciton half lifetime of ∼3 ps and attained nearly 90% of internal quantum efficiency (IQE).[51] Here, the magnitude of the driving force is much smaller than the value 0.3 eV, that suggested for fullerene based solar cells to achieve efficient charge separation.[153] Meanwhile, Baran *et al.* reported that a combination of a low band gap polymer and a non-fullerene acceptor, PffBT4T-2DT:IDTBR achieved a PCE of 10% with a comparatively higher driving force than the SF-PDI_2 blend resulting in slow charge carrier generation, but with a high EQE_{EL} of the order of 10^{-3}, indicating very low degree of non-radiative recombination.[13]

Film morphology

Film morphology of the active layer materials has a major effect on the above mentioned key factors determining the solar cell efficiency. In the field of small molecular acceptors (SMA) design including fullerene acceptors, crystallinity is an important consideration as it favors the charge separation and transport.[195] However, high crystallinity can reduce the formation of the so-called bi-continues network which in turn increases the domain sizes over 20 nm. As organic semiconductors are characterized by limited exciton diffusion lengths, this can be a major issue in the process of free charge carrier generation.

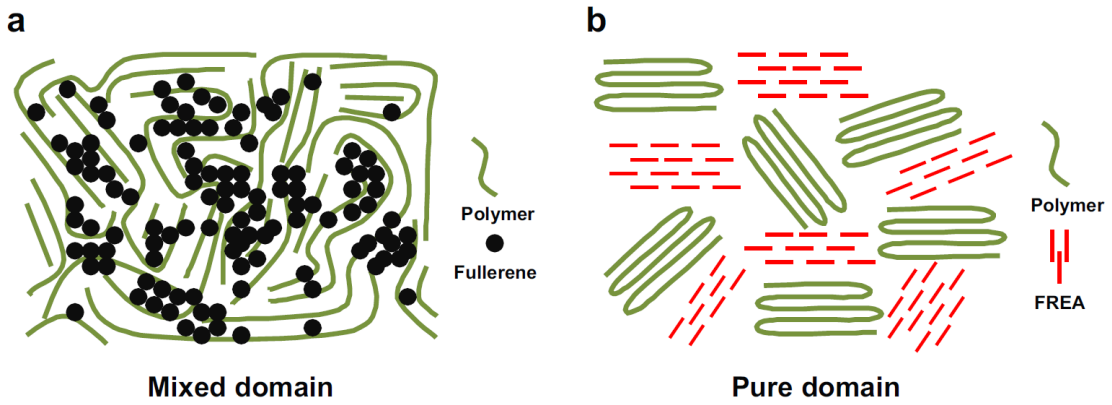

Figure 1.4: Comparison of morphologies in typical **(a)** fullerene based and **(b)** non-fullerene based OPVs.

Due to the 3-dimensional near ball-shaped structure of fullerene acceptors, polymer:fullerene domains are characterized by the presence of very close heterojunctions.[195] There have been a number of reports revealing the tendency of fullerene derivatives and donor polymers to form mixed phases (**Figure 1.4a**) at the interface between pure donor and pure acceptor phases, having domain sizes of the order of 5 - 20 nm.[2,27,130,166] This mixed-phase behavior is shown to have an impact on device performance. The close proximity of heterojunctions in this phase increases the rate of exciton dissociation and thereby the charge carriers are mostly generated promptly.[115,152] The disorder present in the mixed-phase would result in an increase in the HOMO level energy of the mixed donor compared to the pure semicrystalline donor, and a decrease in the LUMO of the mixed acceptor compared to the pure.[2] These changes in the energy levels would create favorable offsets to drive charges from the mixed-phase into more ordered pure phases and thereby increase the charge mobility.

On the other hand, non-fullerene acceptors especially FREAs are characterized by high crystallinity and packing orientation which produces relatively larger and pure domains in the blend systems (**Figure 1.4b**) with sizes in the range 20 - 50 nm reported.[185] The crystalline behavior of FREAs is directly related to the planarity of the core groups in the backbone that tighten the π - π stacking and favors the face-on orientation. Due to the rigid molecular backbone of these acceptor materials, after exciton dissociation at the donor-acceptor interfaces, free electrons can efficiently be transported due to the high electron mobility (10^{-4} - 10^{-2} cm^2 V^{-1} s^{-1}) of the crystalline phases which increases the overall device performance. Addition-

ally, the electron mobility of the FREAs can be tuned to match the hole mobility of the donors which can in turn favors the FF.[23] But the crystalline domains sometimes have a negative impact as they induce large phase separation which does not favor the exciton diffusion as the excitons have to cross larger distances to reach the interfaces. For instance, PDI based SMAs showed a strong tendency to aggregate into large-sized crystal domains because of their large and near planar structure.[198] Several modification methods have been used to reduce the self-aggregation of PDI so far, including the introduction of alkyl side-chains,[16] and design of twisted PDI dimers.[132] Similar to PDI based FREAs, IDT based FREAs also exhibit tunable planarity and crystallinity through the modifications of the fused ring cores, side-chains and end groups which can control the film morphology. While the reduced planarity and crystallinity can enhance the material solubility and exciton dissociation, they can also induce severe charge recombination.[23] So care should be taken while designing NFAs to get a balance between the optoelectronic properties and the morphology which controls the device performance. For instance, Dai *et al.* could successfully achieve this balance and thereby increased photovoltaic performance with their newly designed FREA having 8 fused rings, F8IC compared to its derivative with 10 fused rings, F10IC that possessed higher crystallinity than the other.[31]

Recently, we have studied exciton diffusion in an IDT based FREA, IDIC which when blended with a mid-band gap polymer FTAZ created OPVs with PCEs up to 12-13%.[18] X-ray scattering measurements of those blends revealed large and pure phases 20-50 nm in size, consistent with the observation that charge generation dynamics lacked the ultrafast component that characterizes most fullerene blends. Here we proved that the optimal phase size can be large due to facile exciton diffusion in the FREA by measuring the exciton diffusion coefficient in IDIC. The measured diffusion coefficient is at least 2×10^{-2} cm^{-2} s^{-1}, time-dependent, virtually independent of temperature and an order of magnitude higher than that of typical organic semiconductors. Enhanced 3D diffusion is shown to arise from molecular and packing factors; the rigid planar molecular structure is associated with low reorganization energy, aligned transition dipole moments, and low energetic and structural disorder - all enhancing long-range resonant energy transfer. This implies that although FREAs make pure and large domains in the blends, they can still attain good exciton dissociation rate at the interfaces due to extremely high exciton diffusion.

Device stability

For large scale industrial production, along with high efficiencies, long term stability also serves as an important factor for organic photovoltaic cells. There are several polymer-fullerene systems that have been reported with remarkable device stabilities, even achieving lifetimes of the order of a couple of years.[143] However, an initial rapid degradation in device efficiency termed "burn-in loss" has been observed in many polymer-fullerene systems which are originated in effect from photo-induced reactions in the active layer and formation of sub-band gap states.[97,128,144,195] For instance, the PCDTBT-$PC_{70}BM$ device experienced a burn-in loss up to 25% over the first 100 hours of operation predominantly through a decrease in FF and V_{OC} and to a lesser extent the J_{SC}.[144] Recently, researchers have come out with different burn-in free organic photovoltaic cells based on non-fullerene acceptors.[17,55,72] Gasparini *et al.* in 2017 reported a solution-processed OPV based on an IDT based FREA, IDTBR which exhibits a burn-in loss of only 5% in PCE in the course of 2000 hour exposure of light.[55] This is in stark contrast to the PCBM based device whose PCE shows a burn-in that extends over hundreds of hours and levels off at a loss of ∼34% (**Figure 1.5**). Similarly, Cha and coworkers reported a FREA based OPV, PffBT4T-2OD:EH-IDTBR while encapsulated show negligible efficiency loss compared to the PffBT4T-2OD:$PC_{71}BM$ device which exhibited significant burn-in degradation due to the trap-assisted recombination through increased photo-induced trap states.[17] **Figure 1.5** presents a comparison of the solar cell stability between a FREA based OPV, P3HT:O-IDTBR and other high-performance polymer:fullerene systems, studied by Holliday *et al.* in 2016.[72] These research outcomes show the potential of non-fullerene acceptors as good alternatives for reducing burn-in losses in OPVs.

Cost of production

Besides the potential of reaching high stability, non-fullerene OPVs are highly attractive for their low cost of production compared to that of the fullerene based equivalents. High purity fullerene derivatives like $PC_{71}BM$, $PC_{61}BM$ etc. are very expensive due to the high cost of fullerene raw materials. Furthermore, in many practical applications, fullerenes are required at a purity >98% by weight, which necessitates multiple purification techniques requiring significant energy consumption and solvent costs.[5,167] Meanwhile, properly designed non-fullerene acceptors could greatly reduce

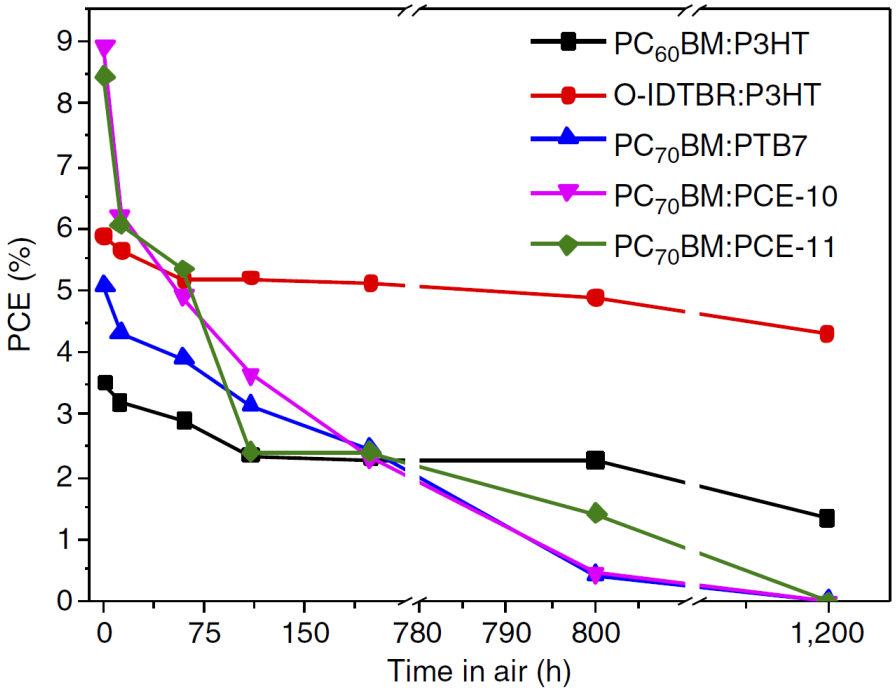

Figure 1.5: Comparison of PCE losses between a non-fullerene based OPV, P3HT:O-IDTBR and high-performance fullerene based OPVs in the course of 1200 hours of light exposure. The figure is adapted from Holliday *et al.*[72]

synthetic and purification costs, compared to fullerenes.[195] For instance, perylene diimide (PDI)-based acceptors can be synthesized from low cost raw materials and be purified *via* inexpensive and scalable re-crystallization processes.[69] PDI-based materials are widely used in industries as pigments and provide superb thermal and photochemical stabilities. These features make non-fullerene based OPVs, more promising candidates for solar energy harvesting.

1.2 Exciton physics

The primary photoexcitations of an organic semiconductor are bound, electron-hole pairs called excitons. They are electrically neutral quasiparticles which can transport energy without transporting net electric charge. On absorption of photons, electrons in HOMO (ground state) are promoted to LUMO (excited) levels, leaving behind positively charged holes in the HOMO. These holes and excited electrons stay together in pairs by the Coulombic force of attraction and form excitons. Compared to the inorganic counterparts, excitons in organic semiconductors are Frenkel type having large binding energies of the order of 0.5 - 1 eV as a consequence of low dielectric screening.

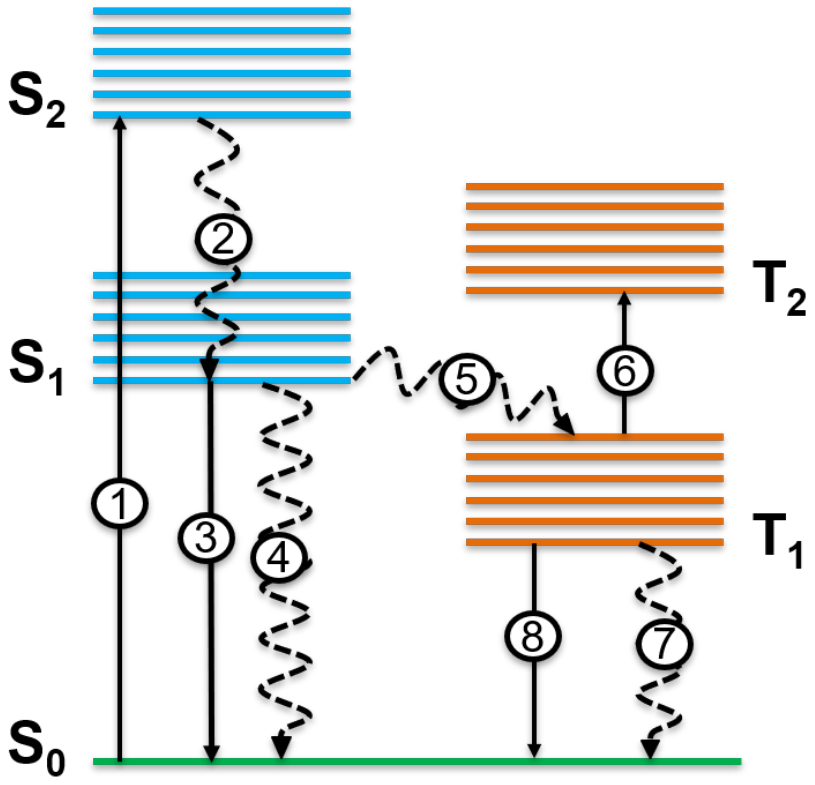

Figure 1.6: Jablonski diagram of possible electronic transitions in an organic semiconductor. (1) absorption, (3) fluorescence, (5) intersystem crossing, (6) photo-induced absorption, (8) phosphorescence, and (2), (4), (7) are non-radiative transitions. Here S and T represent singlet and triplet states, respectively.

The ground state of most of the organic semiconductors is characterized by having net spin-zero. **Figure 1.6** shows the Jablonski diagram for possible electronic transitions in a molecule. According to the figure, there are two types of electronic states in a molecule: singlet (S) and triplet (T) states. When an electron is promoted from the ground state to the excited state, if the states are of net spin-zero, they are called singlet states and the resulting excitons are singlet excitons. The electrons can also make higher singlet state transitions. The radiative emission from the first singlet excited state is called fluorescence. Typical fluorescent lifetimes of organic semiconductors fall in the range of nanoseconds (ns) to microseconds (μs). Singlet excitons can also decay non-radiatively to the ground state *via* processes such as internal conversion, pre-dissociation, and dissociation which decrease the fluorescent quantum yield of the material.

Similarly, excited states with net spin 1 are called triplet excited states and the

generated excitons are called triplet excitons. Since a singlet ground state and a triplet excited state have different spin multiplicities, on photon absorption, a direct transition between these states is forbidden and thereby triplet excitonic states are less probable in a molecule. Meanwhile, they can form *via* intersystem crossing which is a non-radiative transition from a singlet excited state to a triplet state or *vice versa* that includes a spin-flip of the excited electron. This is possible only by some perturbation, where the triplet state wavefunction obtains some contribution from a singlet state wavefunction and *vice versa*. Such a perturbation is provided by the mechanism of spin-orbit coupling where the change in the spin angular momentum (s) during the transition is compensated for by an opposite change in the orbital angular momentum so that the total angular momentum $j = l + s$ is conserved during the optical transition.[89] Since for atoms, the perturbing Hamiltonian of spin-orbit interaction H_{SO} is proportional to the fourth power of the atomic charge, intersystem crossing is commonly observed in heavy atom-based molecules. Moreover, according to El-Sayed rule, the rate of intersystem crossing is relatively large if the radiationless transition involves a change in orbital type.[125] For instance, the rules predict $^1(\pi, \pi^*)$ $\rightarrow$ $^3(n, \pi^*)$ transition to be faster than $^1(\pi, \pi^*)$ $\rightarrow$ $^3(\pi, \pi^*)$ transition and $^1(n, \pi^*)$ $\rightarrow$ $^3(\pi, \pi^*)$ transition to be faster than $^1(n, \pi^*)$ $\rightarrow$ $^3(n, \pi^*)$ transition. The radiative deactivation of the triplet excited state is called phosphorescence. Since triplet state has a long lifetime (10^{-4} to 10 s), as the electron will not fall to the ground singlet state until it flips back to its original spin state, phosphorescence will persist for some time even after the excitation is stopped.

1.2.1 Energy transfer mechanism

Excitons can move from an excited donor (D) molecule to an acceptor (A) molecule through the process of non-radiative energy transfer. At the end of this process, the donor molecule is in the ground state and the acceptor molecule is in the excited state.[93] There are mainly two types of energy transfer mechanisms. One is Förster resonance energy transfer (FRET) and the other is Dexter energy transfer.

Förster transfer is an electrodynamic phenomenon that occurs as a result of the long-range dipole-dipole interactions between the excitons in excited and ground states when there is a spectral overlap between the absorption of the acceptor and the emission of the donor.[93] The term resonant energy transfer is preferred because the process does not involve the appearance of a photon.[93] The rate of energy transfer decreases with the distance, d, between donor and acceptor as d^{-6},[93]

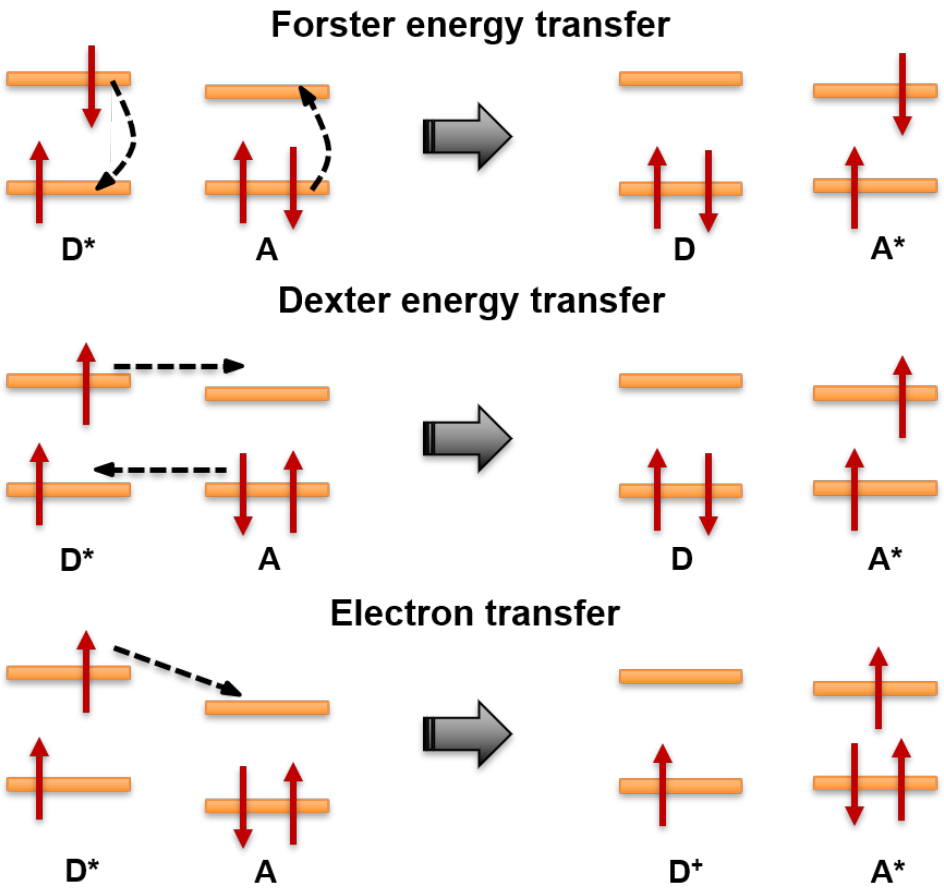

Figure 1.7: Förster and Dexter energy transfer mechanisms in OPVs. Here the horizontal lines represent HOMO and LUMO energy levels of the donor (D) and acceptor (A) molecules; the asterisk denotes an excited state.

$$K_F(d) = \frac{1}{\tau_D}\frac{R_0^6}{d^6} \tag{1.1}$$

where τ_D is the lifetime of the donor in the absence of acceptor. The RET radius R_0, which is the distance at which the energy transfer efficiency is 50%, is given by,[93]

$$R_0^6 = \frac{9000(\ln 10)\kappa^2 Q_D}{128\pi^5 N_{AV}\eta^4}\int_0^\infty F(\lambda)\epsilon(\lambda)\lambda^4 d\lambda \tag{1.2}$$

The value of R_0 strongly depends on the spectral overlap integral between the emission $\mathrm{F}(\lambda)$ (in this case, the fluorescent spectrum is normalized such that $\int \mathrm{F}(\lambda) = 1$) and the $\epsilon(\lambda)$ (in the units of molar extinction coefficient $\mathrm{M}^{-1}\mathrm{cm}^{-1}$), the quantum

yield of the donor Q_D, the refractive index of the medium η and the relative orientation between the emissive and absorptive dipoles (κ^2). Here the orientation factor κ^2 takes the value 4 when the transition dipoles are head to tail oriented and will be 1 for parallel dipoles. FRET is more common for singlet excitons than triplet excitons; however, triplets located at a phosphorescent donor can undergo FRET. FRET has become widely used in all applications of fluorescence including optical imaging, medical diagnosis, photosynthesis, and DNA analysis.[93] So far, FRET radii of the range 2 - 6 nm have been reported for different materials.[18,121]

Dexter energy transfer involves the direct exchange of electrons between donor and acceptor molecules. This is a short-range (D - A distances <1nm) energy transfer mechanism that happens when there is a significant overlap between the molecular orbitals wavefunctions.[135] Both singlet and triplet excitons can be transferred *via* Dexter mechanism and its efficiency exponentially decreases with the D - A distance d, giving the transfer rate,[141]

$$K_D(r) = KJ \exp(-2d/L) \tag{1.3}$$

where K is related to specific orbital interaction, J is the normalized spectral overlap integral, and L is the van der Waals radius. In contrast to Förster transfer, the rate of Dexter transfer does not depend on the magnitude of the extinction coefficient of the acceptor molecule.[134] Since, Dexter energy transfer occurs by the actual physical exchange of electrons, non-radiative states can also take part in the process, and thereby triplet excitons can also migrate *via* this mechanism without an additional need of intersystem crossing.[134,142] Excitons can also migrate *via* a radiative energy transfer process called cascade transfer. This includes the emission and the simultaneous absorption of a photon between two molecules. Cascade transfer is a long-range energy transfer mechanism that relies on the spectral overlap between the absorption and emission of molecules and happens in the range comparable to the absorption length of the material.[134]

If the driving force in an OPV defined by the difference in LUMO/HOMO energies of the donor and acceptor molecules is large enough to overcome the exciton binding energy, then exciton dissociation happens and electron transfer occurs from donor to acceptor. If this is the case, then there can be a competition between energy and

electron transfer processes.[141] Electron transfer is a short-range process that depends on the spatial overlap of the electron donor and the acceptor wavefunctions. The result will be a positively charged donor and negatively charged acceptor molecule as shown in **Figure 1.7**. Hole transfer is also possible if the HOMO levels of the donor and acceptor phases are properly aligned.[135,141]

1.2.2 Exciton diffusion model

In order to generate photo-current, excitons have to diffuse from the position where they are created to the donor-acceptor interface to become dissociated. Several models are used to describe the diffusion of excitons and they have varying degrees of complexity. Generally, the diffusion process can be described as a random walk in the limit of many steps.[145] If the distance between successive hops (mean-free path) is of the order of the lattice spacing of the material, then the excitons hop incoherently through the lattice and are scattered at each molecule. In this case, the diffusion coefficient is a function of lattice spacing and hopping time.[145] On the other hand, if the hopping distance is greater than the lattice spacing, excitons move coherently over several lattice spacings before getting scattered from a molecule and here the diffusion coefficient is expressed in terms of the mean- free path and the exciton velocity.[145] At room temperature, for most of the organic semiconductors, the incoherent exciton hopping model is preferred and is facilitated by the Förster or Dexter energy transfers described above.[141,145]

Based on the hopping model, exciton diffusion process in the donor material of an OPV blend is modelled with a second-order differential equation, where second-order processes like exciton-exciton annihilation and singlet fission are omitted and is given by,[119,134]

$$\frac{\partial n}{\partial t} = D\nabla^2 n(r_i) - \frac{n(r_i)}{\tau} + G(r_i) - n(r_i)k_F(d) \tag{1.4}$$

where n is the exciton density, D is the exciton diffusion coefficient, τ is the exciton lifetime, r is the position at point i, G is the exciton generation rate and k_F is the donor-acceptor Förster energy transfer rate. Here the first term in the RHS represents the exciton migration by diffusion, the second term gives the fraction of excitons naturally decayed, the third term quantifies the exciton generation rate by light absorption and the last term includes the donor-acceptor resonance energy transfer rate.[134] The

exciton diffusion length, the distance over which excitons travel before they decay is given by,

$$L_D = \sqrt{D\tau} \tag{1.5}$$

where τ is the exciton lifetime. According to the dimensionality of the exciton diffusion, sometimes coefficient of $\sqrt{1}$, $\sqrt{2}$ or $\sqrt{3}$ is added to the equation for 1, 2 or 3-dimensions, respectively. Typical values of exciton diffusion constants in organic semiconductors fall in the range 10^{-4} to 10^{-2} cm^2 s^{-1} for singlet excitons and 10^{-6} to 10^{-3} cm^2 s^{-1} for triplet excitons.[135] Exciton diffusion lengths are reported in the range of ∼5 - 20 nm for singlet excitons and ∼30 - 300 nm for triplet excitons.[135]

1.2.3 Temperature dependence of exciton diffusion

As most organic semiconductors, especially polymers, are morphologically disordered, they possess an inhomogeneously broadened density of excitonic states (DOS). This energy distribution can be approximated as a Gaussian line shape having a half-width σ which represents the measure of disorder present in the material. Once the molecule gets excited to the high energy tail of the Gaussian DOS, they lose the excess energy by undergoing a downhill migration (thermalization) towards the lower energy states. This thermalization procedure stops as they reach the level of the most populated state corresponding to the energy $-\sigma^2/KT$ which represents the 0 - 0 peak in the emission spectrum.[136] At lower temperatures, the position of the most populated state is in the low energy tail of the DOS, while at higher temperatures, which will move to the middle of the DOS, as the excitons are thermally disturbed. Corresponding to the change in the position of the most populated state with temperature, the PL spectrum suffers a blue shift.[136,164]

Figure 1.8 shows the temperature dependence of the steady-state PL spectrum of a conjugated polymer MDMO-PPV reported by Mikhenko *et al.* in 2008.[136] At lower temperatures, the T-dependence of the PL spectrum is weak because at these temperatures, the energy separation between the most populated state and its nearest neighbors is large and thereby phonons of high energy are needed to pull it up. At higher temperatures, enough phonons are present to blue shift the most populated states and thereby the PL spectrum suffers considerable T - dependence.

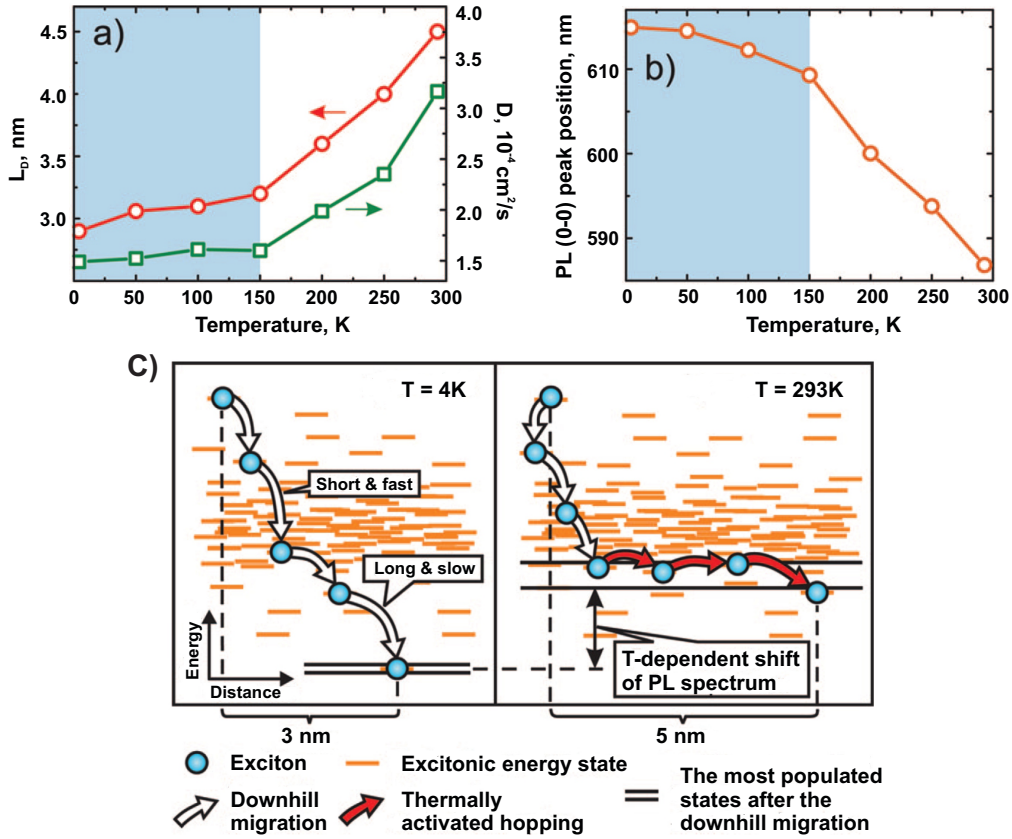

Figure 1.8: Temperature dependence of (a) exciton diffusion length L_D and the diffusion coefficient, (b) steady-state spectrum peak position and (C) schematic illustrating the mechanism behind the temperature dependence of exciton diffusion. The figures are adapted from Mikhnenko *et al.*[136]

The authors used the same physical framework to explain the corresponding temperature regimes of D and L_D. Once formed, excitons undergo downhill migration to the most populated states. But from there, further hopping requires absorption or emission of phonons and therefore, temperature dependence comes into play. At lower temperatures, the diffusion will be limited by the downhill migration process which is only weakly temperature dependent.[136] As temperature increases, exciton - phonon coupling becomes larger and excitons starts to migrate *via* thermally activated hopping.[136,164] This process does not change the exciton energy significantly but contributes to their diffusion. Indeed, the temperature dependence of exciton diffusion becomes strong above 150 K. Thus, at higher temperatures, exciton diffusion becomes a two-step process, downhill migration and thermally activated hopping.

1.2.4 Exciton-exciton annihilation

Exciton-exciton annihilation is suggested as a loss mechanism in OPVs. The occurrence of high exciton densities and exciton diffusion processes increases the chance of different excitons meeting each other during their lifetime.[135] For instance, in singlet-singlet exciton annihilation process, a pair of S_1 excitons interact with each other resulting in one gaining energy and being promoted to a high energy state (S_n). Meanwhile, the other exciton loses energy and is deactivated to the ground state S_0. Similarly, triplet-triplet annihilation is also possible which may result in a ground state exciton (S_0) and an excited singlet exciton.

$$\begin{aligned} S_1 + S_1 &\rightarrow S_0 + S_n \\ T_1 + T_1 &\rightarrow S_0 + S_n \end{aligned} \tag{1.6}$$

Here the newly-formed high energy exciton can either relax back into the S_1 state or it can ionize into an electron and a hole. In small molecules, the probability of ionization is quite small, if it does occur, geminate recombination of the generated charge carriers tends to reform singlet excitons. However, in conjugated polymers, the charges are considerably more mobile, and so geminate recombination might be less likely. The interaction process between two excitons can occur either by a collision like process which is diffusion-limited or by non-radiative energy transfer processes like FRET.

1.2.5 Singlet exciton diffusion measurements in organic semiconductors

There are several spectroscopic techniques available to extract exciton diffusion coefficients and exciton diffusion lengths. They include fluorescence quenching in bilayers, exciton-exciton annihilation measurements, fluorescence volume quenching, microwave conductivity, and electro-optic measurements. Mikhnenko *et al.* provided a good summary of all the available techniques and discussed the advantages and pitfalls of each technique.[135] This section includes a brief literature review on exciton diffusion measurements in selected organic semiconductors exhibited high exciton diffusion parameters.

As per the studies so far, singlet exciton diffusion constants of the order of 10^{-3} cm^2 s^{-1} have been a common constraint of organic photovoltaic (OPV) materials

throughout many generations of material advances. In 1997, Gregg *et al.* conducted exciton diffusion measurements in polycrystalline films of bis(phenethylimide), PPEI, using the fluorescence quenching method and reported one of the longest exciton diffusion lengths of 2.5 μm.[60] Haugeneder *et al.* studied exciton diffusion and dissociation in LPPP:fullerene blends and hetero-structures using photoluminescence (PL) and ultrafast transient absorption spectroscopy.[65] From pump-probe measurements of the blend, they found an exciton diffusion length of 6 nm by modeling the stimulated emission decays with singlet exciton rate equation. For hetero-structures, they modelled fullerene thickness dependent PL decays with the continuity equation and extracted a diffusion coefficient of 4.42×10^{-2} cm^2 s^{-1} and diffusion length of 14 nm. Carlos Silva and coworkers reported a high diffusion coefficient of 1×10^{-2} cm^2 s^{-1} for blue-emitting poly-2,8-indenofluorene (PIF) using exciton - exciton annihilation measurements.[158] In 2001, Stevens *et al.* presented pump-probe studies on semiconductor conjugated polymers, poly(9,9-dioctylfluorene) (F8) and poly(9,9-dioctylfluorene-co-benzothiadiazole) (F8BT) where they used exciton - exciton annihilation measurements to extract diffusion coefficients.[160] They reported high diffusion coefficients of 2.6×10^{-4} cm^2 s^{-1} and 2×10^{-2} cm^2 s^{-1} for F8BT and F8, respectively.

Engel *et al.* recorded a quasi - 1 - dimensional exciton diffusion coefficient of 4×10^{-2} cm^2 s^{-1} with a diffusion length of 61 nm for an organic semiconductor PTCDA from Förster assisted exciton - exciton annihilation measurements.[43] The same method was used by Lewis *et al.* to extract an exciton diffusion coefficient of 3×10^{-3} cm^2 s^{-1} for MEH - PPV films.[95] A high exciton diffusion constant was reported for P3HT ($D = 1 \times 10^{-2}$ cm^2 s^{-1}) by Cook *et al.*, but this study revealed that exciton diffusion is only so high on early timescales, and not sustained when excitons relax through the density of states.[28] Shaw *et al.* in 2008 revealed that the exciton diffusion constant for P3HT under quasi-equilibrium conditions is lower at $D = 1.8 \times 10^{-3}$ cm^2 s^{-1}.[156] Photocurrent spectroscopy is employed to study exciton diffusion in the light emitting organic thin films TPD and Alq_3 by Yang *et al.* in 2009.[181] The diffusion coefficients and diffusion lengths derived are 1.53×10^{-3} cm^2 s^{-1} and 17 nm for TPD and 4×10^{-5} cm^2 s^{-1} and 8 nm for Alq_3, respectively. Marciniak *et al.* studied J-aggregates of perylene bisimide dyes using transient absorption spectroscopy and evaluated a 1 - dimensional diffusion coefficient of 1.3×10^{-2} cm^2 s^{-1} and a diffusion length of 96 nm.[124] Exciton diffusion in ladder-type methyl-substituted polyparaphenylene films was investigated by Gulbinas and coworkers in 2014 and reported a diffusion constant

of 4.3 $\times 10^{-3}$ cm^2 s^{-1}.[61] Hedley *et al.* reported a diffusion coefficient of 1.6 $\times$ 10^{-4} cm^2 s^{-1} for $PC_{71}BM$ films using the PL quenching method.[67]

1.2.6 Factors limiting exciton diffusion length

As exciton diffusion length (L_D) is the critical parameter affecting the device performance of organic photovoltaic cells (OPVs) and organic light-emitting diodes (OLEDs), we should be aware of the factors limiting diffusion length to improve device efficiency. By controlling factors like the degree of crystallinity, Stokes shift, rate of non-radiative energy transfer and degree of disorder that restricts the number of defects or impurity sites and non-radiative decay channels, L_D can be effectively controlled.

Regarding crystallinity, Lunt *et al.* studied exciton diffusion in an archetypal organic semiconductor, PTCDA, in which the diffusion length is increased nearly fourfold over that of corresponding amorphous films when the extent of crystalline order in the film is increased.[120] Here the enhancement in L_D is attributed to the reduction in non-radiative losses at the grain boundaries while increasing the crystal domain size. Similar work has been done by Sim *et al.* on the novel polymer P3HT where they observed an increase in L_D from 3 to 7 nm when the mean crystal size is increased more than twice *via* thermal annealing.[159] The enhanced crystalline order improved the spectral overlap integral and brought the chromophores closer to one another, thereby increased the rate of Förster assisted exciton diffusion. Lin and coworkers in 2014 did a thorough investigation on the dependence of L_D on molecular ordering where they used six experimental methods to study the exciton diffusion in phenyl substituted diketopyrrolopyrrole (DPP) small molecules having different conjugation lengths.[103] It is shown that the L_D in DPP molecules improved from 9 to 13 nm as the conjugation length is decreased which led to an increase in the molecular ordering. Recently, exciton diffusion studies on a FREA, IDIC from our group reported an extraordinarily high diffusion coefficient of the order of $\sim 10^{-2}$ cm^2 s^{-1} with an L_D of at least 16 nm, mainly arised from its rigid molecular packing associated with low reorganization energy, good transition dipole moment alignment, and low energetic and structural disorder - all enhancing long-range resonant energy transfer.[18]

In contrast, there are studies reporting the adverse effect of thermal annealing (which usually improves the crystallinity of phase-separated domains and thereby increases L_D) on exciton diffusion lengths.[88,138] For instance, Mikhnenko *et al.* reported that L_D in the annealed polycrystalline films of C_6PT_2-DPP is 3 times shorter than that

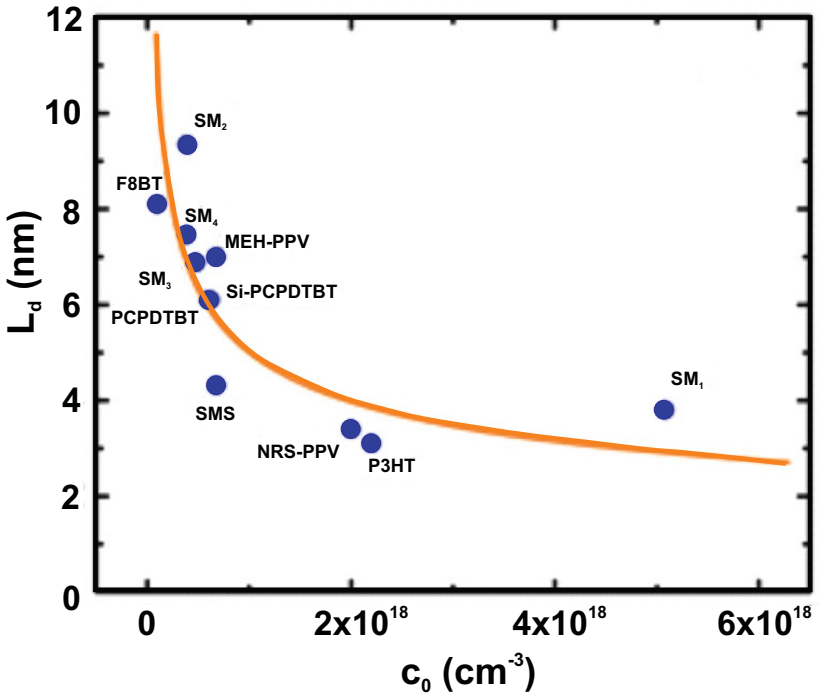

Figure 1.9: Effect of concentration of trap density on one-dimensional exciton diffusion lengths of various organic semiconductors. The solid curve gives the trap limited diffusion lengths calculated from $L_{D,trap} = (2\sqrt[3]{c_0})^{-1}$. The figure is adapted from Mikhnenko *et al.*[137]

of the as-cast amorphous films.[138] This unusual trend is attributed to the exciton delocalization effects and exciton quenching at the grain boundaries of the polycrystalline film. Despite this, the OPV cells formed from annealed C_6PT_2-DPP and C_{70} exhibit PCEs much higher than that of the as-cast devices showing there is not a simple direct correlation between L_D and the overall final performance of a BHJ cell. Here the annealing would improve the film morphology and charge carrier mobility, those compensated for the reduction of L_D.[138]

Another important factor that limits the exciton diffusion in organic semiconductors is the presence of extrinsic quenching defects or traps. Mikhnenko *et al.* investigated the amount of exciton quenching traps in a range of solution-processed organic semiconductors - 6 conjugated polymers and 5 small molecules - using Stern-Volmer analysis and Monte-Carlo simulation.[137] **Figure 1.9**, a plot of 1 - dimensional diffusion lengths versus exciton trap density, summarizes their observations. Here they experimentally extracted exciton diffusion lengths which closely matched the calculated trap limited exciton diffusion lengths ($L_{D,trap} = (2\sqrt[3]{c_0})^{-1}$), represented by the

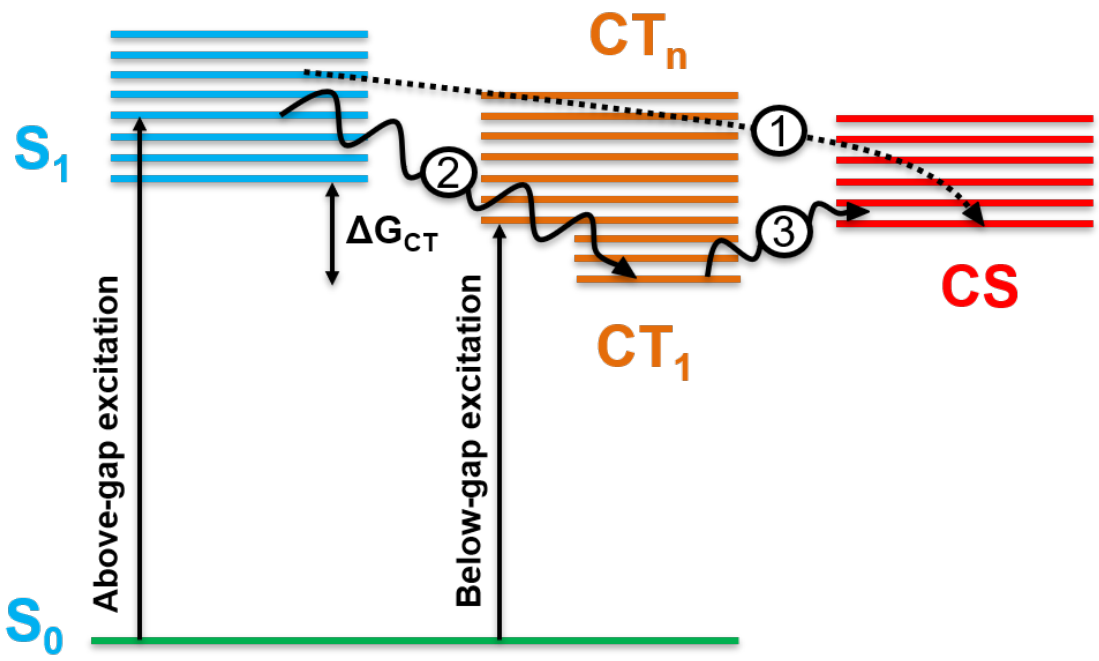

Figure 1.10: Energy diagram showing different possibilities of charge generation. (1) direct dissociation of the hot CT state into the CS state, (2) thermalization of the hot into the relaxed CT state and then dissociate (3) into the CS state.

orange curve. Most of the materials followed a trend that those having a high density of excitonic traps exhibit shorter exciton diffusion lengths and *vice versa*. Moreover, materials with the better molecular arrangement, thereby having higher diffusion coefficients, excitons are able to meet the defect sites quickly, resulting in shorter lifetimes, but maintaining a constant L_D value.[137]

1.3 Exciton to charge conversion

As already mentioned, the central role for the function of an organic photovoltaic cell is played by the bound electron-hole pair states called charge transfer (CT) complexes residing at the donor-acceptor heterointerface. They act as a crucial intermediate step between the singlet exciton dissociation and free charge generation.[37] A common view of charge generation is that the CT excitons formed on photon absorption should overcome the Coulombic potential of attraction between the electron and the hole, given by,

$$V = \frac{e^2}{4\pi\epsilon_r\epsilon_0 r} \tag{1.7}$$

where e is the charge of the electron, ϵ_r is the dielectric permittivity of the organic medium, ϵ_0 is the dielectric permittivity of the free space, and r is the electron-hole distance. For organic semiconductors, this attraction is difficult to overcome as they have low dielectric permittivity (ϵ_r = 2 - 4) compared to the inorganic materials (ϵ_r ~11). An additional complication is introduced by the localized nature of the electronic states in organic materials and thereby small values of r.[141] Otherwise, geminate recombination (radiative or non-radiative recombination electron-hole pair) of excitons will compete with the charge generation process.

There have been a lot of controversial debates on the dissociation of charge transfer (CT) excitons to form free charges. As mentioned earlier, CT states are generated at the donor-acceptor interface as a result of charge transfer with the excess thermal energy of (ΔG_{CT}) due to the energy difference between the exciton and the CT state (**Figure 1.10**).[50] CT states with excess thermal energy are called hot CT states (CT_n). They can either dissociate into free charge carriers (charge separated (CS) state) or thermalize to lower CT states and then undergo dissociation. Literature support both the cases and thus it has become a long-lasting debate among OPV scientists whether charges are forming from hot or relaxed CT states.

1.3.1 Charge generation from hot CT states

In the hot CT state theory, the excess thermal energy present acts as the driving force for CT state dissociation before they deactivate to the relaxed states. Here the dissociation process will compete with the ultrafast thermalization process that happens in several hundred femtoseconds.[50,170] For efficient charge generation from hot CT states, their dissociation time scale should be at least similar to that of the thermalization process. It has been reported that charge generation in OPVs is ultrafast and can happen in the time range of 50 fs.[58] As the theory suggests, the excitons that have relaxed to the ground CT states can not take part in photocurrent generation because of the poor driving force for dissociation.[50] In 2012, Grancini *et al.* studied ultrafast dynamics in PCPDTBT:$PC_{60}BM$ blends and demonstrated that both CT states and free charges are generated in the first tens of femtoseconds after photoexcitation from singlet exciton quenching.[58] They selectively excited the S_1 - S_4 singlet states in the blend and proved that the excess photon energy with respect to the optical band gap is not totally wasted, instead, it allows the formation of hot interfacial CT states which are more delocalized and thus more prone to ultrafast charge separation. Similarly, Drori and coworkers reported that the CT complex generated

upon below gap excitation is more localized and having much slower recombination kinetics compared to that produced from above gap excitation.[40]

1.3.2 Charge generation from relaxed CT states

If the relaxed CT states act as the precursor for the charge generation, then the driving force for exciton dissociation is not direct as in the case of hot CT states. According to Braun-Onsagar (BO) model, the CT state dissociation rate (k) depends on a set of physical parameters including electric field (F), temperature (T), mobility of electrons (μ_e), and holes (μ_h) given by,[37]

$$k(a,T,F) = \frac{q}{\epsilon_0 \epsilon_r} < \mu_e + \mu_h > \frac{3}{4\pi a^3} \exp\left(-E_b/k_B T\right) J_1(2\sqrt{-2b})/(\sqrt{2b}) \qquad (1.8)$$

where $k_B T$ is the thermal energy, $b = q^3 F/(8\pi\epsilon_0\epsilon_r k_B^2 T^2)$ and J_1 is the Bessel function of order 1. Despite, there being some modifications added to the BO model, the CT state dissociation rate always depends on the same set of parameters. Among these parameters, the easiest one to test is the effect of electric field on CT state dissociation which has been performed by several groups in different polymer:fullerene systems.[63,76,168,169,202] For instance, Tvingstedt *et al.* in 2010, investigated the effect of electric field on the dissociation of both Frenkel and intermolecular CT excitons in three different polymer:fullerene BHJs through luminescence quenching.[168] They reported strong evidence supporting the prevention of radiative recombination of both types of excitons by the application of the electric field. However, it is also observed that the CT state radiative quenching rate is marginal and no longer matched with the photocurrent measured under normal device operation conditions (for electric fields less than $\sim 10^7$ V/m). This observation contradicts the fact that polymer:fullerene systems are characterized by high photocurrents at normal electric fields suggesting an efficient CT dissociation rate. The possible reason for this contradiction could be due to a high fraction of the photocurrent being generated from the non-emissive CT precursors which do not produce luminescence. This result is similar to what Inal *et al.* found in their M3EH-PPV:PHVBT (polymer:small molecule) system.[76] Electric field dependent transient absorption (TA) spectroscopy is also explored to investigate the CT dissociation in OPVs. For instance, Marsh *et al.* in 2010 did bias dependent TA measurements on P3HT:$PC_{60}BM$ devices, where they detected long-lived charge carriers at larger electric fields (in the normal device operation regime), suggesting the facilitation of CT dissociation by the applied field, thereby enhanced

charge generation.[127] Similar measurements were performed by the same group on PCDTBT:$PC_{70}BM$ devices where they got similar findings.[47]

The temperature dependence of the CT state dissociation process seems to be more complicated than the electric field dependence as the temperature has a crucial effect on the charge carrier hopping rates. According to the equation 1.8, the CT state dissociation rate decreases exponentially with decreasing temperature which implies a significant decrease in the photocurrent at lower temperatures. However, there are reports revealing notable values of photocurrent at lower temperatures.[24,57] This is explained by the fact that the CT state lifetime increases with decreasing temperature, which in turn makes the dissociation probability still high at low temperatures. Along with the temperature dependence of photocurrent, it is worthy to inspect the temperature dependence of open circuit voltage (V_{OC}) where all the charge carriers recombine and no charge transport issue is involved.[50] A common trend in BHJ OPVs is the linear decrease of V_{OC} with increase in temperature which is attributed to the temperature dependent charge-carrier mobility.[25,82,83] However, there are reports revealing the deviation of linear dependence of V_{OC} on temperature. For instance, Rand *et al.* observed V_{OC} saturation near 150 K in a number of small molecular OPVs which is ascribed to the decrease in photocurrent density because of the decreased electron transfer rate from the donor to acceptor phases.[147]

The third factor influences the CT state dissociation process is the mobilities of electrons and holes. In macroscopic modeling, electron and hole mobilities are usually fitted from the space-charge-limited current regime of the single-carrier devices.[90,91] However, there are reports noting that the mobilities extracted in this way might be significantly underestimating the real local mobilities during the CT dissociation process.[50] For instance, Veldman *et al.* determined that in high concentration, $PC_{60}BM$ can form clusters in their devices. So, they used a high value of electron mobility measured in the micro-crystalline $PC_{60}BM$ powder in their modeling which well described their data.[169] Recently, Burke *et al.* pointed out that it is the high local mobility (such as measured from time-resolved terahertz spectroscopy) that is crucial in the CT dissociation process.[15] They could well reproduce the charge carrier generation employing the kinetics Monte-Carlo simulations using the high mobility values.

In the BO model, the effect of energetic and spacial disorder is neglected. But,

theoretical and experimental results so far suggest that disorder has important implications on the charge generation process. Albreht and Bassler in 1995 reported that charge generation could be favored by the disorder.[3] McMahon *et al.* investigated the electronic and geometric structure of P3HT:PCBM cells using a combination of classical and quantum simulation methods where they found that the exciton and holes are repelled by the disordered donor-acceptor interfaces.[131] The result provided a possible explanation of the low recombination efficiency and supported the direct formation of "quasi-free" charge separated species at the interface. Similarly, D'Avino *et al.* reported that the charge separation process is an energetically favorable process for about 50% of the interfacial excitons, explaining the high internal quantum efficiency (IQE) exhibited by P3HT:PCBM heterojunctions.[33] An experimental evidence for the effect of disorder on CT state dissociation was proved by Vithanage *et al.* where they employed the time-resolved electric field-induced second harmonic (TREF-ISH) technique to probe the electric field dynamics of the separated carriers.[1] Second harmonic generation (SHG) is a second order nonlinear process where two photons are summed into a photon of double the energy. The efficiency of SHG depends on the electric field and hence serves as a measure of changes in the electric field. They then used numerical simulations to show that fast 3-dimensional charge diffusion within an energetically disordered medium, increasing the entropy of the system, is sufficient to drive the charge-separation process.

1.4 Research questions addressed in this thesis

As fused ring electron acceptors are an emerging candidates in the field of organic photovoltaics, many outstanding questions regarding their photophysics are yet to be answered. Among them, the questions having supreme importance are answered in this thesis.

- Why FREA based OPV systems possess excellent exciton dissociation efficiencies at the donor-acceptor interfaces regardless of large domain sizes and short exciton lifetimes in FREAs?
- What is the main mechanism behind the high exciton mobilities in fused ring electron acceptors? What are the molecular factors influencing this mechanism?
- How highly efficient bilayer organic solar cells can be accomplished using FREAs?

- Does the molecular structure of FREAs has major impacts on exciton diffusion and charge transfer processes in OPV systems?
- Why FREAs are more favourable for ternary OPV strategies rather than fullerene-based counterparts?

Chapter 2

Time-resolved spectroscopy for probing molecular photophysics

The photophysical and photochemical processes after light absorption by a material are the fastest events in nature, occurring in the time scales of femtoseconds (10^{-15}s, one millionth of one billionth of a second). To follow these ultrafast events, we need the fastest tool available in nature, light itself. The invention of ultrafast lasers that produce pulses in the range of femtoseconds opened up a new window to probe these processes. This chapter introduces the basic concepts and definitions of the well-known ultrafast spectroscopic technique called **"Transient absorption spectroscopy"**. Presented here is a brief overview of the experimental setup, data collection, and analysis. Additionally, the multivariate curve resolution (MCR) technique for the data analysis is also summarized. Finally, a study of charge generation and recombination in a set of bulk-heterojunction OPVs is presented as a demonstration of transient absorption data analysis*.

*T. Liu, L. Huo, **S. Chandrabose**, K. Chen, G. Han, F. Qi, X. Meng, D. Xie, W. Ma, Y. Yi, J.M Hodgkiss, F. Liu, J. Wang, C. Yang, and Y. Sun, (**2018**). "*Optimized fibril network morphology by precise side-chain engineering to achieve high performance bulk-heterojunction organic solar cells*", 30(26): 1707353.

2.1 Introduction

In scientific research, one of the important goals is to understand the dynamics of various processes. Depending on the size and speed of the entity involved, the timescales and thereby tools used to watch these processes will change. For instance, radio-active dating is one of the slowest scientific tools to follow processes which are stretched over years or even centuries. Further down, on the time scales of human lives, calendars or clocks can be used to describe events of the order of months to seconds. Even faster events that happen in fractions of a second can be recorded using high speed photographic or fast film cameras. But, when it comes to the picosecond (ps) or femtosecond (fs) time frames, we need to explore the fastest tool available in nature, light itself! These events including the motion of atoms or even electrons that happens below microsecond time scales are grouped under the category "ultrafast processes" and the spectroscopic branch that deals with these processes is termed as ultrafast or time-resolved spectroscopy.

Figure 2.1: Different natural processes and their time-scales.

Even though light is the fastest thing in nature, not every light source can be used to describe ultrafast phenomena as they are too fast and thereby we need light that can be controlled in a precise manner. The invention of the **LASER** (light amplification by stimulated emission of radiation) in 1960 solved this problem, as it possesses unprecedented control on its parameters including direction, intensity, colour, pulse duration, and phase polarization. The laser paved the way to the world of ultrafast laser spectroscopy.[19]

In general, the term spectroscopy involves the study of interaction of light with matter. Traditional spectroscopic techniques are described as energy or frequency resolved because the measurements associated with them involve spectrally narrow light that is tuned across discrete energy levels. To follow events in time, we need

time-resolution, *ie*, the equipment used should involve a component that changes faster than the process under investigation. For instance, in order to follow hummingbird flaps, the camera exposure time defined by its shutter speed should be less than the duration of the wing flaps. In spectroscopy, the role of the camera shutter is done by a fastly changing light parameter called intensity. In other words, the time-resolution is coming from short flashes of light called pulses that can provide kinetic information of the processes that are statistical in nature. Ultrafast spectroscopy uses temporally short pulses with pulse durations of fs-ps to investigate the dynamics of the system directly, including even the motion of individual particles like atoms or electrons. This technique involves temporally short, therefore spectrally broad light pulses. These kinds of pulses are used to probe directly the dynamics of the system rather than the energy levels themselves. It is important that the duration of the laser pulses must be shorter than the time-scale of the process under investigation. Along with time-resolution, spectral operation range and resolution are also important factors in the field of spectroscopy as they allow us to resolve spectral features and bands into their separate components. One of the important advantages of laser systems is that their high intensities (order of $\sim$TW/cm^2) can induce non-linear effects in transparent media which can lead to the generation of new wavelengths, and thus making them highly tunable. The invention of white-light continuum generation in transparent media such as gas, liquid, and solids by ultrashort laser pulses helped time-resolved spectroscopic techniques to probe multiple events at the same time.[172] Additionally, if desired, pulses of high intensity can be generated *via* optical parametric amplification processes in which different wavelengths are mixed to produce new wavelengths.[26]

Pump-probe methods based on a pair of laser pulses are an important class of ultrafast laser spectroscopic techniques. Transient absorption (TA) spectroscopy is one of the simplest pump-probe techniques employed for measuring and interpreting molecular dynamics in various material systems. As this thesis concentrates on the photophysics of FREAs and related OPV systems, TA spectroscopy is an effective tool to probe the generation and fate of different photoexcitations.

2.2 Transient absorption spectroscopy

Transient absorption (TA) spectroscopy is a widely used technique in time-resolved spectroscopy, based on absorption measurements (schematic representation of the setup is given in the **Figure 2.2**). In this pump-probe technique, the sample is first excited with a short pump laser pulse, and a probe pulse arrives at some time after the pump is used to measure how the absorption of the sample was altered by the pump.[146] By varying the arrival time of the pump with respect to the probe or *vice versa*; the entire time-dependence of the absorption range can be measured.

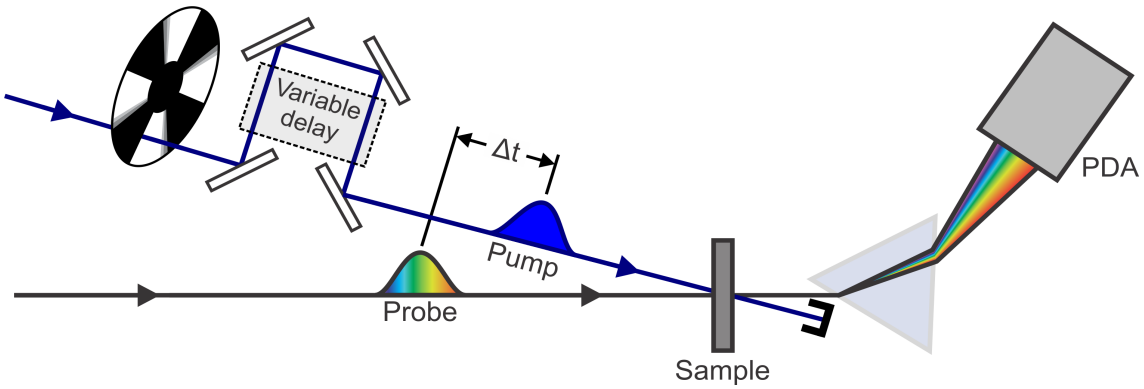

Figure 2.2: Schematic of transient absorption spectrometer setup.

Thus, for a TA experiment, two laser pulses are required, the pump and the probe. Typical pump pulses are spectrally narrow or monochromatic to selectively trigger a specific optical transition of interest. Importantly, the pump pulses should be more intense than the probe as the pump produces changes in the sample, whereas the probe merely interrogates them. In an ideal case, the probe would have no influence on the sample being investigated. The dynamics of the electronically excited states induced by the pump are probed *via* delayed broadband (containing many frequencies) probe pulses that pass through the photo-excited sample, and are then spectrally dispersed and collected using a photodiode array or camera. The time delay between the pump and probe pulses is varied by sending one of the pulses through an optical delay line which consists of a retroreflector mounted on a high precision computer controlled translational stage. The mechanical delay line in our lab can produce delays from femtoseconds to nanoseconds. The delay range can be extended up to microseconds using an electronic delay generator which can control the trigger rate of one of the pulses.

2.2.1 Light sources

As the fundamental light source, an amplified Ti:sapphire laser (Spectra Physics) that delivers pulses of 100 fs duration, 800 nm central wavelength, at a repetition rate of 3 kHz is used. The laser system comprises three main elements, the Mai Tai mode-locked seed laser, the Empower pump laser and the Spitfire regenerative amplifier. The Mai Tai emits femtosecond, mode-locked seed laser pulses (tunable in NIR, from 750 to 850 or 780 to 920 nm) at a frequency of ∼80 MHz generated *via* stimulated emission from a titanium doped sapphire rod pumped by a continuous wave diode-pumped laser at 532 nm. The mode-locking operation in the Mai Tai is accomplished using an acousto-optic modulator (AOM). The Spitfire system amplifies individual laser pulses that are selected from a stream of seed pulses from Mai Tai *via* a technique called chirped pulse amplification (CPA). Here, the pulses are chirped and temporally stretched before amplification using strong dispersive elements like a pair of gratings (pulses stretcher) to reduce the peak power. This is crucial to avoid detrimental effects in the amplifying gain medium (Ti:sapphire crystal) which is pumped by the 532 nm Empower laser. After amplification, the pulses are compressed back to the input pulse duration using an element with opposite dispersion (pulse compressor). The pump and probe pulses for TA experiments are produced from the 800 nm fundamental laser *via* the following steps.

White-light (probe) generation

White-light continuum (WLC) or super-continuum is a dramatic spectral broadening of a monochromatic laser pulse, generated *via* the non-linear propagation of intense laser pulses in a transparent medium.[41] The continuum generation happens as a result of the dynamic interaction of many processes in which the most important one is the optical Kerr effect. This describes an intensity (I) dependent refractive index in the medium given by,

$$n(t) = n_0 + n_2 I(t) \tag{2.1}$$

where n_0 and n_2 are the linear and non-linear refractive index, respectively. The induced change of the refractive index is proportional to the local intensity and therefore is higher at the center of the beam and lower at the ends. Thus, the material itself acts as a lens which causes the beam to self-focus. The self-focusing effect has to be stronger than the natural divergence of the beam to get a decrease in the beam

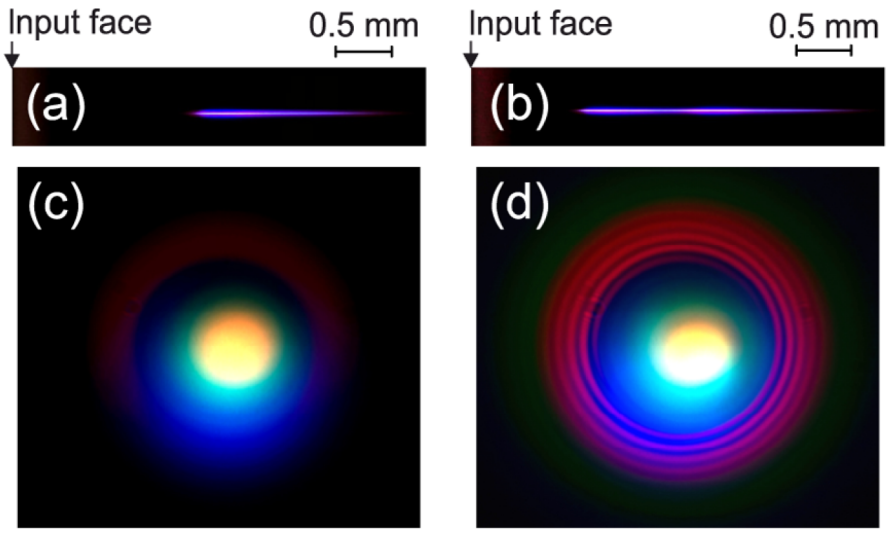

Figure 2.3: White-light super-continuum generation in a YAG crystal by 100 fs, 800 nm input laser pulses with energies (a) 310 nJ and (b) 560 nJ, that induce a single filament and multiple filaments, respectively. The corresponding far-field patterns are shown in (c) and (d). The figure is adapted from Dubietis *et al.*[41]

size and hence is having a threshold input power which is a function of the input wavelength λ,[41]

$$P_{cr} = \frac{3.72\lambda^2}{8\pi n_0 n_2} \tag{2.2}$$

where P_{cr} is called the critical power for self-focusing, defined as the power when the effect of self-focusing balances the diffractive spreading of the beam.[41] Once the input power exceeds P_{cr}, the beam will self-focus at a distance,[123]

$$Z_{sf} = \frac{0.367 Z_R}{\sqrt{[(P/P_{cr})^{1/2} - 0.852]^2 - 0.0219}} \tag{2.3}$$

where Z_R is the Rayleigh length of the input beam of radius ω_0. Here, the beam can not focus to a singularity as the self-collapsing process will be opposed by several processes like multiphoton absorption and ionization creating free electron plasma, group velocity dispersion (GVD), and Kerr effect saturation which further absorb and defocuses the beam. The balance between self-focusing and defocusing is termed as filamentation in which the beam propagates without diffraction. Simultaneously, in the time-domain, the time-dependent refractive index induces changes in the phase

of the pulse in time, termed as self-phase modulation which results in the spectral broadening by shifting the instantaneous frequency components within the pulse. The left panel of **Figure 2.3** shows white-light generation from a Yttrium aluminium garnet (YAG) crystal induced by 100 fs, 800 nm laser pulses with 310 nJ of energy in which a single self-focusing event (filament) was happened. When the input energy is increased to 560 nJ, multi-filamentation occurs which deteriorates the beam and can even causes permanent damage to the crystal.

Optical parametric amplification (OPA)

Generation of highly intense, narrow bandwidth pump pulses is accomplished by a travelling wave optical parametric amplifier of white-light continuum (TOPAS-C) which takes the advantages of second order non-linear processes such as parametric amplification, second harmonic generation (SHG), and sum frequency generation (SFG). TOPAS-C is a two stage parametric amplifier driven by the 800 nm fundamental and comprises several sub-units: pump beam delivery and splitting optics, a pre-amplifier (first amplification stage), a signal beam expander-collimator and a power amplifier (second amplification stage), all arranged in a single compact unit.

A small fraction ($\sim$1 - 3 μJ) of the 800 nm input is used to generate a WLC in a sapphire plate. The WLC and another fraction of the 800 nm input ($\sim$30 - 50 μJ) are focused and non-collinearly overlapped in time inside the pre-amplifier crystal to induce parametric amplification. The generated signal beam is expanded and collimated by a telescope and directed into the power amplifier, whereas the residual pump and the idler beams are blocked after the crystal. The power amplifier is pumped by the bulk of the 800 nm fundamental which is then collinearly overlapped with the signal beam inside a second non-linear crystal. Thus, TOPAS-C outputs collinear and well collimated signal and idler beams. The wavelength tuning in the pre-amplifier stage can be achieved by changing the delay between the WLC and 800 nm input pulses and adjusting the crystal angle for optimal phase-matching. Similarly, the wavelength tuning in the second amplification stage is done by first setting the pre-amplifier wavelength and then adjusting the second crystal angle and time delay between the signal and the second 800 nm pump pulses. The tuning range of TOPAS-C can be extended to UV, visible and NIR range by using different optical frequency mixers at the output.

The home-built TA setup in our lab at Victoria University of Wellington, New Zealand

allows the collimated pump pulses to be delayed with respect to the probe (WLC) which are then non-collinearly overlapped at the sample where the size of the probe is maintained smaller than the pump. After passing through the sample, pump pulses are blocked while the probe pulses are spectrally dispersed using a prism spectrometer and projected into a CMOS camera and an InGaAs photodiode array for collecting visible and IR components, respectively. The intensity of the probe is weak compared to pump so that it does not transfer an appreciable population from ground state to excited states or *vice versa*.

2.2.2 Measured signal

The signal from a TA experiment is the ratio of pump induced change in the probe transmission (ΔT) to the transmission of the ground state which is given by the equation,

$$\frac{\Delta T}{T}(\lambda, t) = \frac{T_{on}(\lambda, t) - T_{off}(\lambda)}{T_{off}(\lambda)} \tag{2.4}$$

where ΔT is the change in transmission of the probe with (T_{on}) and without (T_{off}) the pump excitation. The differential transmission signal can also expressed in terms of the change in optical density (ΔOD) between the ground state absorption and absorption at a fixed time after excitation as,[87]

$$\frac{\Delta T}{T}(\lambda, t) = 10^{-\Delta OD(\lambda,t)} - 1 \tag{2.5}$$

As per the equation (2.4), it is clear that the calculation of a single differential transmission signal requires two probe pulses. This is achieved by periodically blocking the pump pulses using a mechanical chopper at $\omega/2$, where ω is the frequency of the fundamental. Here, the chopper should be triggered by the laser amplifier to get every alternative pulses blocked. It is important for the detector to be synchronized with the chopper in order to separate the measurements of the excited and non-excited sample. The time-resolution of this experiment is given by the duration of the pump and the probe pulses, whereas the wavelength range is limited by the broadband nature of the probe light. In summary, the measured signal will be a function of both delay time (time delay between the pump and probe pulses) and the probe wavelengths.

2.2.3 Transient absorption data

To illustrate the output of a transient absorption measurement, the TA data of a fused ring electron acceptor (FREA), IC-1IDT-IC is presented in the **Figure 2.4**. This data was collected with an excitation of 690 nm and a pump fluence of 1.8 μJ/cm^2. **Figure 2.4a** gives the TA surface where the differential transmission is presented as a function of both time and energy. The spectral traces at different time delays are produced by taking signal slices as a function of energy at corresponding time points (**Figure 2.4b**). Similarly, signal slices as a function of time at different energies produce the time evolution (kinetic traces) of the corresponding spectral features (**Figure 2.4c**).

Transient absorption signals are more complicated than that of other time-resolved spectroscopic techniques (eg. time-resolved photoluminescence) because they contain several different contributions. When the pump pulse excites the sample, some of the molecules from the ground state are transferred to the excited state. Thus, the concentration of the ground state molecules decreases and part of ground state absorption signal disappears. Therefore, at the wavelengths of ground state absorption, the change in absorption becomes negative, *ie*, the change in transmission is positive. This contribution to the transient absorption spectrum is called ground state bleach (GSB) which is the positive part in the **Figure 2.4b**.

The second contribution to the TA signal is photo-induced absorption (PIA) which results from the absorption of the excited state species. After the excitation, additional absorption appears and the related contribution to the ΔT signal is always negative (<1.6 eV in **Figure 2.4b**). The induced absorption can occur from a singlet state to higher singlet state transitions, or if the molecule has relaxed to a triplet state, then higher triplet state transitions. The third contribution is the stimulated emission (SE) which gives a positive contribution to the ΔT signal. It arises when the probe pulse finds some of the molecules in the excited state and the photons of the probe pulse stimulate the emission of the sample molecules. The photons emitted have exactly the same polarization, direction, and wavelength as the incident photons causing the stimulated emission.

There are cases where the TA signals appear to be broad, but are in fact the result of many overlapping signals, which makes the spectra the sum of many underlying

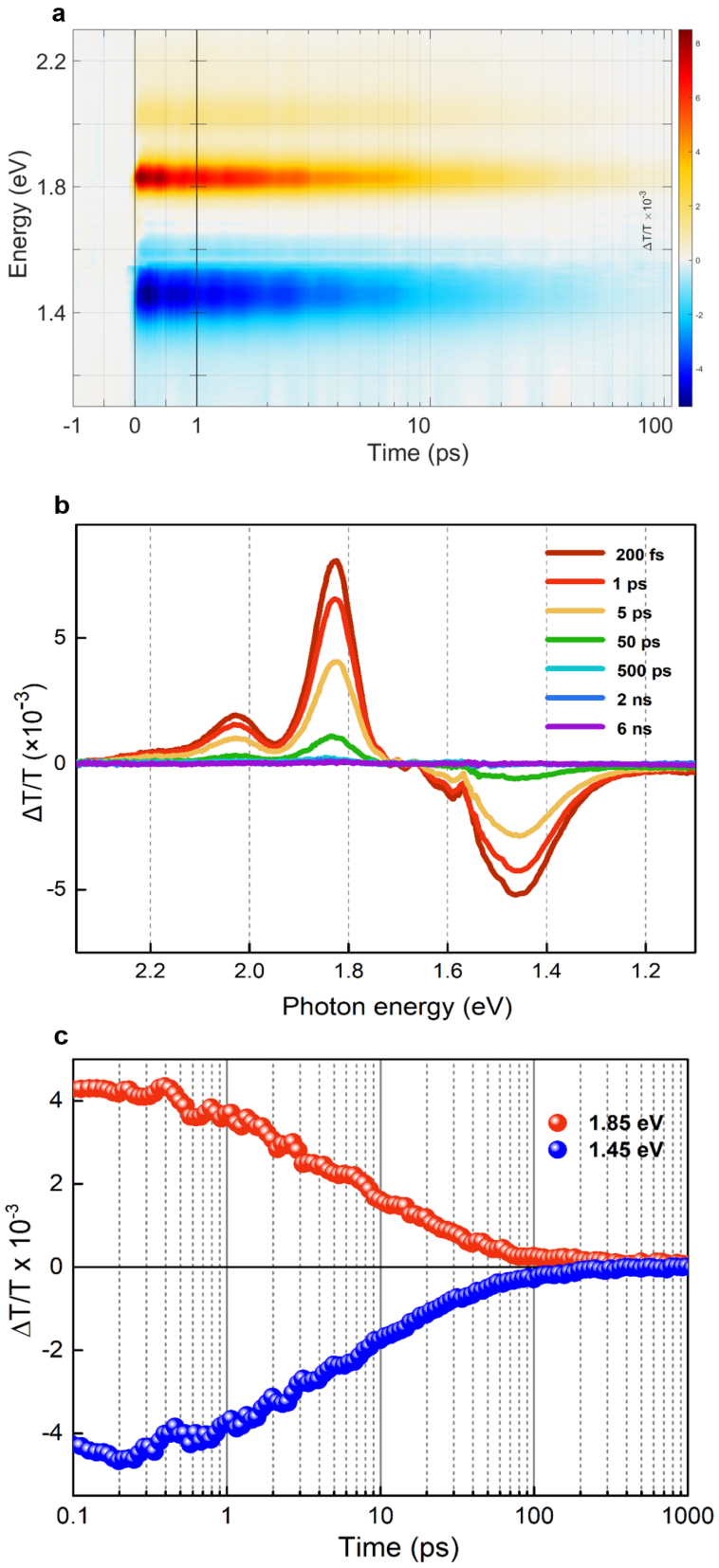

Figure 2.4: Transient absorption measurement of IC-1IDT-IC film showing **(a)** TA surface, **(b)** TA spectra at different time delays, and **(c)** kinetic traces.

features. The separation of these multiple components can be done by a combination of steady-state measurements of both ground state and model compounds, and modelling the kinetic data.

2.2.4 Artifacts in transient absorption data

There are a number of possible artifacts that might affect the transient absorption data. The most significant causes of their appearance are application of high power pump pulses, spectrally broad probe pulses and highly sensitive detection system.[118]

Group velocity dispersion (GVD) or chirp: Group velocity of a wave represents the velocity at which energy or information is carried along the wave which is usually a function of the wave's frequency. When these waves cross a transparent medium like air or prisms, they suffer wavelength dependent refractive index that results in the temporal spreading of different wavelengths within the pulse. This is termed as group velocity dispersion (GVD) or chirp. The pulses get positively chirped if they propagate through a normally dispersive medium where the shorter wavelengths arrive later than the longer wavelengths. Similarly, they get negatively chirped if they travel through an anomalously dispersive medium where the longer wavelengths arrive later.[86] In TA spectroscopy, the spectral broadening in the WLC or probe generation is induced by the self-phase modulation (SPM). But the SPM process intrinsically gives rise to chirped WLC at the same time.[84] This can generate observable effects in the transient absorption data as the onset of the signal at time zero varies with the wavelengths (**Figure 2.5a**) which affects the interpretation of kinetics data, especially for the shorter lifetime signals.

The chirp in the WLC can be quantified by separate measurements in reference samples which can produce either optical Kerr effect or second order SFG. But the chirp extracted by this method can not be described well in time-resolved spectroscopy as the refractive index and thickness, which are the crucial factors determining the chirp, can vary from sample to sample.[84,172] In this work, the chirp correction is done by a straightforward method *via* estimating the wavelength dependent signal onsets in the measured dataset (**Figure 2.5b**).

Instrument response function (IRF): The instrument response function represents the minimum temporal resolution achievable in any spectroscopic instrument. The IRF is important in TA as the temporal width of the pump and the probe pulses

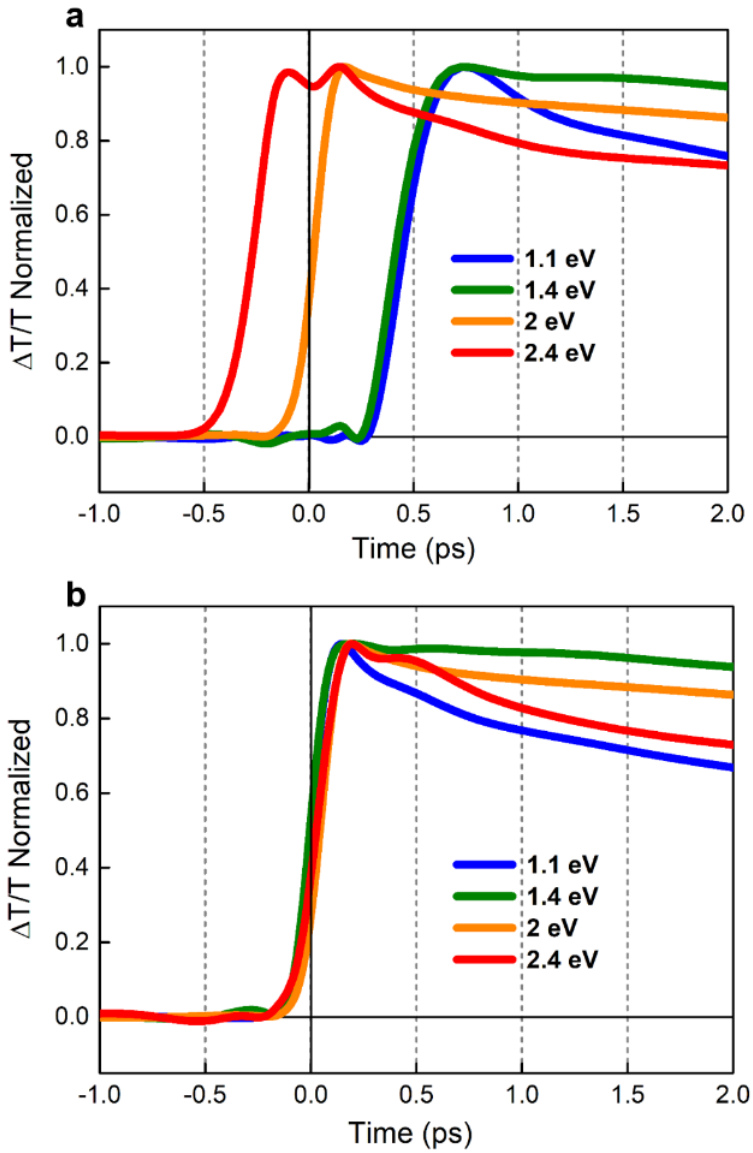

Figure 2.5: Example of a transient absorption surface (a) before chirp correction where the onset of signal at time zero varies with wavelengths and (b) after chirp correction with all onset times centered around zero.

are longer than the minimum time step generated by adjusting their path length.[146] Since time-resolution is shorter than the pulse width, the pump pulse can not generate an instantaneous population at time equal zero. Instead, the output signal will be convoluted by the temporal intensity profile of the pump pulse as some molecules are excited by the pulse's leading edge and others by the trailing edge. Mathematically, the output will be the integral of the signal and the temporal intensity function of the excitation pulse. The IRF makes it difficult to predict the initial amplitude of the signal as the signal decay happens within the pulse that affects the comparison of

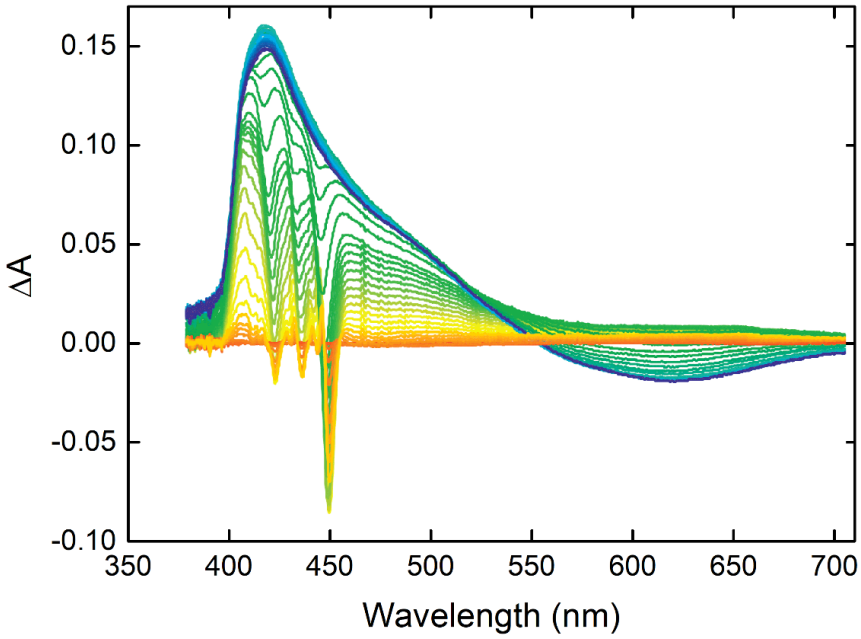

Figure 2.6: Example of TA spectra affected by the unwanted contributions from SRA - strong negative signals around 425, 437 and 450 nm. This figure is adapted from Ruckebusch *et al.*[150] and here the y-axis is represented in terms of differential absorption.

initial yields. Additionally, it can also lead to shifted peak maxima, making it appear as if signals are growing in at different times.

Two photon absorption: Many media are transparent in the visible and near UV spectral range when a low intense laser field is applied. Meanwhile, in a high intense ultrashort laser pulse application, they can absorb efficiently through multiphoton absorption.[118] In TA experiments, for sufficient input power density, the sample can absorb two photons simultaneously, one from the monochromatic pump and the other from the broadband probe. The sum of energy of these photons should be higher than the energy of the long-wavelength limit of the material's absorption band. This happens only when the pump and the probe pulses overlap at the same time, with the absorption of the probe pulse adding a positive signal to the TA surface.

Stimulated Raman amplification (SRA): SRA is generated when at least two photons interact each other in time and space inside a medium, so that there occurs stimulated emission of a third photon provided that the energy difference between the incident photons matches with the molecular oscillation energy of the medium.[118] In transient absorption spectroscopy, the role of the incident photons is played by the

pump pulses and a suitable wavelength component from the broadband probe white-light continuum. The generation of SRA signals produce undesired optical density changes in the transient absorption spectra at specific wavelengths (**Figure 2.6**).

Cross phase modulation: Cross phase modulation is a non-linear optical process in which the intense pump pulse induces a time-dependent modulation in the real part of the refractive index of the optical medium[118] (equation 2.1). When pump and probe pulses overlap in space and time, this modulation is experienced by the spectrally broad probe pulse and as a result, the spectral distribution of the probe pulse is modified.[118] This results in the generation of unwanted signals at time zero.

2.3 Transient photoluminescence spectroscopy

One of the ways for a molecule or an exciton to lose it's excited state is *via* the radiative deactivation or fluorescence. As steady-state fluorescence spectroscopy measures the fluorescence intensity integrated over time, it can not give any information of how and when the molecule is deactivated. Meanwhile, time-resolved photoluminescence spectroscopy does not integrate the fluorescence intensity in time and therefore it carries both spectral and kinetic information. Here, the molecules are usually excited using a short laser pulse and their fluorescence spectrum is recorded as a function of time. This requires the use of an optical shutter that allows the fluorescence signal to be collected by the camera at specific time intervals after the laser excitation.

One of the most common methods of time-resolved PL spectroscopy is fluorescence upconversion which make use of non-linear optics to generate the optical shutter. In this method, there are two laser pulses, one of which is delayed using an optical delay line (gate pulse) while the other is used to excite the sample. Then, the emitted fluorescence and the gate pulse are overlapped in a non-linear crystal which is oriented in such a way that the phase-matching condition is achieved for the sum frequency generation between the gate and fluorescent wavelengths. In other words, the gate pulse cut time slices out of the long fluorescent pulse. But, this method is unable to read the broadband PL spectra as the phase- matching condition in the upconversion process is wavelength dependent.

In 2014, Chen *et al.* (from our group at Victoria University of Wellington) developed a

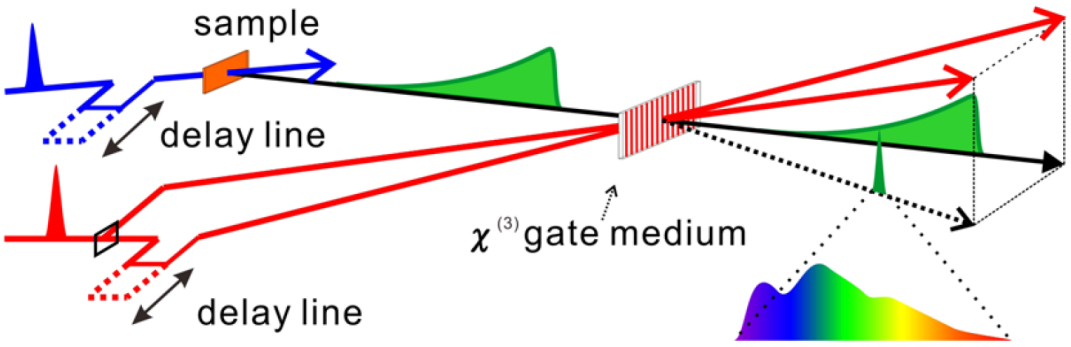

Figure 2.7: Schematic of transient grating photoluminescence experimental setup. The figure is adapted from Chen *et al.*[21]

novel ultrafast PL method called transient grating photoluminescence (TGPL) spectroscopy which is free from all the constraints in upconversion.[21] **Figure 2.7** gives the schematic of the experimental setup. Here, the ultrafast PL spectra is sampled *via* a diffraction grating generated by the interference of two gate pulses, where the optical Kerr effect modulates the refractive index of the medium. The output of the 800 nm fundamental laser is split into excitation and gate beams. Excitation wavelength is tuned *via* an optical parametric amplifier and then focused on to the sample. The emitted PL is collected using off-axis parabolic mirrors and is focused into the Kerr medium (1 mm thick fused silica). Approximately 30 μJ/pulse of the 800 nm is used for the gate pulses, which are then overlapped with the PL in the Kerr medium at a crossing angle of $\sim 5^0$. Thus, the PL spectra at different time delays after photoexcitation is sampled *via* diffraction off the transient grating generated from the interference of the two gate beams. This separates the gated PL from the ungated PL background signal, acting like an effective ultrafast shutter. The gated PL is then collected using the fast electronic shutter of a CCD camera.

There are two delay lines used to get the time-resolution of the experiment. The first one is the time delay introduced in the excitation beam which alters the overlap of the emitted PL with the transient grating at the Kerr medium. This is achieved *via* a retroreflector connected to a motorized translational stage. The second one is the temporal overlap between the two gate pulses at the grating medium which is achieved by a manual delay line. This controls the time at which the PL is sampled since the diffraction grating is only present when there is a temporal overlap between the gate pulses. The time-resolution of the experiment is governed by the cross-correlation of

the excitation and gate pulses, in the same way as TA spectroscopy.

2.4 Data structure and analysis

The output of a typical transient absorption measurement is a 3-dimensional data set or a matrix D where each raw represents a spectrum at a certain pump-probe delay and each column corresponds to the signal intensity as a function of time delay. The size of D is $m \times n$, where m represents the number of rows which is the number of time delays generated by the delay generator, and n represents the number of columns which is the number of pixels on the detector. Ideally, the TA data matrix D is formed by the signals from different photo-active species, which can be either absorbing or emitting. For instance, if there are r number of species or components involved in the photo-active process, then the data matrix D can be written as $D = K^T \times S$. The columns of K^T are sized $m \times r$ which represent the time-dependent concentrations or kinetics of r components and the rows of S are sized $r \times n$ which are the spectral signatures at each time delay. Here K^T is the transpose of K.

Usually in TA measurements, thousands of data points are collected, depending on the number of time and wavelength points used. To extract valuable information from this huge data set, one could simply take spectral slices at different time points to see the spectral evolution of a species and similarly kinetics slices at corresponding wavelength regions to get the species evolution in time. This can be considered as a primary step in the data analysis, usually performed when we have an idea about the process or the components involved. But, there are situations where we are not sure about the species involved or when signals from different components overlap together. Then we can explore global analysis techniques, which can be done by modelling the data matrix to decompose it into individual components. There are mainly two modelling techniques, soft modelling and hard modelling.

2.4.1 Soft modelling

Soft modelling is a technique usually implemented if there is not a *priori* knowledge about the number of components or the underlying model involved in the system. This approach involves decomposing the data matrix to get physically meaningful components by the application of constraints or boundary conditions that can be obtained from the physical knowledge and mathematical investigation of the observed data structure.[74]

MCR-ALS technique: Multivariate curve resolution (MCR) by alternating least squares (ALS) is one of the powerful methods of soft modelling used so far for separating the overlapping components from time-resolved data. It is an iterative tool that works by optimizing a set of initial guesses of spectral and kinetic profiles under the action of specific constraints until a convergence criterion is achieved.[34] MCR describes the data set D as the sum of the signal contributions from each component. Here each contribution term can be represented by the corresponding spectrum s_i^T weighted by it's time profile k_i, which is termed as bilinear model[34] given by,

$$\begin{aligned} D = \sum_i k_i s_i^T + E = KS^T + E \\ = D^* + E \end{aligned} \tag{2.6}$$

where E represents the residual matrix which is usually the experimental noise. The first step of MCR-ALS is the estimation of the number of components or species in the system which is usually done by singular value decomposition (SVD). It is a mathematical technique in which the $m \times n$ data matrix D has undergone a factorization given by,

$$D = U\Sigma V^T + E \tag{2.7}$$

where U is an $m \times m$ unitary matrix ($U^T U = U^{-1} K = I$), Σ is a diagonal $m \times n$ matrix whose values are the singular values (singular values are the square roots of the eigen values of $D^T D$, where D^T is the conjugate transpose of D) of the matrix D arranged in decreasing order and V^T is the conjugate transpose of V. The columns of U and V represent the left and right singular vectors of D which are the eigen vectors of DD^T and $D^T D$, respectively. The number of significant values in Σ gives the rank of the matrix D, which is the maximum number of linearly independent columns or rows of D. This is meaningful as it represents the number of species that defines the matrix D.

The second step is making initial guesses of the spectral and temporal profiles. This can come from the previous knowledge available, for instance, if we know the spectral profiles of the neat components in the system, they can be used to make guesses. There are methods like error factor analysis (EFA) which can help in completing this task. In EFA, first SVD of the submatrix containing only the first two spectra of D is made and the corresponding singular values are plotted as y-values with an x-value

of 1. Then the third spectrum of the data matrix is added to the initial submatrix and the SVD is then made in this new submatrix. The new singular values are plotted with an x-value of 2. This process is repeated until there are no more rows to add. Lines are then drawn connecting the biggest singular value at every x-values (or time points), the second-largest, the third-largest etc.[74] This arrangement is called forward-going EFA which indicates the evolution of different species in time. Similarly, a backward-going EFA graph that represents the species's disappearance in time is also made by repeating the same procedure above, but starting from the last spectra. The number of excited-state species n can be made by looking at the movement of singular values relative to the noise level. The initial concentrations can be estimated by iterating $i = 1$ to n and taking the i^{th} component of the forward-going EFA until it intersects the $(n - i + 1)^{th}$ component of the backward-going EFA from which time the $(n - i)^{th}$ is taken to give the excited state concentration.[74]

After the local rank analysis, we move to the optimization of the guessed concentration files using ALS method. First, we apply different constraints to shape the guessed concentration profiles. Possible constraints are non-negativity (force the profiles to be positive), unimodality (presence of a single maximum per profile) and equality constraint (makes the profile to be equal to a known predefined shape). Constraints related to mathematical conditions can also be applied here as if, from EFA, regions with only one species is detected. In these regions, the concentration of other species is forced to be equal to zero.[34,74] With this concentration profiles, the unknown species spectra is calculated using the bilinear equation $S^T = K^+ D^*$, where K^+ is the pseudo-inverse of K. The calculated spectra can be adjusted by constraints like normalization or known spectra of species. From there, the new estimation of the concentration files can be obtained by $K = D^*(S^T)^+$. These steps are repeated until the data matrix D is well explained by the calculated profiles. The quality of fit can be checked after each iteration using lack of fit (LOF) defined by,[34,78]

$$LOF(\%) = 100\sqrt{\frac{\sum_{i,j} e_{ij}^2}{\sum_{i,j} d_{ij}^2}} \tag{2.8}$$

where d_{ij} is the element of the data matrix D and e_{ij} is the corresponding element of the residual matrix obtained by taking difference between matrix D and the MCR-ALS reproduced matrix. The ALS iteration can also start with the initial estimation

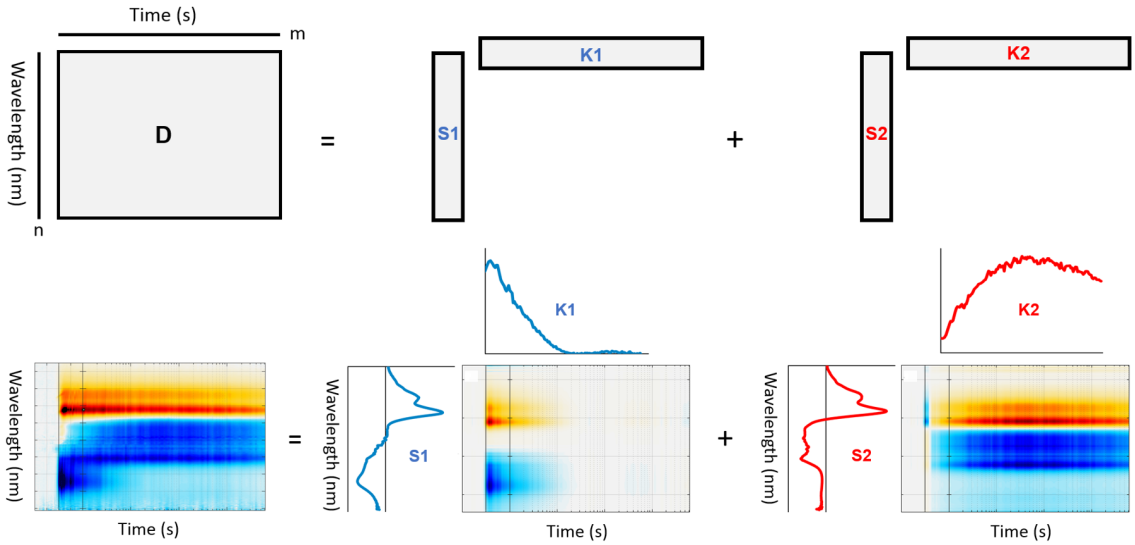

Figure 2.8: First panel shows the decomposition of a data matrix D in the case of a two component system. Second panel gives the application of MCR-ALS to the TA data of an OPV blend. The algorithm could extract 2 components (excitons and charges) and their corresponding spectral and concentration profiles are presented.

of the spectral profile S^T which is usually derived from the spectra of pure components. An example of separating components using the MCR-ALS of an OPV blend is presented in **Figure 2.8**. Here, we used the MCR-ALS graphical user interface (GUI) developed by Roma Tauler and a team from Environmental Chemistry Department, IDAEA-CSIC, where the algorithm is implemented under the MATLAB environment.

Rotational ambiguity: The concept of ambiguity or uncertainty in MCR means that the data matrix D can be decomposed into different combinations of sets of concentration profiles and spectra with same fit quality. More clearly, the solution, we derive by the bilinear model is not mathematically unique. This ambiguity can be expressed as,

$$\begin{aligned} D &= KS^T + E \\ &= KIS^T + E \\ &= (KR)(R^{-1}S^T) + E \end{aligned} \tag{2.9}$$

where R is any transformation matrix. Here the new concentration matrix (KR) and the spectra matrix $(R^{-1}S^T)$ can also reproduce the data matrix D with the same fit quality. This clearly shows the mathematical ambiguity of the decomposition as

there are infinite number of choices for R. The main solution for suppressing the ambiguities in MCR analysis is to introduce various constraints.

2.4.2 Hard modelling

Hard modelling data analysis technique is based on kinetic models, or reaction mechanisms, which can quantitatively describe the system dynamics. Here we should have a *priori* knowledge about the functional form of the concentration of the species involved.[74] A general form of the population equation is given by,

$$\frac{dK_n}{dt} = F_n(p_n, K_1, K_2....K_n) \tag{2.10}$$

where n and p represent the number of components and kinetic parameters (rate constants), respectively. Usually, non-linear least square method is used to fit the experimental data with the kinetic model. The optimization of the parameters is done by making the sum of the squares of all elements in the residual matrix to minimum.[35,74] Now the concentration matrix can be extracted as the numerical solution to the population equation with the current parameter set. Then the corresponding spectra matrix can be evaluated explicitly as $S^T = K^+D^*$ where K^+ is the pseudo-inverse of K.[35] This technique can also start from a spectra model in which the parameters are usually the molar absorptivities of the components involved at different wavelengths.[35]

The difficult part of hard modelling is the selection of the right model. Usually, the simplest model which can fit the data in the experimental error limit is chosen. But this doesn't mean that the selected model is right. Additionally, fitting with different models and comparing the results can be time consuming.

2.5 Charge generation in high performance OPVs

This section includes an example of applying ultrafast transient absorption spectroscopy to track the charge generation and recombination in three high performance bulk-heterojunction donor-acceptor blends. The focus is given to transient absorption data collection, analysis, and interpretation. All the results presented here are published elsewhere.[115]

Materials used

It has been reported that many donor-acceptor (D-A) based conjugated polymers can form fibrils of the order of nanometers parallel to their conjugated backbone through co-facial $\pi-\pi$ stacking or interactions of aliphatic side-chains. These fibrils which can act as efficient channels for hole transport along with fullerene embedded in between for electron transport will make a morphology similar to a bi-continuous network.

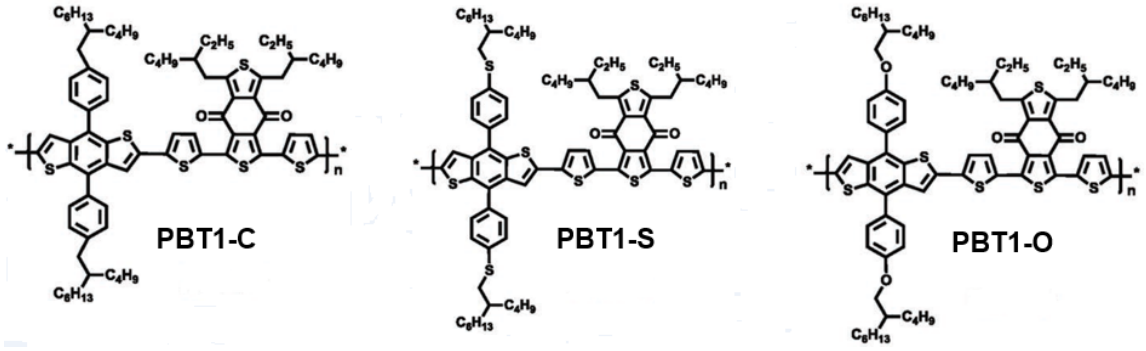

Figure 2.9: Chemical structures of the conjugated polymers PBT1-C, PBT1-S and PBT1-O. The figure is adapted from Liu *et al.*[115]

Here, fullerene blends based on three conjugated polymers PBT1-C, PBT1-S, and PBT1-O are used which are fabricated by fine tuning the atomic linker between the side-chains and backbone without affecting the molecular geometry, instead tuning the side-chain interactions to improve the device efficiency. OPV based on PBT1-C showed the highest PCE of 10.1% with a high fill factor of 80.5% in which a well defined fibrillar network is developed. All the polymers and blends were provided by collaborators at Beihang University, China from the research group of Yanming Sun and the chemical structures are shown in the **Figure 2.9**.

Data collection and analysis

Transient absorption spectroscopy was applied on neat polymer and blend films with an excitation wavelength of 580 nm where the donors can absorb most of the light. All the samples were measured under continuous vacuum environment to avoid degradation. For the measurements, 6000 probe shots (3000 with pump on and 3000 with pump off) were collected at each time delay point and was repeated for 4 times. TA data were saved as binary files along with the corresponding wavelength calibration and pump spot-size files. Data processing was done *via* the MATLAB software including data averaging, wavelength calibration, background correction, and chirp

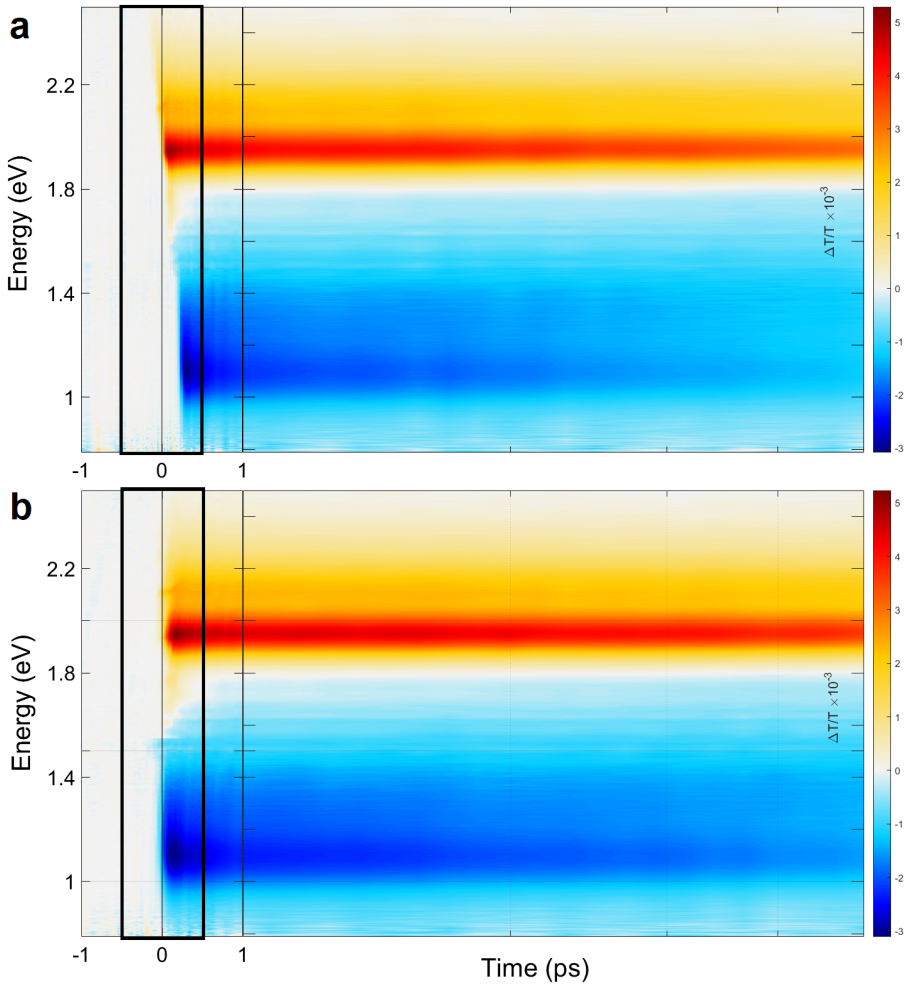

Figure 2.10: Transient absorption surface of neat PBT1-C film (a) before and (b) after chirp correction (excitation at 580 nm at a pump fluence of 5.7 μJ/cm^2).

correction. For wavelength calibration, a filter wheel with four color filters was used which could be rotated into the probe beam successively. At the beginning of measurements, the transmission of all filters were recorded as a function of the pixel number on the detector. The known wavelength positions were then fitted with a non-linear function (since the dispersion of prism is non-linear) to find the positions of all wavelengths on the detector. Chirp correction is done by estimating the wavelength dependent signal onsets in the measured data set (refer section 2.2.4). For instance, **Figure 2.10** provides the TA surface of neat PBT1-C film before and after chirp correction.

Data interpretation

Figure 2.11 gives a series of transient absorption spectra of the neat polymer PBT1-C following a weak excitation at 580 nm (2.14 eV). These are produced by taking spectral slices from the TA surface at different time points. The spectra include positive ground state bleach (GSB) in the visible wavelengths which is consistent with its steady-state absorption spectrum and negative photoinduced absorption (PIA) around 1.1 eV which represents the excitonic absorption (refer section 2.2.3). In this polymer no stimulated emission feature is observable. The similar decay kinetics between GSB and PIA confirms the dominance of singlet excitonic species. There is a shoulder around 1.4 eV is observed whose ratio with the peak at 1.1 eV changes with delay. This reveals the formation of some free charges in the neat polymer which persist beyond 6 ns. TA measurements of the neat polymer can be used as a guide for the interpretation of spectroscopic features in the blends.

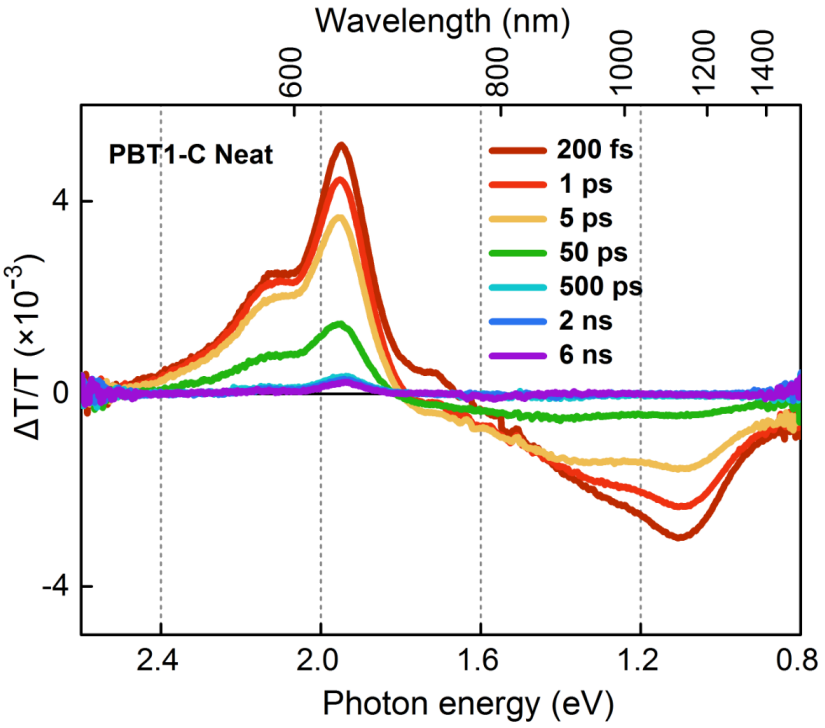

Figure 2.11: Series of transient absorption spectra of the neat polymer PBT1-C after an excitation at 580 nm at a pump fluence of 5.7 μJ/cm^2.

Figure 2.12 includes the TA spectra of all the three blends after laser excitation at 580 nm where the donor polymers dominate the absorption. Their spectra are virtually identical with highly evident charge transfer through the fast decay of exciton band (1.1 eV) and the emergence of new absorption peak at 1.4 eV which appears as

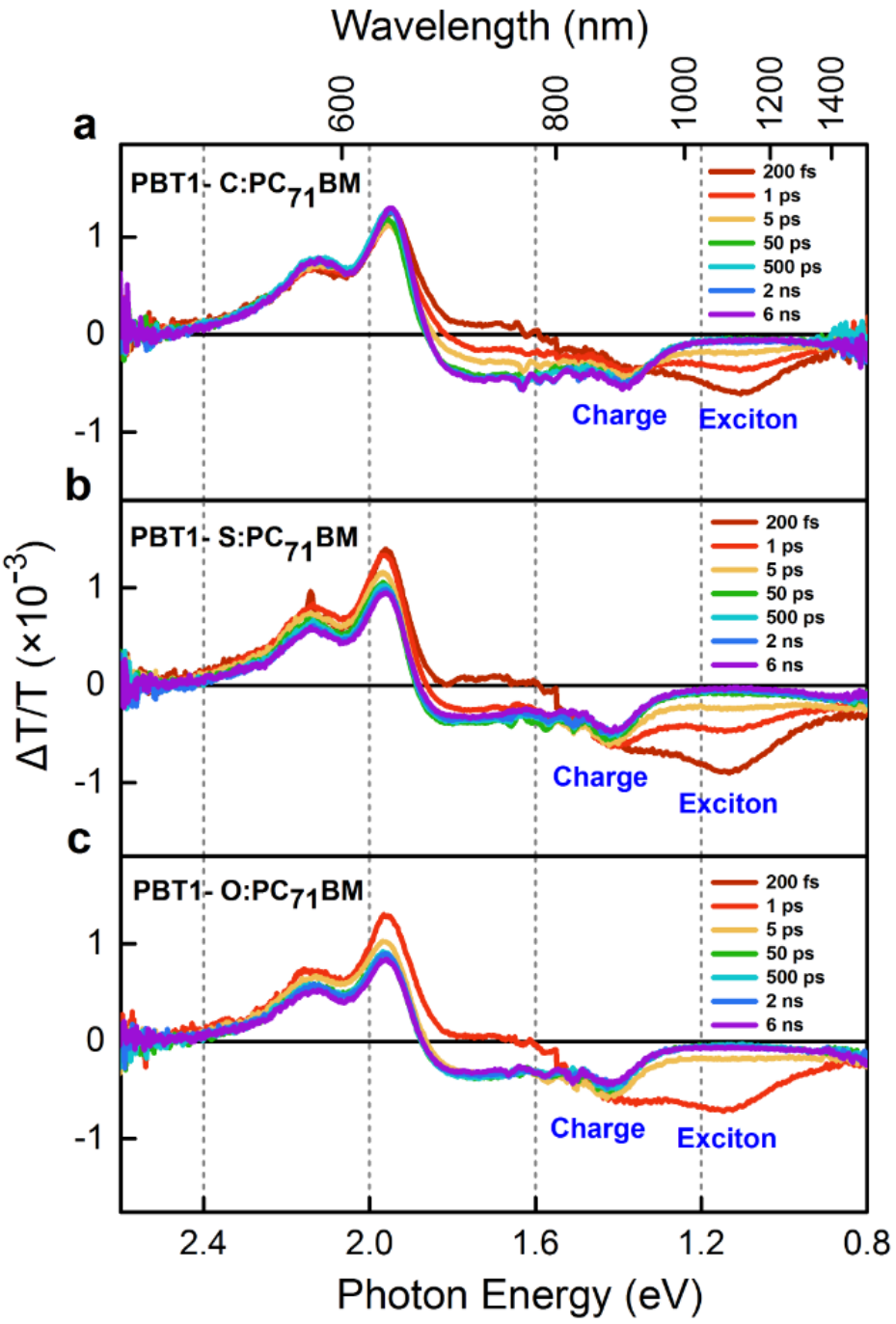

Figure 2.12: Transient absorption spectra of blends **(a)** PBT1-C:$PC_{71}BM$, **(b)** PBT1-S:$PC_{71}BM$, **(c)** PBT1-O:$PC_{71}BM$ following excitation at 580 nm at pump fluences of 7.2 $\mu J/cm^2$, 5.7 $\mu J/cm^2$ and 3.4 $\mu J/cm^2$ respectively.

a shoulder in the earlier time of 200 fs and persists beyond 6 ns time scale of this measurement. Compared to others, the GSB of the most efficient blend PBT1-C:$PC_{71}BM$ is retained throughout the entire 6 ns window probed, indicating unit charge conver-

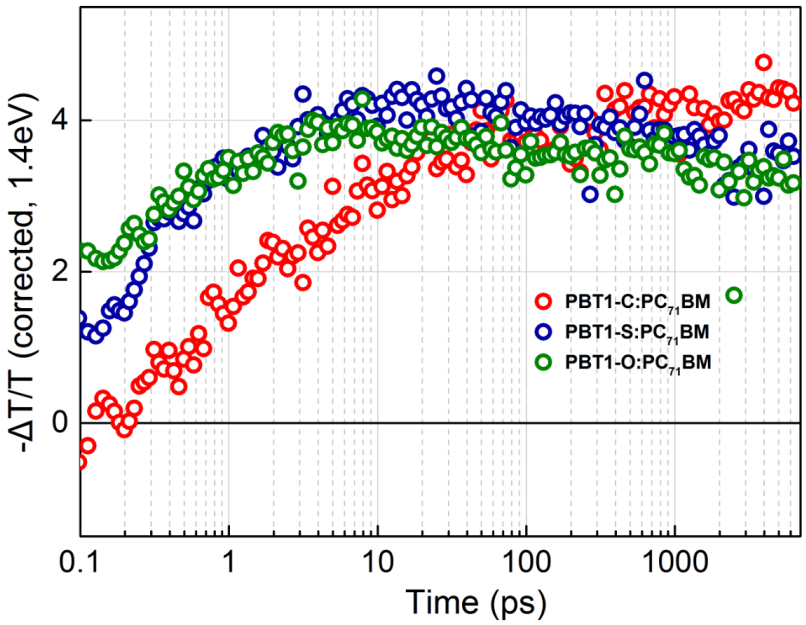

Figure 2.13: Kinetics of polaron peak at 1.4 eV for the three blends after laser excitation at 580 nm (7.2, 3.4, and 3.4 μJ/cm^2, respectively). Here the overlapping contribution from the exciton absorption is subtracted.

sion efficiency and the absence of charge recombination in this time scale.

Since the blend spectra comprise distinct excitonic and charge PIA signals and little features from $PC_{71}BM$ due to its weak absorption, MCR-ALS is not necessary here to produce charge kinetics. So the integrated intensity of the polaron band at 1.4 eV is used to track the charge generation and recombination dynamics. **Figure 2.13** compares the charge dynamics of all three blends. Here, the overlapping contribution from excitons is subtracted based on the time-dependent magnitude of the 1.1 eV exciton peak and the ratio of exciton at 1.4 - 1.1 eV for the neat polymer PBT1-C. As the figure shows, PBT1-S and PBT1-O blends show prompt charge photogeneration and are having almost similar dynamics. The charge growth stops around 100 ps after which they suffer significant geminate charge recombination, which is confirmed from the fluence dependent measurements. In contrast, little charge generation is observed in the PBT1-C blend up to 200 fs followed by a slow growth beyond 10 ps with no geminate recombination in the 6 ns window probed.

The kinetic profile of the PTB1-C blend reveals the fact that the excitons have undergone longer diffusion before generating charge pairs which reflects the presence of pure donor domains. The suppression of geminate charge recombination is attributed

to the absence of dissolved fullerene molecules. Additionally, the prompt generation and germinate recombination of charges in PTB1-S and PTB1-O blends indicate the signs of impure phases and dissociation of excitons before reaching the interface.

2.6 Summary

Transient absorption (TA) spectroscopy is an effective tool to probe the photophysics of organic photovoltaic materials. It possesses a broad spectral window which allows us to interrogate the dynamics of multiple excited state species like singlet excitons, triplet excitons and charges. High time-resolution of the order of ∼100 fs is highly favorable to track ultrafast excited state events. Unlike TRPL, TA is efficient in detecting non-emissive species like charges as it measures the change in absorption/transmission between the ground and excited states. These advantages come with the penalty that pump-probe spectra are more complicated and harder to interpret than those of any other time-resolved techniques and one has to rely on several modelling techniques to disentangle the dynamics of different species involved. Finally, the application of TA spectroscopy on different fullerene based donor-acceptor bulk heterojunctions revealed ultrafast charge photogeneration process which is consistent with their high efficiencies.

Chapter 3

High exciton diffusion in fused ring electron acceptor films

One of the most promising advances in the field of organic photovoltaics is the development of non-fullerene acceptors. Recently, fused ring electron acceptors (FREAs) have been widely researched because their excellent electron transport is matched with strong optical absorption that compliments that of electron donors in the visible and NIR range. So far, FREA based OPV systems have shown record PCEs up to 16%. This chapter includes a detailed spectroscopic insight to answer the fundamental question: how the FREA based BHJ systems attain high efficiencies compared to the fullerene-based counterparts in spite of their large and pure domains. A highly efficient FREA, **IC-C6IDT-IC** (IDIC) is selected as a model system in which an extraordinarily high quasi-activationless exciton diffusion coefficient is extracted by employing ultrafast laser spectroscopic tools. Enhanced exciton diffusion in IDIC is shown to arise from it's rigid molecular structure with low reorganization energy, low energetic disorder, and good transition dipole alignment - all enhancing the long-range resonance energy transfer. The high exciton diffusion rate of IDIC is consistent with its exceptional performance as an acceptor in OPV cells, and highlights the excellent potential of FREAs in optoelectronic applications. This work has been published in the Journal of the American Chemical Society (JACS)*.

*S. Chandrabose, K. Chen, A.J Barker, J.J Sutton, S.K.K Prasad, J. Zhu, J. Zhou, K.C Gordon, Z. Xie, X. Zhan and J.M Hodgkiss, (**2019**). "*High exciton diffusion coefficients in fused ring electron acceptor films.*" 141(17): 6922-6929.

Collaborators contributed to the work

Material design and fabrication:

Prof. Xiaowei Zhan and students from Peking University, Beijing, China.

Raman spectroscopy measurements:

Prof. Keith C. Gordon and students from University of Otago, New Zealand.

Research focused on

Steady-state absorption measurements: UV-vis absorption and PL measurements and (**b**) Temperature dependent PL measurements.

Transient absorption spectroscopic measurements:

(**a**) Exciton diffusion measurements, (**b**) Temperature dependent exciton annihilation measurements and (**c**) Polarization anisotropy measurements.

Data processing and analysis: (**a**) Huang-Rhys factor fittings, (**b**) Singlet-singlet exciton annihilation (SSA) fittings, (**c**) Activation energy calculation, (**d**) Polarization anisotropy calculation, (**e**) Energetic disorder calculation, and (**f**) Förster resonance energy transfer calculations.

3.1 Introduction

Low dielectric constants and strong electron-phonon coupling in π-conjugated organic semiconductors create strongly bound electron-hole states known as excitons, which control light absorption and emission, and which move as electrically neutral quasi-particles. In OPV cells, donor-acceptor heterojunctions for separating bound singlet excitons into free charge pairs must be distributed on a comparable length scale to the exciton diffusion length. This length scale is rarely more than 5 – 10 nm for solution processed OPVs,[134,135] which introduces a trade-off between exciton harvesting and subsequent charge collection efficiencies, and motivates the need to understand and control blend nanomorphology.[113]

The apparent universality of 5 – 10 nm diffusion lengths in OPVs arises from several features common to solution processed organic semiconductors.[134,135] The diffusion length, L_D is given by $\sqrt{D\tau}$, where D is the diffusion constant and τ the exciton lifetime. Since τ is intrinsically linked to the transition dipole moment (which varies little for strongly absorbing π-conjugated materials) and is suppressed *via* non-radiative relaxation in low band gap materials,[68] the diffusion constant is the critical parameter. On the time and length-scales governing the diffusion length, the dominant transport mechanism is incoherent resonant energy transfer hopping, with two parameters accounting for most of the variation between materials. First, the spectral overlap integral for self-energy transfer correlates strongly with diffusion length, however the vibronic progressions and Stokes shifts typical of organic semiconductors make up the majority of reported R_0 values for self-energy transfer in the range of 1 - 2 nm.[121] Second, the energetic disorder governs the density of available sites within the transfer radius.[135] The energetic disorder of solution-processed organic semiconductors typically exceeds thermal energies at room temperature (e.g., 44 – 125 meV Gaussian disorder widths for PPV derivatives),[126,136] reducing the density of accessible states and decreasing the exciton diffusion coefficient. The magnitude of disorder relative to thermal energy also accounts for dispersion in exciton diffusion coefficients, whereby an initial energetically downhill phase produces rapid diffusion that is not sustained for long distances.[28,134,135] In addition to spectral overlap integral and energetic disorder, dipolar orientation also affects the resonant energy transfer rate, however, solution-processing generally leaves little scope to engineer molecular alignment, particularly for polymers.

The highest reported exciton diffusion coefficients are for polymers with a high degree of rigidity and planarity, notably ladder-type poly-p-phenylene ($D = 4.42 \times 10^{-2}$ cm^2/s)[65] and poly(9,9-di-n-octylfluorenyl-2,7-diyl) ($D = 2 \times 10^{-2}$ cm^2/s).[160] A high exciton diffusion constant was also reported for P3HT ($D = 1 \times 10^{-2}$ cm^2/s),[28] but this study revealed that exciton diffusion is only so high on early time scales, and not sustained when excitons relax through the density of states. The exciton diffusion constant for P3HT under quasi-equilibrium conditions is lower at $D = 1.8 \times 10^{-3}$ cm^2/s,[156] similar to other OPV materials such as PPV derivatives ($D = 0.3$ - 3×10^{-3} cm^2/s),[95,126] PCPDTBT ($D = 3 \times 10^{-3}$ cm^2/s),[137] and even materials used in OPV devices with power conversion efficiencies exceeding 10% ($PC_{71}BM$ ($D = 1.6 \times 10^{-4}$ cm^2/s).[67] Exciton diffusion constants on the order of 10^{-3} cm^2/s have been a common constraint of OPV materials throughout many generations of material advances. Here, a detailed examination of exciton diffusion in one of a new class of fused ring electron acceptors (FREAs), indacenodithiophene (IDT) endcapped with 1,1Dicyanomethylene-3-indanone (IDIC) is presented. This was recently blended with a mid-band gap polymer based on benzodithiophene and difluorobenzotriazole units (FTAZ) to create OPVs with power conversion efficiency of 12 - 13%.[110]

3.2 Material under investigation

IC-C6IDT-IC with the short name IDIC was invented by our collaborator Xiaowei Zhan and coworkers in 2016. It is a planar IDT based FREA with four n-hexyl sidechains synthesized using one step facile reaction and is characterized by a strong and broad absorption in 500 - 800 nm region which compliments that of donors in the visible and near infrared range (Chemical structure is shown in the **Figure 3.1**). IDIC is characterized by a highly planar backbone unlike the twisted backbone of rylene diimide-based acceptors.[105] It possesses a smaller band gap of 1.62 eV and having a strong and broader absorption which can effectively enhance J_{SC} in OPVs.

Initially, IDIC was blended with a polymer donor PDBT-T1 where the blended film exhibited a very smooth and uniform surface with a relatively small RMS roughness of 0.86 nm and highly ordered molecules with preferential "face-on" orientation. The device attained a maximum efficiency of 8.71% with a good charge transport and thereby outreached the other as-cast fullerene free PSCs reported. Later, Lin *et al.* blended IDIC with different wide band gap polymer donors such as PDCBT, J51, PTFBDT-BZS, PDBT-T1, and PTB7-Th in which the PTFBDT-BZS system

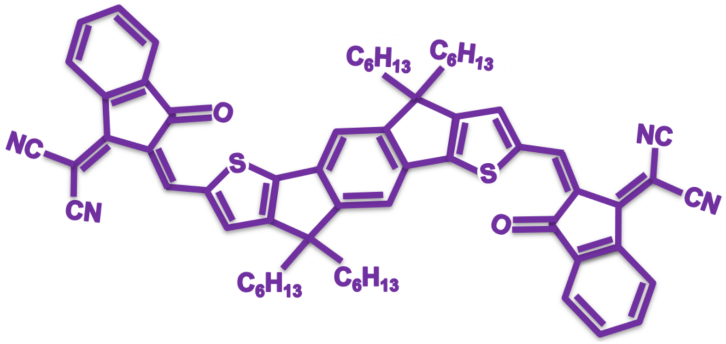

Figure 3.1: Chemical structure of IDIC

achieved a highest efficiency of 11.39% when DIO is used as the solvent additive.[111] Here, the addition of DIO improved the molecular packing of both donor and acceptor in the blend films with an enhancement in the domain purity of IDIC which resulted in very little bimolecular charge recombination and better charge transport. Recently, the same group reported a record efficiency of 12.5% for the combination of a medium band gap polymer donor, FTAZ and IDIC acceptor.[110] X-ray scattering measurements of those blends revealed large and pure phases 20 - 50 nm in size, consistent with the observation that the charge generation dynamics lacked the ultrafast component that characterizes most fullerene blends. To test the hypothesis that the phase size can be large due to facile exciton diffusion, ultrafast spectroscopic tools were employed to make a detailed study of the exciton diffusion in IDIC films.

3.3 Steady-state optical spectroscopy in IDIC films

When molecules make transition from their ground states to excited states on photon absorption, the electronic configuration changes which tempts nuclei to reorganize to new configurations by generating molecular vibrations. In other words, each electronic transition is accompanied by vibrational dynamics. The relative strengths of these vibrational transitions rely on the overlap of the corresponding vibrational wavefunctions which is referred to as the Franck-Condon overlap integral.[93] Moreover, the intensity of transitions from the zeroth level of ground state to m^{th} vibrational level of excited state defines a Poisson's distribution of the form,[93,141]

$$I_{0-m} = \frac{e^{-S} S^m}{m!} \tag{3.1}$$

where S is the Huang-Rhys parameter of the transition given by,

$$S = \frac{1}{2} M \omega_m \frac{\Delta Q^2}{\hbar} \tag{3.2}$$

where ΔQ defines the change in the nuclear coordinate during the transition. If there is no change in the nuclear coordinate ($\Delta Q = 0$) on excitation, then the absorption spectrum contains only the 0-0 transition line. When $\Delta Q \neq 0$, the higher the Huang-Rhys factor is, and the more intense are transitions to the higher vibrational levels as compared to 0-0.[141] Here the Huang-Rhys factor is related to the nuclear reorganization energy λ by $\lambda = S\hbar\omega$. In the presence of several vibrational transitions, the absorption or the emission spectra of a molecule can be described by Frank-Condon progression of Gaussians, which has previously been applied to the emission spectra of oligothiophenes.[48] This model is based on the assumption that vibronic structure in the absorption and emission spectra are caused from an electronic transition that is coupled to a single vibrational mode (example, C-C stretch). Accordingly, the spectra can be modelled by a progression of Gaussian line shapes displaced by the phonon energy of the vibrational mode by using the equation,[48,93]

$$I(\omega) \propto (\hbar\omega)^3 n(\omega) \times \sum_{m=0} \frac{S^m}{m!} \Gamma(E_{0-0} \pm m E_{ph}, \sigma) \tag{3.3}$$

where $\hbar\omega$ is the Einstein coefficient of spontaneous emission, $n(\omega)$ is the refractive index at a frequency ω (which is taken as a constant throughout the frequency range), S is the Huang-Rhys factor, m is the vibrational transition index, E_{ph} is the phonon energy of the C-C stretch, and Γ is a Gaussian line shape with full width half maximum σ.

To investigate the steady-state optical properties of IDIC, neat films were prepared from chloroform (12 mg/mL) *via* spin coating onto spectrosil fused silica substrates in air and at room temperature at 3000 rpm. The substrates were cleaned using ultrasound sonicator in chloroform followed by Isopropyl alcohol. Air was not found to be detrimental when comparing complete devices cast in air versus from N_2. **Figure 3.2** displays the UV-visible absorption and photoluminescence (PL) spectra for solutions and thin films. Here the UV-visible absorption spectra were recorded using a Cary 50 Bio UV-vis spectrometer over the range 190 - 1100 nm. A Horiba Fluorolog – 3 spectrometer was used to collect the steady-state photoluminescence. The film thickness was measured by the Dektak, Veeco surface profiler and found to be ∼90 nm for

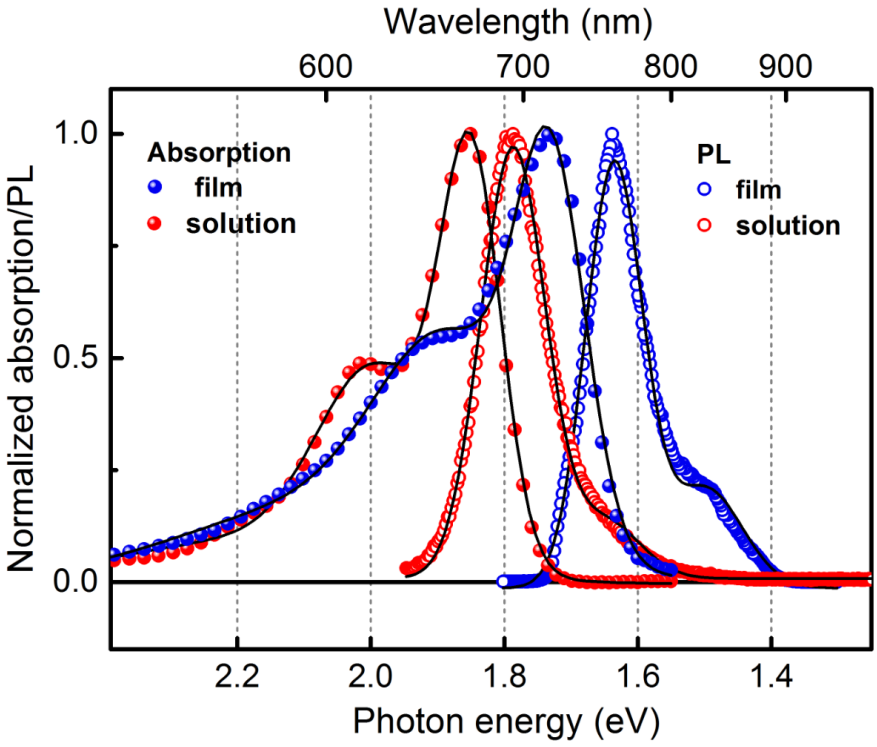

Figure 3.2: Steady-state absorption and PL spectra of IDIC in both solution and thin film along with their fits to the vibronic progression model (equation 3.3).

neat IDIC. As the figure shows, the thin film absorbs at 712 nm with a dominance of the 0-0 vibrational peak. The film absorption gives a red shift compared to the solution as expected, while their similar spectral shape suggests that aggregate coupling effects do not play a major role. Their fluorescent emissions are characterized by small Stokes shifts which is suitable for long-range resonant energy transfers.

The Frank-Condon progression model fits well with the absorption and emission spectra of IDIC and are shown in **Figure 3.2**. In the fitting procedure S, E_{0-0} and σ were the free parameters while $n(\omega)$ and E_{ph} were fixed. Here, the Huang-Rhys factor S is the main parameter of interest as it represents the measure of displacement of the equilibrium positions of the ground and excited state potential energy surfaces. For the 0-0 vibronic transition, m is zero and thereby the factor $\frac{S^m}{m!}$ will be equal to 1. The peak ratio of all higher vibrational transitions are determined by S. Optimized fits yield a Huang-Rhys factor of 0.2 which is very low compared to the values reported for conjugated polymers like oligothiophenes.[48] This clearly indicates that IDIC is a stiff molecule with rigid bonds and correspondingly small displacement between the excited and ground state potential energy curves that makes the 0-0 transition

dominant.

Collaborators from Peking University, China and University of Otago, New Zealand conducted electronic structure calculations and Raman measurements in IDIC films. Electronic structure calculations matched to experimental Raman spectra (Appendix: **Figure A.3** and **Figure A.4**) depict the S_1 state of IDIC as a strongly absorbing $\pi-\pi$ excited state with a high oscillator strength of 2.87, localized along the molecule with a minimal structural distortion (Appendix: **Figure A.5**). Using the same computational approach as Swick *et al.*, a reorganization energy of 0.17 eV was obtained, in line with the low reorganization energies recently found for other members of this class of fused ring electron acceptors.[163]

3.4 Time-resolved spectroscopy in IDIC films

A series of transient absorption spectra for an IDIC film at various time delays are shown in the **Figure 3.3a**. Here the neat IDIC film was excited by 100 fs, 716 nm laser pulses and the excitations were probed *via* a broadband white-light continuum generated by focusing the 800 nm fundamental beam to an undoped YAG crystal. The polarization of the pump and the probe pulses were set to the magic angle (54.7^0) at the sample in order to prevent orientational dynamics. For the measurements, 6000 shots were averaged for each time delay and were repeated at least 4 times. The data were saved as binary files and then processed *via* the MATLAB software including chirp and background corrections. To avoid degradation, the samples were measured under vacuum environment. It was confirmed that photo-product build-up did not affect the measured dynamics by comparing the correspondence of signals and dynamics from sequential TA scans.

TA spectra of IDIC film give a positive differential transmission feature around 1.6 - 2 eV which can be largely attributed to the ground state bleaching. But it extends further to the red where PL occurs, explained by stimulated emission from the S_1 state which is confirmed from the PL spectrum. The TA spectrum also features a sub-gap excitonic photoinduced absorption peak around 1.4 eV. The similar decay dynamics of ground state bleach and photoinduced absorption features confirm the presence of only one species - singlet excitons. The spectrum displays negligible change with time (Appendix: **Figure A.1**). **Figure 3.3b** gives the normalized exciton dynamics in the IDIC film probed at 1.45 eV, taken at a very low pump fluence of 1.55 $\mu J/cm^2$.

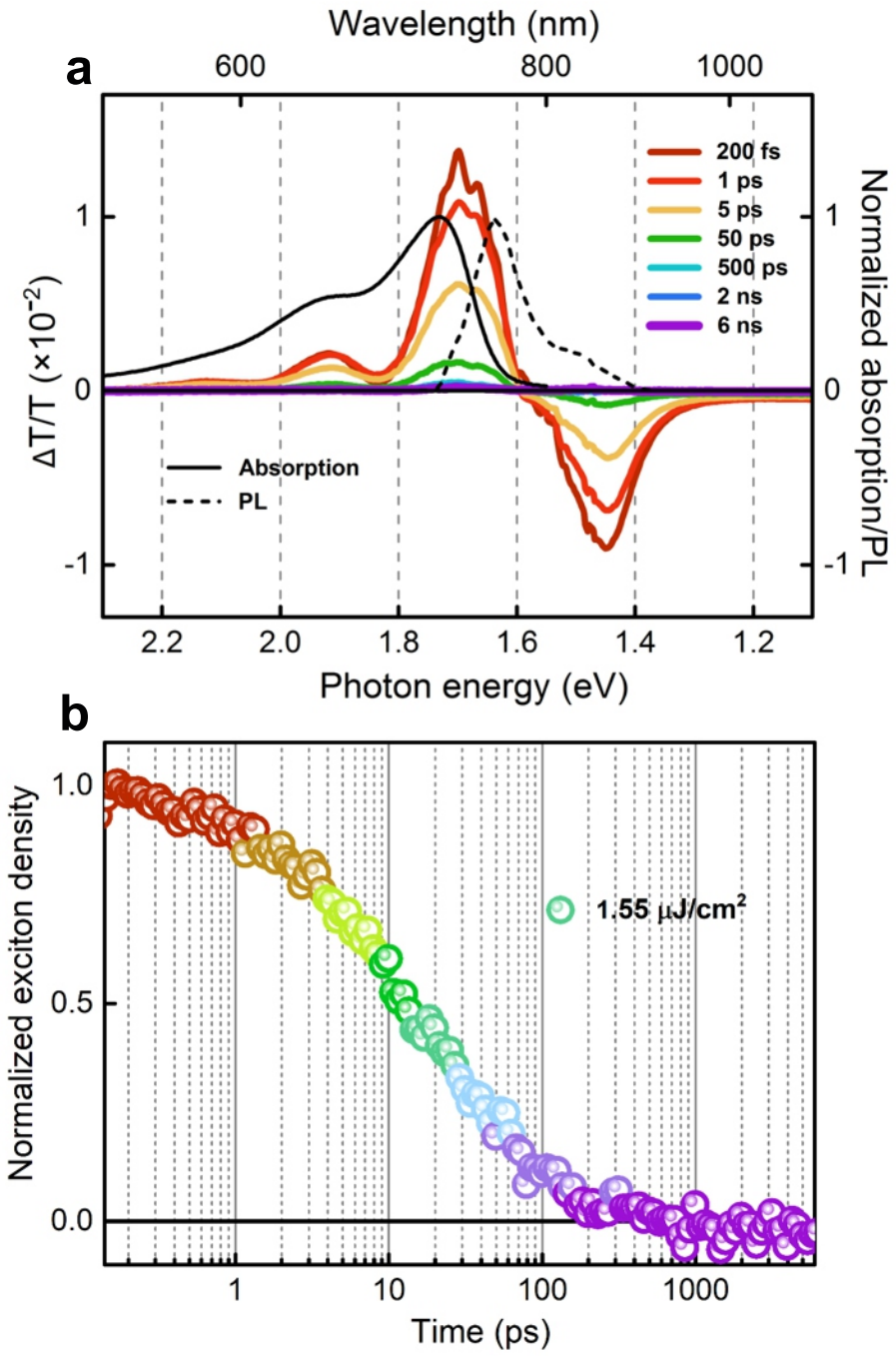

Figure 3.3: (a) Series of transient absorption spectra of IDIC film at different time delays (excited at 716 nm, at a pump fluence of 6.56 μJ/cm^2) along with the normalized steady-state absorption and photoluminescence spectra and (b) normalized exciton dynamics in the IDIC film probed at 1.45 eV after a low pump fluence excitation (1.55 μJ/cm^2).

The apparent half-life of only ~10 ps already reflects substantial exciton annihilation at this fluence, as confirmed from the 126 ps lifetime measured in a dilute polystyrene

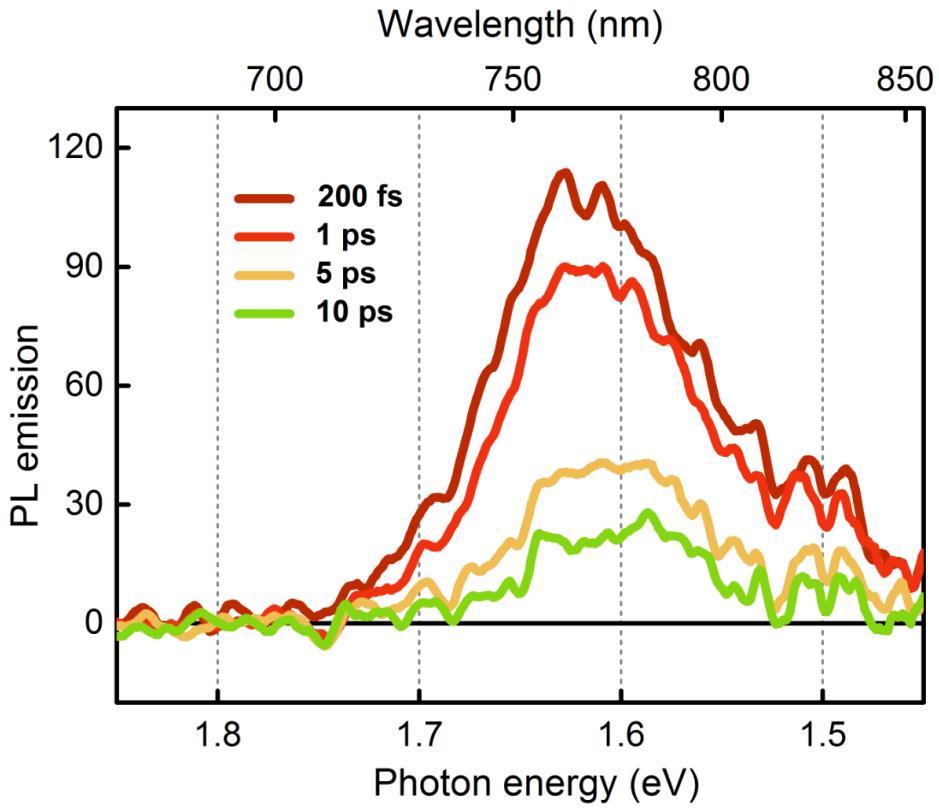

Figure 3.4: Series of transient photoluminescence spectra of IDIC film at various time delays, excited at 515 nm, at a fluence of 7.8 μJ/cm^2. The measurement was performed by Dr. Kai Chen, Victoria University of Wellington, New Zealand.

blend film (Appendix: **Figure A.2**). Here the important question arises: how the IDIC excitons cross the 20 - 50 nm sized domains in the OPV cells within such a short lifetime.

Figure 3.4 gives the time-resolved PL spectra of IDIC film measured using transient grating PL spectroscopy. Here, instead of a Ti:Sapphire laser, a 100 kHz fiber amplifier producing 130 fs pulses, attenuated to a pulse energy of 200 μJ/pulse was used. The 1030 nm fundamental output of the fiber laser was used to generate the transient grating in an undoped YAG crystal, which makes the near IR region where IDIC emits accessible. Here the sample was excited at 515 nm and the transient PL was measured by a spectrometer equipped with back-illuminated CCD camera. The high energy PL edge red shifts only by $\sim$<0.02 eV within the first picosecond, beyond which the PL spectrum exhibits little shift within its lifetime. This lack of spectral dynamics is a sign of energetic order, and contrasts with even moderately ordered π-conjugated semiconductors such as P3HT, where dispersive energy relaxation shifts

the PL spectrum by ∼0.2 eV over its lifetime.[20]

3.5 Exciton diffusion constant measured *via* annihilation

The exciton annihilation method is used to measure exciton diffusion constants. This method employs ultrafast TA spectroscopy to measure exciton lifetimes as a function of exciton density. Annihilation occurs when excitons collide and exchange energy, thus the diffusion constant is readily obtained from the bimolecular rate constant for a series of known excitation densities. The advantages of this method include its fast time-resolution, and that it can be carried out in bulk films without requiring sharp exciton quenching interfaces.

Integrated intensity of the exciton band at 1.45 eV was used to track the exciton recombination dynamics. **Figure 3.5** gives the exciton kinetics of IDIC film at different pump fluences with minimal spectral shift. Here the excitation fluences range from 1.55 μJ/cm^2 to 14.44 μJ/cm^2 with exciton half lives of ∼10 ps and ∼2 ps, respectively. The intensity dependent dynamics of excitons is discussed by analyzing bimolecular recombination or more specifically singlet-singlet exciton annihilation (SSA).[140,155,156,165] At low fluences, the PIA signal decays exponentially. At high excitation fluences, however, this behavior changes - at shorter time scales, a rapid non-exponential decay is observed, while for longer time scales, the decay remains exponential. The faster decay is dependent on the excitation intensity, suggesting higher order recombination pathways, most probably SSA. The slower decay is independent of intensity, suggesting monomolecular decay due to radiative and non-radiative deactivations of singlet excitons. In IDIC samples, even at low fluence, fast intensity dependent decay of excitons were observed, which reveals the dominance of SSA. The rate equation for the singlet exciton decay is given by,

$$\frac{dn(t)}{dt} = -kn(t) - \frac{1}{2}\gamma(t)n^2(t) \tag{3.4}$$

where $n(t)$ is the exciton density at a delay time t after laser excitation, k is the monomolecular decay rate due to radiative and non-radiative deactivations, and $\gamma(t)$ is the time-dependent singlet-singlet exciton annihilation constant. The factor $\frac{1}{2}$ in the second term of the right hand side indicates that the singlet exciton-exciton annihilation arises when the two excitons are in sufficient proximity to be able to fuse,

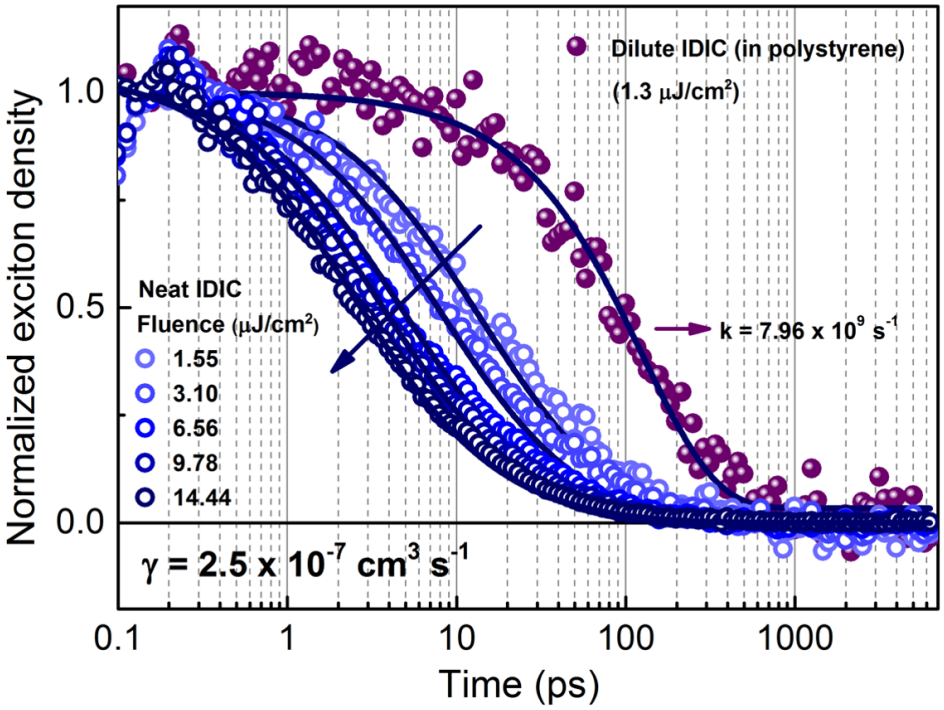

Figure 3.5: Fluence dependent singlet exciton decays of neat IDIC film fitted to the singlet-singlet exciton annihilation model (equation 3.6) where the arrow indicates increasing fluence. The reference kinetics from a film of IDIC diluted in a polystyrene matrix is also shown.

yielding a higher-energy exciton, which then relaxes back to the lowest excited state with net effect that one of the excitons has been lost to heat. The γ parameter is time-dependent when exciton diffusion is slow or occurs in systems with low dimensionality (1D or 2D).[165] Here 3D diffusion of excitons is assumed, where excitons diffuse randomly in all directions with an isotropic diffusion coefficient. For the 3D system, the bimolecular reaction rate $\gamma_{3D}(t)$ is given by,

$$\gamma_{3D}(t) = 8\pi DR\left[1 + \frac{R}{\sqrt{2\pi Dt}}\right] \tag{3.5}$$

where D is the isotropic diffusion coefficient and R is the effective interaction radius, or annihilation radius, of singlet excitons which is the exciton separation at which annihilation occurs. For a later time stage ($t >> \frac{R^2}{2\pi D}$), the annihilation rate becomes time independent as $\gamma_{3D} = 8\pi DR$, which then solves the annihilation rate equation given by,

$$n(t) = \frac{n(0)\exp(-kt)}{1 + \frac{\gamma}{2k}n(0)\left[1 - \exp(-kt)\right]} \tag{3.6}$$

where $n(0)$ is the exciton density immediately after the laser excitation. Here it is assumed that one absorbed photon produces one singlet exciton as there is no polaron formation directly from photon absorption observed in the neat IDIC film. The intensity dependent exciton decays at different pump fluences were globally fitted to equation 3.6 to determine the values of annihilation constants γ_{3D}. Here the intrinsic monomolecular decay constant k was fixed at 7.96 $\times$ 10^9 s^{-1}, extracted from the dilute IDIC:polystyrene film where diffusion and annihilation does not occur. The global fits shown in **Figure 3.5** account for absolute excitation densities, which were ascertained from the TA signal after accounting for the fluence, the optical density at the excitation wavelength, and the film thickness.

The exciton decays in **Figure 3.5** were well fitted by equation 3.6, where the only free parameter was the bimolecular rate constant fitted as (2.5 $\pm$ 0.05) $\times$ 10^{-7} cm^3/s. The bimolecular rate constant was then used to determine the 3D exciton diffusion coefficient;

$$D = \frac{\gamma}{8\pi R} \tag{3.7}$$

The annihilation radius is generally assumed to be 1 nm, which yields D = 1 $\times$ 10^{-1} cm^2/s in this case.[156] However, from the **Figure 3.3a**, it is clear that there is a strong resonance between the exciton absorption (PIA) and the emission (PL) spectra. (re-plotted in the **Figure 3.6**, with the spectral overlap highlighted). This led the investigation of the role of Förster resonance energy transfer (FRET) in the exciton-exciton annihilation process observed in IDIC films. In the FRET mediated exciton annihilation process, excitons act as both donors and acceptors of energy which can inturn boost the annihilation radius. The role of energy transfer in exciton annihilation can be quantified in terms of Förster radius, R_0 (equation 1.2, here it represents the annihilation radius) which is defined as the distance at which the energy transfer efficiency is 50%. The value of R_0 strongly depends on many parameters: the spectral overlap integral between the excited state absorption (PIA) and emission (PL), the quantum yield of the material (Q_Y), the refractive index of the medium (η), and the relative orientation between emissive and absorptive dipoles

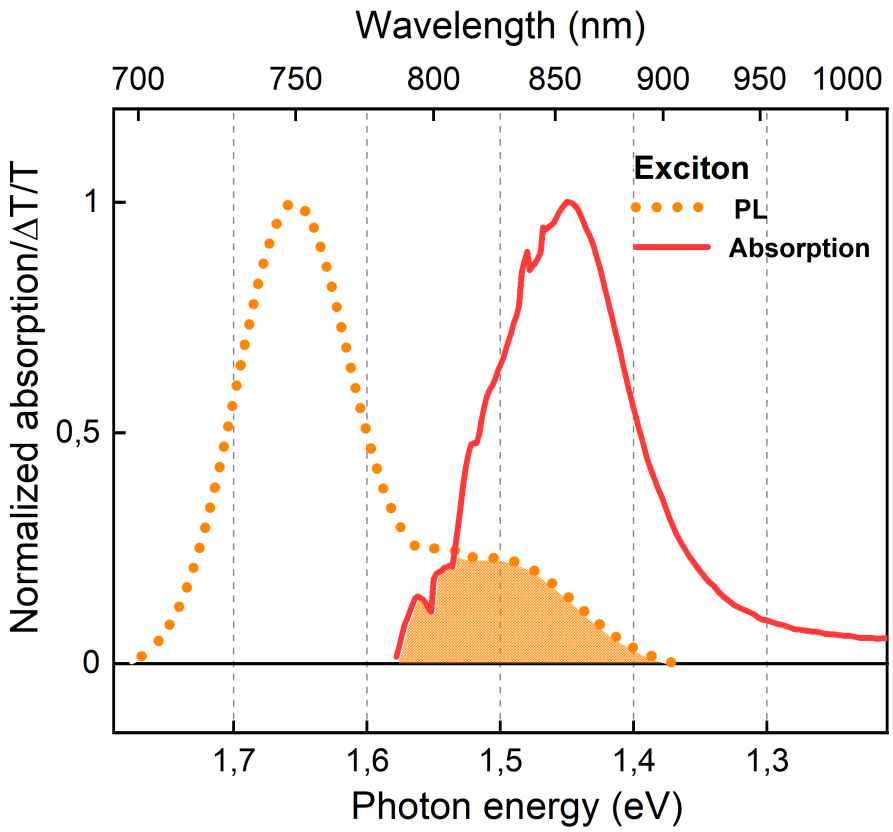

Figure 3.6: Steady-state emission and photoinduced absorption spectra of IDIC film with the spectral overlap highlighted.

(κ^2). Here a spectral overlap integral of 1.863×10^{16} nm^4 was extracted where the exciton absorption spectrum was calculated from the 1 ps PIA data from the low fluence measurement. It is noted that the PIA peak was normalized to the same peak extinction coefficient as the ground state absorption. This yielded a Förster radius for exciton-exciton annihilation of 2.9 nm (the calculation was done using a PL quantum efficiency of 3% and with the assumption that transition dipoles in the IDIC film have parallel orientations; κ^2 =1), which then gave a 3D diffusion coefficient of 3.4×10^{-2} cm^2/s.

The measured exciton diffusion coefficient for the solution-processed IDIC films is substantially higher than most solution-processed organic semiconductors, including P3HT ($D = 1.8 \times 10^{-3}$ cm^2/s, measured *via* time-resolved surface quenching),[156] PPV derivatives ($D = 0.3 - 3 \times 10^{-3}$ cm^2/s, *via* time-resolved volume quenching and exciton-exciton annihilation),[95,126] PCPDTBT ($D = 3 \times 10^{-3}$ cm^2/s, *via* time-resolved volume quenching),[137] and $PC_{71}BM$ ($D = 1.6 \times 10^{-4}$ cm^2/s, *via* time-

resolved volume quenching).[67] Moreover, the satisfactory fit of our data using a single and time-independent annihilation constant suggests that the dispersive behaviour characterizing other solution-processed films does not play a major role for IDIC. The only organic semiconductors found to rival this present work are the structurally rigid and ordered ladder-type poly-p-phenylene ($D = 4.42 \times 10^{-2}$ cm^2/s)[65] and poly(9,9-di-n-octylfluorenyl-2,7-diyl) ($D = 2 \times 10^{-2}$ cm^2/s),[160] however it is noted that that those values may be overestimated due to the assumed annihilation radii of 1 nm (neglecting resonance enhancement).

Exciton annihilation data for films of two further fused ring electron acceptors are also included in the Appendix (**Figure A.6** and **Figure A.7**). One is a derivative of IDIC with different side-chains (IC-1IDT-IC) and the other is a lower band gap acceptor FOIC, whose blends were recently shown to exhibit similar charge generation kinetics as IDIC blends.[98,106] Like IDIC, these other fused ring electron acceptors exhibited strongly fluence dependent decays due to exciton annihilation at low excitation density. Annihilation data for the IDIC derivative fitted well to the 3D bimolecular annihilation model, producing a comparable bimolecular rate constant (3.2 $\times$ 10^{-7} cm^3/s) to IDIC. The FOIC data, while showing strong fluence dependence indicative of a high diffusion coefficient, was not well fitted by the 3D diffusion model.

Exciton diffusion length L_D for a given organic active material in an OPV is the critical device parameter as it reflects a characteristic distance over which an exciton can migrate before it decays.[135] It can be calculated by,

$$L_D = \sqrt{D\tau} \tag{3.8}$$

where τ is the intrinsic exciton lifetime. L_D is estimated as $\sim$ 35 nm if typical 1 nm annihilation radius is assumed, or 16 nm for a 4.8 nm annihilation radius. Here τ is taken as 126 ps, calculated from the dilute IDIC:polystyrene measurement. There are a few materials reported with exciton diffusion length larger than 10 nm with 1D diffusion, like perylene bisimide aggregates (96 nm),[124] ladder-type PPV derivatives (11-14 nm),[61,65] but they are not particularly suited for OPV cells. The comparatively long exciton diffusion length measured for IDIC also explains an intriguing observation in previously reported OPVs using IDIC as an acceptor. In FTAZ:IDIC blends with 12 - 13% power conversion efficiency, scattering measurements revealed phase sizes 20 -

50 nm, and in contrast to typical polymer:fullerene blends, charge generation kinetics lacked an ultrafast component associated with excitons generated at interfaces. With such a high exciton diffusion coefficient, diffusion from the center to the edge of a 20 - 50 nm IDIC phase can easily occur on the picosecond timescale.

3.6 Activationless exciton diffusion

To investigate the role of temperature on the fast exciton diffusion, temperature dependent exciton-exciton annihilation measurements were performed on IDIC films.

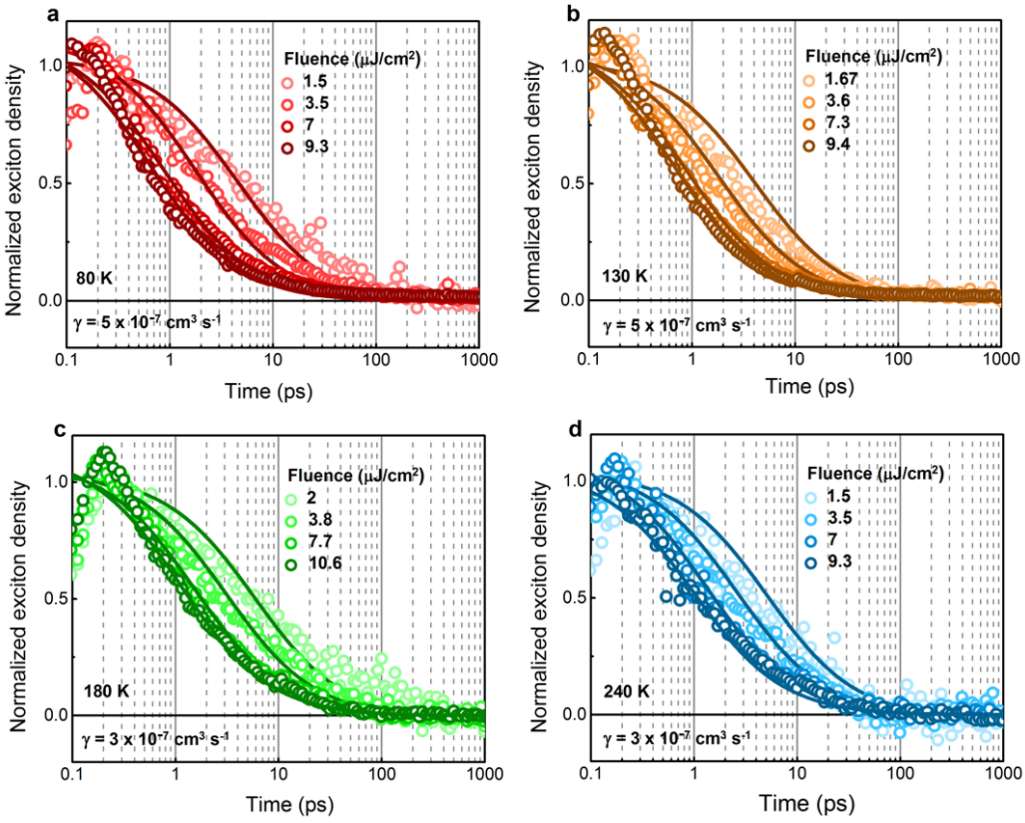

Figure 3.7: Fluence dependent singlet exciton decays at different temperatures fitted to the singlet-singlet exciton annihilation model. The corresponding annihilation constants are noted in the figures.

The cryo-measurements were carried out using "Janis Research Model VPF-100" liquid nitrogen (LN_2) cryostat for five different temperatures starting from 80 K to 290K and then returning to 80 K to confirm that the sample did not change during the measurements. Here the intensity dependent exciton kinetics at each temperature were globally fitted to equation 3.6 and the corresponding γ_{3D} was extracted (**Figure 3.7**).

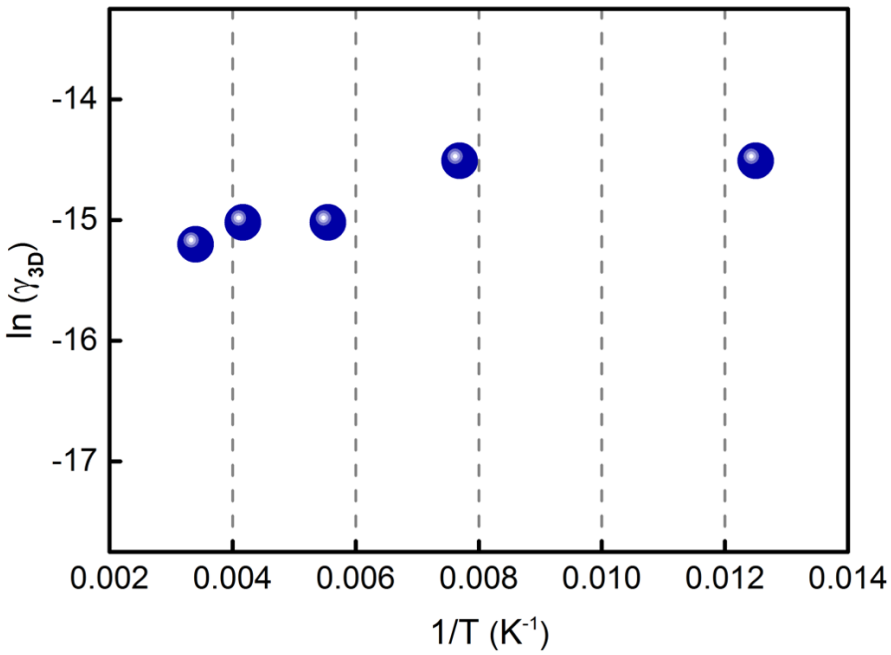

Figure 3.8: Arrhenius plot of exciton–exciton annihilation constants versus reciprocal temperature.

To calculate the thermal activation barrier for bimolecular recombination of excitons, an Arrhenius plot of $\ln \gamma_{3D}$ versus reciprocal temperature was constructed (**Figure 3.8**). As per the plot, it is clear that the bimolecular decay constant of IDIC has little effect on temperature that suggests activationless diffusion of excitons. In contrast to typical disordered organic semiconductor films whose exciton transport is suppressed at low temperature, it is found that high exciton diffusion coefficients in IDIC were maintained at least as low as 80 K.[136]

3.7 Key factors for high exciton mobility in IDIC

3.7.1 Structural order

Polarization anisotropy is a tool that provides structural information by probing the relaxation of electronic excited states. When a material with randomly oriented chromophores interacts with polarized light, the probability of chromophores being excited depends on the direction of their transition dipole moments with respect to the polarization of the electric field of the incident light. In other words, this probability is higher for the chromophores whose dipoles are aligned parallel to the light polarization which will be the polarization of the initial excited state, thus the population of excitations which are aligned close to the axis of polarization can be

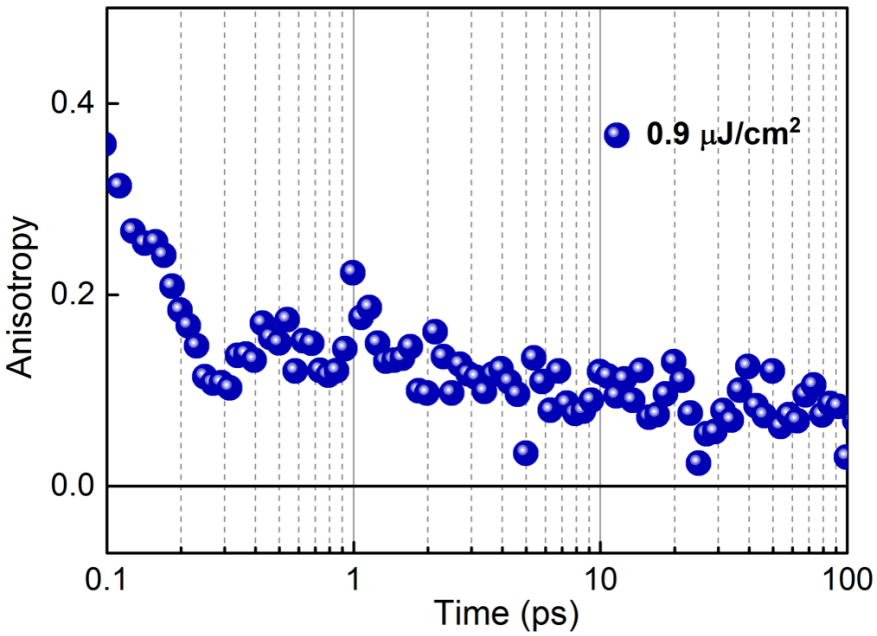

Figure 3.9: Transient absorption polarization anisotropy of neat IDIC film excited at 716 nm, at a pump fluence of 0.9 μJ/cm^2.

obtained. If the state undergoes a relaxation or the excitations migrate, there can be changes in the orientation of the dipoles which introduces a change in the anisotropy. The anisotropy that describes the extent of polarization of excitations in a material is calculated using the equation,

$$r = \frac{[\frac{\Delta T}{T}]_{\parallel} - [\frac{\Delta T}{T}]_{\perp}}{[\frac{\Delta T}{T}]_{\parallel} + 2[\frac{\Delta T}{T}]_{\perp}} \tag{3.9}$$

where $\frac{\Delta T}{T}_{\parallel}$ and $\frac{\Delta T}{T}_{\perp}$ are the differential transmissions signals corresponding to the parallelly and perpendicularly oriented chromophores, respectively. The maximum theoretical value of anisotropy for a dipole absorption in the absence of any relaxation process is 0.4.

Anisotropic measurements were carried out in IDIC films using the same transient absorption experimental setup apart from including a waveplate to selectively excite the parallelly and perpendicularly oriented dipoles in the film and then isolating the corresponding TA signals using a fixed broadband polarizer applied to the probe. Here, it is noted that the pump power incident on the sample was equal in both of its polarization states.

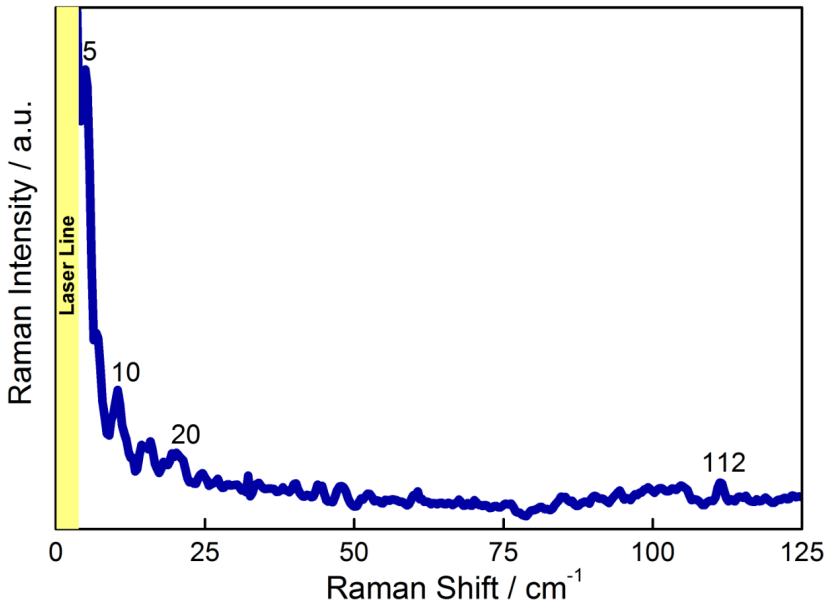

Figure 3.10: Low frequency Raman spectrum for IDIC recorded at 830 nm, using a 830 nm SureBlockTM XLF-CLM THz-Raman system (Ondax Inc. Monrovia, CA, USA), coupled fibre optically to a SpectraPro 500i (Acton Research. Acton, MA, USA) and liquid nitrogen cooled Spec-10:100 B CCD (Roper Scientific, Trenton, NJ, USA). The measurements were performed by Prof. Keith C. Gordon and students from University of Otago, New Zealand.

The anisotropy result given in the **Figure 3.9** reveals that excitons predominantly hop between aligned chromophores as they diffuse. The figure displays an initial ultrafast decay of anisotropy from the maximum theoretical value 0.4 to 0.1 in the first 400 fs after the excitation. This is similar to what Banerji *et al.* observed in the PL anisotropy measurements of a conjugated polymer P3HT where they got an initial anisotropy of 0.2, which is considerably lower than the theoretical value expected in the absence of relaxation process.[10] They noted that this strong emission depolarization within the time-resolution was caused by several processes such as local structural rearrangements, the localization of the initially delocalized excitations, and Förster assisted excitation energy transfers.[11] Following the ultrafast decay, the polarisation anisotropy in IDIC film is maintained above 0.1 for it's entire lifetime indicating that the excitations maintained their memory of polarisation throughout their lifetime which confirms their high mobility and rapid diffusion. High mobility of excitations is usually achieved with a film containing highly aligned chromophores. This confirms the structural order in IDIC films that create arrays of near parallel transition dipole moments, well-suited for rapid, long-range resonant energy transfer.

Raman spectroscopy was used to probe the structural order in neat IDIC film. Prof. Keith C. Gordon and his students from University of Otago, New Zealand carried out the experiment in the 100 cm^{-1} frequency range, where Raman scattering comes from intermolecular phonon modes, and the occurrence of sharp peaks signifies long-range order. As per the Raman spectrum given in the **Figure 3.10**, IDIC film shows sharp peaks below 25 cm^{-1}, confirming that the solution processed IDIC adopts a structurally ordered packing arrangement. The presence of such sharp low frequency bands is consistent with a high level of ordering or crystallinity, as has been observed for other semiconducting materials. This finding is in agreement with previous X-ray scattering measurements that revealed a crystal domain size of 20 - 50 nm.

3.7.2 Energetic order

Density of excitonic states (DOS) in a material can be represented as a Gaussian distribution with a full width half maximum σ which is a measure of disorder present in the material. As the materials absorb light, excitons are created in the high energy tail of the Gaussian DOS, after which they undergo a downhill migration to the lower states which is usually called thermalization. This process ends as the excitons reach the most populated states corresponding to an energy of $-\sigma^2/KT$ which is responsible for the 0-0 emission peak in the PL spectrum.[136] Temperature has a crucial role on the position of most populated state. At low temperatures, it is situated deep in the tail of the DOS while at higher temperatures, it is closer to the middle of the DOS as the excitons are thermally disturbed. The increase in the energy of the most populated states with temperature gives a blue shift of the PL spectrum.[136]

In order to study the effect of energetic disorder in the exciton diffusion in IDIC films, temperature dependent steady-state photoluminescence was employed. For typical measurements, the sample was kept in the "Janis Research Model VPF-100 System" cryostat and the spectra were recorded by a polychromator (SP2300 by Princeton Instruments) and an intensify CCD camera (PIMAX 3 by Princeton Instruments) following by a laser excitation at 680 nm. **Figure 3.11a** gives the PL spectra of IDIC film measured over the temperature range 80 - 293 K. Spectra at each temperatures were fitted to Frank-Condon progression model (equation 3.3) to calculate the exact position of E_{0-0} peak which corresponds to the energy of the most populated state. Here it was assumed that the excitons reach the equilibrium state within their lifetime. The Gaussian disorder σ, experienced by the excitons can be obtained from the slope of the plot of E_{0-0} versus 1/T (**Figure 3.11b**). The data exhibits

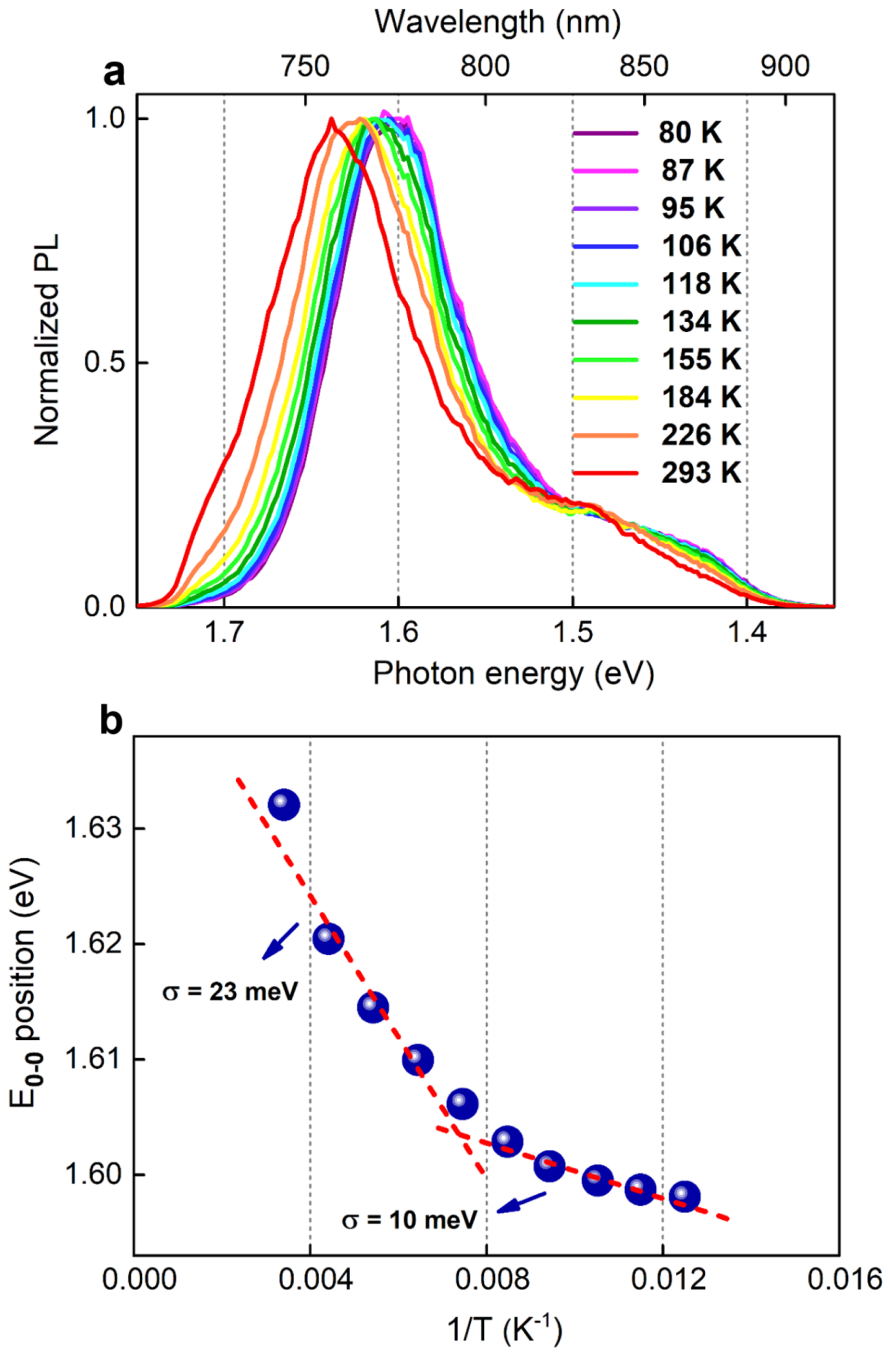

Figure 3.11: (a) Temperature dependent steady-state emission spectra of neat IDIC film after 680 nm excitation and (b) temperature dependence of 0-0 emission peak energy extracted from the fits to the Frank-Condon vibronic progression model. The range of Gaussian energetic disorder is obtained from the slopes at each extreme and are noted in the figure.

pronounced curvature, with an apparently higher slope at high temperature. This is consistent with the activated diffusion model and data reported by Mikhenko and

coworkers for the disordered conjugated polymer MDMO-PPV.[136] Here Gaussian disorder in the range of 10 - 23 meV was extracted for IDIC films which is substantially lower than that of MDMO-PPV (44 meV). Organic semiconductors, especially conjugated polymers, are characterized by inhomogeneously broadened DOS and thereby high energetic disorder. Low disorder widths are rarely observed, generally in structurally rigid molecules such as ladder type conjugated materials.[175] Importantly, the measured disorder is less than the thermal energy at room temperature (26 meV) which is consistent with the lack of dispersive exciton transport observed for IDIC.

3.7.3 Förster resonant energy transfer for exciton diffusion

The good spectral overlap between ground state absorption and emission led the investigation of the role of Förster resonant energy transfer (FRET) in the large exciton diffusion lengths observed in IDIC films.

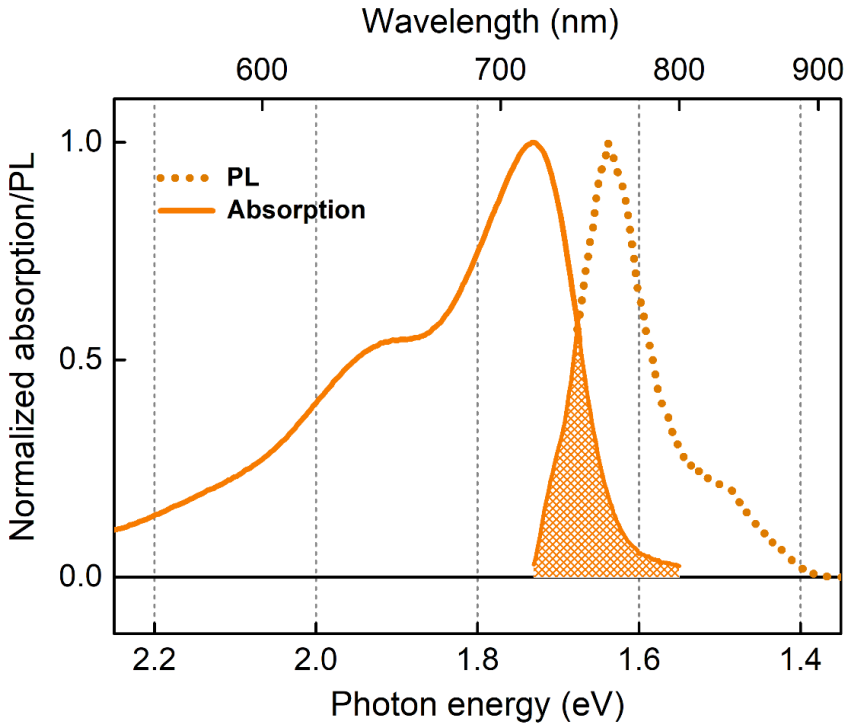

Figure 3.12: Steady-state absorption and emission spectra of IDIC film with the spectral overlap highlighted.

Figure 3.12 presents the absorption and the emission spectra of an IDIC film with the spectral overlap highlighted. As described in the chapter 1, in the FRET mediated diffusion process, the excitons move from an excited molecule (energy donor) to a molecule in the ground state (energy acceptor) such that at the end of the process,

the energy donor molecule is in the ground state and the energy acceptor molecule is in the excited state.

In the same way as exciton-exciton annihilation (section 3.5), the role of Förster energy transfer in exciton diffusion can also be quantified in terms of the Förster radius R_0, which in this context represents the distance between the energy donor and energy acceptor molecules at which the FRET efficiency for diffusion is 50%. Unlike exciton-exciton annihilation, R_0 for exciton diffusion strongly depends on the spectral overlap integral between the emission and ground state absorption of the material (all other parameters remains the same). The self-FRET radius of IDIC excitons is calculated as 2.8 nm. The calculation was done using a PL quantum efficiency of 3%, an estimated spectral overlap integral of 1.524×10^{16} nm^4 and also with the assumption that transition dipoles in the IDIC film have parallel orientations ($\kappa^2 = 1$). The extraordinarily high value of FRET radius directly gives the reason for large exciton diffusion length in IDIC films. This also reflects the fact that the inefficient exciton diffusion in polymers is due to the large Stokes shift between their absorption and emission spectra.

3.8 FRET parameters: molecular basis, intrinsic limits and chance of further enhancements

The high exciton diffusion coefficient observed for IDIC is well described *via* the simple resonant energy transfer mechanism; the same physics previously used to describe materials with substantially slower diffusion. Aggregate effects such as supertransfer[81] do not appear to play a role when considering the similar spectral shapes for neat films and dilute films where aggregates can not form. The facile exciton diffusion for IDIC thus results from many FRET parameters being optimized for long-range transport (**Figure 3.12** summarizes the mechanism of exciton diffusion in IDIC films). This section considers the molecular basis of these factors, their intrinsic limits, and the possibility of further enhancements.

The most important factor for transfer between the same chromophore is the spectral overlap. When expressed as the FRET radius, R_0 (assuming random dipolar alignment for comparison with published results), R_0 value in IDIC of 2.8 nm substantially exceeds previously reported values, which are in the range of 1.0 - 2.0 nm.[121] Since

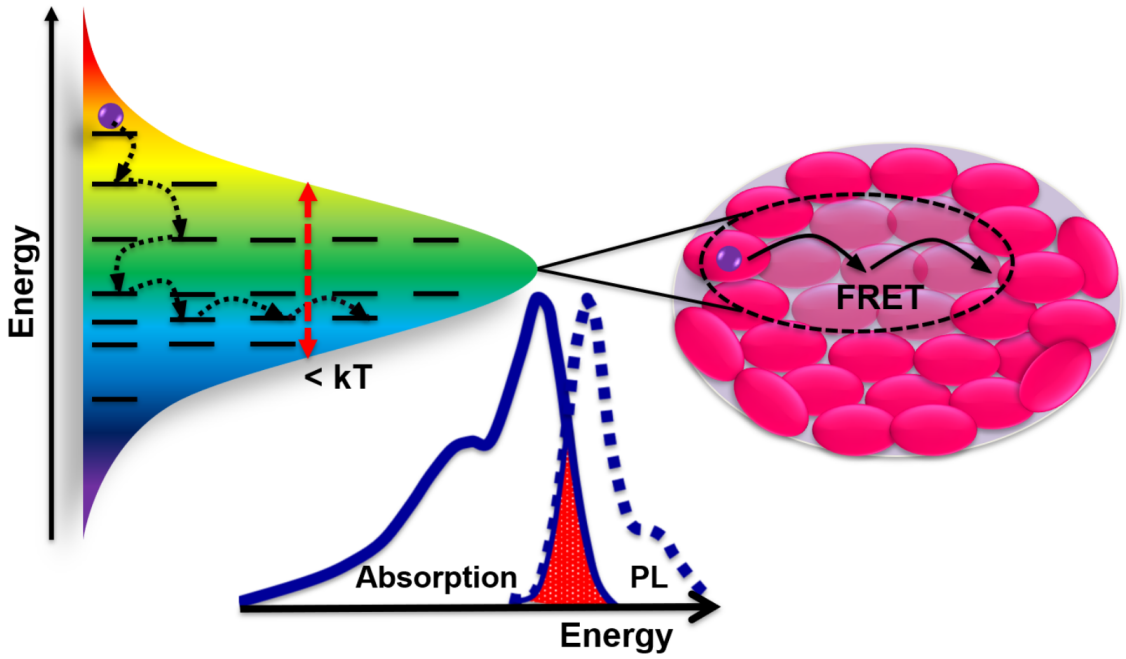

Figure 3.13: Mechanism of high exciton diffusion in IDIC film at a glance.

resonant overlap between the absorption and PL of IDIC comes from the 0-0 vibrational peaks, the dominance of the 0-0 peaks for absorption and PL in IDIC (*ie.*, low Huang Rhys factor, low reorganization energy) means that its high oscillator strength is concentrated in the overlapping region. The strong self-overlap ultimately arises from the rigidity imparted by the fused ring structure of IDIC and other fused ring electron acceptors - again reminiscent of ladder-type polymers. It is estimated that the spectral overlap integral would be increased by a factor of 2.6 if the energy offset between 0-0 peaks in absorption and PL were completely eliminated, which would enhance the diffusion length by the same factor.

The low energetic disorder of IDIC is an important factor for its facile exciton diffusion, and is another consequence of it being a rigid, crystalline small molecule. Dispersive exciton transport is a hallmark of disordered materials, whereby excitons undergo diffusion only while relaxing within the density of states, before running out of spatially and energetically accessible transfer sites. Since the Gaussian disorder of IDIC spectroscopically measured from excited state energies is lower than the thermal energy, excitons in IDIC can sustain long-range energy transfer throughout their lifetime.

The parameters outlined above benefit substantially from the fused ring molecular

structure of IDIC, yet there is room for further enhancement. With optimized BHJ domain sizes already 20 - 50 nm, further increases in self-spectral overlap and energetic order may push the exciton diffusion length toward the absorption length of ∼100 nm. An exciton diffusion length exceeding the optical absorption length would obviate the need for a BHJ morphology and introduce the possibility of solution-processed bilayer devices. Bilayer devices with sharp interfaces, or even BHJs with very large domains, may not suffer from morphology-dependent effects like reduced fill-factor, variability in morphology, and the requirement to tune side-chains and deposition conditions to optimize morphology. Moreover, new low band gap semiconductors are expected to require enhanced exciton diffusion coefficients to compensate for their generally shorter exciton lifetimes.[68]

Finally, it can be noted that care must be taken when undertaking time-resolved spectroscopy on fused ring electron acceptor materials like IDIC. Facile exciton diffusion means that their exciton-exciton annihilation thresholds are substantially lower than expected for most OPV materials. Indeed, annihilation still dominates the picosecond dynamics of IDIC at fluences as low as ∼1 μJ/cm^2.

3.9 Conclusion

A quasi-activationless diffusion coefficient of at least 2×10^{-2} cm^2/s is derived for the fused ring electron acceptor, IDIC using ultrafast transient absorption spectroscopy. This property is consistent with the 20 - 50 nm domains found in optimized BHJ devices with 12 - 13% power conversion efficiency, and it is a consequence of molecular factors favoring long-range resonant energy transfer. The rigid planar structure of the molecule focuses its absorption and emission oscillator strength into overlapping 0-0 vibronic peaks, enhancing resonant energy transfer. Low energetic disorder means that facile diffusion is sustained throughout the exciton lifetime, and structural order also boosts the orientation factor. These results challenge long-held assumptions of exciton diffusion constraints, and raise the prospect of high performing solution-processed bilayer OPV devices.

Chapter 4

Bilayers - a new paradigm in photovoltaic device design

One of the major challenges, the bulk-heterojunction (BHJ) OPV devices face is the extremely arduous formation process of the so-called BHJ morphology which is highly influenced by the balance between many parameters including domain size, miscibility, and purity. The morphology control is even more complicated when it comes to large scale industrial production. This is an appropriate time to have an amendment and go back to the world of **bilayer OPVs**. The barricade created by the short exciton diffusion lengths in active layer components has been opened by the invention of facile exciton diffusion in fused ring electron acceptors (FREAs). Here lay the first stone to the world of highly efficient and perfect bilayer heterojunctions with a 11% efficient FREA based bilayer OPV favored from high molecular packing densities and absorption coefficients, long exciton diffusion lengths, and efficient, resonant, long-range donor to acceptor layer FRET*.

*__S. Chandrabose__, S.Y Park, M.B Price, H.S Rhu, T.H Lee, Y.S Shin, Z. Wu, W. Lee, K. Chen, S. Dai, J. Zhu, P. Xue, X. Zhan, H.Y Woo, J.Y Kim, and J.M Hodgkiss, (**2020**). "*Photophysics of high efficiency bilayer organic solar cells: effect of large extinction coefficients, high exciton diffusion coefficients, and interlayer energy transfer*", submitted for publication.

Collaborators contributed to the work

Material design and fabrication: (**a**) Prof. Xiaowei Zhan and students from Peking University, Beijing, China and (**b**) Prof. Han Young Woo and students from Korea University, South Korea.

Device design and fabrication, Morphology and photovoltaic characterization: (**a**) Prof. Jin Young Kim and group from Ulsan National Institute of Science and Technology (UNIST), South Korea and (**b**) Prof. Han Young Woo and students from Korea University, South Korea.

Research focused on

Transient absorption spectroscopic measurements: (**a**) Exciton diffusion measurements in neat donor and acceptor materials and (**b**) transient absorption measurements in bilayer films.

Data processing and analysis: (**a**) Singlet-singlet exciton annihilation (SSA) fittings, (**b**) calculation of exciton diffusion parameters and (**c**) application of MCR-ALS algorithm on bilayer data.

4.1 Introduction

Bulk-heterojunction (BHJ) organic solar cells are promising candidates for solar energy harnessing as they offer diverse advantages such as lightweight, low cost, solution-processibility, and non-toxicity.[85,186] Solution-processed BHJs have gained a serious attention in the last two decades due to their ability to dissociate excitons very efficiently over the whole extent of the cell unlike planar heterojunctions and could achieve PCEs as high as ∼16%.[45,189] However, from a material and device design perspective, BHJ structure devices possess severe drawbacks. The first and the most important one is the morphology which is crucial for attaining high performance. The formation of BHJ morphology is an extremely arduous process and is highly depending on the balance between many parameters such as donor and acceptor ratios, their solubility and crystallinity, deposition solvents, miscibility, and processing temperature.[39] The morphology control becomes much more challenging when it comes to large scale production which caused OPV devices to suffer efficiency drops when the device area is scaled-up.[148] The challenge in optimizing the BHJ for a given set of materials has led to insufficient focus on intrinsic optoelectronic properties, as well as lack of ability to perform any form of interfacial engineering.[171] This means that materials designed for their favorable absorption and electronic properties often perform poorly in BHJ OPVs due to unfavorable morphologies, resulting in just a handful of OPV materials setting efficiency records, out of >35,000 publications to date.[177] Additionally, the BHJ systems are highly affected by severe non-geminate charge recombination at the interfaces which can occur either directly or *via* an intermediate polaron pair state.[38] This results in a trade-off between exciton dissociation where a fine grained phase segregation is ideal, and charge transport where a planar configuration is appropriate.

On the other hand, sequential deposition of the donor and acceptor materials to form a bilayer junction is conceptually more straightforward. The bilayer structure is optimal for charge transport due to the low possibility of recombination at the interface. This is mainly due to the device configuration of two separate layers which decreases the chances of meeting between the separated charge carriers. Additionally, the bilayer structure exhibits less dependence on the donor to acceptor ratio, solvent, and miscibility as the layers are processed and optimized independently.[39] They are particularly favorable for printing large-area devices, as the bilayer morphology forming process is mainly controlled by thermodynamic diffusion and is less sensitive to

the device area. However in practical world, the efforts of achieving perfect bilayer junctions have been severely hindering by percolation and interpenetration between the donor and acceptor layers.[94] To date, the most efficient bilayer OPV systems with well-separated bilayer morphologies have PCEs only up to 3%.[7,103] In this work, FREA based bilayer systems exhibiting high efficiencies without having intermixed morphologies are studied. Here the problem of intercalation is solved *via* judicial selection of orthogonal solvents and materials processing. This has enabled to make use of different favourable properties of the active layer components such as high donor and acceptor layer absorption coefficients, high exciton diffusion lengths, and significant donor to acceptor layer energy transfer, in order to create record OPV bilayer devices with efficiencies up to 11%.

4.2 Motivation to bilayer devices

Apart from intermixed morphology, the apparent pervasiveness of 5 - 10 nm exciton diffusion lengths in organic semiconductor films has been creating an obstruction for an era of high efficiency bilayer solar cells for a long time.[134,135] As per the definition, the exciton diffusion length is a characteristic physical quantity, which is expressed as $L_D = \sqrt{D\tau}$, where D is the exciton diffusion coefficient and τ is the exciton lifetime. In most of the conjugated polymers, the singlet exciton lifetimes are found to be very short, typically less than 1 ns, which limits the diffusion lengths to much shorter values compared to the ∼100 - 200 nm absorption path lengths in the devices.[68] The remaining criterion, D is optimized *via* several important parameters in which the rate of incoherent resonant energy transfer has an apical influence. As already explained in the first chapter, FRET is an electrodynamic phenomenon that occurs because of long-range dipole-dipole interactions between the excitons in the excited and ground state of a material. Many parameters account for the variation of self-FRET rates in different materials including absorption-emission oscillator strengths, spectral overlap integral, structural and morphological order and energetic disorder.[18] As most of the conjugated polymers are characterized by large Stoke-shifted emission spectra, their self-FRET radii are bounded in the range of 1 - 2 nm. Additionally, owing to the large disorder present in conjugate polymer films, their Gaussian density of states (DOS) are inhomogeneously broadened in energy having widths (measure of energetic disorder) exceeding thermal energy at room temperature (eg., 44 - 125 meV energetic disorder in PPV derivatives[136]). All these aspects result in a substantial suppression of exciton diffusion coefficients that limits the probability of excitons to reach the

interface to become dissociated. In short, the diffusion dynamics in conjugated polymers is much more complicated than in small molecules and is difficult to be improved.

The invention of fused ring electron acceptors (FREAs) gave a great mitigation to all these issues and become excellent partners to conjugate polymer donors. Unlike polymers, FREAs are more crystalline which directly relates to the planarity of their core groups that tightens the $\pi-\pi$ stacking and favors the face-on orientation. Generally, in BHJ OPVs, crystal domains have negative impacts as they induce large phase separation which doesn't favor the exciton diffusion since the excitons have to cross large distances to reach the interfaces. Additionally, the singlet exciton lifetimes are greatly suppressed in FREA like low band gap materials due to the increased rate of non-radiative relaxation. Recently, we have conducted a detailed examination of the exciton diffusion in a FREA, IDIC, whose blend with a mid-band gap polymer donor achieved an efficiency of 12 - 13% regardless of its 20 - 50 nm domain sizes[18,110] (refer chapter 3). We extracted a high, quasi-activationless exciton diffusion coefficient of 1×10^{-1} cm^2/s, proving that the phase size in the devices can be large owing to the facile exciton diffusion in FREAs. The diffusion coefficient of IDIC excitons is two orders of magnitude higher than that of the famous conjugated polymers such as P3HT (1.8×10^{-3} cm^2/s) and PCPDTBT (3×10^{-3} cm^2/s).[137,156] The high exciton diffusion in IDIC films resulted from many optimized parameters including very low energetic disorder, good transition dipole moment alignment, low reorganization energy, and high spectral overlap integral - all boosting the long-range resonant energy transfer. We estimated a FRET radius of 2.8 nm which would be further increased by a factor of 2.6 for zero Stokes shift, which would enhance the diffusion length by the same factor. All the parameters for an enhanced diffusion length of 35 nm in IDIC substantially benefited from its rigid fused ring molecular structure. All these hallmarks of IDIC introduced the possibility of solution-processed bilayer devices using FREAs which will be a new paradigm in the photovoltaic device design.

4.3 Bilayer working principle

In this work, various polymer:FREA bilayer devices were fabricated based on a simple working principle. **Figure 4.1** presents a schematic of the key processes in a bilayer solar cell. The processes include exciton diffusion, long-range donor to acceptor FRET, and charge generation and transport.

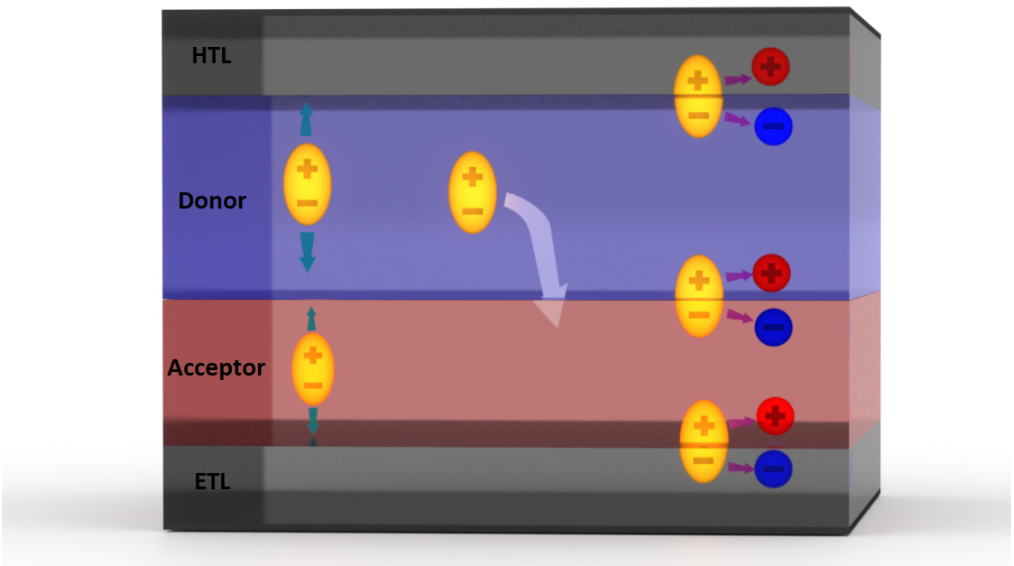

Figure 4.1: Schematic of key processes in a typical bilayer solar cell.

Exciton diffusion: On light illumination, excitons are generated in donor and acceptor layers. Unlike a BHJ device, a bilayer cell has single interface so that excitons have to travel large distances from their origin to reach the interface in order to become dissociated. Excitons directed by green arrows represent the process of exciton diffusion in the active layer components. The diffusion process is highly mediated by FRET especially in the acceptor layer as FREAs are characterized by large absorption and emission spectral overlap.

Donor to acceptor layer FRET: Simultaneously, a major part of the excitons formed in the donor layer is transferred into the acceptor layer *via* FRET due to the high spectral overlap integral between the donor emission and acceptor absorption spectra. The process of donor to acceptor layer FRET is represented by the white arrow.

Charge generation and transport: Once the excitons reached the interface, they separate into electrons and holes due to the energy offset between the LUMO or HOMO levels of donor and acceptor (purple arrows). The separated electrons drift through the acceptor material and are transported to the cathode of charge collection *via* the electron transporting layer (ETL). ETL facilitates the photo-generated electrons in reaching the cathode as fast as possible while operating as a hole blocking layer restricting the holes from reaching the cathode and recombining with electrons.[4] Similarly, holes travel through the donor material and are collected at the anode *via*

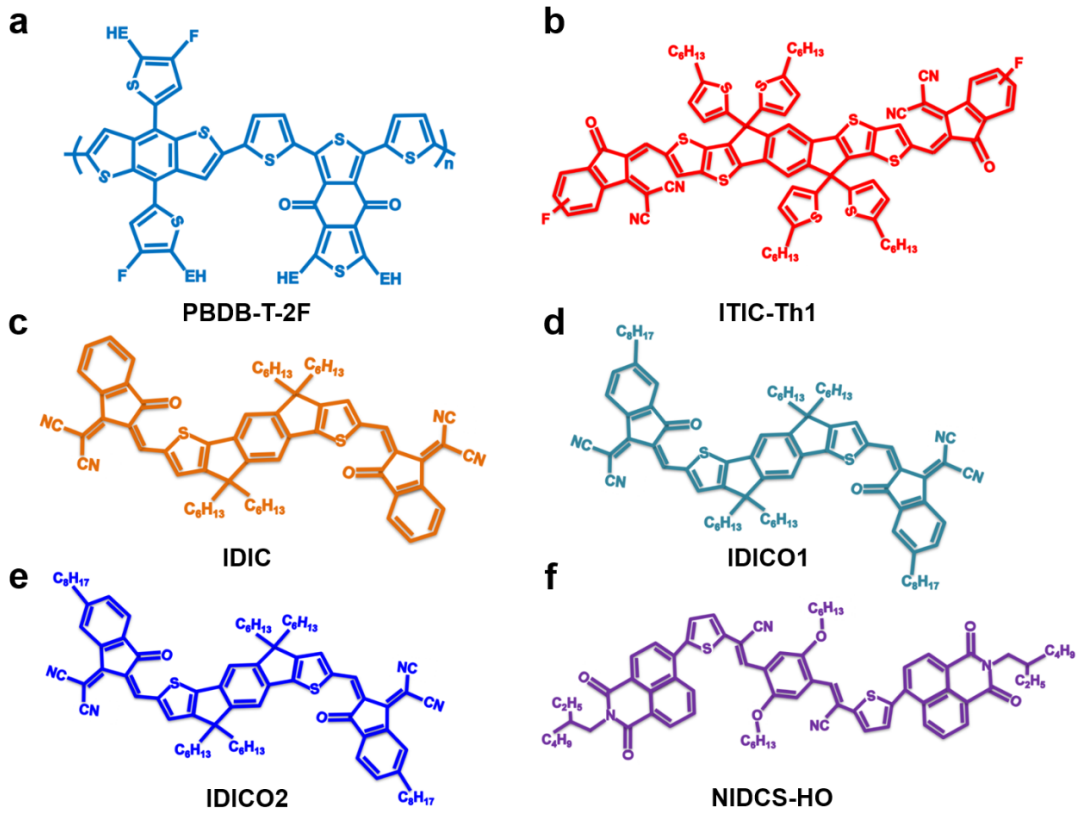

Figure 4.2: Molecular structures of (a) PBDB-T-2F, (b) ITIC-Th1, (c) IDIC, (d) IDICO1, (e) IDICO2, and (d) NIDCS-HO.

hole transporting layer (HTL). The charge generation process can also takes place at the donor/HTL and acceptor/ETL interfaces.

4.4 Materials selection

There are several key factors regarding the active layer components that contribute to the performance of a typical bilayer system. They include high absorption coefficients, complementary donor and acceptor absorption profiles, large exciton diffusion lengths, and high donor and acceptor spectral overlap. The main criterion for materials selection was particularly the high light harvesting efficiency of the resulting bilayer cells which is governed by the ratio between exciton diffusion length and absorption length of donor and acceptor materials. Larger self-FRET radii can be a good proxy for longer diffusion lengths and hence enhanced exciton harvesting.[135] Self-FRET radius for exciton diffusion is governed by the spectral overlap of ground state absorption and emission. Therefore, as the first step of device design, materials with high spectral overlap (low Stokes shift), large absorption coefficients (short ab-

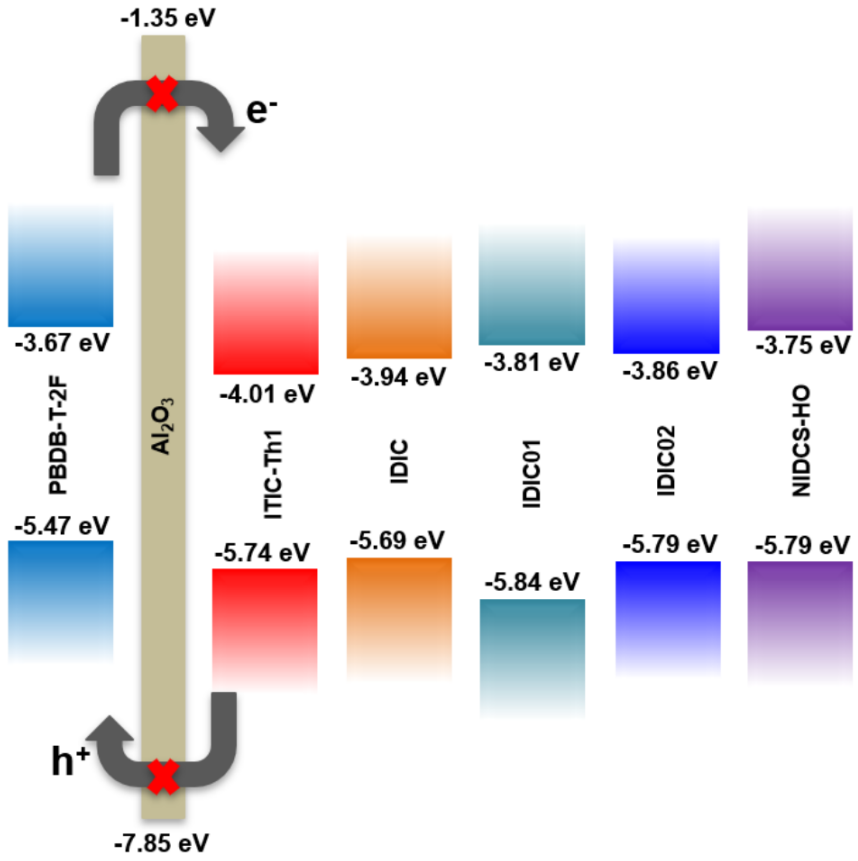

Figure 4.3: Energy band diagram of the bilayer active layer components. The energy levels were measured by Prof. Jin Young Kim and students from UNIST, South Korea.

sorption lengths), and high molecular densities were selected.

PBDB-T-2F (PM6, molecular weight: ≥80000 g/mol and polydispersity index: 2.9) was chosen as the donor which has been reported as a highly efficient conjugated polymer in various non-fullerene BHJ systems.[96,189] Five different FREAs, ITIC-Th1,[199] IDIC,[99,111] IDICO1, IDICO2, and NIDCS-HO[92] were selected based on their Stokes shifts and the degree of spectral overlap integral between the donor emission and acceptor absorption. These acceptors have already shown high efficiencies in various non-fullerene OPV systems. **Figure 4.2** provides detailed molecular structures of the selected donor and acceptor materials. Appendix: **Figure A.8** presents the exceptionally high absorption coefficients of the materials. This enables a high absorption fraction across the visible spectrum for very thin layers of the active layer components. Absorption lengths were calculated by taking the inverse of the peak absorption coefficients and are shown in the **Table 4.1**. Energy band diagrams are

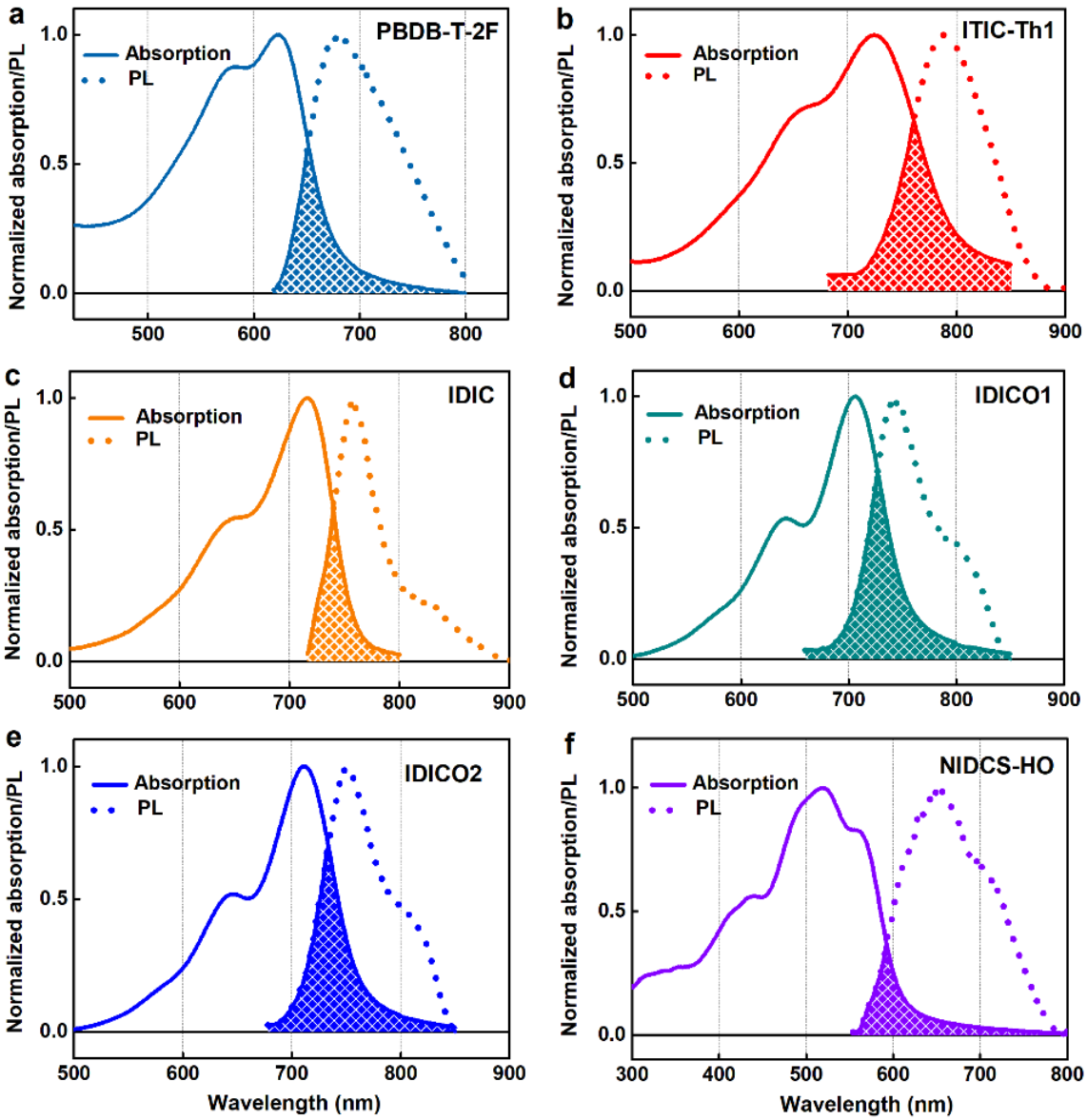

Figure 4.4: Steady-state absorption and emission spectra of (a) donor (PBDB-T-2F) and acceptors - (b) ITIC-Th1, (c) IDIC, (d) IDICO1, (e) IDICO2 and (f) NIDCS-HO - with the corresponding spectral overlaps highlighted.

presented in the **Figure 4.3** which shows that each donor and acceptor combination is energetically suitable to provide photovoltaic effect.

Figure 4.4 gives the steady-state absorption and emission spectra of the donor and acceptor materials highlighting the corresponding spectral overlaps. A Cary 50 Bio UV-vis spectrometer was used to record the absorption spectra of all neat films in the range 190 - 1100 nm. Photoluminescence spectra were obtained using a Cary

Table 4.1: Summary of materials selection parameters, absorption lengths, Stokes shifts, PLQE, Self-FRET radii (R_0) and predicted diffusion lengths (L_D) for neat donor and acceptor materials.

Material	**Abs.length (nm)**	**Stokes shift (nm)**	**PLQE (%)**	**R_0 (nm)**	**L_D predicted (nm)**[a)]
PBDB-T-2F	67.6	55	1.4	2.1	3.8
ITIC-Th1	29.0	66	2.5	3.0	5.0
IDIC	20.2	48	3.0	2.8	5.6
IDICO1	18.9	38	8.4	3.5	17.5
IDICO2	20.4	40	9.3	3.4	16.0
NIDCS-HO	64.0	133	8.4	2.9	10.0

[a)] Calculated according to equation 4.1.

Eclipse (Varian) spectrometer. Absorption and PL spectra of materials could be influenced by the solvent used. So, all the neat films were prepared from solutions with dichloromethane (DCM) which is used in the fabrication of the corresponding bilayer cells. The donor absorption possesses high intensity contribution from both the 0-0 and 0-1 vibrational peaks which is inline with the high Huang-Rhys factors and thereby non-rigidity observed in conjugated polymers.[48] The PL emission is featureless with a small Stokes shift of 55 nm. While ITIC-Th1, IDIC, IDICO1, and IDICO2 feature absorption spectra dominated by the 0-0 vibrational peak and emissions with small Stokes shifts of 66, 48, 38 and 40 nm, respectively. NIDCS-HO is characterized by a large Stokes shift of 133 nm. Self-FRET radii of the neat films were calculated using equation 1.2 and are presented in the **Table 4.1**. All the materials are characterized by large self-FRET radii and hence could expect high exciton diffusion lengths which is crucial for bilayer device performance. Moreover, the complimentary absorption between the donor (PBDB-T-2F) and FREAs (except NIDCS-HO), spans the whole visible light region, even extending to NIR with large absorption coefficients is apt for boosting EQE, IQE, J_{SC}, and in turn the overall device efficiency. Here the photoluminescence quantum yield measurements were obtained in an integrating sphere using the method of de Mello *et al.*[36]

A rough estimate of diffusion length based on self-FRET hopping transport to nearest neighbours can be estimated from the self-FRET radius (R_0), according to,[135]

$$L_D = \sqrt{\tau_f D} = \frac{R_0^3}{d^2\sqrt{6}} \tag{4.1}$$

where d is the nearest neighbour distance. The predicted diffusion lengths are presented in the **Table 4.1**. For the calculations, d for each material was taken from their structure measurements and are 1 nm for IDIC,[18] IDICO1 and IDICO2, 1.5 nm for ITIC-Th1[64] and 1 nm for PBDB-T-2F and NIDCS-HO. Nonetheless, there are well known limitations to this analysis. Importantly, this assumption only considers energy transfer to nearest neighbours. This equation is valid in the vast majority of systems whose R_0 values have been evaluated around 1 - 2 nm; however, longer transfer steps should clearly be considered in all the materials here due to the high values of their self-FRET radii. Hence, advanced spectroscopic measurements were conducted to confirm high exciton diffusion in the active layer components which is discussed in the section 4.7. However, a prior inspection of the aforementioned optical parameters is an inevitable task in the materials selection process for bilayer devices.

4.5 Bilayers without intermixed morphology

The story of bilayer OPVs started in the late 1980's, but the limited exciton dissociation efficiencies at the interfaces created a barricade in their development in the past three decades. In 1998, Friend *et al.* invented the layer-by-layer (LBL) deposition technique which greatly improved the exciton dissociation and charge transport.[59] Nowadays, LBL deposition has been considered as one of the most effective ways to fabricate bilayer junctions, which includes the consecutive deposition of solutions of neat donor and acceptor materials to form a photoactive layer. But, the LBL processing strategies can only generate pseudo-bilayer configurations in which the active layer is composed of a donor dominated bottom layer, a donor-acceptor mixed middle layer and an acceptor rich top layer.[30,39,193,194]

To form a perfect bilayer heterojunction, the LBL processing needs a set of so-called orthogonal solvents which allow sequential spin-casting of donor and acceptor layers. The concept of orthogonal solvents implies that the solution of the top acceptor layer should not be dissolved in that of the bottom donor layer. At present, the selection of orthogonal solvents finds difficulties as most of the high-performance donor and acceptor materials are designed for conventional BHJ structures and hence they are enabled to show similar solubilities in organic solvents.[30] Thus, when the acceptor

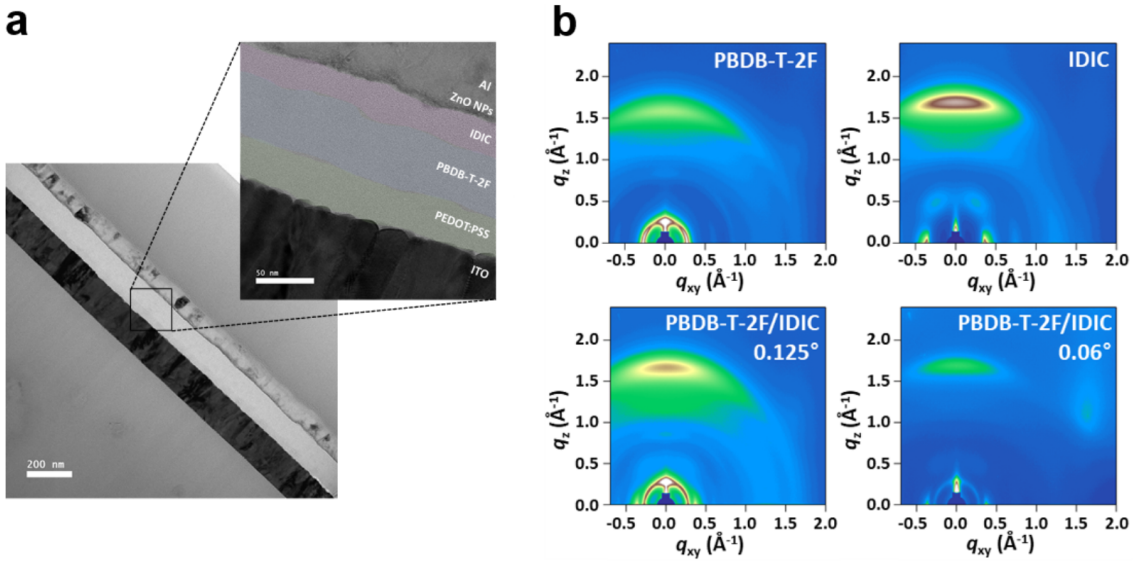

Figure 4.5: (a) Cross-section TEM images of PBDB-T-2F:IDIC bilayer and (b) GIWAXS pattern images for PBDB-T-2F, IDIC pristine films and PBDB-T-2F:IDIC bilayer film with different X-ray incident angles of 0.125^0 and 0.06^0. The data were obtained by Prof. Jin Young Kim and students from UNIST, South Korea.

layer is spin-coated on top of the donor layer, the polymer will be quickly dissolved and washed-off partially, resulting in an unfavorable morphology and poor reproducibility. Additionally, there are reports showing that the small molecule acceptors have the tendency to diffuse into the polymer donor film after being spin-cast on to the bottom donor layer and this inter-diffusion is difficult to be controlled.[22,149]

In this work, a series of bilayer heterojunctions were fabricated with the fixed donor polymer, PBDB-T-2F and the five highly efficient non-fullerene acceptors, ITIC-Th1, IDIC, IDICO1, IDICO2, and NIDCS-HO. In the typical fabrication process, the donor polymer solution in chlorobenzene (CB):1,8-octanedithol (ODT) (100:1 volume ratio) was spin-cast onto PEDOT:PSS coated ITO substrate after which it was undergone thermal annealing at 100 ^{0}C for 5 minutes in an N_2 filled glove box. For the spin-casting of acceptor layer on top of PBDB-T-2F layer, solutions were made in such a way that IDIC, ITIC-Th1 and NIDCS-HO were dissolved in dichloromethane (DCM) while IDICO1 and IDICO2 were dissolved in DCM:ODT and DCM:(1-chloronaphthalene) CN, respectively. Here, the selection of orthogonal solvents CB and DCM was done carefully such that the final films exhibited strong donor-acceptor phase separation. All the bilayer devices were prepared by Prof. Jin Young Kim and students from UNIST, South Korea.

The single junction bilayer configuration in the films was confirmed by cross-sectional TEM (Transmission electron microscopy) where IDIC was selected as a representative material. **Figure 4.5a** provides the cross-sectional TEM image of PBDB-T-2F:IDIC bilayer, where the sample was prepared using a focused ion beam (FIB) instrument of Helios 450HP FIB (FEI) and the high resolution image was obtained using JEM-2100F (JEOL) (the measurements were carried out by Prof. Jin Young Kim and students from UNIST, South Korea). The TEM image shows that the donor and acceptor layers are well distinguished each other with slightly different contrast which is originated from the different molecular structure of conjugated polymer and small molecules. The neat and the bilayer films of IDIC were also characterized by grazing-incidence wide angle X-ray scattering (GIWAXS) where different X-ray angles (θ) of 0.125^0 and 0.06^0 were used to distinguish between the top and the bottom layers, respectively (**Figure 4.5b**). At $\theta = 0.125^0$, all the crystalline packing peaks from both the pristine PBDB-T-2F and IDIC were observed while at $\theta = 0.06^0$, only the crystalline peaks of IDIC were detected. In the in-plane mode (q_{xy}) (probing lamellar structure), the (100) plane peak from IDIC was dominant while that from PBDB-T-2F was almost disappeared. In the out-of-plane mode (q_z), (010) peaks in the bilayer film were observed identical to that of pristine IDIC, implying that the donor and the acceptor layers are well separated in the bilayer system. Furthermore, the surface morphology probed *via* atomic force microscopy (AFM) and absorption of the bottom layer (PBDB-T-2F) of the bilayer film after washing out the IDIC layer were almost identical to that of the pristine PBDB-T-2F film (Appendix: **Figure A.9** and **Figure A.10**, respectively). This implies that the donor layer was not affected during film formation of the acceptor layer. However, if some intermixing happened, it might not be playing a functional role in the device operation as the bilayer excitonic data is well described by the donor to acceptor Förster resonance energy transfer model discussed below (section 4.8).

4.6 Bilayer devices with record efficiency of 11%

Table 4.2 gives a close outlook of the photovoltaic parameters of all the bilayer solar cells compared with that of the corresponding BHJ devices. All the photovoltaic characterizations were performed by Prof. Jin Young Kim and students from UNIST, South Korea. The bilayer devices were fabricated through the spin-casting of donor and acceptor layers from their respective orthogonal solvents. In BHJ OPVs, the donor to acceptor ratio was fixed at 1:1 and pre-annealing or solvent additive

strategies were used to optimize the film morphologies. Out of all BHJs, the PBDB-T-2F:ITIC-Th1 device showed the best PCE of 11.2% with a high short-circuit density (J_{SC}) of 16.9 mA/cm^{-2}, open-circuit voltage (V_{OC}) of 0.93 V and a fill factor (FF) of 0.71. Other devices except that of NIDCS-HO exhibited high and similar PCEs. The low PCE of PBDB-T-2F:NIDCS-HO device is evident from the low band gap of NIDCS-HO that limits the absorption range of the blend and thereby J_{SC}. However, all the BHJ devices exhibited adequate FFs over 0.60 indicating that the charge carriers were well extracted at the electrodes.

Table 4.2: Summary of photovoltaic parameters of PBDB-T-2F:non-fullerene acceptor bilayer and BHJ solar cells. The data were obtained by Prof. Jin Young Kim and students from UNIST, South Korea.

Active layer	**Acceptor**	**Thickness (nm)**	**J$_{SC}$ (mA/cm^2)**	**V$_{OC}$ (V)**	**FF**	**PCE (%)**
BHJ	ITIC-Th1	124	16.9	0.93	0.71	11.2
	IDIC	113	14.4	0.95	0.72	9.87
	IDICO1	114	11.8	1.01	0.64	7.57
	IDICO2	125	13.8	1.00	0.66	9.19
	NIDCS-HO	120	6.35	1.23	0.61	4.78
Active layer	**Acceptor**	**Thickness (D/A nm)**	**J$_{SC}$ (mA/cm^2)**	**V$_{OC}$ (V)**	**FF**	**PCE (%)**
Bilayer	ITIC-Th1	50/35	16.9	0.94	0.69	11.0
	IDIC	50/30	14.1	0.96	0.71	9.59
	IDICO1	50/20	13.6	1.02	0.69	9.51
	IDICO2	50/18	13.7	1.01	0.66	9.15
	NIDCS-HO	50/33	6.46	1.13	0.35	2.57

Remarkably, the bilayer systems of PBDB-T-2F:ITIC-Th1, IDIC, IDICO1 and IDICO2 exhibited outstanding device performance with excellent PCEs in the range of 9 - 11%. Particularly, the ITIC-Th1 bilayer device showed the best PCE of 11% with a J_{SC} of 16.9 mA/cm^{-2}, V_{OC} of 0.94 V and a FF of 0.69 which are almost similar to that of the corresponding BHJ device. All the devices except that of NIDCS-HO exhibited similar photovoltaic parameters with their respective BHJ versions. Surprisingly, the PBDB-T-2F:IDICO1 system showed higher PCE than that of the corresponding BHJ device. Meanwhile, the NIDCS-HO device performance was poor with a low FF of 0.35.

4.7 High exciton diffusion in active layer components

Owing to the exceptional device efficiencies, advanced spectroscopic studies were performed to confirm the basic working principle and elucidate the photophysical processes occurring in these devices. As the first step, high exciton diffusion lengths in the active layer components were confirmed using ultrafast spectroscopic tools which is crucial as the analytical expression for L_D given by equation 4.1 is limited to materials with short self-FRET radii. Exciton-exciton annihilation measurements are one of the simplest spectroscopic methods to extract exciton diffusion lengths.[18] This method employs ultrafast transient absorption (TA) spectroscopy to measure singlet exciton lifetime as a function of excitation fluence. The advantage of this method over others include its fast time-resolution and can be easily done in bulk films without requiring sharp exciton quenching interfaces.

A home-built ultrafast TA setup was used to probe the singlet excited states of all of the neat materials. Appendix: **Figure A.11** provides a series of TA spectra of neat films at different pump-probe delay times. The spectra include positive differential transmission signals, representing ground state bleach (GSB) consistent with the corresponding steady-state absorption spectra and negative sub-band gap photoinduced absorption (PIA) signals assigning the exciton absorption. The neat donor PIA includes a shoulder near 1.3 eV which is attributed to free charge carriers generated in the disordered polymer chains.[115] The GSB signals from the acceptors except NIDCS-HO are extended towards red where the respective PL emissions occur. All the spectra display negligible change with time. Similar decay rates of GSB and PIA signals in each film confirm the dominance of single species, singlet excitons.

Exciton-exciton annihilation measurements were carried out in each film by repeating the TA measurements as a function of input pump fluence. Then, the intensity-dependent exciton decays were modelled with the exciton rate equation (equation 3.4) accounting for both exciton annihilation and monomolecular decay pathways for obtaining singlet-singlet exciton annihilation (SSA) rate constants (γ). The exciton decays of all the materials except NIDCS-HO were well fitted to the 3D diffusion model (equation 3.6) from which the corresponding time-independent SSA rate constants were extracted. The fitting results for PBDB-T-2F, IDIC and ITIC-Th1 are provided in the **Figure 4.6** and that for IDICO1, IDICO2, and NIDCS-HO are given in the Appendix: **Figure A.12**. In the 3D global fit, γ was the only fitting parameter

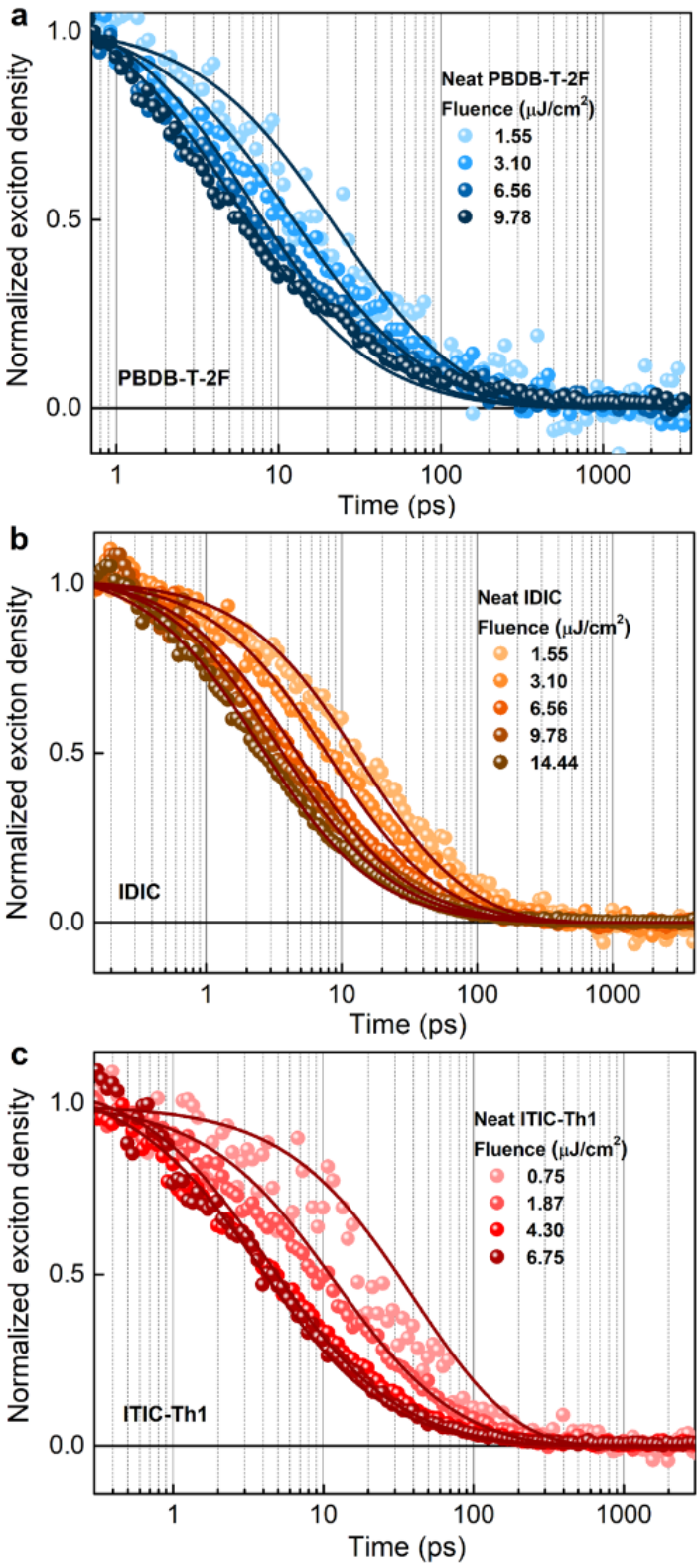

Figure 4.6: Singlet-singlet exciton diffusion model (equation 3.6) applied to the fluence dependent exciton decays in the neat films of (a) PBDB-T-2F and (b) IDIC, and (c) ITIC-Th1 (excited at 560 nm, 712 nm and 665 nm, respectively).

from which the corresponding exciton diffusion coefficients and diffusion lengths were determined (equation 3.7 and 3.8). Here, all the calculations were done assuming 1 nm effective annihilation radius (R) due to the minimum resonance enhancement of the annihilation radius.

Table 4.3: Summary of exciton diffusion parameters, monomolecular lifetime, annihilation coefficients, diffusion coefficients and diffusion lengths (L_D) for neat donor and acceptor materials.

Material	**Lifetime (ps)**	γ **(10^{-7}cm^3/s)**	**D (10^{-2}cm^3/s)**	**L$_D$(nm)**
PBDB-T-2F	178	1.8	7.2	35.8
ITIC-Th1	28 - 800	1.0	4.0	10.6 - 56.6
IDIC	126	2.5	10.0	35.0
IDICO1	62	2.02	8.0	20.3
IDICO2	52	2.24	8.9	23.5
NIDCS-HO[a)]	685	-	2.0	37.0

[a)]The diffusion parameters are obtained from 1D diffusion model (equation 4.2).

The most likely reason for the poor fit to the 3D model of NIDCS-HO is that there could be a substantial time-dependence to the SSA rate constant. This happens in systems with low dimensionality (1D or 2D) where the exciton rate equation solves as,[164]

$$n(t) = \frac{n(0)\exp(-kt)}{1 + n(0)F(t)} \tag{4.2}$$

where

$$F(t) = \begin{cases} \pi DR\tau[1 - \exp(-kt)] + 2\pi R^2\sqrt{\frac{D\tau}{2}}\,\mathrm{erf}(\sqrt{kt}) & (2D) \\ 2\pi R^2\sqrt{\frac{D\tau}{2}}\,\mathrm{erf}(\sqrt{kt}) & (1D) \end{cases}$$

where D is the diffusion coefficient, τ is the monomolecular exciton lifetime, k is the monomolecular rate constant, and R is the annihilation radius. Here, "erf" denotes the error function defined as, $\mathrm{erf}(t) = 2/\sqrt{\pi}\int_0^t \exp(-x^2)dx$. The exciton decays of NIDCS-HO were well fitted to the 1D model where the only free parameter was the diffusion coefficient which fitted as 2×10^{-2} cm$^2/s$.

Table 4.3 summarizes the exciton diffusion parameters of the active layer components. Here exciton lifetimes of all the neat materials were extracted from low pump fluence measurements. It is noted that the there is substantial uncertainty in the lifetime of ITIC-Th1, and hence its diffusion length due to the possibility of a portion of intrinsic charge generation in the neat film,[116] and limitations on the lowest excitation fluence that was able to achieve in annihilation measurements. Thus these measurements confirm the high exciton diffusion lengths (>30 nm) of the donor and the best performing acceptor materials, affirming the vital importance of this parameter on the performance of bilayer architectured OPVs. Moreover, high values of exciton diffusion lengths lead to light harvesting efficiencies exceeding 1 for ITIC-Th1, IDIC, IDICO1, and IDICO2 acceptor materials.

4.8 Significant donor to acceptor long-range FRET

Apart from the large exciton diffusion lengths for the active layer components, the bilayer devices are highly favored from long-range Förster resonance energy transfer (FRET) between donor and acceptor layers. The energy transfer occurs when there is resonance between the donor emission and acceptor absorption spectra. The best performing bilayer devices especially that of ITIC-Th1 and IDIC were highly benefited from donor to acceptor (D-A) FRET, as illustrated by the large spectral overlaps between the PBDB-T-2F emission and absorption of ITIC-Th1 and IDIC in the **Figure 4.7**. The estimated Förster radii for PBDB-T-2F:ITIC-Th1 and PBDB-T-2F:IDIC bilayers are 4 nm and 2.8 nm, respectively. Bulk-heterojunction OPVs will also benefit from this effect,[56,62] while the bilayer configuration lend itself to easier optimization of this process through dipole alignment, and also to easier quantification[42] of the degree D-A FRET.

To demonstrate the effect of D-A FRET, a series of bilayers were constructed with inorganic Al_2O_3 interlayer of varying thicknesses between the donor and acceptor slabs, *via* spatially resolved atomic layer deposition (ALD) process (All the films were prepared by Prof. Jin Young Kim and students from UNIST, South Korea). The deeply aligned HOMO/LUMO energy levels of Al_2O_3 act as barriers for holes/electrons formed after photoexcitation, but allowing D-A energy transfer (Appendix: **Figure A.9**). Ultrafast TA spectroscopy was applied to probe the D-A excitation energy transfer process in which the bilayer films were excited with 100 fs, 562 nm laser pulses where the donor absorbs most of the light. Unlike BHJ films, care was taken

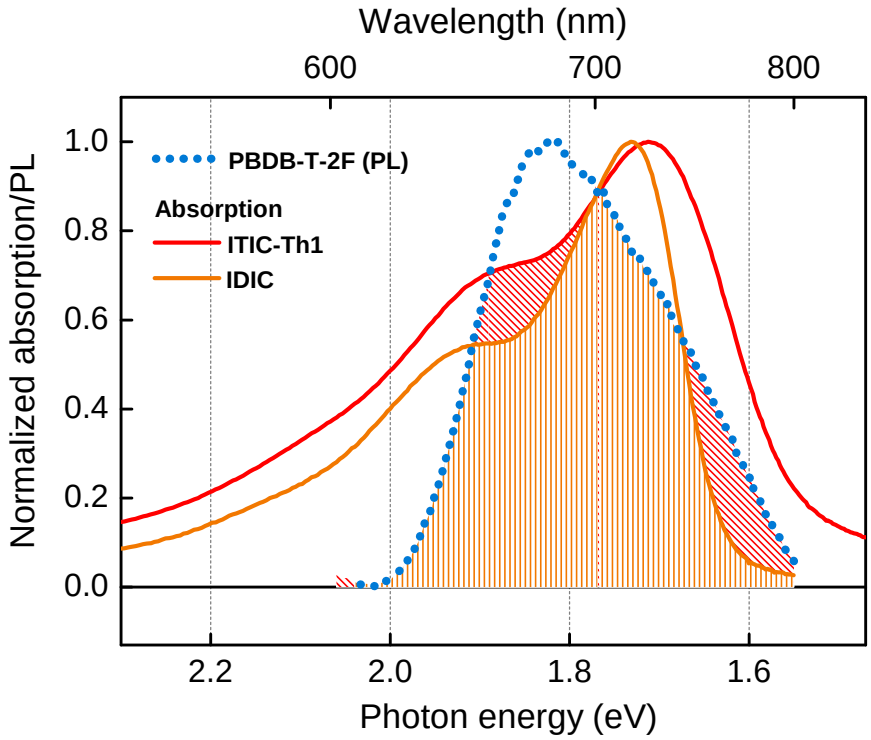

Figure 4.7: Steady-state absorption and emission spectra of donor (PBDB-T-2F) and acceptors (IDIC and ITIC-Th1) with the corresponding spectral overlaps highlighted.

to properly excite the bilayer films from the donor side due to the high absorption coefficients of acceptors at the excitation wavelengths.

Figure 4.8 provides a series of TA spectra (PIA) of PBDB-T-2F:IDIC bilayer films with different Al_2O_3 thicknesses ranging from 0 - 10 nm, at different pump-probe time delays. As per the figure, the 10 nm Al_2O_3 bilayer PIA only features the donor exciton absorption centered at 1.05 eV apart from a shoulder at 1.3 eV assigning free charges generated in the disordered polymer chains and is consistent with the neat donor spectra. When the interlayer thickness is reduced to 7 nm, a new feature is originated near 1.4 eV indicating IDIC excitons, confirmed from the TA spectra of neat IDIC in Appendix: **Figure A.11** whose absorption overlaps with the charge based PIA, suggesting ultrafast D-A FRET. It is noted that the charges observed in the bilayers with sufficient interlayer thicknesses might be after some charge separation happened at the D/A-Al_2O_3 interfaces. However, this way of excitation inquest was inevitable as the 0 nm Al_2O_3 bilayer PIA is overwhelmed with the contribution from the charge pairs which makes it difficult to recognize the transfer of excitons

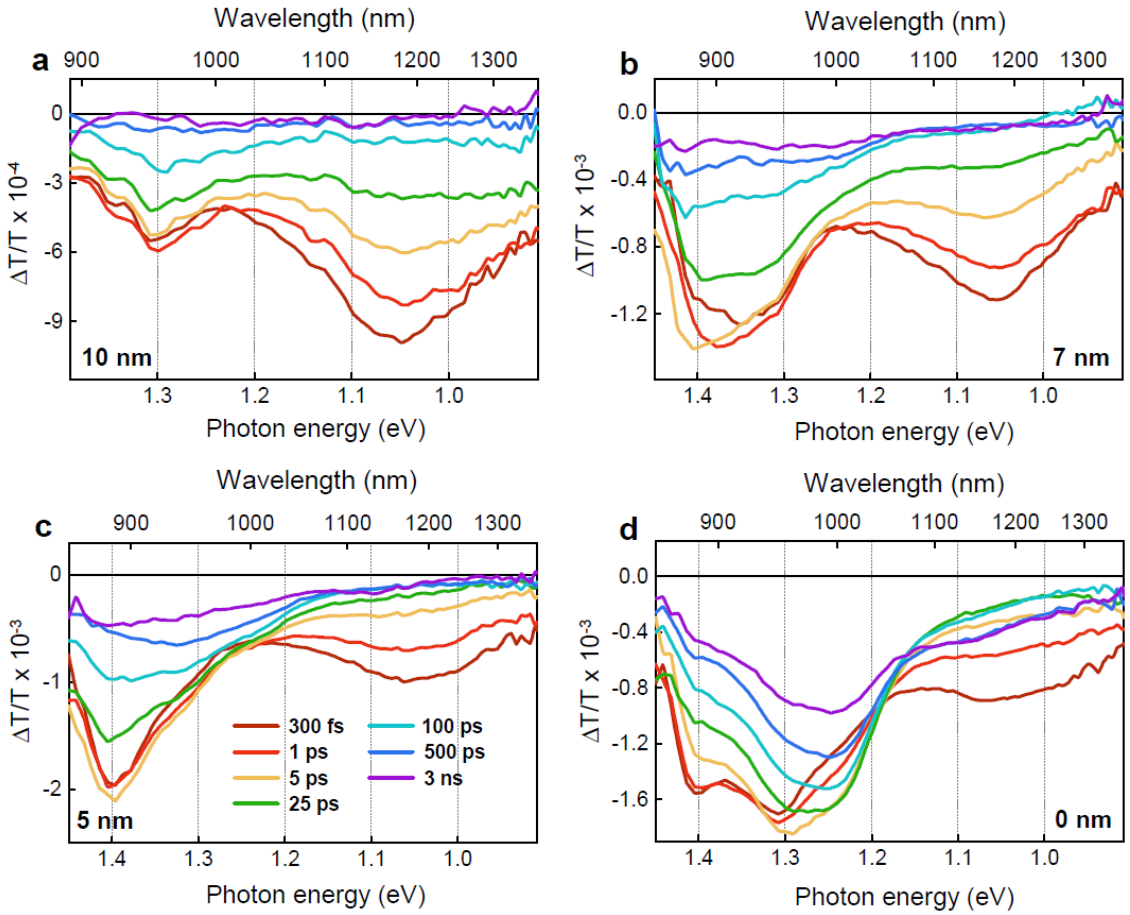

Figure 4.8: Series of TA spectra (PIA) of PBDB-T-2F:IDIC bilayer stack with varying Al_2O_3 interlayer thicknesses (a) 10 nm, (b) 7 nm, (c) 5 nm and (d) 0 nm at different pump-probe time delays. All the samples were excited with 562 nm pump pulses at a fluence of 2.47 $\mu J/cm^2$.

from the donor to acceptor phases (**Figure 4.8d**). Meanwhile, the long-lived charge signal in the 0 nm Al_2O_3 bilayer, centered around 1.25 eV testify to the high rate of charge separation at the D/A interface, consistent with the high value of PCE of the device.

By simultaneously probing the donor PBDB-T-2F exciton signature and IDIC acceptor signature, the picosecond energy transfer kinetics from the donor to the acceptor is resolved. This happens due to exciton diffusion in the donor layer and FRET into the acceptor. **Figure 4.9** provides the donor and acceptor kinetics in the PBDB-T-2F:IDIC bilayer (thickness 50:30 nm) with an interlayer thickness of 7 nm in which the donor to acceptor FRET is clearly visible by the decay in the donor exciton signal and concomitant rise in the acceptor signal that occurs within 30 ps.

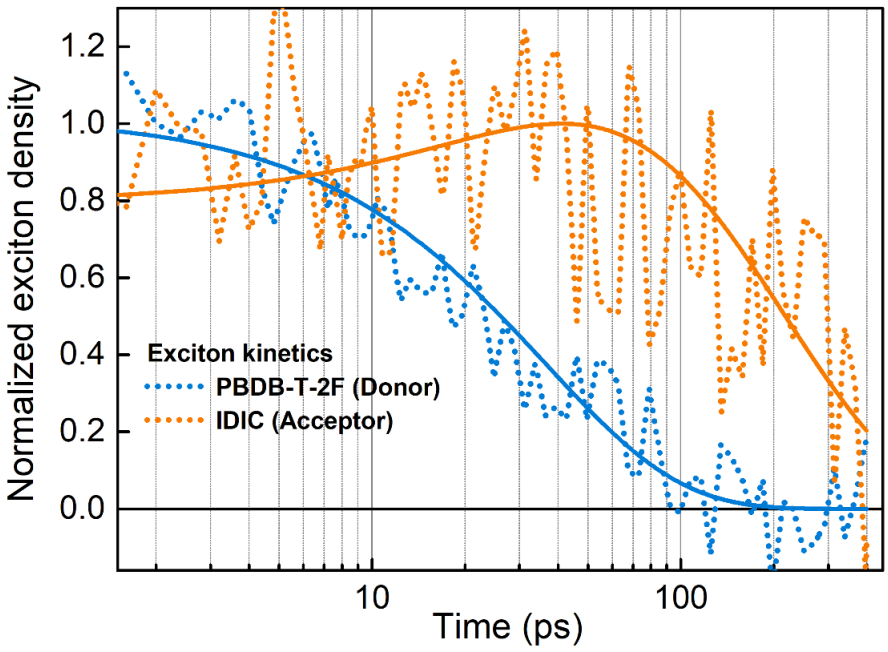

Figure 4.9: Donor and acceptor exciton kinetics in PBDB-T-2F:IDIC bilayer with an interlayer thickness of 7 nm. The fittings to the 1D model (equations 4.3 and 4.5) are overlaid on the kinetics (fitting is performed by Dr. Michael B. Price, Victoria University of Wellington.)

The acceptor signal is long-lived compared to that of the neat films as the exciton PIA overlaps with that of charges formed at later time scales. Additional evidence of efficient transfer is shown by the increased quenching (decreased lifetime) of the donor exciton signal in PBDB-T-2F:IDIC bilayer films, as the thickness of the blocking interlayers is decreased (Appendix: **Figure A.13**). The exciton dynamics in the PBDB-T-2F:IDIC bilayer was modelled with the 1D diffusion model that includes a contribution from Förster resonance energy transfer from donor to acceptor, for a given interlayer thickness which is given by,[154]

$$\frac{\partial n_d}{\partial t} = D\frac{\partial^2 n_d}{\partial^2 x} - \frac{n_d}{\tau_d} - K_F(x)n_d \tag{4.3}$$

where n_d is the donor exciton density, x is the distance from the donor quencher interface, D is the exciton diffusion coefficient of the donor, τ_d is the monomolecular lifetime of the donor excitons and $K_F(x)$ denotes the spatially dependent donor to acceptor energy transfer rate. Equation 4.3 satisfies the boundary conditions, $n_{quench} = 0$ (perfectly quenching interface which the D-A heterointerface ideally acts as) and $-D\frac{\partial n}{\partial x}_{nonquenching} = 0$ (perfectly reflecting interface). The Förster energy

transfer rate given by the equation 1.1 considers that between two point dipoles. But, in the case of a planar hetero-structure, the exciton can be transferred to any quencher molecule in the quencher film. This is similar to an energy transfer process that happens from a point dipole to a slab where the rate goes as x^{-3},[66,154]

$$K_F(x) = \frac{C_A \pi R_0^6}{6\tau x^3} \tag{4.4}$$

where C_A is the molecular density of the acceptor and R_0 is the donor to acceptor Förster radius. Similarly, the acceptor (IDIC) exciton kinetics was modelled with the 1D differential equation,

$$\frac{\partial n_a}{\partial t} = -\frac{n_a}{\tau_a} + K_{transfer} \tag{4.5}$$

where n_a is the acceptor exciton density, τ_a is the monomolecular lifetime of acceptor excitons and $K_{transfer}$ is the time dependent total exciton transfer from the donor to the acceptor layer as obtained from solving equation 4.3. Using the measured neat donor exciton lifetime and diffusion length, and the calculated Förster radius from PBDBT-2F to IDIC, of $R_0 = 2.8$ nm, a good agreement was obtained with the measured transient absorption kinetics of donor and acceptor excitations. Here the molecular density of the acceptor (IDIC) was fixed at 0.64 chromophores/nm^3 as calculated from the molecular structure.[18] The fitting results are overlaid on the exciton kinetics in **Figure 4.8** (done by Dr. Michael B. Price, Victoria University of Wellington).

4.9 Paths to future efficiency improvements

Based on the results presented above, a clear connection between the design of new materials and device function in the bilayer structure can be suggested which can boost the pace of development of efficient organic photovoltaic devices. By diverting our attention to the design of new materials for planar bilayers with major focus on their intrinsic optoelectronic properties, the arduous process of morphology optimization in the BHJ systems can be ruled out. This section covers the summary of parameters, active layer materials should possess to generate high performing bilayer systems.

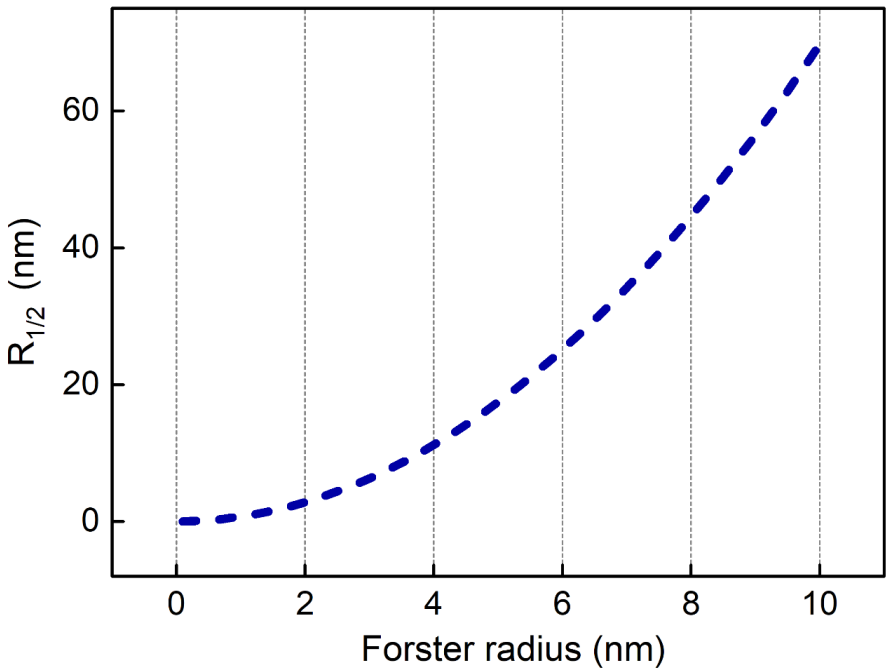

Figure 4.10: Relationship between dipole-dipole Förster radius R_0 and slab-to-slab radius $R_{1/2}$, the distance at which there is a 50% chance for energy transfer from a donor to an acceptor layer.

In the bilayer device fabrication process, it is important to have active layer components with large absorption coefficients so that enough solar photons can be absorbed by thin layers of materials. High absorption coefficients in materials can be achieved *via* increasing intermolecular packing. For instance, Erb *et al.* reported that the optical absorption in P3HT:PCBM composite films was increased upon annealing due to the increase in the crystallinity of P3HT domains.[44] Moreover, considering the optical cavity effects (light trapping), the optical absorption of the active layer can be enhanced by a factor of $4n^2$, where n is the refractive index of the material.[174]

As mentioned earlier, the key processes behind the working of a bilayer heterojunction are efficient excitonic transport within the donor and acceptor layers, and significant long-range energy transfer between the layers. More specifically, the donor and acceptor materials should possess large self-exciton diffusion lengths and efficient donor to acceptor layer FRET. Paths to improve exciton diffusion length lie in the direction of decreasing energetic disorder, increasing structural order, enhancing radiative lifetimes and most importantly, increasing the self-FRET radii. The molecular basis of these factors, their intrinsic limits and the possibility of further enhancements were discussed in the section 3.10 of chapter 3. While, maximising donor to acceptor

layer FRET can be achieved *via* increasing donor PL efficiencies, selecting materials with high absorption emission spectral overlap, and tuning the dipole alignment in both donor and acceptor layers. For a true slab-to-slab bilayer architecture having the aforementioned properties, the high potential of donor to acceptor FRET can be represented as a channel for efficient exciton harvesting. For a donor exciton in a bilayer configuration device, the distance $R_{1/2}$, at which there is a 50% probability of undergoing FRET to the acceptor layer is approximately given by,

$$R_{1/2} = (\frac{\pi C_a}{6})^{\frac{1}{3}} R_0^2 \tag{4.6}$$

where R_0 is the standard point-to-point Förster radius, and C_a is the acceptor layer molecular density. **Figure 4.9** gives a graphical illustration of equation 4.5 for PBDB-T-2F:ITIC-Th1 bilayer. The nonlinear dependence means that even small changes in R_0 will results in large increase in $R_{1/2}$. For instance, with the materials studied here, an R_0 of 5 nm will give an $R_{1/2}$ of 20 nm - a substantial portion of the depth of bilayer devices due to their large absorption coefficients.

4.10 Conclusion

A series of highly efficient planar bilayer heterojunction devices favoured from high molecular packing densities and absorption coefficients, long exciton diffusion lengths, and efficient, resonant long-range donor to acceptor layer FRET were designed and fabricated *via* layer-by-layer deposition from orthogonal solvents. The donor polymer PBDB-T-2F was paired with a series of fused ring electron acceptors where a power conversion efficiency of 11.1% was achieved in the PBDB-T-2F:ITIC-Th1 device. Ultrafast transient absorption spectroscopy was employed to confirm the high exciton diffusion lengths in acceptor films along with the donor to acceptor layer resonant energy transfer. Design of new materials with the aforementioned characteristics along with the selection of proper orthogonal solvents for layer-by-layer deposition of clean bilayers will accelerate the development of more efficient photovoltaic devices.

Chapter 5

Efficient exciton and charge transport in FREA based OPV systems free from $\pi - \pi$ stacking

The molecular packing of active layer components has a crucial role in the device performance of organic photovoltaic devices. Especially for FREA based OPV systems, the long-range structural order induced by end group $\pi - \pi$ stacking is considered as the critical factor for achieving high power conversion efficiency. This chapter includes a deep spectroscopic insight into the exciton and charge transport processes in a series of FREA based OPV systems having different molecular packing and ordering. Here the molecular stacking manipulation in FREAs is achieved by changing the length of alkyl side-chains so that the FREA backbone is changed from a $\pi - \pi$ stacking mode to a non-stacking mode. Transient absorption spectroscopic analysis of neat FREAs and blends reveals that exciton diffusion and intermolecular charge transfer processes do not necessarily rely on the molecular $\pi - \pi$ stacking, while close atom contact can also enable these processes*. This work provides new insights into the design of advanced materials for next generation organic photovoltaics considering diverse transport channels formed by close atom interactions.

*L. Ye, K. Wng, J. Xu, X. Du, **S. Chandrabose**, K. Chen, J. Zhou, G. Han, S. Tan, Z. Xie, Y. Yi, N. Li, F. Liu, J.M Hodgkiss, C.J Brabec, and Y. Sun, (**2020**). "*Unravelling the $\pi - \pi$ stacking-free charge transport channels in non-fullerene acceptor based organic photovoltaics*", submitted for publication.

Collaborators contributed to the work

Device design and fabrication, morphology and photovoltaic characterization: Prof. Yanming Sun and students from Beihang University, Beijing, China.

Research focused on:

Steady-state optical spectroscopic measurements:
UV-vis measurements of all neat and blend films.

Transient absorption (TA) spectroscopic measurements: (**a**) Exciton diffusion measurements in neat acceptor films, (**b**) polarization anisotropy measurements in acceptor films and (**c**) TA measurements in blend films.

Data analysis: (**a**) Singlet-singlet exciton annihilation (SSA) fittings, (**b**) calculation of exciton diffusion parameters and anisotropy and (**c**) application of MCR-ALS algorithm on blend data.

5.1 Introduction

Over the past decade, many efficient design strategies have been employed to tune the optoelectronic properties of photovoltaic materials to achieve high efficiency OPV systems. For fullerene derivatives, their spherical symmetry allows isotropic charge transport and thus simplifies the morphology control. However, studies show that there are not many morphology control handles for fullerene derivatives expect for their amorphous cluster sizes and density.[73,162] So recently, more attention has devoted to non-fullerene acceptors (NFAs) especially fused ring electron acceptors (FREAs) due to their excellent ability to harness long-wavelength radiation and possessing distinct advantages like well defined molecular structure and readily controllable morphology which can effectively tune the chemistry variables such as band gap, crystallinity, and energy levels.[203,204] The key factor that critically influences the morphology of FREAs is the chemical structure which plays a crucial role in PCE enhancement by tuning the optical and electronic properties of the material. The chemical structure modification in FREAs is carried out by careful engineering on the core-groups,[204] end-capping groups[184] and side-chains.[109]

There are reports showing that in NFAs, effective $\pi - \pi$ stacking is an important factor which can control both exciton and charge transport. For instance, Herz *et al.* used time-resolved spectroscopic techniques to study the chiral stacks of conjugated *p*-phenylene vinylene molecules and reported that $\pi - \pi$ interactions between these molecules give rise to fast exciton diffusion.[70] Regarding charge transport, using atomistic molecular dynamic simulations, Han *et al.* proved that 3D molecular packing is formed in the FREA, ITIC through local intermolecular $\pi - \pi$ stacking between terminal acceptor groups which effectively increased the charge transport and electron mobility in BHJ films.[64] Studies also show that different molecular stacking geometries in organic semiconductors induce different charge transport properties and anisotropy. Recently, we have conducted time-resolved spectroscopic measurements on a novel FREA, IDIC and reported that exciton diffusion process in FREAs is highly governed by the resonant energy transfer rate rather than electronic coupling between the chromophores. In order to demonstrate the unique, $\pi - \pi$ stacking free exciton transport channels, a family of FREAs are constructed with systematic chemical structure modifications which induce different molecular packing. The molecular stacking manipulation is achieved by changing the length of alkyl side-chains which led to a fine control of aliphatic chain interactions even in the complicated BHJ blends.

By the side-chain engineering approach, the FREA backbone is manipulated from a strong $\pi - \pi$ stacking mode to a non-stacking mode to improve its solid-state properties. Here it is also demonstrated that in contrast to previous reports, efficient charge transport in NFAs do not necessarily depend on $\pi - \pi$ stacking induced transport channels. The optimized OPVs free from $\pi - \pi$ stacking exhibited a high efficiency of 12.7% compared to the 10% efficient OPVs that rely on classic $\pi - \pi$ stacking formed exciton and charge transport channels. Ultrafast transient absorption spectroscopic analysis of neat FREAs and blends proves that high exciton diffusion rate and intermolecular charge transport are maintained in OPVs lacking $\pi - \pi$ interactions. This work provides new insights into the design of advanced materials for next generation organic photovoltaics considering diverse transport channels formed by close atom interactions.

5.2 Materials

IDTT-C6-TIC, IDTT-C8-TIC, and IDTT-C10-TIC are the three FREAs designed to investigate the role of molecular packing on the photovoltaic properties of different BHJ systems. They are characterized by the same molecular skeleton, but exhibiting different stacking properties by modifying side-chains. **Figure 5.1** provides the detailed molecular and single crystal structure of all the materials used. The materials were designed and fabricated Prof. Yanming Sun and students from Beihang University, China. By changing the alkyl side-chain length, a fine control of aliphatic chain interaction can be induced which opens the broader frame for backbone $\pi - \pi$ reorganization, and thus leads to different solid-state properties. Here, with increasing the length of the alkyl side-chains on FREAs, the highest occupied molecular orbital (HOMO) energy levels gradually decrease and the lowest unoccupied molecular orbital (LUMO) energy levels gradually increase, indicating reduced intermolecular interactions (Appendix: **Figure A.14**).

In IDTT-C6-TIC, the hexyl side-chains exhibit a fully extended geometry that stretch out from the conjugated backbone. In the π-plane, the molecules are connected *via* side-chain interdigitation while the long-axis of the molecules are formed through end-group overlapping (Appendix: **Figure A.15a**). IDTT-C8-TIC is characterized by slightly longer alkyl side-chains which lead to a different crystal packing (Appendix: **Figure A.15b**). Here, three pairs of interactions can be identified between the molecules; frustrated side-chain interaction, symmetric side-chain interaction and

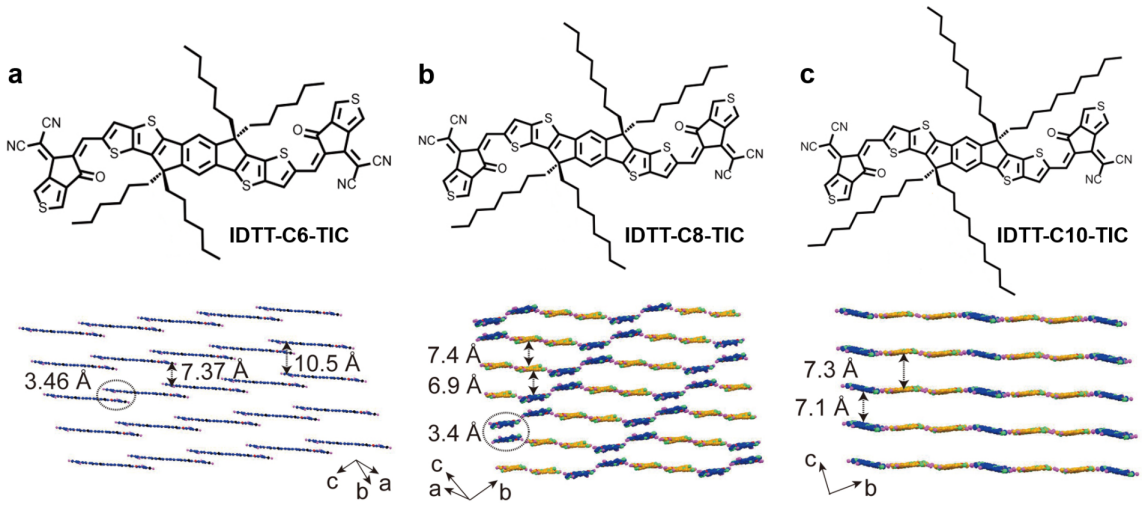

Figure 5.1: Molecular and single crystal structures of (a) IDTT-C6-TIC, (b) IDTT-C8-TIC, and (c) IDTT-C10-TIC. The structures are provided by Prof. Yanming Sun and group from Beihang University, China.

mixed side-chain interaction. In the frustrated side-chain model, a close backbone packing is achieved as the octyl (C_8) side-chains maintain a random extension without structure order. The symmetric side-chain interaction is similar to the side-chain interdigitation observed in IDTT-C6-TIC in the π-plane. But, the side-chain extended geometry would result in a reduced $\pi - \pi$ interaction. The mixed side-chain interaction occurs between the adjacent molecules of two pairs which leads to an anomalous solid-state packing in the single crystal. Here the crystal can be dissected into two domains as marked by blue and yellow regions in **Figure 5.1b**. IDTT-C10-TIC exhibits decyl side-chains which give rise to two types of interactions; the harpoon type of side-chain extension and the crankshaft type of side-chain extension (Appendix: **Figure A.15c**). Both of the interactions result in a large $\pi - \pi$ distance. To study the impacts of molecular packing on charge transport, BHJ blends were fabricated based on the three FREAs and a fixed donor polymer PBT1-C (molecular weight: ~55800 g/mol and polydispersity index: 1.9). Energy band diagram presented in Appendix: **Figure A.14** shows that each donor and acceptor combination is energetically suitable to provide photovoltaic effect.

5.3 Morphology characterization

The morphology of neat IDTT-CX-TIC (X = 6, 8, and 10) and blend films were characterized using the combination of grazing incidence wide-angle X-ray scattering (GI-

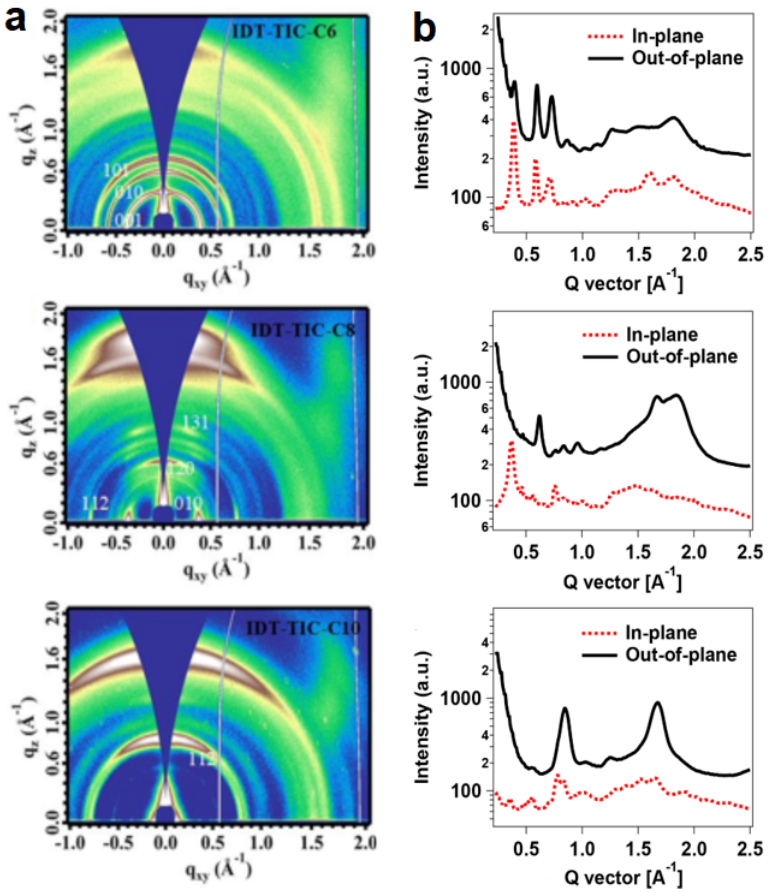

Figure 5.2: (a) 2D GIWAXS patterns of IDTT-CX-TIC neat films, and (b) the corresponding in-plane and out-of-plane line-cut profiles. The measurements are performed by Prof. Yanming Sun and students from Beihang University, China.

WAXS), transmission electron microscopy (TEM), atomic force microscopy (AFM), and resonant soft X-ray scattering (R-SoXS). All the measurements were carried out by our collaborators, Prof. Yanming Sun and students from China. **Figure 5.2** provides the 2D GIWAXS patterns and 1D line-cut profiles of neat IDTT-CX-TIC films. According to the figure, IDTT-C6-TIC film features three major diffraction peaks at 0.39, 0.60, and 0.72 Å^{-1}, corresponding to the (001), (010), and (101) planes, respectively. In the out-of-plane mode, the diffraction peak detected at 1.8 Å^{-1} represents the $\pi - \pi$ stacking. For IDTT-C8-TIC film, more detailed Brag spots are observed in small Q regions along with a broad diffraction peak at 1.8 Å^{-1} in the out-of-plane direction representing close $\pi - \pi$ stacking. While, IDTT-C10-TIC film shows a simple diffraction feature with two major rings at 0.8 and 1.6 Å^{-1} with a large $\pi - \pi$ stacking distance which is consistent with its single crystal structure. The GIWAXS results of PBT1-C:IDTT-CX-TIC blends presented in Appendix: **Figure A.16** reveal that the

major structural features from the acceptors are well preserved in their BHJ films. Here the broad diffraction peak observed at 0.28 $Å^{-1}$ in the in-plane lamellar assembly represents the (100) diffraction from the donor polymer.[115]

TEM, AFM and R-SoXS characterizations in the IDTT-C6-TIC blend film revealed large-sized aggregations distributed inside the donor fibril networks with a mode-domain size of 200 nm. While, the IDTT-C8-TIC blend exhibited much refined morphology with a moderate phase separation of 90 nm. A smooth morphology with fibril networks was detected in IDTT-C10-TIC blends with a weak phase separation due to good mixing between the materials.

5.4 Photovoltaic characterization

To understand the effect of solid-state molecular packing on the photovoltaic performance of BHJ films, OPVs based on PBT1-C:IDTT-CX-TIC (X = 6, 8, and 10) were fabricated with an inverse device architecture of ITO:ZnO:PBT1-C:IDTT-CX-TIC:MoO_3:Ag. All the devices were optimized using DIO as the solvent additive. The current density - voltage (J - V) characteristics and EQE spectra of OPVs are displayed in the **Figure 5.3** and the detailed parameters are listed in the Appendix: **Table 5.1**. All the photovoltaic measurements were performed by Prof. Yanming Sun and students from Beihang University, China.

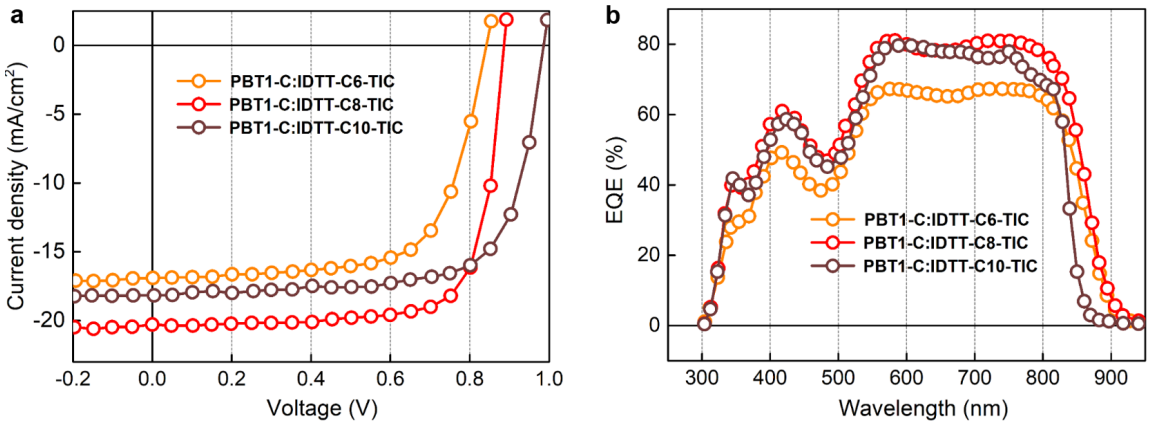

Figure 5.3: (a) J - V characteristics, and (b) EQE spectra of PBT1-C:IDTT-CX-TIC devices. The measurements are performed by Prof. Yanming Sun and students from Beihang University, China.

Out of all BHJ cells, IDTT-C8-TIC devices showed the best PCE of 13.7% with the highest J_{SC} of 20.3 mA/cm^2 and FF of 74.6%. The small values of J_{SC}, FF,

Table 5.1: Summary of photovoltaic parameters pf PBT1-C:IDTT-CX-TIC BHJ solar cells. The data is provided by Prof. Yanming Sun and students from Beihang University, China.

Active layer	V_{OC} **(V)**	J_{SC} **(mA/cm^2)**	**FF** (%)	**PCE**$_{max}$ (%)
PBT1-C:IDTT-C6-TIC	0.85	17.0	66.7	10.0
PBT1-C:IDTT-C8-TIC	0.88	20.3	74.6	13.7
PBT1-C:IDTT-C10-TIC	0.98	18.1	71.3	12.7

and thereby the overall device efficiency of IDTT-C6-TIC device is consistent with its large phase separation which might lead to inefficient charge generation. While IDTT-C10-TIC based devices exhibited a high PCE of 12.7% with a J_{SC} of 18.1 mA/cm^2 and a FF of 71.3%. As per the table, the V_{OC} of OPVs is found to be influenced by the molecular ordering of FREAs. The increase in V_{OC} is inline with the increasing/decreasing LUMO/HOMO energies of the acceptors with side-chain length, which boosts the driving force for exciton dissociation.

5.5 Steady-state optical spectroscopy in films

Figure 5.4a gives the steady-state absorption spectra of neat donor PBT1-C and FREA films. PBT1-C is characterized by a strong absorption ranging from deep UV to near IR with two obvious vibronic shoulder peaks.[115] While FREA films exhibit strong absorption in the near IR region and are having very similar absorption profiles with slightly shifted absorption peak maxima. The optical band gaps of FREAs are determined from absorption onsets and are 1.52, 1.50, and 1.56 eV for IDTT-C6-TIC, IDTT-C8-TIC, and IDTT-C10-TIC, respectively.

Steady-state absorption spectra of IDTT-CX-TIC blend films optimized with the DIO solvent additive is presented in **Figure 5.4b**. The blend spectra comprise contributions from both donor and corresponding acceptor phases. However, the vibronic peak ratios (0-0 to 0-1) of acceptor phases in PBT1-C:IDTT-C8-TIC and PBT1-C:IDTT-C10-TIC blend films show remarkable increase compared to that of the corresponding neat acceptor films. This is an indication of strong J-aggregate formation in the blend films which is consistent with the acceptor crystal structures with weak or no $\pi - \pi$

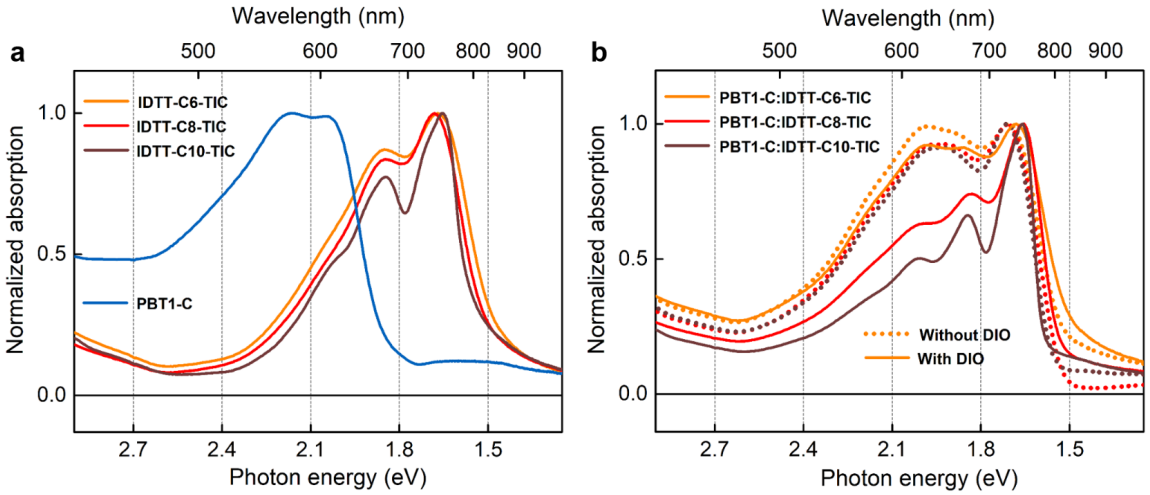

Figure 5.4: Steady-state absorption spectra of (a) neat donor and acceptor films, and (b) blend films with and without the DIO solvent additive.

stacking. Additionally, the film absorption spectra exhibit notable red shift compared to that of the solution phase which is a common characteristic of J-aggregates (Appendix: **Figure A.17**). Furthermore, J-aggregate formation in the films is induced by the DIO solvent additive which is confirmed from the absorption spectra of blends fabricated without the addition of DIO. While, the PBT1-C:IDTT-C6-TIC blend spectrum doesn't show any special features apart from the strong contribution from donor and IDTT-C6-TIC phases. The band gaps of the OPVs were determined from the intersection of EQE edge and the local EQE maximum rather than from the absorption onset. This way of band gap determination takes into account the aggregation of FREAs in the blend films and thereby avoid the underestimation happens in the case of disordered materials. IDTT-C10-TIC blend exhibits a slightly higher band gap (1.61 eV) compared to that of IDTT-C6-TIC (1.6 eV) and IDTT-C8-TIC (1.59 eV) blends which is consistent with the absence of $\pi - \pi$ stacking in the IDTT-C10-TIC blend film.

5.6 Time-resolved spectroscopy in films

Ultrafast transient absorption spectroscopy was employed to probe the effect of molecular packing on the exciton dynamics and charge generation process in IDTT-CX-TIC blend films. The first stage of analysis was to examine the spectra and kinetics of excitons in neat FREA films. This information was then used to identify the spectral signatures in the corresponding blend films. All the neat films were excited with pump pulses of 710 nm wavelength. The excitation fluences were selected in such a way that

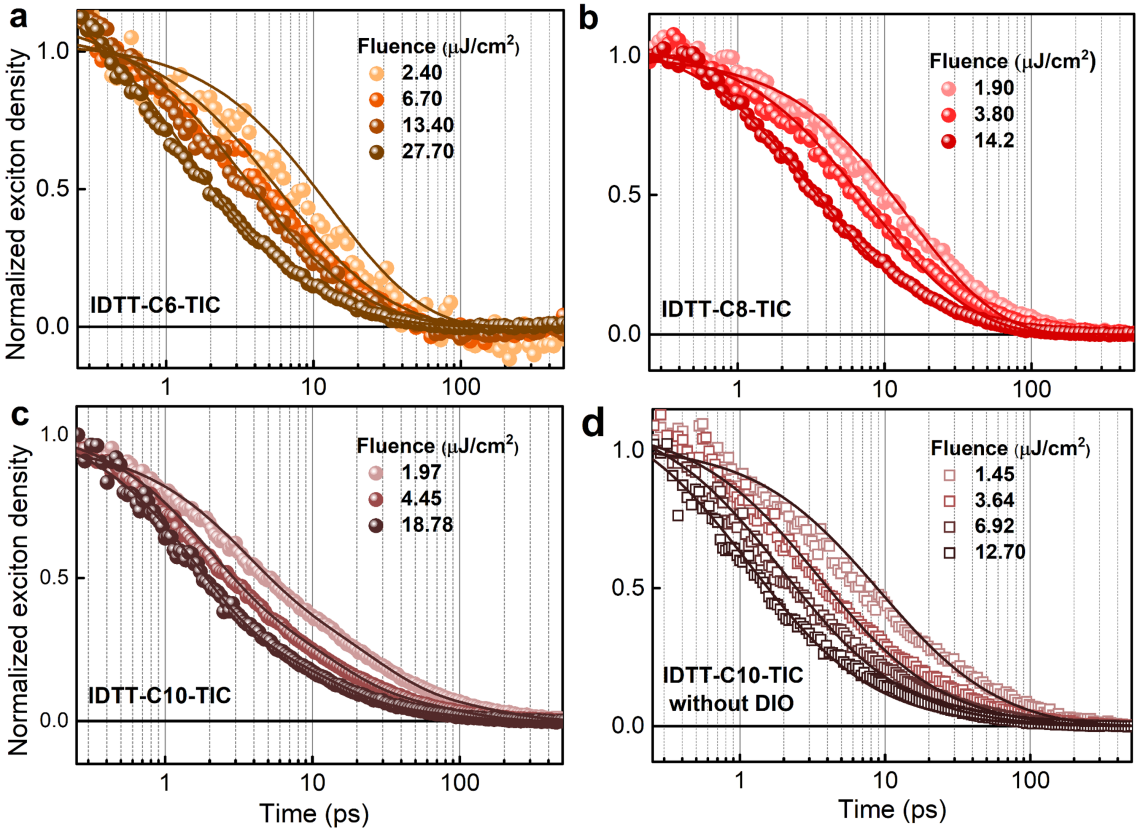

Figure 5.5: Singlet-singlet exciton annihilation model (equation 3.6) applied to the fluence dependent exciton decays in neat films of (a) IDTT-C6-TIC, (b) IDTT-C8-TIC, (c) IDTT-C10-TIC, and (d) IDTT-C10-TIC without DIO (all excited at 665 nm).

similar exciton densities are generated in the neat films which makes the dynamics comparison easier. Appendix: **Figure A.18** provides a series of TA spectra of neat films at different pump-probe time delays. The spectra of all neat films comprise positive differential transmission signals representing ground state bleach (GSB) which is consistent with their steady-state absorption spectra. They also feature negative photoinduced absorption (PIA) signals near 1.3 eV suggesting excitonic absorption. The near equal kinetics of GSB and PIA signatures confirm the dominance of singlets.

5.6.1 Exciton diffusion

There are reports suggesting that the direct electronic coupling between molecular constituents has major implications on exciton diffusion in organic semiconductors.[70] Recently, we have conducted a deep spectroscopic analysis of a fused ring electron acceptor IDIC (presented in chapter 3) and reported that the prime factor that controls

the exciton diffusion process in FREAs is self spectral overlap integral which boosts the radius for resonant energy transfer *via* space resonant coupling. To prove that molecular packing doesn't affect exciton diffusion, exciton-exciton annihilation measurements were carried out in neat FREA films to extract the corresponding exciton diffusion coefficients (refer chapter 3). The films were excited with pump pulses of 665 nm wavelength with fluences in the range 1.5 - 30 $\mu J/cm^2$.

Figure 5.5 provides a series of intensity-dependent exciton dynamics of IDTT-CX-TIC neat films revealing singlet-singlet exciton annihilation (SSA). To extract the annihilation rate constants (γ), fluence-dependent decays were globally fitted to the rate equation (equation 3.4) accounting for both bimolecular (exciton annihilation) and monomolecular decay pathways (refer chapter 3). The exciton decays are well fitted to the 3D diffusion model and the fittings are overlaid on them (**Figure 5.5**). The extracted annihilation constants were then used to calculate the diffusion coefficients and diffusion lengths according to equations 3.7 and 3.8. Here, all the calculations were done assuming 1 nm effective annihilation radius (R) due to the minimum resonance enhancement of the annihilation radius.

Table 5.2: Summary of exciton diffusion parameters, exciton lifetimes, annihilation coefficients (γ), diffusion coefficients (D) and diffusion lengths (L_D) for neat acceptor materials.

Material	**Lifetime (ps)**	γ **($10^{-7}cm^3/s$)**	**D ($10^{-1}cm^3/s$)**	L_D**(nm)**
IDTT-C6-TIC	15	2.6	1.0	12.2
IDTT-C8-TIC	23	3.0	1.2	16.5
IDTT-C10-TIC	24	10.0	4.0	31.1
IDTT-C10-TIC[a)]	21	3.1	1.2	15.8

[a)] without DIO solvent additive.

Table 5.1 presents the summary of exciton diffusion parameters of all neat acceptor films. Here it is noted that the intrinsic lifetimes and hence the exciton diffusion lengths in the neat materials are underestimated due to substantial exciton annihilation at the lowest excitation fluence used. As per the table, it is proved that acceptor molecules having different molecular packing geometries possess high diffusion parameters. This confirms that $\pi - \pi$ stacking is not a crucial criteria for effective excitonic transport in non-fullerene acceptors. Meanwhile, parameters like energetic

disorder and rate of resonance energy transfer have primary roles on exciton diffusion as demonstrated in chapter 3. Here it is also noted that IDTT-C10-TIC optimized with DIO solvent additive exhibits high exciton diffusion coefficient and diffusion length compared to others which is expected to be due to a high spectral overlap integral between the material's absorption and emission that boosts the self-resonance energy transfer (the application of FRET model on exciton diffusion will be a part of the future work).

5.6.2 Polarization anisotropy

Polarization anisotropy was performed to probe the excitations in FREAs with different molecular packing. The measurements were carried out using the same transient absorption experimental setup apart from inserting a waveplate in the pump path to selectively excite the parallelly and perpendicularly oriented dipoles and then isolating the corresponding TA signals using a fixed broadband polarizer applied to the probe. **Figure 5.6** shows the anisotropic results of all neat acceptor films.

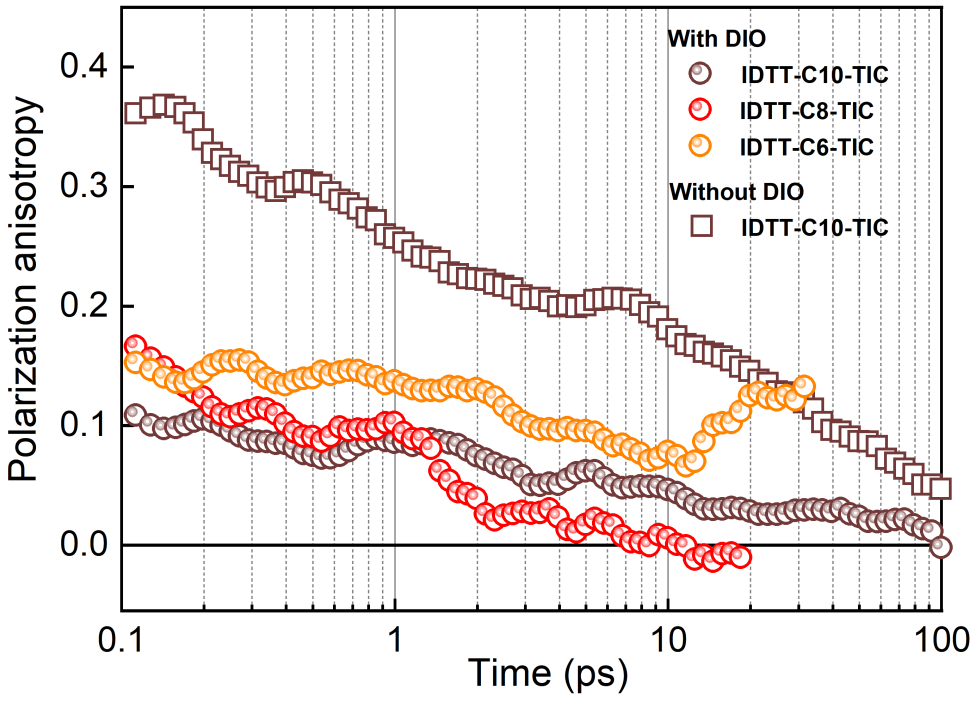

Figure 5.6: Transient absorption polarization anisotropy of neat FREA films IDTT-C10-TIC, IDTT-C8-TIC, IDTT-C6-TIC, and IDTT-C10-TIC (without DIO) excited at 665 nm, at pump fluences of 5.4 μJ/cm^2, 3.8 μJ/cm^2, 6.2 μJ/cm^2, and 5.4 μJ/cm^2, respectively.

According to the figure, the initial anisotropies of all neat films optimized with DIO

solvent additive are considerably lower than the maximum theoretical value (0.4) which reveals that the initial excitations were delocalized which then rapidly localized onto orientationally disordered chromophores. While, IDTT-C10-TIC without DIO is characterized by an initial anisotropy of 0.4 which explains that the initial excitations were not delocalized over the molecules. Additionally, when comparing the anisotropy decay dynamics, the IDTT-C6-TIC sample optimized with DIO approximately maintains the memory of polarization throughout its lifetime which indicates that the exciton migration in this material is happening through aligned chromophores. While, IDTT-C8-TIC suffers a rapid decrease in the anisotropy that vanishes in ∼10 ps revealing that the excitations are crossing disordered chromophores so that they lose their memory of initial polarization. The fast decay in the anisotropy also indicates that the excitons in IDTT-C8-TIC undergo rapid diffusion which is consistent with its high value of exciton diffusion constant (**Table 5.1**). On the other hand, the anisotropies in IDTT-C10-TIC samples fabricated with and without DIO additive show relatively slower decays and the decay dynamics are similar to the exciton dynamics at the corresponding pump excitation fluences. This is attributed to the fact that unlike IDTT-C8-TIC, the excitons in these materials diffuse through chromophores which are more or less aligned so that they can approximately maintain their initial polarization during the whole diffusion process.

5.6.3 Charge generation and transport

To study the effect of molecular packing on charge generation and transport, transient absorption spectroscopy was applied on IDTT-CX-TIC blends. A series of TA spectra of optimized PBT1-C:IDTT-CX-TIC blends are given in the **Figure 5.7** at various pump-probe delay times which are produced after the selective photoexcitation of corresponding acceptor phases at 710 nm. At early time scales, the spectra of all blends exhibit positive differential transmission signals representing GSB around 1.7 eV and the corresponding negative PIA signals near 1.3 eV. These features are attributed to the singlet excitons generated in the acceptor phases as confirmed from the TA spectra of pristine acceptor films (Appendix: **Figure A.18**). After ∼5 ps, with the decay of excitons, new features were originated with blue shifted GSBs around 2 eV, retaining the bleach signals from acceptor excitons and with different PIA signatures. These secondary features are attributed to charge pairs which persisted beyond 3 ns time window of the experiment. As supported by the TA spectra of the neat polymer excited at 580 nm, the new GSBs represent the holes occupying the polymer donor whose PIA overlaps with that of electrons in the acceptor phases. In the blend

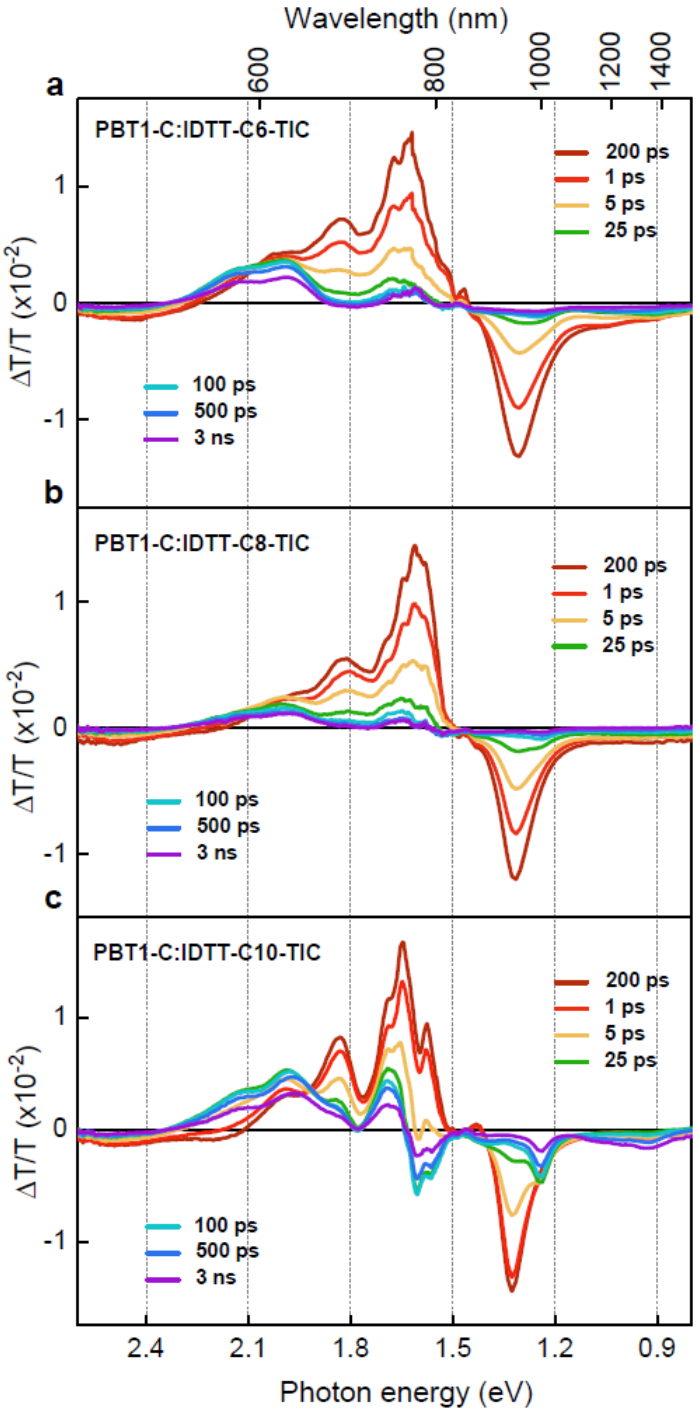

Figure 5.7: Series of transient absorption spectra of blends, (a) PBT1-C:IDTT-C6-TIC (13 μJ/cm^2), (b) PBT1-C:IDTT-C8-TIC (4.7 μJ/cm^2), and PBT1-C:IDTT-C10-TIC (4.7 μJ/cm^2) at various pump-probe delay times after the selective excitation of the corresponding acceptor phases at 710 nm.

PBT1-C:IDTT-C10-TIC, the charge generation process is further confirmed by the

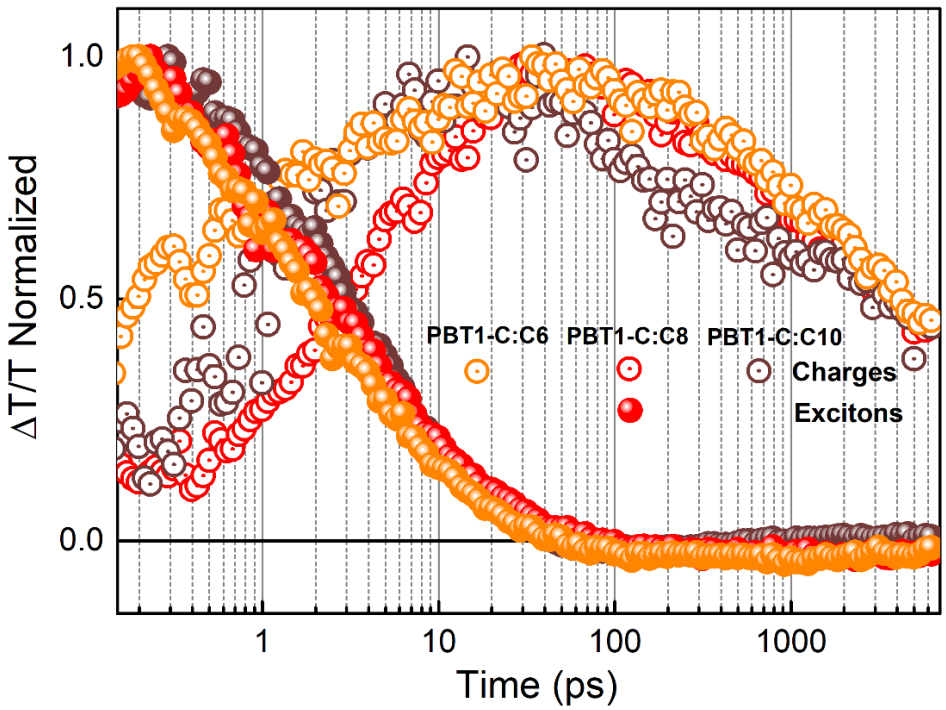

Figure 5.8: Transient absorption kinetics of excitons and charges in PBT1-C:IDTT-CX-TIC blend films after pump excitations at 710 nm.

presence of a negative electro-absorption (EA) feature near 1.65 eV overlapping with the bleach of electrons which resembles the first derivative of the GSB spectra. This signature is observed when the electric field created by the charge pairs perturbs the energy levels of the polymer donor *via* the Stark effect.

As the excitons and charge signals in the blends overlap each other, the MCR-ALS algorithm was applied to the TA surfaces to separate the spectral components. In the bilinear decomposition process, the exciton spectra from the corresponding neat films were used as spectral masks to extract the charge signals. **Figure 5.8** compares the exciton to charge conversion dynamics in PBT1-C:IDTT-CX-TIC blends after an excitation at 710 nm, where mostly the acceptors absorb. As per the figure, the signals from photo-generated charge populations reach their maximum on the same time-scales (∼50 ps) as the complete quenching of the excitons in the acceptor phases. These observations agree well with the previous studies of FREA based blends and imply that FREA excitons can efficiently transport across the acceptor phase domains in BHJs.[110,185] The data analysis shows different prompt charge ratios and charge generation dynamics in the sub-10 ps region as the charge signals are buried under very strong exciton signals. However, the exciton lifetimes in the blends

are shorter compared to that in neat films which confirms efficient exciton quenching in all blends. The exciton dissociation efficiencies for IDTT-C6-TIC, IDTT-C8-TIC, and IDTT-C10-TIC blends are calculated to be 42%, 68%, and 60%, respectively. Here it is noted that the calculated exciton quenching efficiencies for the blends are comparatively lower than EQE values as the intrinsic lifetimes of acceptors are underestimated due to the strong exciton-exciton annihilation at the excitation fluences used. The lower dissociation efficiency of IDTT-C6-TIC blend agrees well with its low value of J_{SC} that resulted from large domain sizes. Thus, fs TA results confirms that the charge generation dynamics in BHJs is not affected by the different FREA crystal structures induced by side-chain engineering. Similar to charge transport, the exciton diffusion in FREA thin films is not strongly affected by the differing crystal structure and molecular packing. Nevertheless, the low energetic disorder and good spectral overlap plays a more crucial role for efficient exciton transport in three NFAs studied.

5.6.4 Charge generation at interfaces

When excitons undergo dissociation at donor-acceptor interfaces, they form electron-hole pairs which act as local electric dipoles and induce a Stark shift on the energy levels of the surrounding chromophores. Normally, the Stark shift causes a red shift in the absorption spectra of surrounding molecules due to lowering of optical band gap.[77] In transient absorption, the difference between the two absorption spectra (with and without electric field) takes the form of a derivative of the absorption spectra and is referred to as electro-absorption (EA). The electro-absorption signal provides a unique signature of the dynamics of electronic states in the interfacial region. Here PBT1-C:IDTT-C10-TIC blend was used as a model system to study the interfacial dynamics using EA signals. The weight ratio between the donor and small molecule was varied as 1:4, 1:1, and 4:1 such that different donor-acceptor domains and interfacial regions were generated in the blends which affects the exciton dissociation efficiencies and thereby the charge based EA signals. Here all the subsequent analysis were done based on the charge population represented by the EA signals.

Figure 5.9 provides a series of transient absorption spectra (visible region) of PBT1-C:IDTT-C10-TIC blends with different donor-acceptor weight ratios after laser excitations at 665 nm. The spectra include GSB signals from acceptor excitons around 1.8 eV in the early time scales and long-lived charge based GSB signals from ∼5 ps, representing holes and electrons occupying the donor and acceptor phases, respectively.

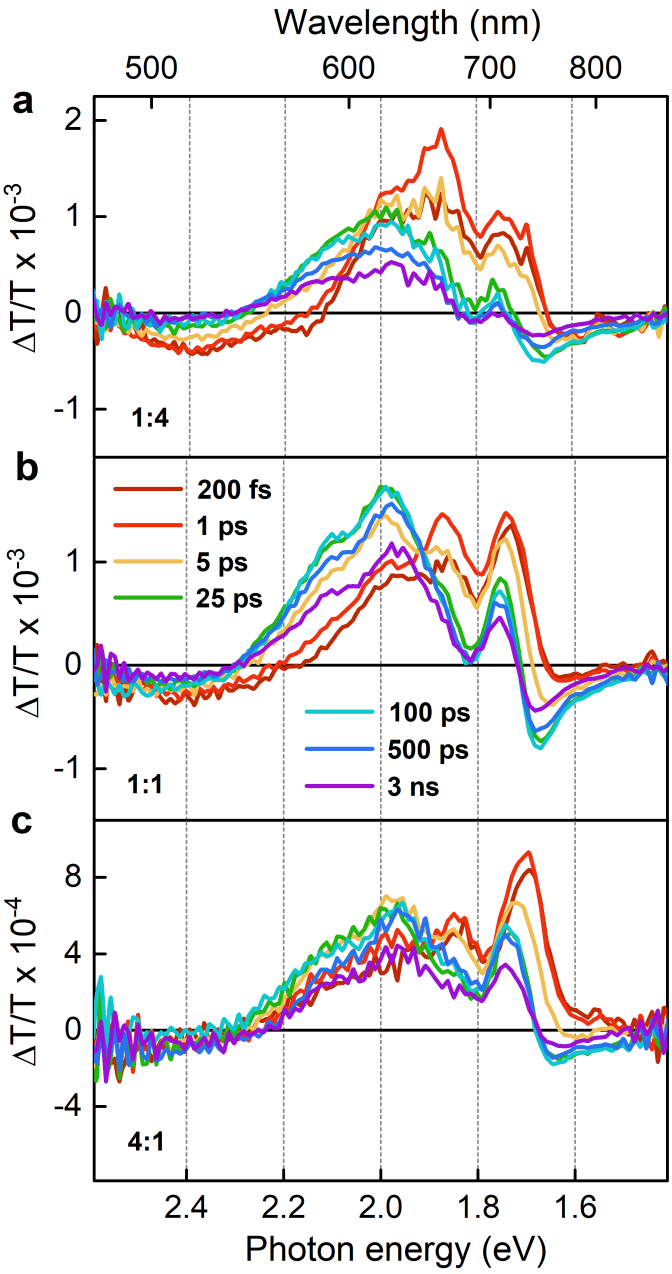

Figure 5.9: Series of transient absorption spectra of PBT1-C:IDTT-C10-TIC blends with different donor-acceptor weight ratios, (a) 1:4, (b) 1:1, and (c) 4:1 after laser excitations at 665 nm and at pump fluences of 3.1 μJ/cm^2.

The red shifted electro-absorption signals from the charge carriers were detected at ~1.65 eV, overlapping with the GSB signals from acceptor excitons. To separate the charge signals from overlapping exciton contribution, MCR-ALS algorithm was applied to blend TA surfaces with fixed exciton spectral mask extracted from the TA data of neat IDTT-C10-TIC.

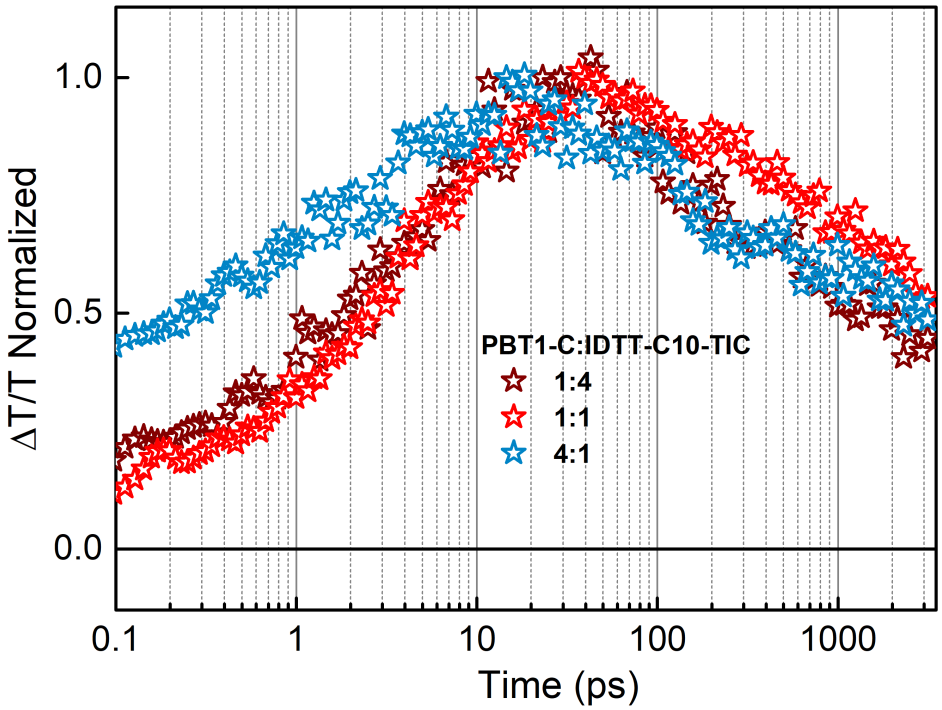

Figure 5.10: Transient absorption kinetics of charges in PBT1-C:IDTT-C10-TIC blends with different donor-acceptor weight ratios after laser excitations at 665 nm and at pump fluences of 3.1 μJ/cm^2.

Figure 5.10 displays the dynamics of long-lived charge signals of all the donor-acceptor blends, calculated from the bilinear decomposition process. The blend with the donor-acceptor weight ratio 1:4 is characterized by a very low fraction of prompt charges at the interface which is consistent with its large acceptor domain sizes that hinders most of the acceptor excitons from reaching the interface for undergoing dissociation. On the other hand, the blend with 4:1 donor-acceptor weight ratio possesses a large fraction of prompt charges, nearly 50% of the maximum population. This is in-line with the blend composition with large donor polymer domains in which the acceptor small molecules are well dispersed. Even though the exciton dissociation process is efficient in this blend, it does not give rise to long-range charge separation. The fraction of prompt charges and the pace of charge growth in the optimized blend with 1:1 donor-acceptor weight ratio appeared to be similar to that of the blend with 4:1 composition. This suggests that the acceptor small molecules might have generated large aggregate domains within the system which is commonly observed in many non-fullerene OPV systems.[110]

The difference in charge dynamics in the blends is more evident in the charge re-

combination region. The charge recombination process is highly accelerated in the blends with large donor or acceptor content compared to that of the optimized blend. This is consistent with the fact that high crystalline (blend with high acceptor content) and disordered (blend with high polymer content) domains enhance the charge recombination as they increase the chance of meeting of charge carriers with the opposite charges and defect cites, respectively.

5.7 Conclusion

A series of FREAs with different molecular packing were designed and constructed to investigate the effect of molecular packing on exciton and charge transport processes. Side-chain engineering approach was employed for molecular stacking manipulation where the length of the alkyl side-chains was varied so that the FREA backbone was changed from a $\pi - \pi$ stacking mode to a non-stacking mode. Exciton-exciton annihilation measurements in neat acceptor films proved that exciton diffusion process in FREAs doesn't rely on molecular packing, rather it is highly regulated by the resonant energy transfer rate as reported earlier. Finally, transient absorption spectroscopic analysis of blend films revealed that intermolecular charge transfer processes also have no crucial dependence on molecular $\pi - \pi$ stacking, while close atom contact can also enable these processes.

Chapter 6

High-performance FREA based ternary solar cells

Ternary OPV strategy has been widely applied in the field of organic photovoltaics to fabricate OPVs with either two donors:one acceptor or one donor:two acceptors as it improves the device efficiency *via* broadening the light absorption and energy level modulation. Here we report the first example of a ternary OPV based on **polymer donor:small molecule donor:non-fullerene acceptor** (PTB7-Th:TR:FOIC) which achieved a champion efficiency of 13%. Moreover, the study includes the first transient absorption spectroscopy analysis of a non-fullerene ternary blend. The introduction of the third component TR into the binary blend PTB7-Th:FOIC improves V_{OC}, J_{SC}, FF, and thereby the overall device performance. Transient absorption spectroscopy reveals ultrafast resonant energy transfer from TR to PTB7-Th domains, consistent with their strongly intermixed morphology. Additionally, the study also discusses the rapid long-range energy transfer from PTB7-Th to FOIC phases, that benefits both the binary and ternary blends. This work has been published in the Journal of Materials Chemistry A*.

*S. Dai, **S. Chandrabose**, J. Xin, T. Li, K. Chen, P. Xue, K. Liu, K. Zhuo, W. Ma, J.M Hodgkiss, and X. Zhan (**2019**). "*High-performance organic solar cells based on polymer donor/small molecule donor/non-fullerene acceptor ternary blends.*" 7(5): 2268-2274.

Collaborators contributed to the work

Device design and fabrication, morphology and photovoltaic characterization: Prof. Xiaowei Zhan and students from Peking University, Beijing, China.

Research focused on

Transient absorption spectroscopic measurements: (**a**) Transient absorption measurements in neat, binary and ternary blend films and (**b**) Exciton diffusion measurements in neat and binary blend films.

Data processing and analysis: (**a**) Singlet-singlet exciton annihilation (SSA) fittings, (**b**) calculation of exciton diffusion parameters and (**c**) application of MCR-ALS algorithm on blend data.

6.1 Introduction

Owing to the intrinsically narrow absorption bands of organic semiconductors, numerous strategies have been proposed in the last decade to improve the absorption window and thereby the efficiency of OPVs. Among them, multi-junction devices such as tandem OPVs with two or more sub-active layers connected monolithically with interfacial recombination layers, have been widely investigated.[53,133,188,197] Apart from attaining high efficiencies, the fabrication of tandem devices with optimal recombination layers between the sub-active layers is challenging.[53] To tackle this issue, the concept of ternary organic solar cells (TSCs) have been put forward with three active layer components to make a wider absorption window while keeping the simplicity of single-layer fabrication.[12,54,75] In ternary OPVs, the addition of a third component brings multiple advantages. It enhances the light-harvesting ability of the active layer as it is an additional absorber with a complimentary absorption spectrum and thus increases the J_{SC} of the device. Additionally, by carefully selecting the components based on the relative energies of their LUMO and HOMO levels, V_{OC} can be tuned through the formation of an energy cascade alignment. Moreover, the third component can facilitate exciton dissociation and charge transport *via* optimizing the film morphology.[187]

Recently, ternary OPVs have experienced a rapid development due to the design of abundant varieties of high performing non-fullerene acceptors (NFAs). Ternary OPVs based on two donors and one NFA have shown excellent photovoltaic performances. For instance, Li and co-workers fabricated a high-performance ternary blend with two donors, J51 and PTB7-Th having similar HOMO levels and a narrow band gap acceptor ITIC.[200] With the addition of 20 weight% PTB7-Th as a third component, the device could achieve a peak PCE of 9.7% with an enhanced J_{SC} of 17.8 mA/cm^{-2}, which were attributed to the synergistic effects of enhanced light absorption, efficient energy transfer between the donors, more balanced carrier mobility, and improved morphology. Similarly, Hou *et al.* reported a ternary system based on J52 and PTB7-Th as donors and an ultra low band gap NFA, IEICO-4F which exhibited a record PCE of 10.9% with an excellent J_{SC} of 25.3 mA/cm^{-2}, one of the highest short circuit current values ever reported.[183] This chapter includes the first example of ternary OPVs based on polymer donor (PTB7-Th):small molecule donor (TR):NFA (FOIC) which exhibit a champion efficiency of 13% with a high tolerance to thickness variation. Transient absorption spectroscopic analysis of the ternary

blend (PTB7-Th:TR:FOIC) films reveals the ultrafast resonant energy transfer from TR to PTB7-Th domains, inline with their strongly intermixed morphology. Furthermore, the spectroscopic study also discusses the rapid long-range energy transfer from PTB7-Th to FOIC phases that benefits both the binary (PTB7-Th:FOIC) and ternary blends.

6.2 Fundamental mechanisms in ternary OPVs

Due to the different energy properties of active layer components and various resulting morphology features, three fundamental mechanisms are governing the photovoltaic processes in ternary OPVs: (a) charge transfer, (b) energy transfer, and (c) parallel-linkage transfer (**Figure 6.1**).[182,187] In the charge-transfer dominant case, a cascade energy level alignment is required for an efficient charge transfer.[46] Here, both donors can directly contribute to the charge carrier generation process upon interfacing with the acceptor. Cascade charge transfer is an efficient strategy to facilitate the charge transfer process by providing additional pathways, while exquisitely suppressing the charge recombination rather than generating charge traps in the active layers.[187]

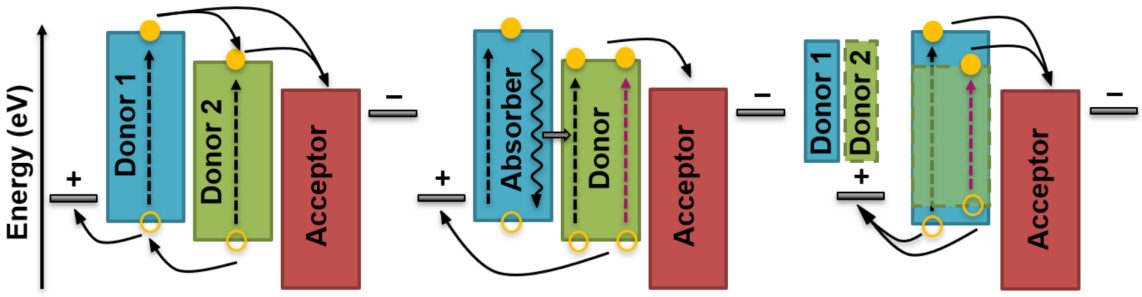

Figure 6.1: Three fundamentally different mechanisms in ternary OPVs: charge transfer, energy transfer, and parallel-linkage. The figure is reproduced according to Yang *et al.*[182]

On the other hand, in the energy transfer mechanism, all holes are generated within only one donor domain, while the other donor functions as an energy transfer agent.[14,112] Long-range Förster resonance energy transfer (FRET) and short-range Dexter energy transfer are the two main energy transfer mechanisms that can happen when there is a spectral overlap between the emission of the energy donor and the absorption of the energy acceptor. The energy donor harvests solar photons and transfers the photo-generated excitations to the energy acceptor in which the excitons undergo dissociation and generate extra free charges, resulting in a high value of J_{SC}. In general, both charge transfer and energy transfer mechanisms require subtle engineering of

frontier energy levels and band gaps of all involved components.

Ternary OPVs can also function as parallel-linked tandem cells where there is an independent charge transfer network is formed between the two donors or acceptors after the addition of a third component.[114] In this scheme, excitons generated in each donor domain can migrate to their respective donor/acceptor interface to dissociate into charge carriers. The generated holes travel through their corresponding donor-linked channels to the anode, while electrons still transport *via* the acceptor-enriched domain to the cathode. This is equivalent to a parallel connection of two individual binary-based solar cells.

6.3 Materials

Figure 6.2a presents the chemical structures of PTB7-Th, TR and FOIC which play the roles of polymer donor, small molecule donor and the non-fullerene acceptor in the ternary blend studied here, respectively. All the materials including the blends were provided by our collaborators from the Key laboratory of polymer Chemistry and Physics of Ministry of education, Peking University, China. PTB7-Th (molecular weight: $\geq$145000 g/mol and polydispersity index: 3) is a narrow band gap polymer donor, designed by incorporating 2-ethylhexyl-thienyl group into the benzo-[1,2-b:4,5-b']dithiophene (BDT) unit of the novel polymer PTB7, to improve the co-planarity of the main chain that extends the absorption into longer wavelengths.[101] TR (molecular weight: $\sim$1901.14 g/mol) is a 2D-conjugated small molecular donor with alkylthio-thienyl substituted BDT as the central unit, terthiophene end-capped with electron-withdrawing rhodanine as two arms.[29] While, FOIC is a near IR absorbing fused ring electron acceptor (FREA), designed and synthesized by Li *et al.* in 2018, which when blended with PTB7-Th exhibited a high PCE of 12%.[99]

In this work, the small molecular donor TR was introduced as a third component to the binary blend PTB7-Th:FOIC in order to enhance the photovoltaic performance. Here the selection of the third component was done based on different considerations.[98] The first and the most important reason is the high compatibility between TR and PTB7-Th as both of them contain alkylthio-thienyl substituted BDT units. TR exhibits a blue-shifted absorption relative to that of PTB7-Th which gives panchromaticity (ability to absorb light in the entire visible spectral region) to the ternary blend. Additionally, the HOMO levels of both donors are nearly aligned which ensures

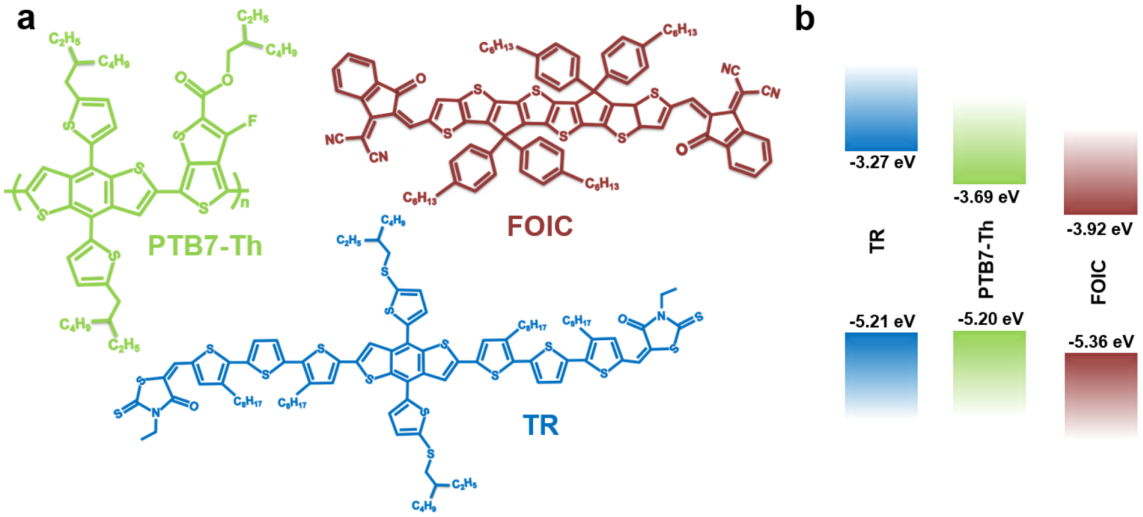

Figure 6.2: (a) Chemical structures and (b) energy levels of TR, PTB7-Th and FOIC. The energy levels are measured by Prof. Xiaowei Zhan and students from Peking University, China.

free movement of holes between these materials without any morphological trapping induced by the third component (**Figure 6.2b**). Moreover, TR exhibits high crystallinity and hole mobility (3.2×10^{-3} $cm^2V^{-1}s^{-1}$) which could enhance the molecular packing and hole mobility of PTB7-Th by tuning the morphology of the blended film. The ternary devices based on TR, with a weight ratio of 25% with respect to PTB7-Th, yielded the best PCE of 13.1%, higher than that of the reference PTB7-Th:FOIC binary blend (12.1%).

6.4 Device characterization

The effect of TR on photovoltaic performance was characterized using inverted devices with ITO/ZnO/Donors:FOIC/MoO_x/Ag structure. The binary blend, PTB7-Th:FOIC with a weight ratio of 1:1.5, optimized with 0.5% solvent additive (diphenyl ether, DPE) achieved a PCE of 12.1%. The device was characterized by a high V_{OC} of 0.722 V with J_{SC} and FF of 24.73 mA/cm^{-2} and 66.8%, respectively. The ternary devices were prepared with different TR weight ratios ranging from 0 to 100%. When the TR ratio is increased from 0 - 60%, the V_{OC} appeared to be increased from 0.722 to 0.748 V, while J_{SC} and FF exhibited a boost up to 25% of the TR weight ratio after which they showed sudden reductions. The optimized ternary device was found to be the one with a TR weight ratio of 25% which yielded the best PCE of 13.1% with V_{OC} of 0.734 V, J_{SC} of 25 mA/cm^{-2} (**Figure 6.3a**) and FF of 70.9%. Our col-

laborators also tried different active layer thicknesses ranging from 80 - 300 nm where they got the maximum efficiency of 13.1% for the 110 nm thick device. Even with 300 nm layer thickness, the device could achieve an efficiency of 10.8%, suggesting high tolerance to thickness variation which is promising for industrial-scale roll to roll printing.

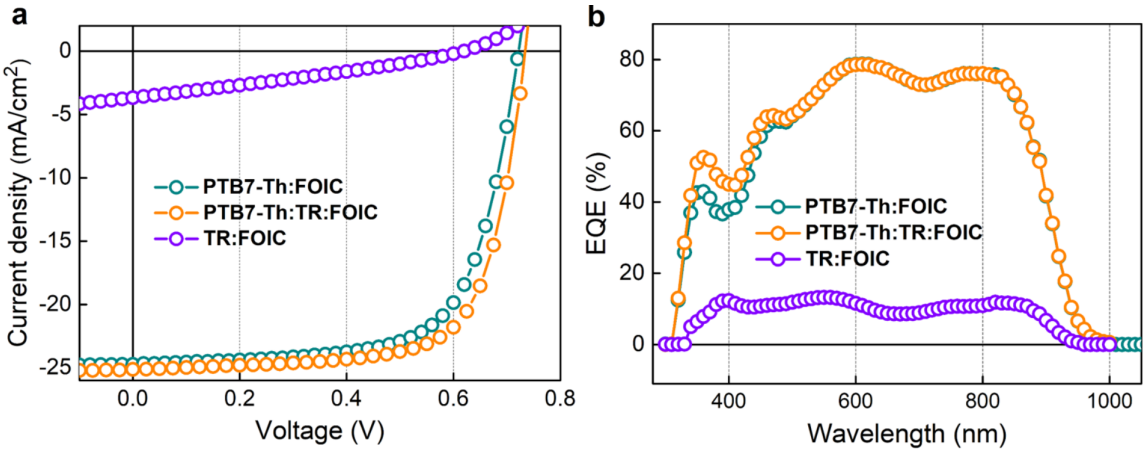

Figure 6.3: (a) J - V characteristics and (b) EQE spectra of the binary and the ternary OPVs under illumination of an AM 1.5G at 100 mW/cm^2. These measurements were performed by Prof. Xiaowei Zhan and students from Peking University, China.

Regarding external quantum efficiency (EQE), binary devices showed high EQE in 450 - 900 nm, but a weaker response in the UV region. When TR was introduced, the photo-response in 300 - 450 nm region was increased significantly due to the high absorption of TR in blue (**Figure 6.3b**). Meanwhile, the ternary device suffered a decrease of EQE in the 700 - 950 nm region and the reduction was boosted upon increasing the TR weight ratio.[98]

Table 6.1: Summary of hole and electron mobilities of ternary (PTB7-Th:TR:FOIC) and parent binary (PTB7-Th:FOIC and TR:FOIC) blends. The data is provided by Prof. Xiaowei Zhan and students from Peking University, China.

Blend	μ_h $(\mathbf{cm^2V^{-1}s^{-1}})$	μ_e $(\mathbf{cm^2V^{-1}s^{-1}})$	μ_h/μ_e
PTB7-Th:FOIC	4.0×10^{-4}	4.8×10^{-4}	0.8
PTB7-Th:TR:FOIC	6.8×10^{-4}	5.3×10^{-4}	1.3
TR:FOIC	3.4×10^{-4}	2.8×10^{-5}	12.1

The hole and electron mobilities of the blended films are given in the **Table 6.1**

(measured by Prof. Xiaowei Zhan and students from Peking University, China). The optimized ternary blend exhibited higher hole mobility of 6.8×10^{-4} $cm^2V^{-1}s^{-1}$ than PTB7-Th:FOIC (4.0×10^{-4} $cm^2V^{-1}s^{-1}$) and TR:FOIC (3.4×10^{-4} $cm^2V^{-1}s^{-1}$) parent binary blends. The electron mobility of the ternary blend (5.3×10^{-4} $cm^2V^{-1}s^{-1}$) was slightly higher than that of PTB7-Th:FOIC (4.8×10^{-4} $cm^2V^{-1}s^{-1}$) but much higher than that of TR:FOIC (2.8×10^{-5} $cm^2V^{-1}s^{-1}$). The high charge carrier mobilities of ternary device directly relates to its higher J_{SC} and FF compared to that of parent binary devices.

6.5 Morphology characterization

The morphology characterization of the blends were done by the collaborators from China. This section includes the major findings with the full details being published elsewhere.[98] Grazing-incidence wide angle X-ray scattering (GIWAXS) measurements were carried out to probe the molecular packing information of all neat and blend films. **Figure 6.4** provides the 2D GIWAXS patterns and 1D line-cut profiles of binary and ternary blend films. In the blend films, the scattering peaks detected at 0.28 and 0.84 $Å^{-1}$ arised from the lamellar packing of PTB7-Th, consistent with the scattering profiles of neat PTB7-Th film given in the Appendix: **Figure A.19**. While, the peaks with q = 0.43, 0.86 and 1.29 $Å^{-1}$ originated from the lamellar packing of FOIC. The scattering peaks arised from the lamellar packing of TR were detected at q = 0.31, 0.62 and 0.93 $Å^{-1}$. The $\pi - \pi$ stacking peaks of PTB7-Th, TR and FOIC were noticed at 1.58, 1.71 and 1.82 $Å^{-1}$, respectively (Appendix: **Figure A.19**). The absence of $\pi - \pi$ stacking peak of PTB7-Th located at 1.58 $Å^{-1}$ in both PTB7-Th:TR and PTB7-Th:TR:FOIC blends proves that the two donors are miscible each other. While the (100) peak of PTB7-Th (q = 0.27 $Å^{-1}$) became sharper and coherence length increased from 5.0 to 7.5 nm, indicating that TR enhanced the molecular packing of PTB7-Th.

Additionally, resonant soft X-ray scattering (R-SoXS) was employed to characterize the phase-separation of the blend films. The study revealed a mode domain size of 97 nm in TR:FOIC blends, indicating high immiscibility between the components and is consistent with the high crystallinity of TR. Additionally, the mode domain size of PTB7-Th:FOIC blends was calculated to be 38 nm. The scattering profiles of ternary and PTB7-Th:FOIC binary systems found to be similar indicating the good miscibility of PTB7-Th and TR.

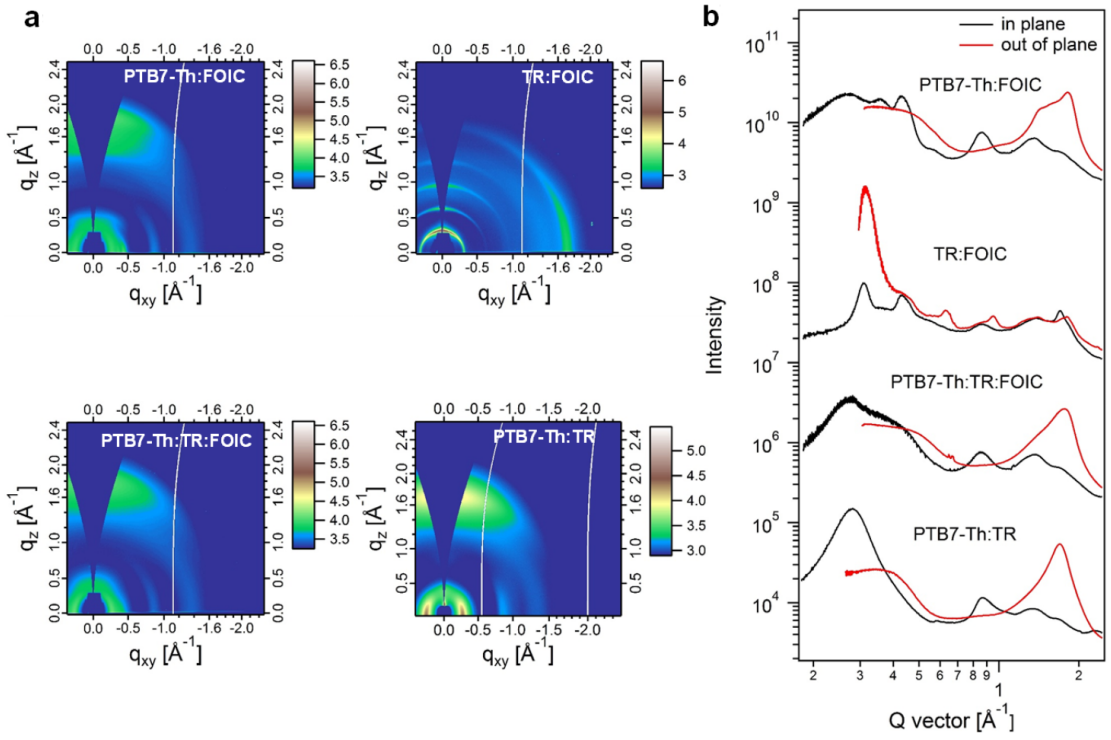

Figure 6.4: (a) 2D GIWAXS patterns and (b) 1D line-cuts for optimized PTB7-Th:FOIC, TR:FOIC, PTB7-Th:TR:FOIC and PTB7-Th:TR blend films. The measurements were performed by Prof. Xiaowei Zhan and students from Peking University, China.

The immiscibility observed between the guest donor (TR) and one of the host materials (FOIC) is a common feature of high efficiency ternary systems.[122,196] The low miscibility between the components results in pure domains which facilitate efficient charge transport and reduce bimolecular charge recombination at the grain boundaries and thus leads to improved J_{SC} and FF. Moreover, for energy transfer driven ternary systems, the low immiscibility is an additional benefit as the guest component is only an energy transfer agent and doesn't take part in charge generation process where a mixed phase morphology is ideal.

6.6 Steady-state absorption in films

Figure 6.5 gives the steady-state absorption spectra of PTB7-Th, TR, and FOIC neat films along with the binary and ternary blended films. The spectra were recorded using a Cary 50 Bio UV-vis spectrometer over the range 190 - 1100 nm.

The absorption spectrum of neat PTB7-Th exhibits clear vibronic features in the vis-

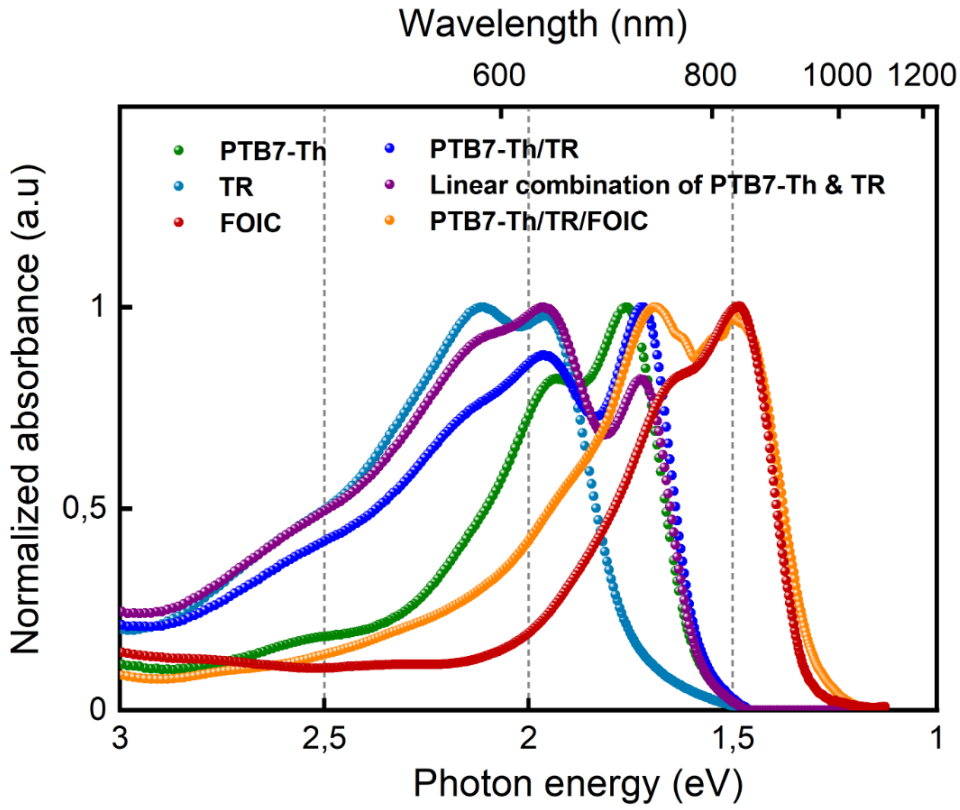

Figure 6.5: Steady-state absorption spectra of PTB7-Th, TR, FOIC neat films, PTB7-Th:TR blend (0.75:0.25), linear combination of PTB7-Th and TR and PTB7-Th:TR:FOIC (0.75:0.25:1.5) ternary blend films.

ible range of 500 - 785 nm which are peaked at ∼704 nm and ∼640 nm with an optical band gap of 1.58 eV. While the thin film of TR is characterized by a blue-shifted and broad absorption starting from UV to near IR, with the main absorption peak at 588 nm and a vibronic shoulder at 632 nm, indication of strong $\pi - \pi$ stacking between the molecular backbones.[29] FOIC exhibits strong absorption in 600 - 900 nm region with a maximum molar extinction coefficient of 2×10^5 $M^{-1}cm^{-1}$ at 782 nm.[180] As the absorption spectra of these materials span the whole visible spectrum of the solar light, the ternary blends could achieve panchromaticity which in turn increased the overall device performance.

As expected, the absorption spectrum of the ternary blend, PTB7-Th:TR:FOIC comprises contributions from each of the components. Meanwhile, a clear difference is observed between the spectrum of the binary blend PTB7-Th:TR and that made from the linear combination of pure PTB7-Th and TR spectra. This reveals the strong alteration of the PTB7-Th based spectrum developed from the presence of TR. This

spectral perturbation is also observed in the photoluminescence spectra given the Appendix: **Figure A.20**. In the PTB7-Th:TR blend, TR enhanced the redder PL from PTB7-Th, but the PL peak from TR, expected at 715 nm, completely disappears. This confirms the full miscibility of TR with PTB7-Th along with the chance of excitation energy transfer between them.

6.7 Time-resolved spectroscopy in films

Transient absorption spectroscopy is an effective tool to study the exciton and charge dynamics in photovoltaic materials. To probe the photophysical properties of blends, it is essential to get the spectral signatures of the neat films so that the features in the blend spectrum can be easily identified. Unlike fullerene-based acceptors having very weak excited-state absorption signals, non-fullerene acceptors are characterized by strong PIA signals as they have high excited-state absorption coefficients. This makes the data analysis of the blend complex since the signals from different spectral features of donor and acceptor overlap each other. **Figure 6.6** gives a series of transient absorption spectra of the neat materials, FOIC (excited at 800 nm, pump fluence 4.1 μJ/cm^2), TR (excited at 500 nm, pump fluence 0.7 μJ/cm^2) and PTB7-Th (excited at 600 nm, pump fluence 6.4 μJ/cm^2) at different pump-probe time delays. All the films were kept under continuous vacuum environment during the measurements to avoid degradation.

The TA spectral slices of neat FOIC film consist of a positive ground state bleach (GSB) ranging from 1.4 - 2 eV, consistent with its steady-state absorption spectrum (**Figure 6.5**). This feature is accompanied by a negative photoinduced absorption (PIA) signal centered around 1.3 eV, representing the excited-state absorption of excitons. All the features are characterized by similar decay rates suggesting the dominance of singlet excitons. In the case of TR, the GSB feature resolves the vibronic progression peaking at ∼1.9 eV and ∼2 eV, representing 0-0 and 0-1 transitions, respectively. A broad excited-state absorption signal ranging from 0.8 - 1.5 eV is also observed whose decay rate matches with that of GSB, representing singlet excitons. Similarly, the TA spectra of neat PTB7-Th film feature a GSB in the range of 1.6 - 2.1 eV and a broad photoinduced absorption that extends from 0.85 - 1.4 eV. Here also it is confirmed that only singlet excitons are formed on photoexcitation from the similar decay kinetics of GSB and PIA spectral features. Additionally, the spectra of all neat materials display negligible change with time.

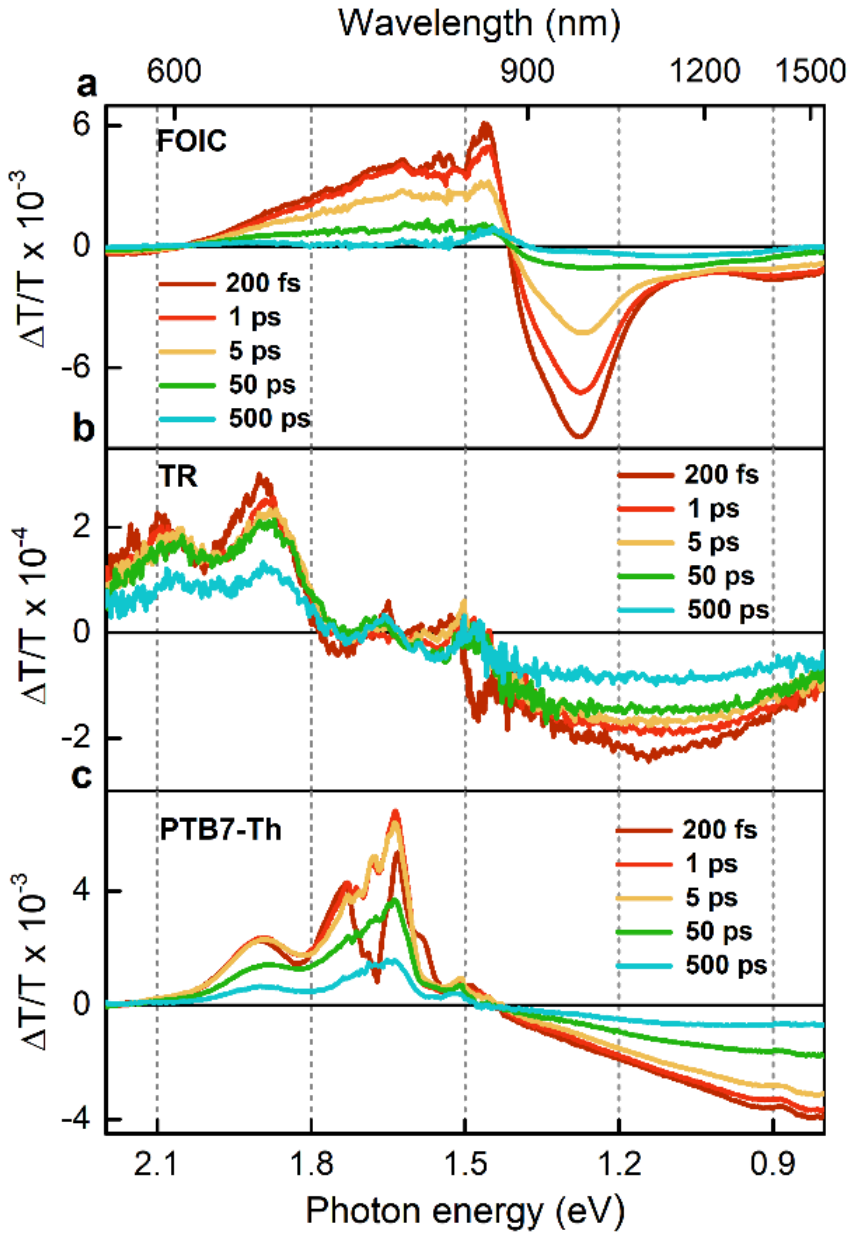

Figure 6.6: Series of TA spectra for **(a)** a neat FOIC film following excitation at 800 nm (4.11 μJ/cm^2), **(b)** a neat TR film following excitation at 500 nm (0.7 μJ/cm^2) and (c) a neat PTB7-Th film following an excitation at 600 nm (6.4 μJ/cm^2).

6.7.1 Effect of TR on PTB7-Th

To investigate the effect of TR on PTB7-Th, transient absorption spectroscopy was performed in a binary blend comprising both the donors. Here an excitation wavelength of 500 nm was selected to excite the PTB7-Th:TR binary blend so that the photo-reaction of both components was obtained. **Figure 6.7a** gives the TA surface

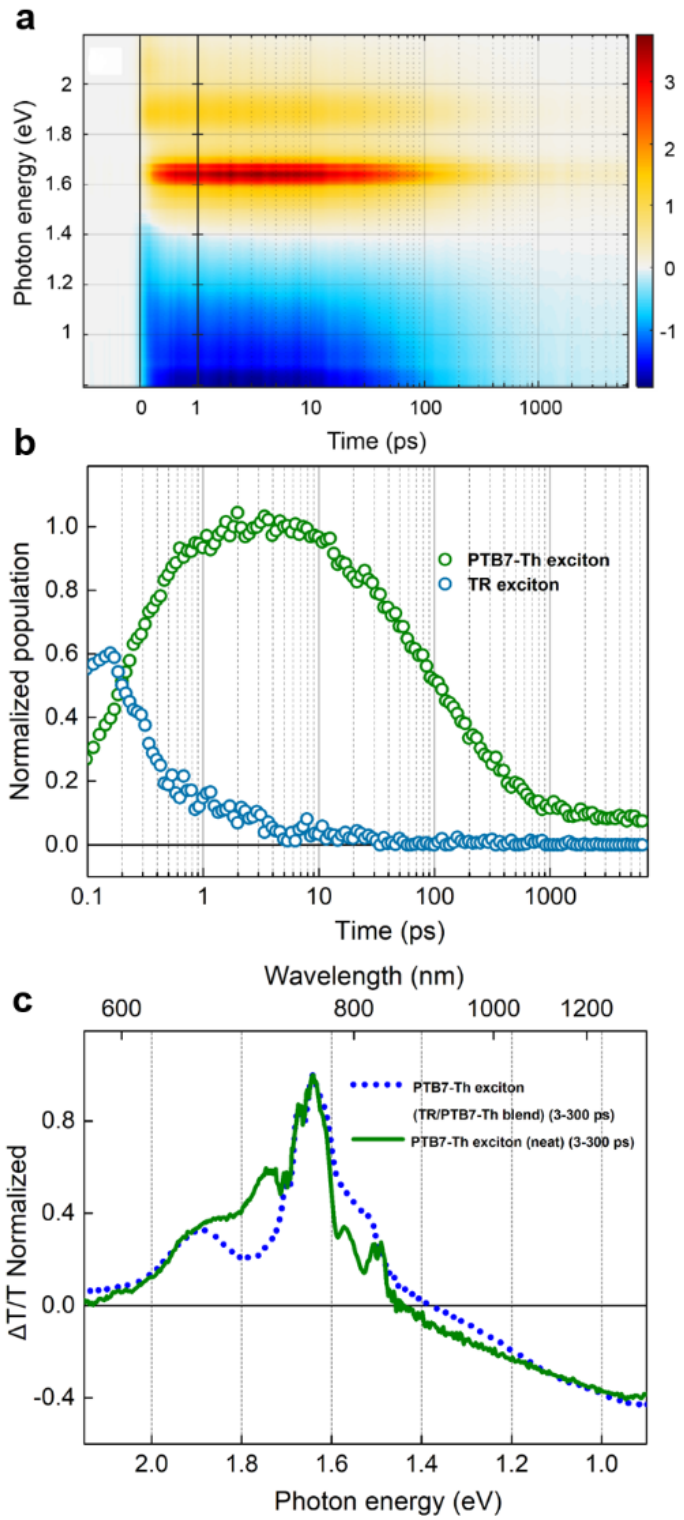

Figure 6.7: **(a)** Transient absorption surface of TR:PTB7-Th blend (excited at 500 nm, pump fluence 3.78 μJ/cm^2), **(b)** energy transfer from TR to PTB7-Th, extracted from a bilinear decomposition of TR:PTB7-Th blend (excited at 500 nm, pump fluence 3.78 μJ/cm^2) and **(c)** spectra of neat PTB7-Th exciton and TR modulated PTB7-Th exciton.

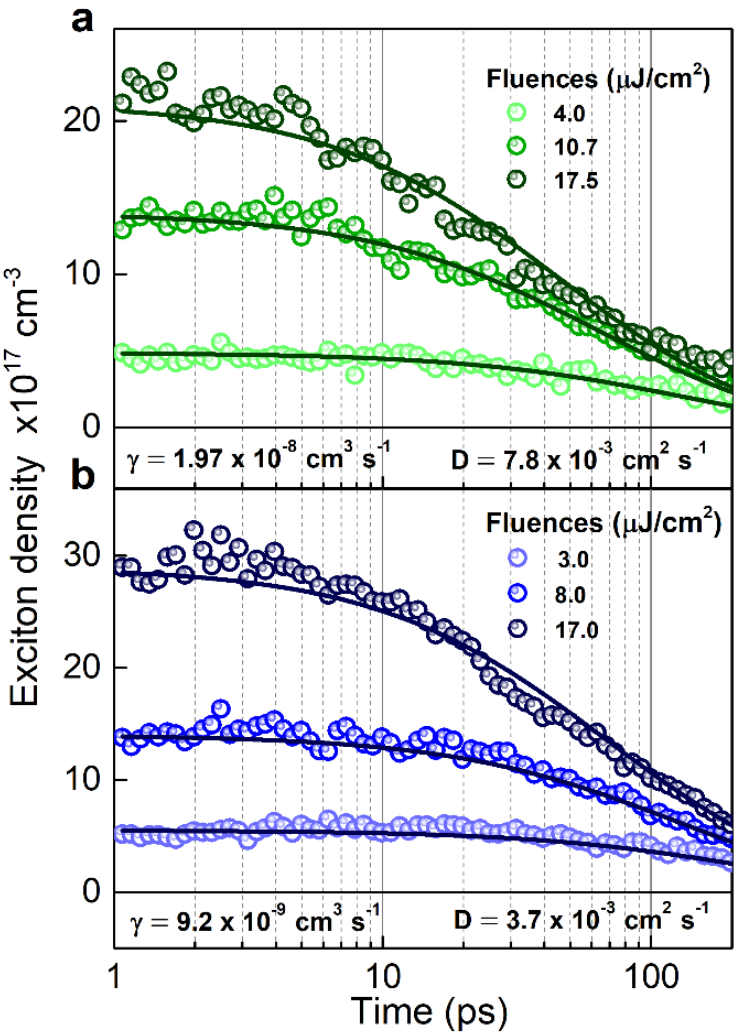

Figure 6.8: Exciton-exciton annihilation model (equation 3.6) applied in **(a)** neat PTB7-Th and **(b)** TR:PTB7-Th (0.25:0.75) excitons, and the corresponding annihilation and diffusion constants are noted in the figures.

of the PTB7-Th:TR blend (weight ratio of 0.75:0.25) after an excitation at a pump fluence of 3.78 μJ/cm^2. Since both the donors have significant overlap in their GSB and PIA regions as seen in the spectra of pristine films, multivariate curve resolution (MCR) with appropriate constraints was applied to differentiate the contribution from each component. The TA data of TR was used as a spectral mask to retrieve both the spectral and kinetic information of the TR modulated PTB7-Th exciton. **Figure 6.7b** gives the response of TR and TR modulated PTB7-Th excitons in time. Here the TR exciton population decreases with a half-life of ~500 fs with a simultaneous enhancement in the PTB7-Th exciton population which gives clear cut evidence of the sub-picosecond energy transfer occurs from TR to PTB7-Th. This is inline with

the large spectral overlap integral between the TR emission and PTB7-Th absorption (Appendix: **Figure A.21**) which increases the rate of resonance energy transfer as shown in chapter 4. Also, the spectrum of PTB7-Th excitons differs when TR is present which reveals that TR modifies the energy levels of PTB7-Th (**Figure 6.7c**) which is consistent with the corresponding steady-state absorption spectrum.

To investigate the effect of TR on PTB7-Th exciton diffusion, exciton-exciton annihilation measurements were performed in neat PTB7-Th and PTB7-Th:TR blend films. The excitation fluence was varied from 3 - 18 $\mu J/cm^2$ to initiate the bimolecular recombination of excitons in the films. The annihilation process was confirmed from the reduction in the half-life of excitons when the excitation fluence was increased. It was also made sure that the decrease in the half lifetime of excitons didn't have a contribution from any other photo-buildups like free charges which are probable at high pump fluences. This was simply confirmed from the similar decay rates of GSB and PIAs of neat PTB7-Th and TR modulated PTB7-Th excitons. Here it is also noted that the exciton lifetime in the TR modulated PTB7-Th domains was slightly longer than that of the neat PTB7-Th excitons at comparable fluences and is consistent with the increased molecular ordering of PTB7-Th in the presence of TR. To extract the bimolecular rate constants γ, the intensity-dependent exciton decays were modelled with the bimolecular annihilation rate equation (equation 3.4), accounting for both exciton annihilation and monomolecular decay pathways. Then, the 3D diffusion constants were calculated using, $D = \gamma/8\pi R$ where R is the annihilation radius which was assumed to be 1 nm here. The extracted diffusion coefficients revealed that the presence of TR lowered the PTB7-Th exciton diffusion by half (**Figure 6.8a** and **b**). The underlying reasons for the decreased diffusion coefficient are beyond the scope of this study. Perhaps it can be related to the reduced spectral overlap integral of the steady-state absorption and PL spectra of PTB7-Th:TR blend that lowers the resonant energy transfer which has an extensive effect on the exciton mobility, or to the film morphology. But the decreased diffusion coefficient of PTB7-Th excitons is not expected to reduce the charge yield or hamper the device performance in this case, since the excitons are quickly transferred to the acceptor (FOIC) phase (confirmed below).

6.7.2 Effect of TR on FOIC

To investigate the effect of TR on FOIC, transient absorption spectroscopy was employed on the binary blend TR:FOIC (0.25:1.5), where the film was excited with 500

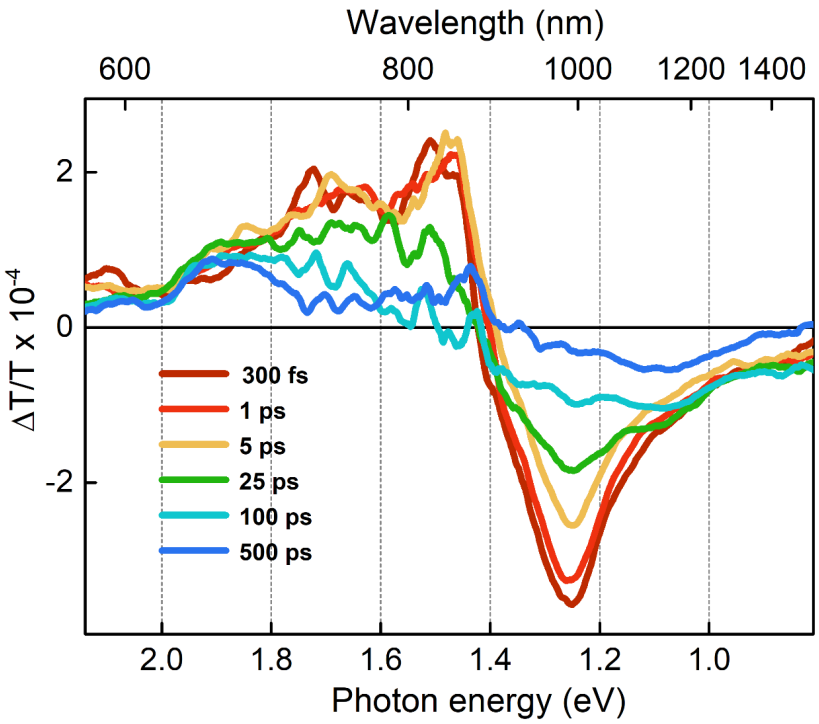

Figure 6.9: Series of transient absorption spectra of TR:FOIC (0.25:1.5) blend film at different pump-probe time delays (excited at 500 nm, pump fluence 0.84 μJ/cm^2).

nm pump pulses, at a fluence of 0.84 μJ/cm^2 where both the components absorb. **Figure 6.9** provides a series of TA spectra of TR:FOIC blend at different pump-probe delay times.

The PIA signal near ~1.3 eV is attributed to the excitonic absorption in the FOIC phase with a GSB ranging from 1.4 - 1.9 eV, consistent with the TA spectra of the neat FOIC film. After ~5 ps, a new feature with a shifted bleach around 1.9 eV was originated, retaining bleach signals from the acceptor phase and with a PIA at ~1.1 eV. These secondary excitations are attributed to charge pairs which persisted beyond 0.5 ns time window of this experiment. Here the blue shifted bleach comes from the holes occupying TR as evident from the GSB of neat donor excited at 500 nm. But, the FOIC exciton signal appears to have an unperturbed and near complete decay which reveals the fact that there is no energy transfer happening from TR to FOIC phases regardless of the large spectral overlap integral between TR emission and FOIC absorption. This confirms the immiscibility of TR with FOIC phase. The same reason accounts for the minimum charge-based absorption signal in the blend. This is consistent with the large phase-separation with a mode domain size of 97 nm observed in the R-SoXS profiles of TR:FOIC blends.[98]

6.8 Transient absorption spectra of ternary blend

Transient absorption spectroscopy was applied in the optimized ternary blend film to investigate the effect of TR on charge generation and recombination. **Figure 6.10** gives a series of transient absorption spectra of the ternary blend at different pump-probe delay times after an excitation at 500 nm where mostly the donors absorb.

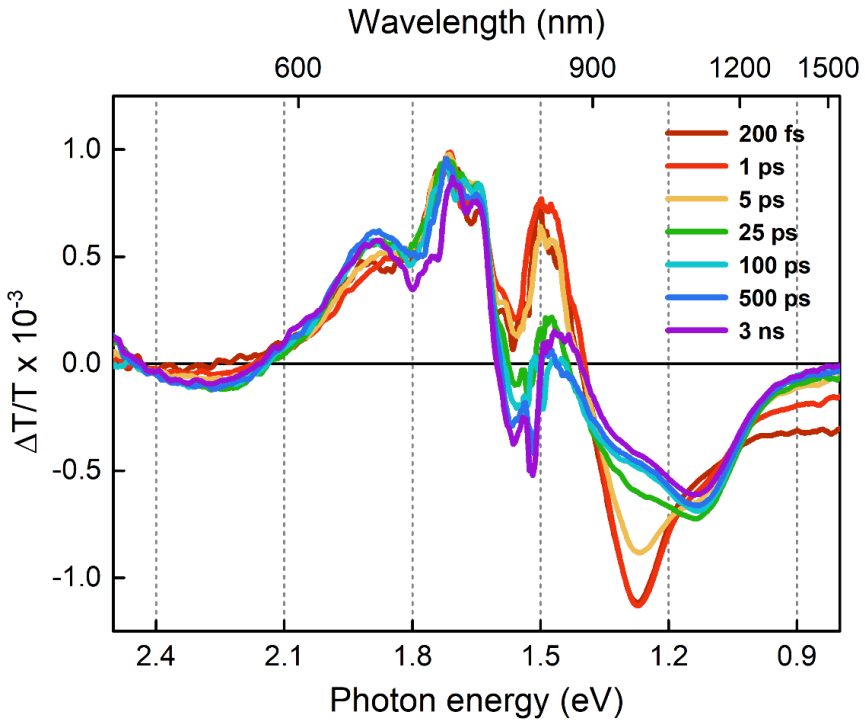

Figure 6.10: Series of transient absorption spectra for an optimized PTB7-Th:TR:FOIC ternary blend (0.75:0.25:1.5) film after excitation at 500 nm at a pump fluence of 0.9 μJ/cm^2.

In accordance with the spectral signatures of neat materials (**Figure 6.6**), the PIA feature near 1.3 eV can be attributed to the FOIC excitons and PTB7-Th excitons are responsible for the lower energy tail around 0.9 eV. The signal contribution from TR based excitons is not identifiable and may make a minor contribution <500 fs timescale due to the sub-picosecond energy transfer from TR to PTB7-Th, confirmed from the PTB7-Th:TR blend. The near absence of TR based excitons beyond this ultrafast timescale confirms the strong miscibility of TR with PTB7-Th, consistent with the GIWAXS data. Simultaneously with the decay of exciton features, a new peak is originated near 1.1 eV that persists beyond the 6 ns time window of this experiment, is attributed to the charge pairs. The charges retain the ground state

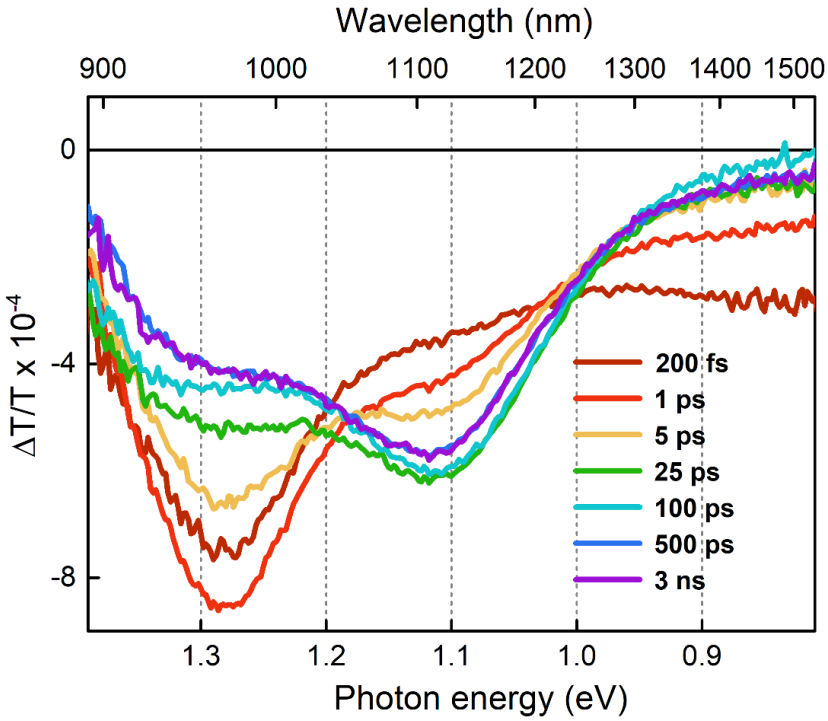

Figure 6.11: Series of transient absorption spectra for an optimized PTB7-Th:FOIC binary blend (1:1.5) film after excitation at 500 nm at a pump fluence of 0.8 $\mu J/cm^2$.

bleach signals from FOIC and PTB7-Th, complimented by the charge based photoinduced absorption from holes occupying PTB7-Th around 1.13 eV and electrons occupying FOIC presumed to account for the shoulder around 1.3 eV. The TA analysis confirms that energy transfer is the dominant mechanism behind the working of PTB7-Th:TR:FOIC ternary OPVs where the third component TR acts as an energy transfer agent while the charges are generated in the PTB7-Th and FOIC domains.

6.9 Transient absorption spectra of binary blend

The TA measurement of the binary blend, PTB7-Th:FOIC, after an excitation at 500 nm is presented in **Figure 6.11**. Data is the visible region is absent due to the low transmission of the visible part of the probe beam through the film. As per the figure, the excited-state spectral signatures are similar to that of the ternary blend. The PIA feature near 1.3 eV is attributed to the FOIC excitons while that at the lower energy, near 0.9 eV is coming from PTB7-Th based excitons. The TA spectrum remaining on the nanosecond time scale can be attributed to charge pairs, which strongly overlaps with that of FOIC excitons.

6.10 Exciton-to-charge conversion dynamics

As the excitons and charge signals from the donors and acceptor in the blends overlap each other, the direct integration of the corresponding spectral signatures doesn't give an exact picture of the exciton to charge conversion process. So, the MCR-ALS algorithm was applied to the TA surfaces of the binary and ternary blends to separate the spectral components. The number of components constituting the surface was guessed from the comparison of blend spectra with that of the neat materials and was confirmed by performing singular value decomposition (SVD). In the bilinear decomposition process, the exciton spectra from the corresponding neat films were used as spectral masks to extract the charge signal.

Figure 6.12 compares the exciton to charge conversion dynamics for the binary and the ternary blends after an excitation at 500 nm, where mostly the donors absorb. As per the figure, PTB7-Th excitons are mostly quenched in the sub-picosecond time scale, but a negligible growth of charge is observed in this region. Instead, the charge signal started growing slowly on a ∼10 ps timescale, associated with the decay of FOIC excitons. The charge population then peaks around 50 ps, beyond which non-geminate recombination sets in at the excitation densities used (confirmed from the fluence dependent decay). This is justified by the sub-picosecond resonant energy transfer from PTB7-Th to FOIC, as expected from the overlap of donor PL and acceptor absorption spectra. Additionally, the short lifetime of PTB7-Th based excitons within pure phases exceeding 10 nm dimensions (from R-SoXS data from Dai *et al.*[98]) suggests that the energy transfer operates over a long-range. Similar dynamics are observed when the blends are excited at 800 nm, where FOIC absorbs most of the light (Appendix **Figure A.24**). Here the early contribution of PTB7-Th excitons and the associated energy transfer to the FOIC phase is not observed due to the near-zero absorption of PTB7-Th at 800 nm. Both the ternary and binary blends are characterized by zero/very low fraction of prompt charge generation at the excitation wavelengths. This confirms the presence of pure domains which is an important peculiarity of non-fullerene based OPV systems.[110]

The exciton dissociation and charge generation dynamics were remarkably similar in both PTB7-Th:FOIC and PTB7-Th:TR:FOIC blends. This similarity can be expected based on the identical external quantum efficiencies (EQEs) found at these excitation wavelengths. Moreover, this can be justified based on the slower exciton

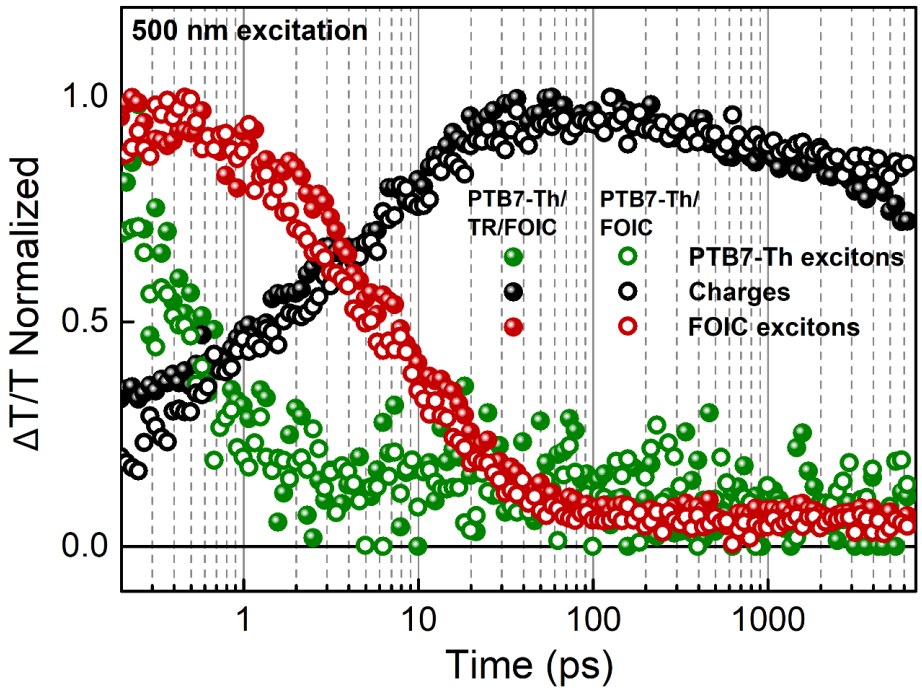

Figure 6.12: Transient absorption kinetics of excitons and charges in the ternary (PTB7-Th(0.75):TR(0.25):FOIC(1.5)) and the binary (PTB7-Th(1):FOIC(1.5)) blends, excited at 500 nm with pump fluences of 0.9 μJ/cm^2 and 0.8 μJ/cm^2, respectively.

diffusion in the ternary blend being compensated by its enhanced red PL for resonant energy transfer into FOIC.

6.11 Conclusion

A mid-band gap small molecule donor TR was used as a third component to fabricate non-fullerene ternary OPVs based on a narrow band gap polymer donor PTB7-Th and a low band gap fused ring electron acceptor FOIC. The ternary devices yielded the best PCE of 13.1%, higher than that of the parent PTB7-Th:FOIC binary blends. Ultrafast transient absorption spectroscopy results revealed the occurrence of efficient resonant energy transfer from TR to PTB7-Th domains which is consistent with the structural characterization measurements that proves the high miscibility between the donors. Additionally, TR boosted the hole mobility and charge generation of the ternary blends and ultimately improved the device performance compared to the parent binary blends. Transient absorption spectroscopy also revealed the rapid long-range resonant energy transfer from PTB7-Th to FOIC phases that benefits both the binary and the ternary blends.

Chapter 7

Summary and future works

7.1 Summary

Owing to the high crystallinity and packing orientation of acceptors, FREA based OPV systems are characterized by large and pure domains having sizes in the range 20 - 50 nm reported. This is consistent with the observation that charge generation dynamics in these systems lacked the ultrafast component that characterizes most fullerene blends. To test the hypothesis that phase sizes can be large due to facile exciton diffusion in FREAs, a planar indaceno-dithiophene (IDT) based FREA, IDIC is selected as a model system to study the exciton dynamics which when blended with a donor, already outperforms fullerene-based OPV cells. **Chapter 3** comprises temperature-dependent ultrafast exciton annihilation measurements in IDIC films which resolved a quasi-activationless exciton diffusion coefficient of at least 2×10^{-2} cm^2/s, substantially exceeding typical organic semiconductors and is consistent with the large domain sizes in optimized blends. Enhanced three dimensional diffusion in IDIC films is shown to arise from molecular and packing factors; the rigid planar molecular structure is associated with low reorganization energy, good transition dipole alignment, high chromophore density, and low disorder, all enhancing long-range resonant energy transfer. Relieving exciton diffusion coefficients has important implications for OPVs; large, ordered, and pure domains enhance charge separation and transport, and suppress recombination, thereby boosting fill factors.

Large exciton diffusion length (35 nm) exceeding optical absorption length in IDIC films introduced the possibility of solution-processed bilayer devices. **Chapter 4** includes both device and photophysics of planar bilayer devices whose power conversion efficiency of 11% is readily accounted for in the material and device design. The

bilayer devices were fabricated *via* layer-by-layer deposition technique in which orthogonal solvents were used to spin-cast the donor and acceptor layers which allowed great vertical phase separation. By pairing the polymer donor PBDB-T-2F with a range of FREAs (ITIC-Th1, IDIC, IDICO1, IDICO2, and NIDCS-HO), it is shown that the combination of molecular packing densities and absorption coefficients, long exciton diffusion lengths, and efficient, resonant energy transfer between donor and acceptor materials enable efficient bilayer devices. A combination of TEM, AFM, and GIWAXS was used to confirm that the devices have clean bilayer interfaces with minimum percolation. Ultrafast transient absorption spectroscopy was used to verify the high exciton diffusion lengths in acceptor films along with the donor to acceptor layer resonant energy transfer. The study shows that efficient photovoltaic devices can be fabricated from organic materials without requiring the complexities of the BHJ architecture, and paves the way for a new wave of advancement through new and simplified material and device design rules.

The molecular packing of active layer components has an important role in the device performance of OPV systems. Especially in FREA based OPV systems, the long range structural order induced by the end group $\pi - \pi$ stacking is considered as the critical factor for achieving high power conversion efficiency. **Chapter 5** presents a deep spectroscopic insight into the exciton and charge transport processes in a series of OPV systems based on FREAs having different molecular packing and ordering. Side-chain engineering approach was employed to manipulate the molecular packing where the length of the alkyl side-chains is varied such that the FREA back bone was changed from a $\pi - \pi$ stacking mode to a non-stacking mode. Exciton-exciton annihilation measurements in neat acceptor films proved that exciton diffusion process in FREAs doesn't rely on molecular packing, rather it is highly regulated by the resonant energy transfer rate as reported earlier. Finally, transient absorption spectroscopic analysis of blend films revealed that intermolecular charge transfer processes also have no crucial dependence on molecular $\pi - \pi$ stacking, while close atom contact can also enable these processes. This work provides new insights into the design of advanced materials for next generation organic photovoltaics considering diverse transport channels formed by close atom interactions.

Introduction of a ternary component is a facile and effective method to improve the photovoltaic performances of binary OPV systems comprising single donor and

acceptor combination. Ternary OPV systems based on non-fullerene electron acceptors have got great attention as their strong and broad absorption in the visible and near IR range together with the donors bring panchromaticity to the blends. **Chapter 6** discusses the device and photophysics of a non-fullerene ternary blend based on polymer donor:small molecule donor:non-fullerene acceptor architecture which exhibits a champion efficiency of 13%. The mid-band gap small molecule donor TR was introduced to the PTB7-Th:FOIC binary system which improved V_{OC}, J_{SC}, FF, and thereby the overall device performance. Morphology studies confirmed that TR was fully miscible with PTB7-Th, but not with FOIC phases. Ultrafast transient absorption spectroscopy revealed the occurrence of efficient resonance energy transfer from TR to PTB7-Th domains which is consistent with the morphology characterization. Moreover, presence of TR strongly altered the energy levels of PTB7-Th which lead to higher V_{OC} compared to that of the binary counterpart. Furthermore, high crystallinity of TR enhanced the molecular packing of PTB7-Th that lead to increased hole mobility which resulted in higher FF in the ternary blend. Transient absorption spectroscopy also revealed rapid long-range resonant energy transfer from PTB7-Th to FOIC phases which benefited both binary and ternary devices.

7.2 Future works

- Recently, Yuan *et al.* reported a novel non-fullerene acceptor Y6, which comprises a ladder-type electron-deficient-core-based central fused ring with a benzothiadiazole (BT) core which fine tune its absorption and electron affinity.[189] OPVs made from Y6 and the donor polymer PBDB-T-2F exhibited a record efficiency of 15.7% with a high J_{SC} of 25.3 mA/cm^2 and a FF of 74.8% regardless of large Y6 domains sizes of 44 nm. Immediately as a future work of **Chapter 3**, exciton diffusion coefficients and lengths in neat Y6 films should be measured. Additionally, the role of Förster resonance energy transfer (FRET) on exciton diffusion of Y6 should be studied. Furthermore, bilayer OPVs based on PBDB-T-2F and Y6 should be fabricated which are expected to work well with strong donor to acceptor energy transfer due to the high spectral overlap integral between PBDB-T-2F emission and Y6 absorption.

- In **Chapter 4**, transient absorption measurements of the FREA, ITIC-Th1 reveals intrinsic charge generation in neat films which caused substantial uncertainty in its lifetime. This is similar to what Liu *et al.* observed in neat films of ITIC where they extracted a very low exciton binding energy of ∼117

meV which led to free charge carrier generation at room temperature. So the possibility of making monolayers with ITIC-Th1 can be tested.

- Application of Förster resonance energy transfer model to the exciton diffusion measurements of side-chain engineered IDTT-CX-TIC FREA films.

Appendix A

Additional Figures

Chapter 3

Normalized transient absorption spectra of IDIC film

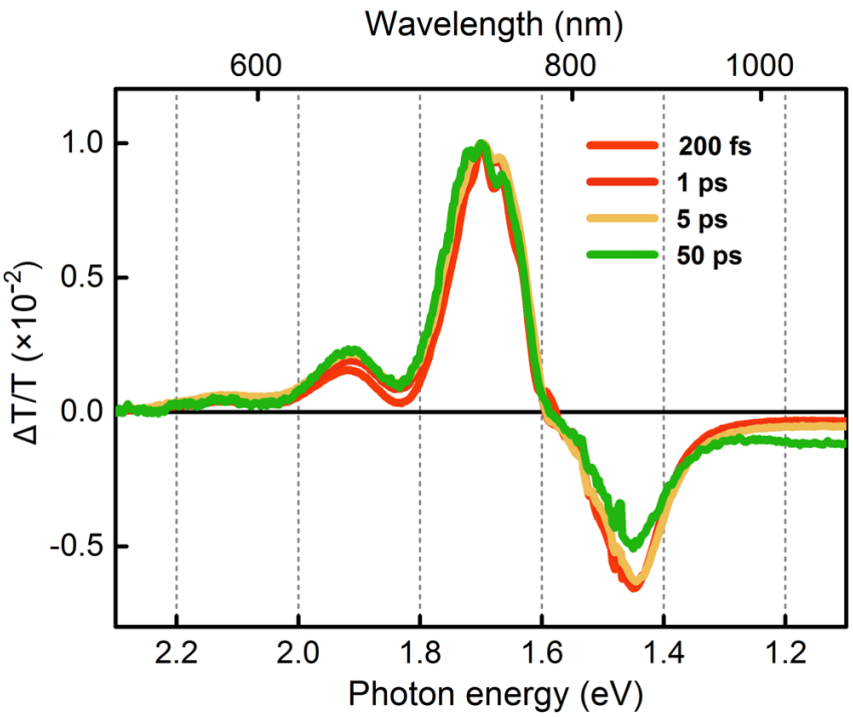

Figure A.1: Normalized transient absorption spectra of neat IDIC film at different time delays (excited at 716 nm, at a pump fluence of 6.56 μJ/cm^2).

Transient absorption in IDIC:polystyrene film

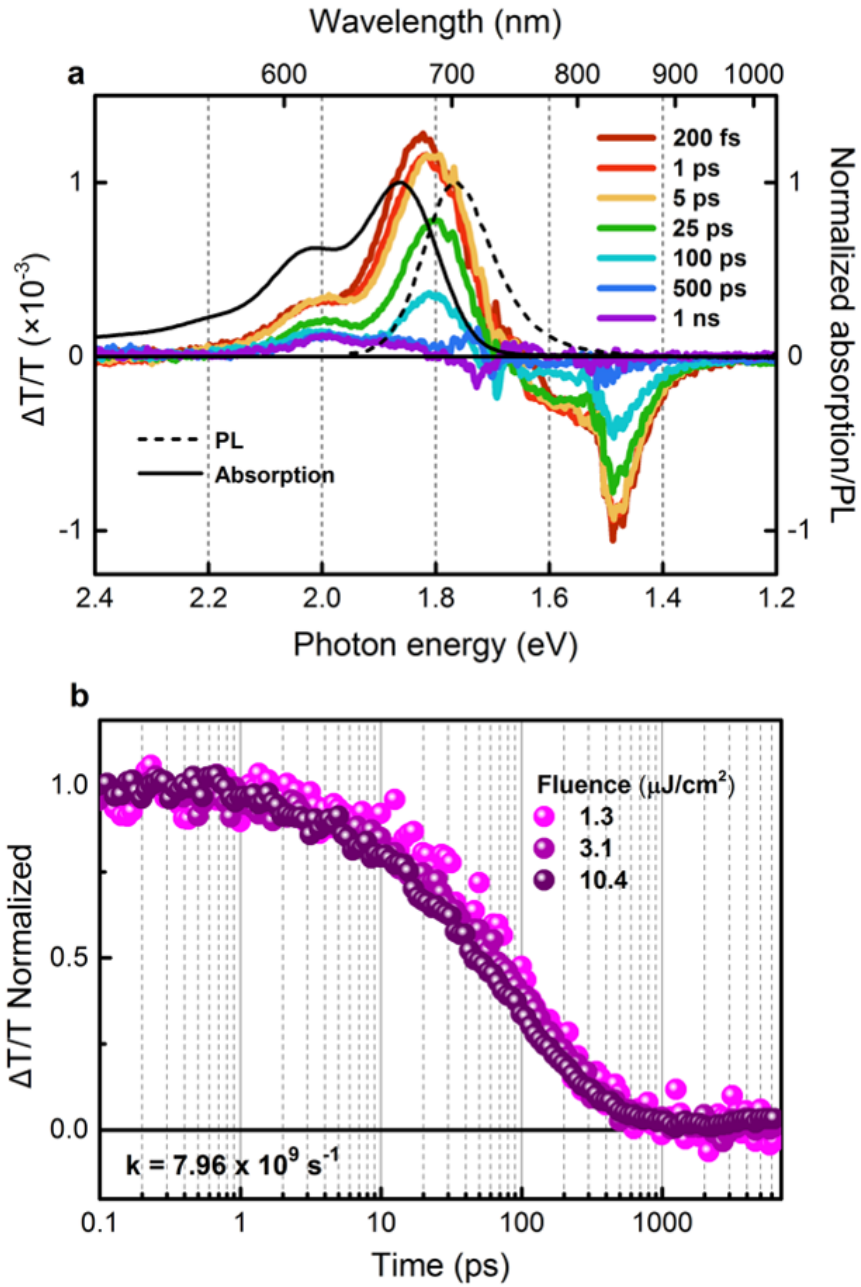

Figure A.2: Transient absorption in IDIC:polystyrene film. (a) Series of transient absorption spectra of the film with IDIC blended to dilute polystyrene (excited at 665 nm, at a pump fluence of 1.3 μJ/cm^2) along with the steady state absorption and PL spectra and (b) fluence dependent exciton kinetics confirming the monomolecular deactivation, from which a decay constant of 7.96 $\times$ 10^9 s^{-1} is obtained.

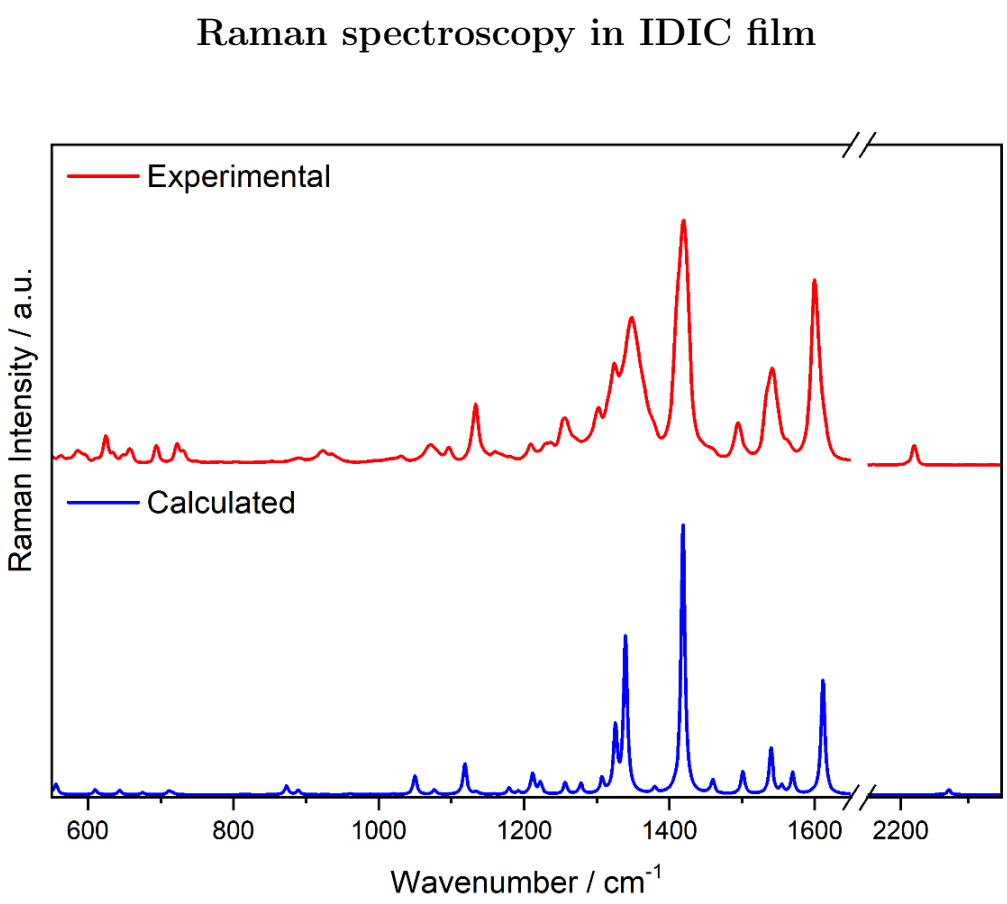

Figure A.3: Raman spectrum for IDIC, as measured experimentally in the solid state and modeled, at the CAM-B3LYP/6-31G(d) level, in a vacuum, using Gaussian 09 D0.1. An adjustment factor of 0.95 was applied to the calculated frequencies to account for the anharmonicity of the potential energy well. The measurements were performed by Prof. Keith C. Gordon and students from Otago University, New Zealand.

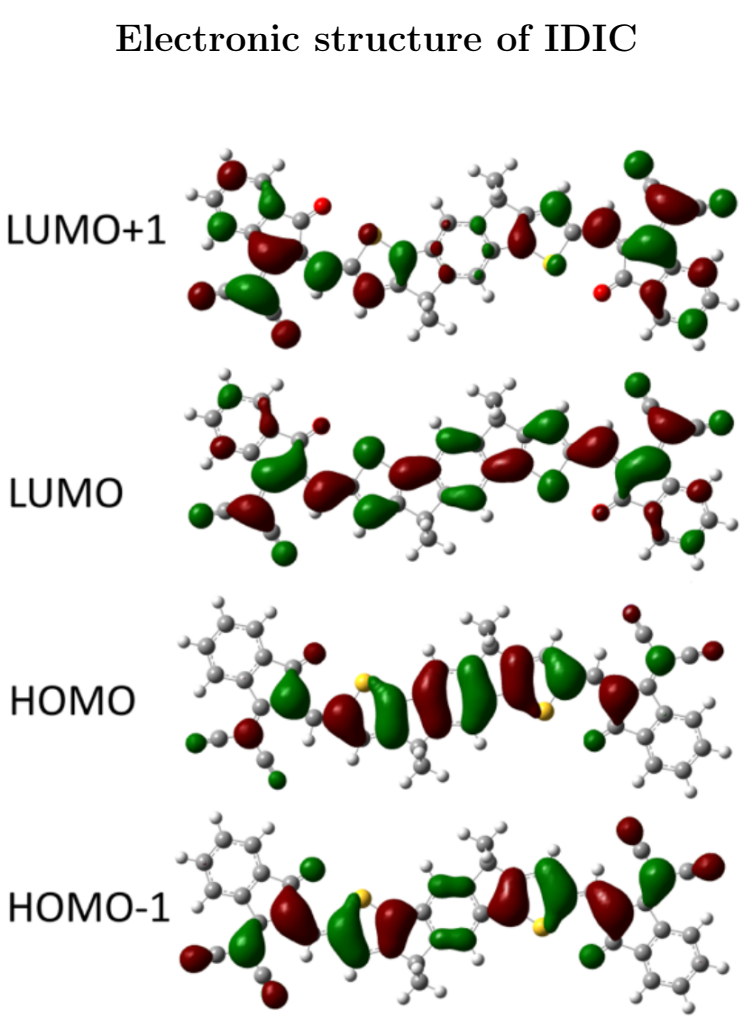

Figure A.4: Frontier molecular orbitals for IDIC as calculated at the CAM-B3LYP/6-31G(d) level using Gaussian 09 D0.1. The structure is obtained by Prof. Xiaowei Zhan and students from Peking University, China.

Excited state structural distortion in IDIC

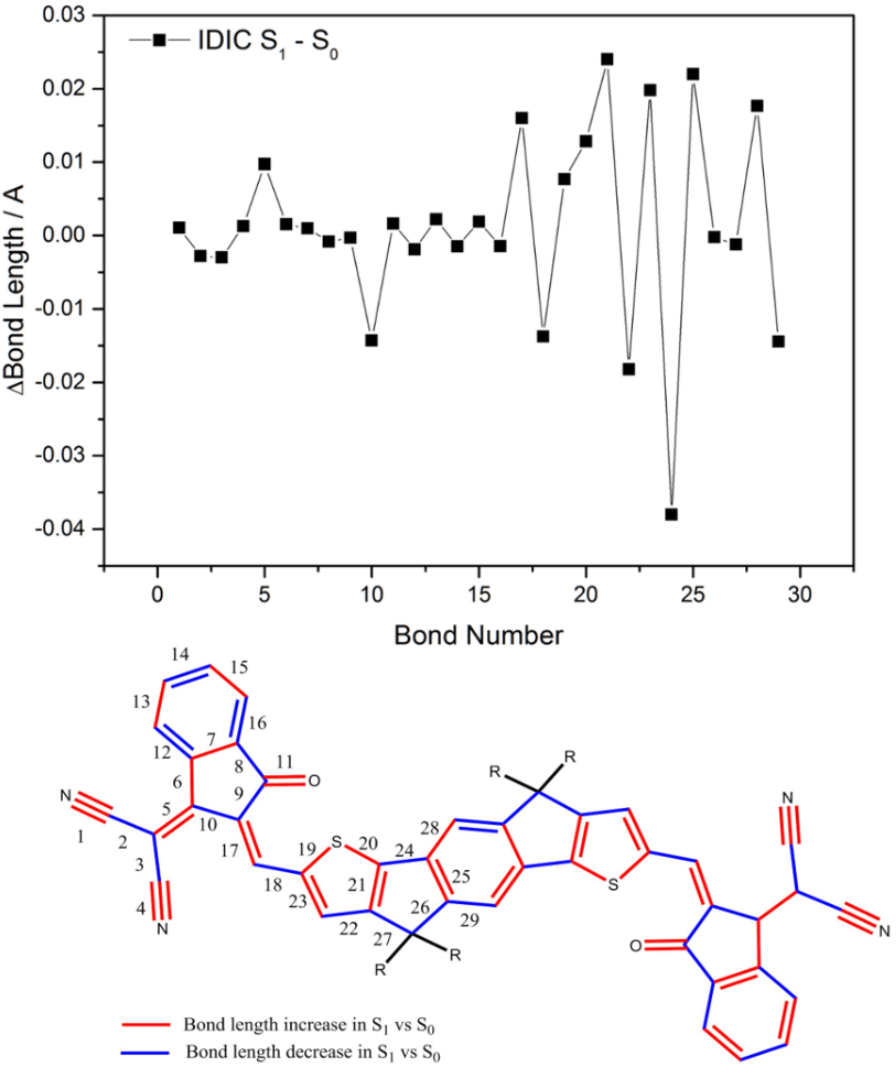

Figure A.5: (top) Bond length alternations (BLA) between the ground (S_0) and first excited states (S_1) of IDIC. The structure fro the S_1 state was found by carrying out an optimisation on the first transition predicted by the TD-DFT calculations in Gaussian at the CAM-B3LYP/6-31G(d) level, using a dichloromethane solvent field. Bond number and direction of bond length changes in the excited state (bottom). The data were obtained by Prof. Xiaowei Zhan and students from Peking University, China.

Exciton-exciton annihilation in IDIC derivative

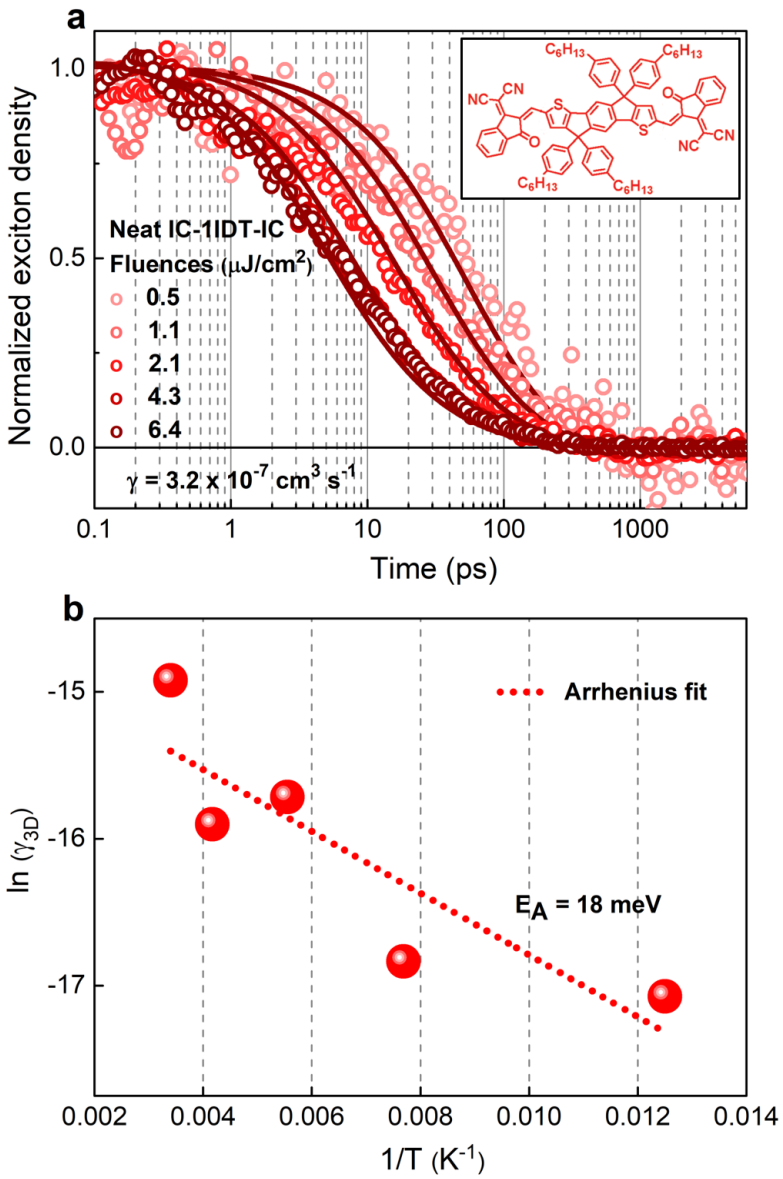

Figure A.6: Singlet-singlet exciton annihilation in IDIC derivative. (a) Fluence dependent singlet exciton decays in IC-1IDT-IC (chemical structure is shown in the inset) neat film (excited at 690 nm) fitted to the singlet-singlet exciton annihilation model. The extracted value of annihilation constant is noted in the figure. (b) Arrhenius plot of annihilation constants versus reciprocal temperature producing an activation energy (E_A) of 18 meV. Here the films are prepared under the same conditions as IDIC films where the material synthesis and purification can be found in the reference.[106]

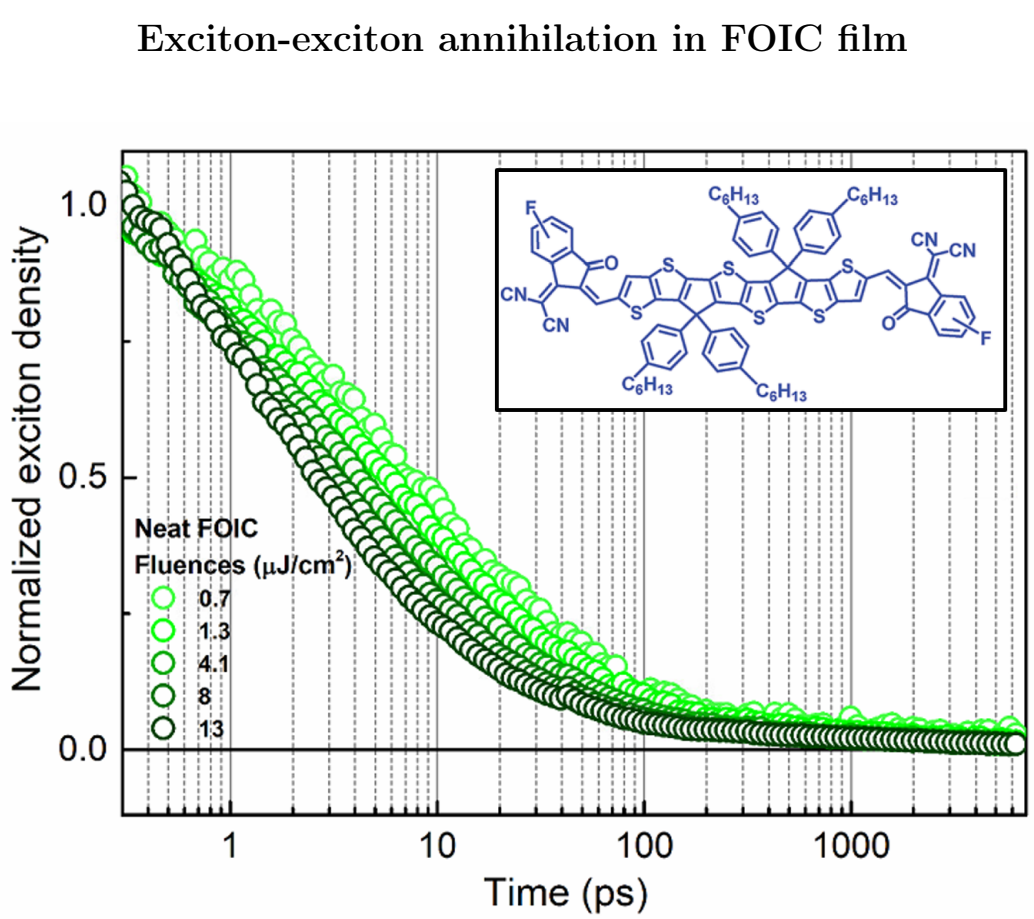

Figure A.7: Fluence dependent singlet exciton decays in FOIC (chemical structure is shown in the inset) neat film (excited at 800 nm). Here the films are prepared under the same conditions as IDIC films while the material synthesis and purification can be found in the reference.[180]

Chapter 4

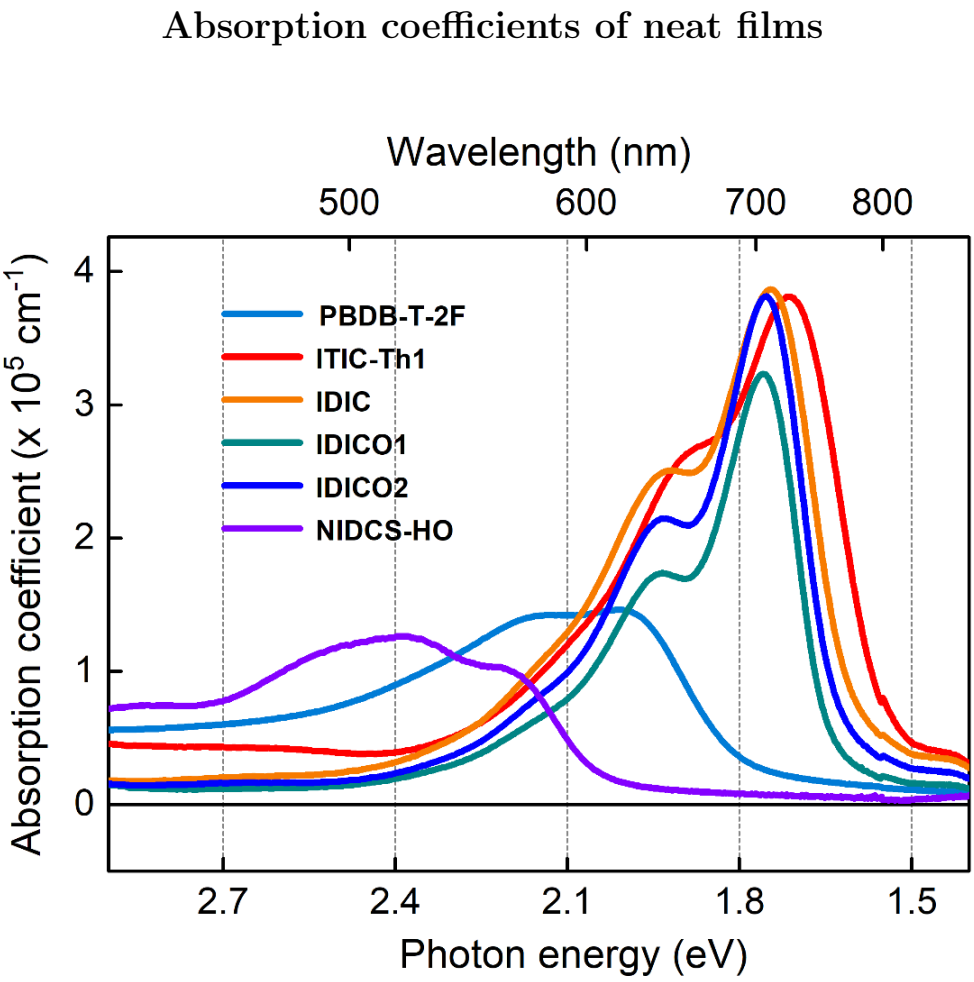

Figure A.8: Absorption coefficient spectra of neat films obtained *via* ellipsometric measurements. The measurements were performed by Prof. Jin Young Kim and students from UNIST, South Korea.

Surface roughness and morphology

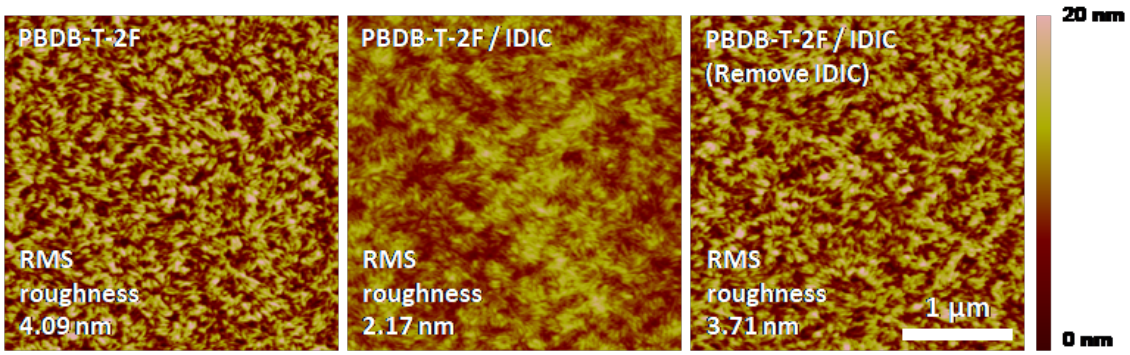

Figure A.9: Surface structure and morphologies for PBDB-T-2F pristine, PBDB-T-2F:IDIC bilayer films and PBDB-T-2F:IDIC bilayer film after IDIC removal. The data was obtained by Prof. Jin Young Kim and students from UNIST, South Korea.

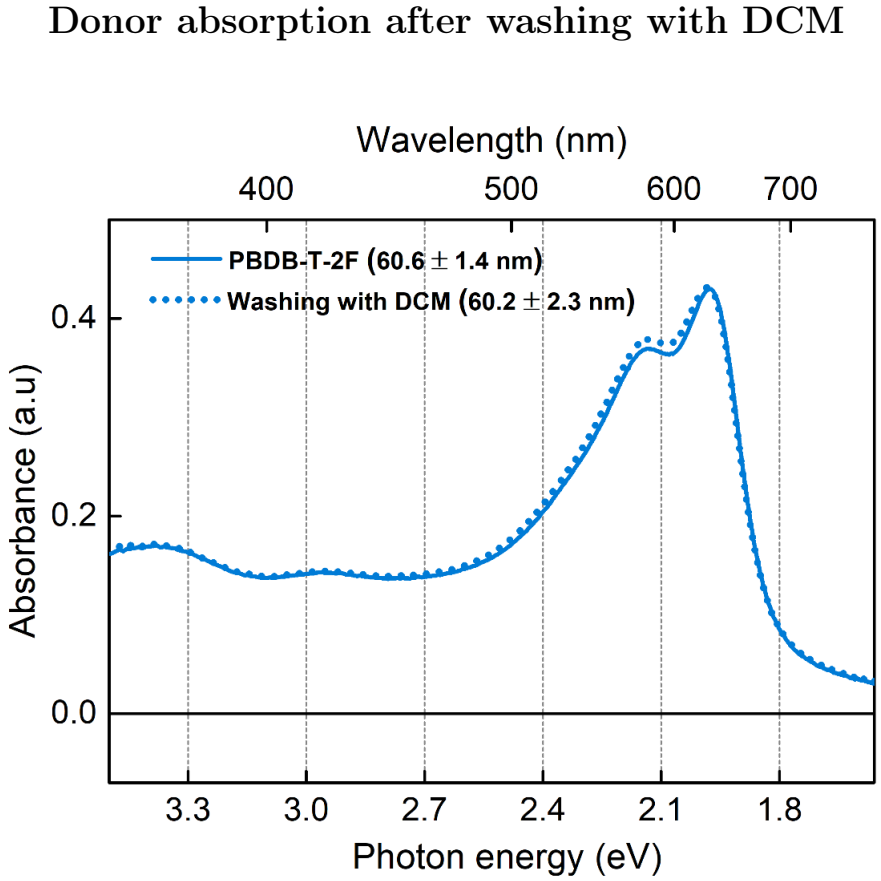

Figure A.10: UV-vis absorption spectra of pristine PBDB-T-2F before and after washing with dichloromethane (DCM) which is the solvent of acceptor layer deposition. The spectra were obtained by Prof. Jin Young Kim and students from UNIST, South Korea.

TA spectra of neat active layer components

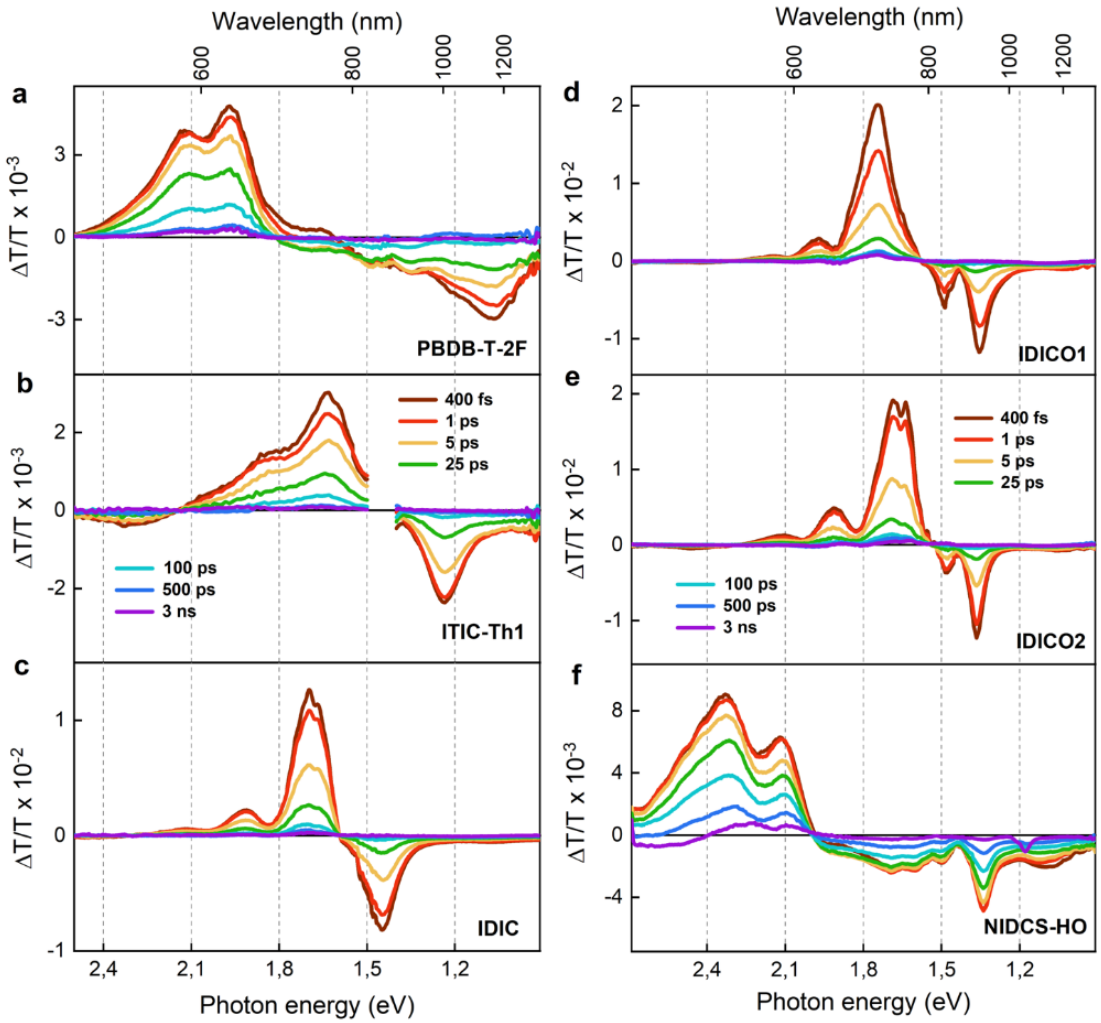

Figure A.11: Series of transient absorption spectra of (a) PBDB-T-2F (excited at 560 nm, at a pump fluence of 1.65 μJ/cm^2), (b) ITIC-Th1 (excited at 665 nm, at a pump fluence of 1.87 μJ/cm^2), (c) IDIC (excited at 712 nm, at a pump fluence of 6.56 μJ/cm^2), (d) IDIC01 (excited at 665 nm, at a pump fluence of 4.3 μJ/cm^2), (e) IDIC02 (excited at 665 nm, at a pump fluence of 3.5 μJ/cm^2) and (e) NIDCS-HO (excited at 600 nm, at a pump fluence of 13.8 μJ/cm^2).

Exciton diffusion in neat acceptor films

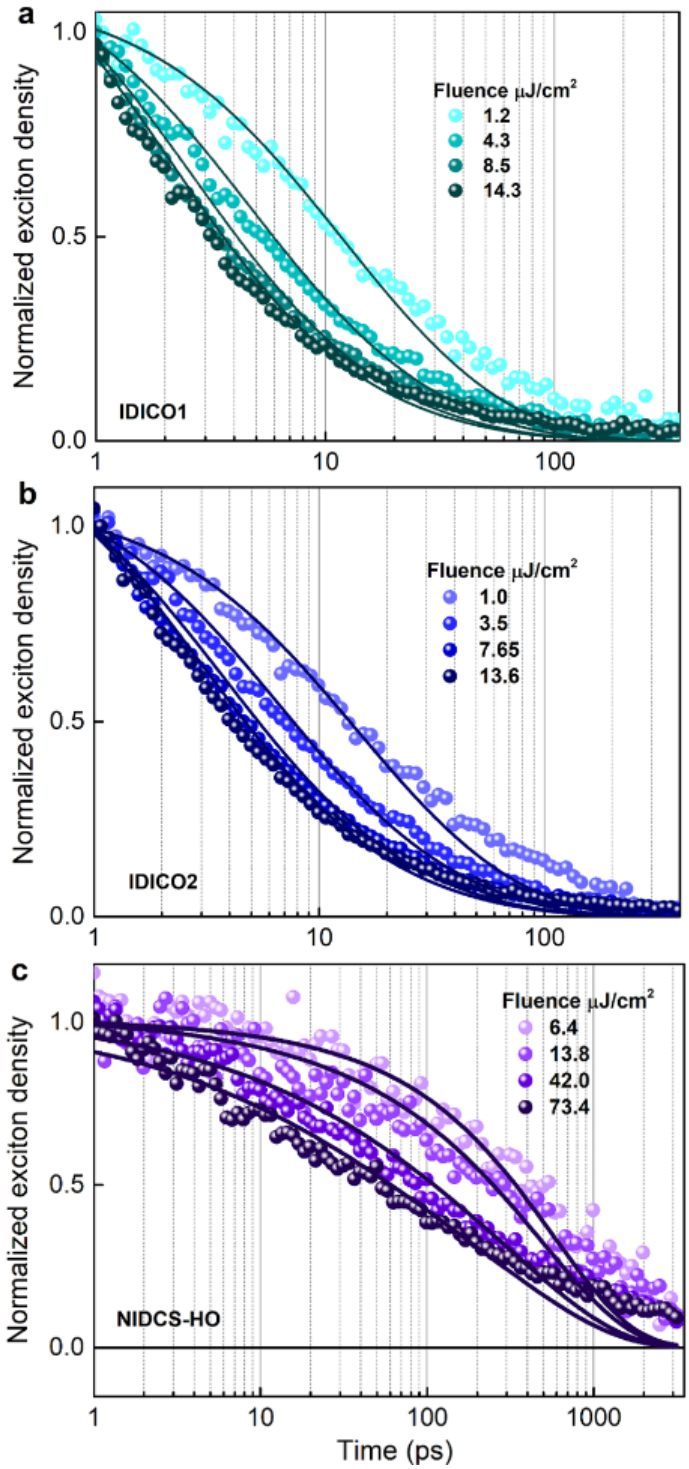

Figure A.12: Singlet-singlet exciton diffusion model applied to the fluence dependent decays in the neat films of (a) IDICO1 and (b) IDICO2, and (C) NIDCS-HO (excited at 665 nm, 665 nm, and 560 nm, respectively).

Donor exciton quenching PBDB-T-2F:IDIC bilayer series

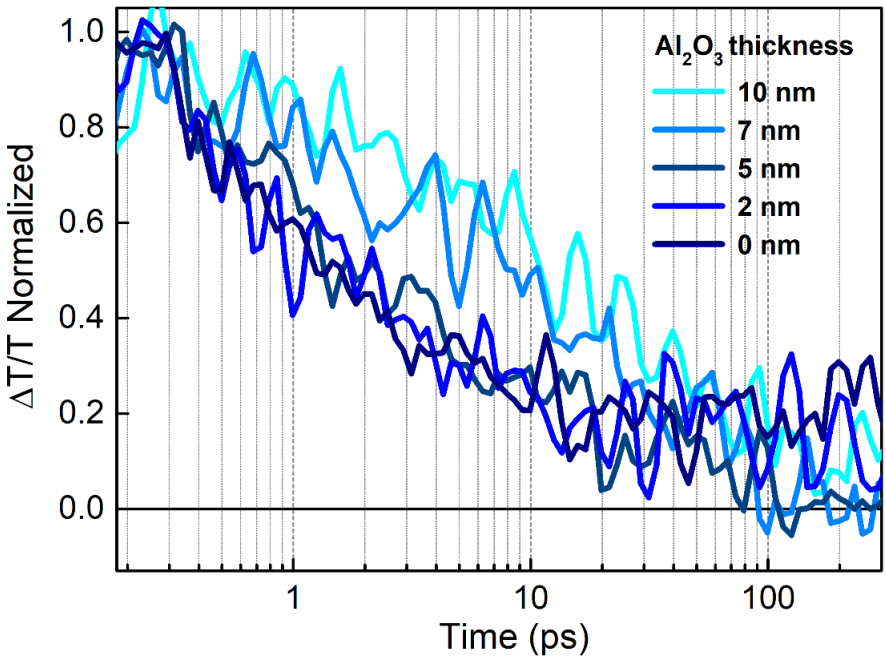

Figure A.13: Donor exciton quenching in PBDB-T-2F:IDIC bilayer series with varying Al_2O_3 interlayer thickness. Here, all the films were excited with 562 nm pump pulses at a fluence of 2.47 $\mu J/cm^2$. The kinetic traces were obtained by integrating the corresponding spectra at 0.95 eV.

Chapter 5

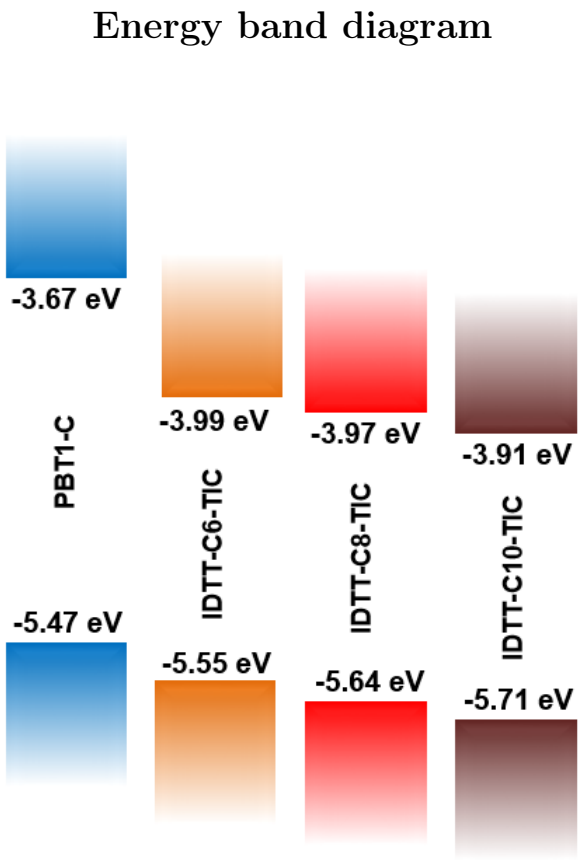

Figure A.14: Energy band diagram of the donor polymer and IDTT-CX-TIC FREAs. Energy levels were measured by Prof. Yanming Sun and students from Beihang University, China.

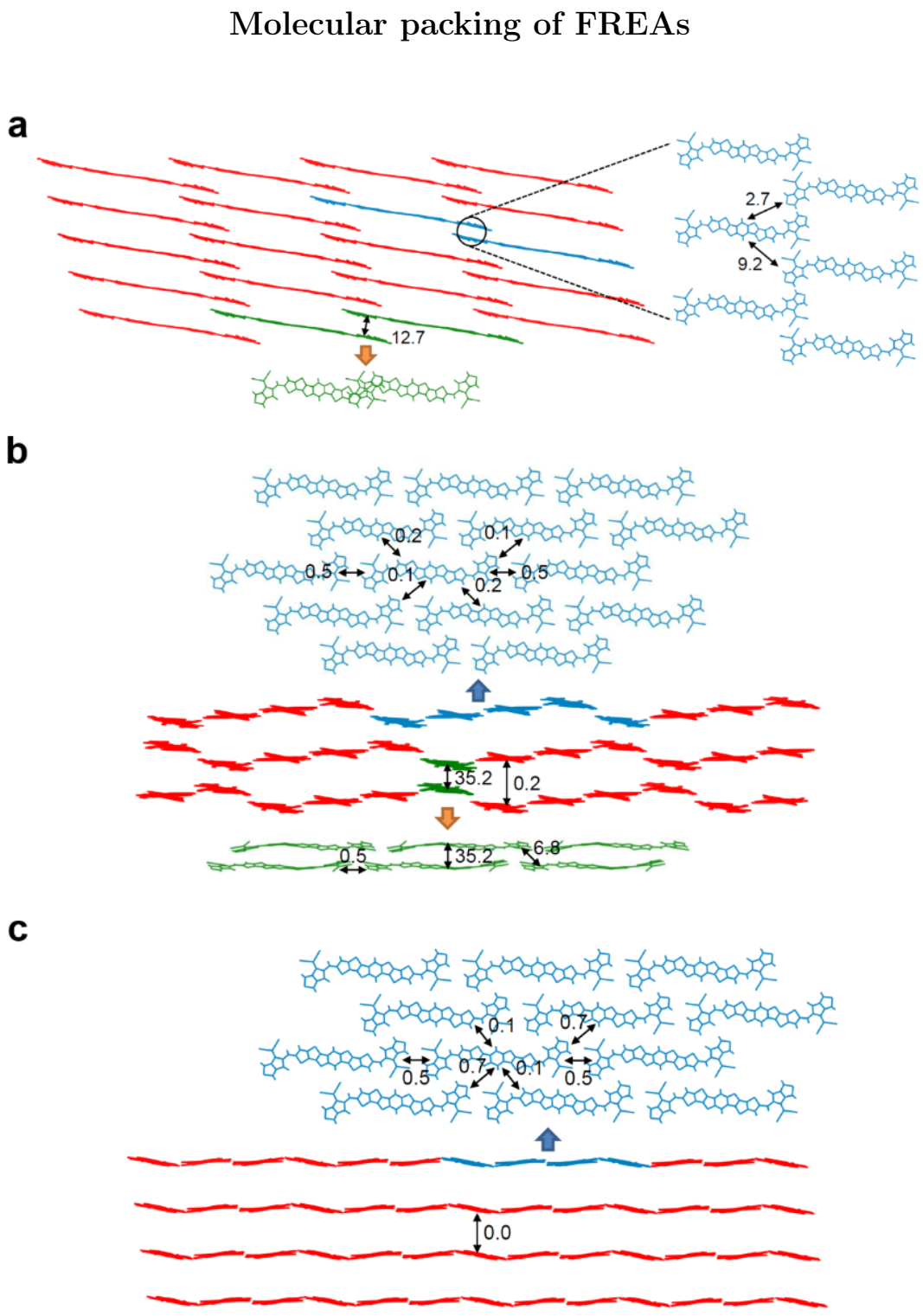

Figure A.15: Molecular packing of (a) IDTT-C6-TIC, (b) IDTT-C8-TIC, and (c) IDTT-C10-TIC. The structures are provided by Prof. Yanming Sun and students from Beihang University, China.

GIWAXS measurements of PBT1-C:IDTT-CX-TIC blends

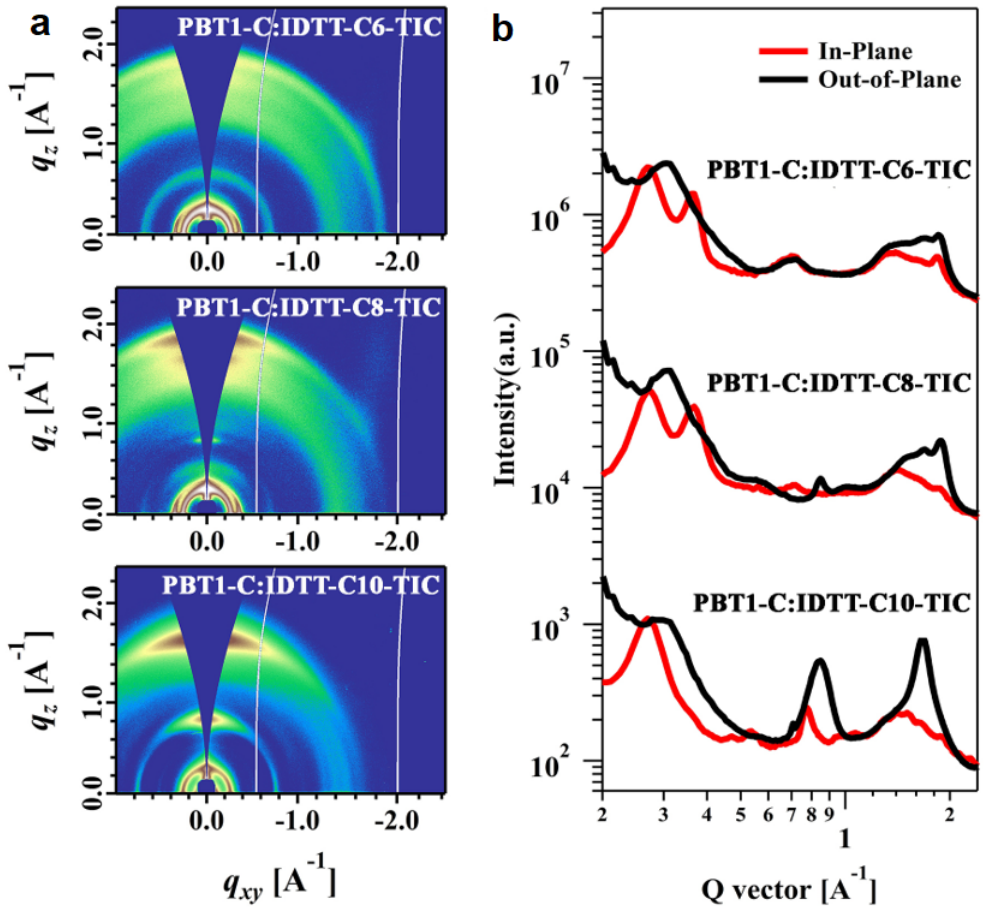

Figure A.16: (a) 2D GIWAXS patterns of PBT1-C:IDTT-CX-TIC blend films, and (b) the corresponding in-plane and out-of-plane line-cut profiles. The measurements were performed by Prof. Yanming Sun and students from Beihang University, China.

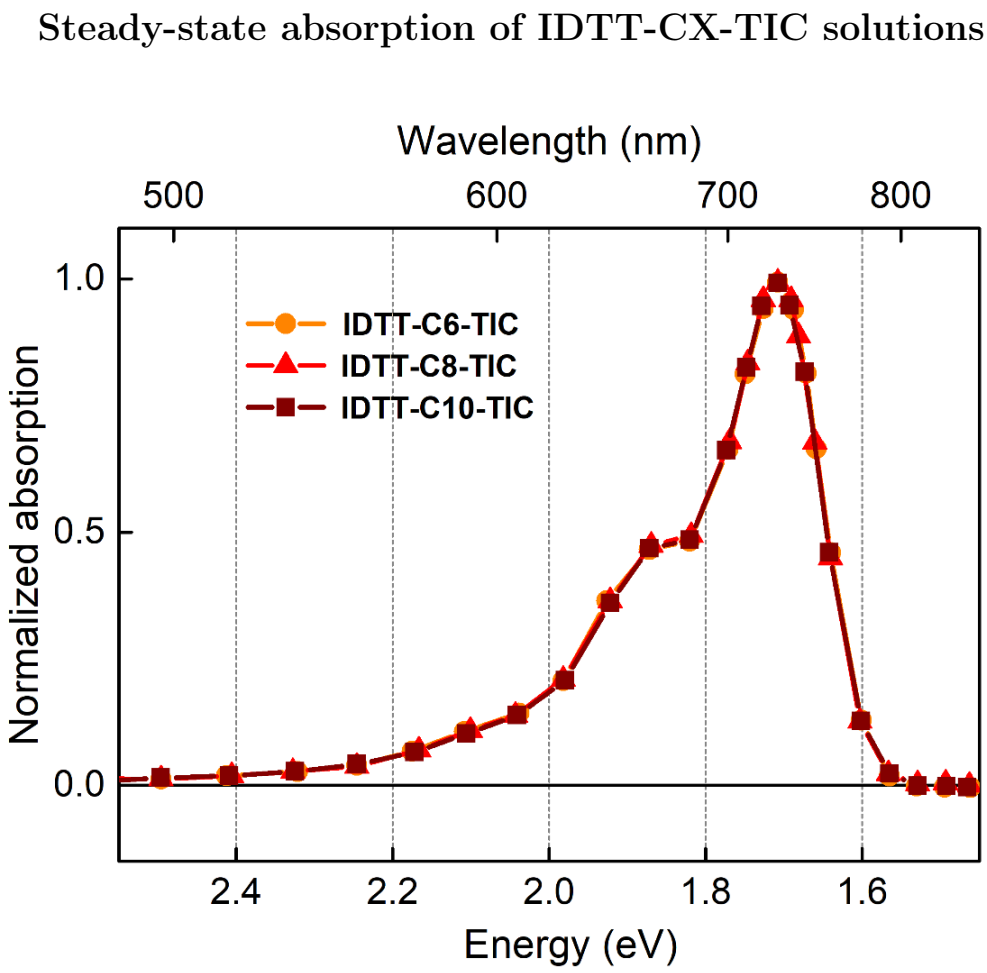

Figure A.17: Steady-state absorption spectra of IDTT-CX-TIC solutions.

Transient absorption spectra of neat IDTT-CX-TIC films

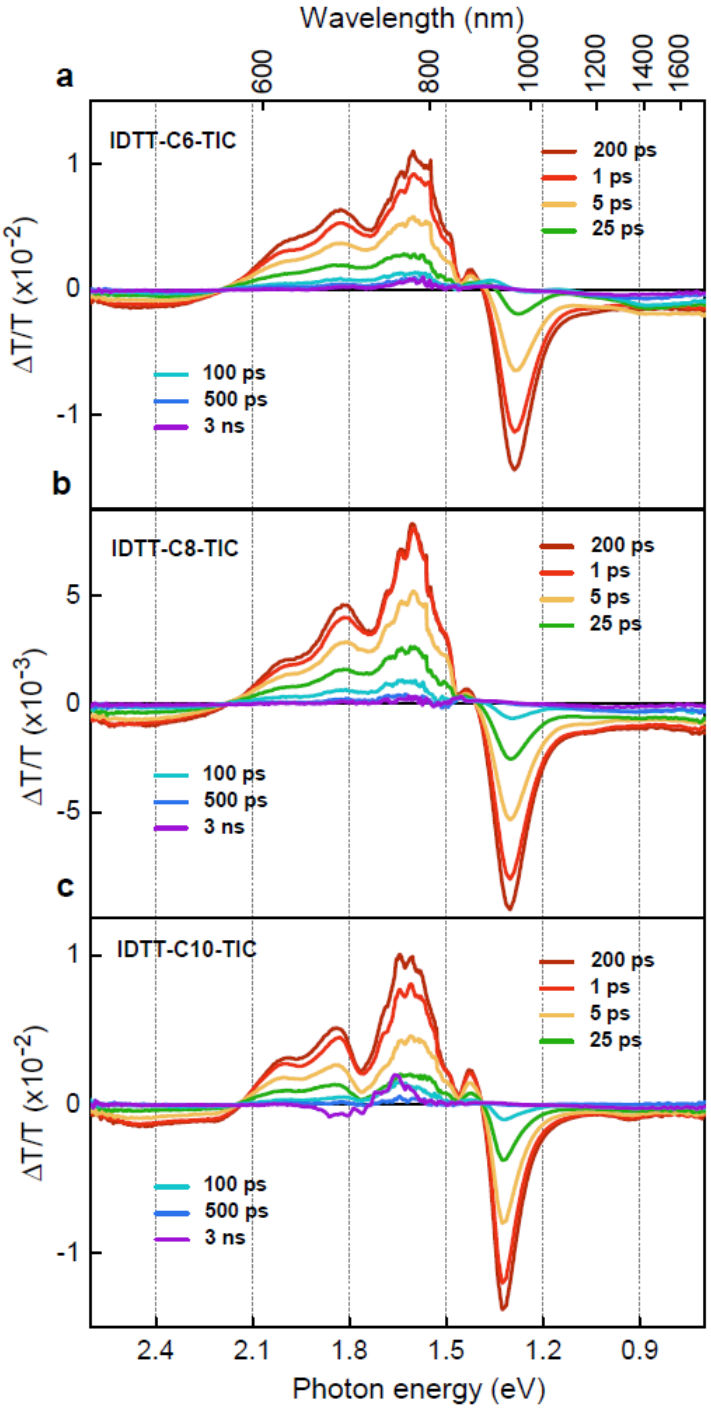

Figure A.18: Series of transient absorption spectra of pristine films, (a) IDTT-C6-TIC (5.1 μJ/cm^2), (b) IDTT-C8-TIC (4.7 μJ/cm^2), and IDTT-C10-TIC (5.8 μJ/cm^2) at various pump-probe delay times after an excitation at 710 nm.

Chapter 6

GIWAXS measurements of neat films

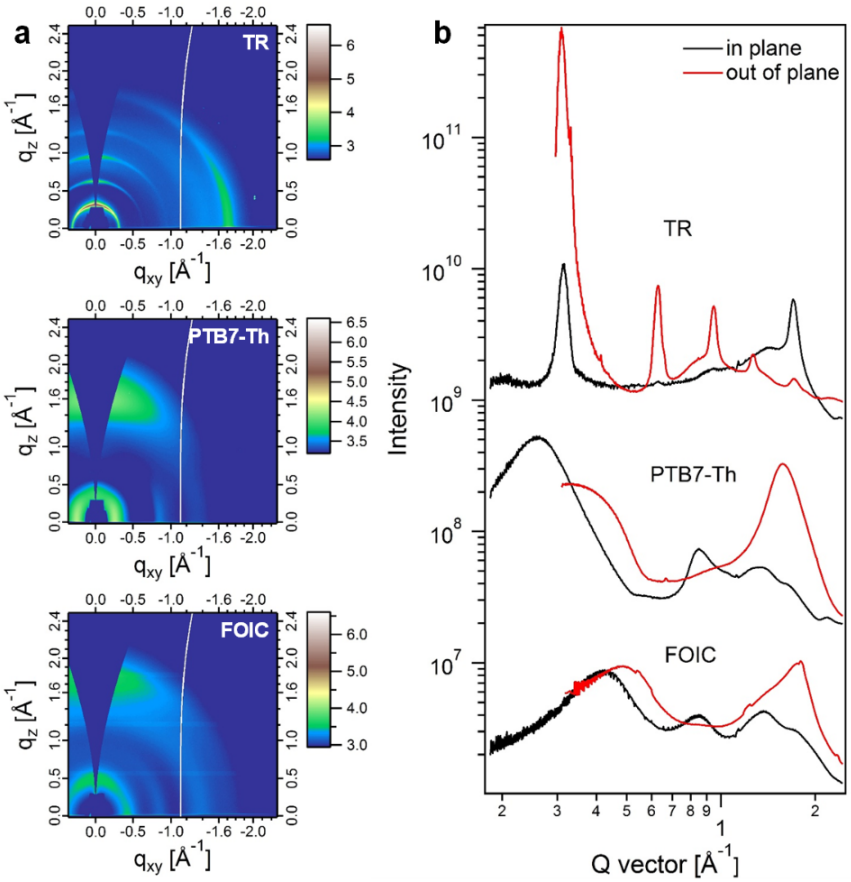

Figure A.19: (a) 2D GIWAXS pattern and (b) 1D line-cuts for TR, PTB7-Th and FOIC neat films. The measurements were performed by Prof. Xiaowei Zhan and students from Peking University, China.

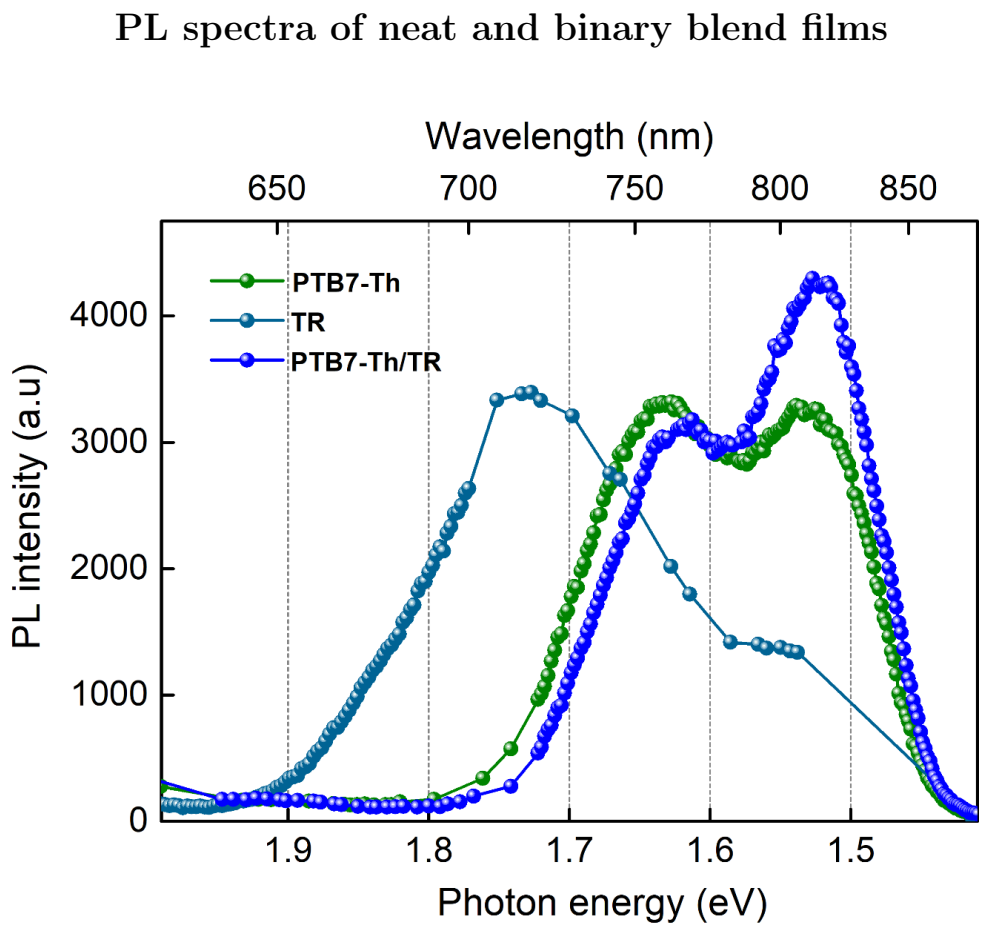

Figure A.20: PL spectra of PTB7-Th, TR neat films and PTB7-Th/TR (0.75:0.25, w/w) blended films (excitation at 600 nm). The measurements were performed by Prof. Xiaowei Zhan and students from Peking University, China.

Spectral overlap of TR emission, PTB7-Th and FOIC absorption

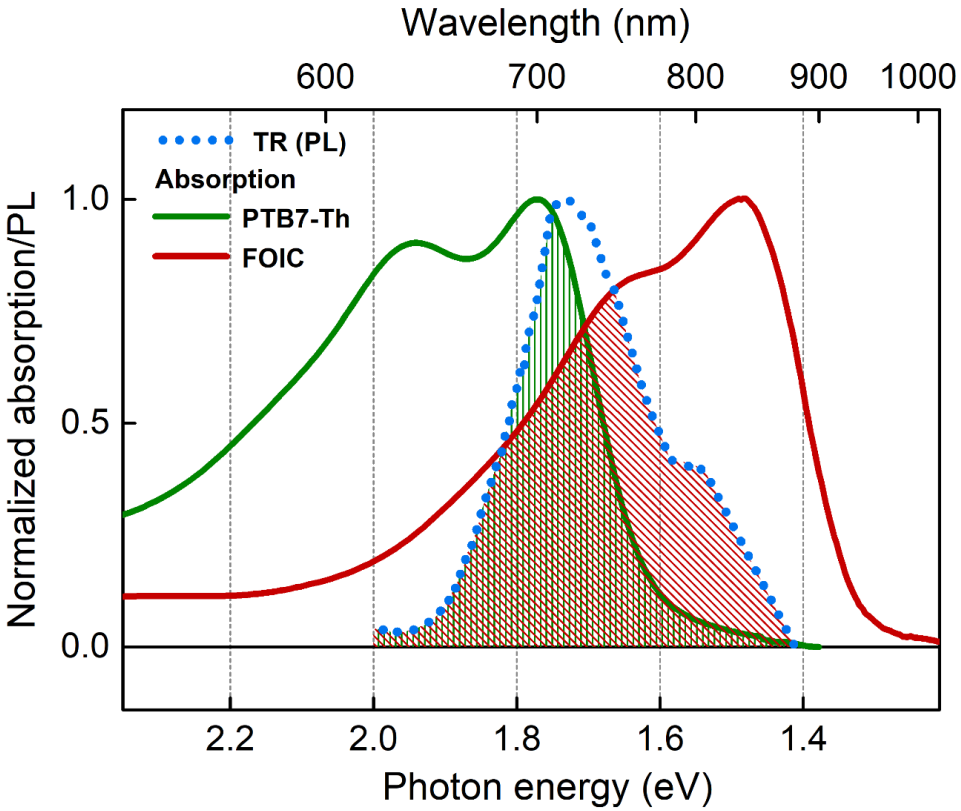

Figure A.21: Steady-state absorption spectra of PTB7-Th and FOIC and PL spectra of TR with the corresponding spectral overlaps highlighted.

TA spectra of ternary and binary blends at 800 nm

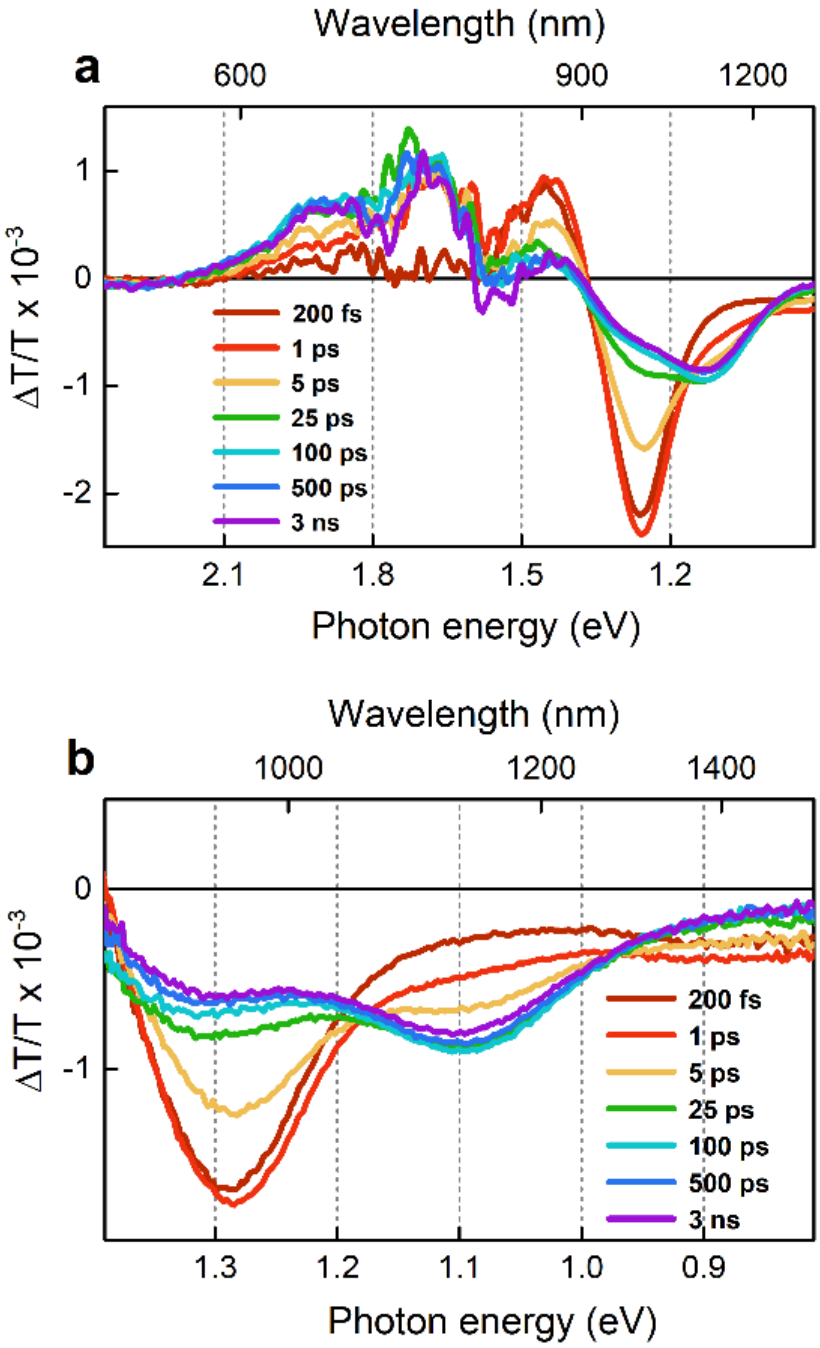

Figure A.22: Series of transient absorption spectra for **(a)** a ternary PTB7-Th/TR/FOIC film following excitation at 800 nm (0.7 μJ/cm^2), and a binary PTB7-Th/FOIC film following an excitation at 800 nm (0.6 μJ/cm^2). Data in the visible region is poor quality for the ternary blend, and absent in the binary blend, due to low transmission of the probe beam.

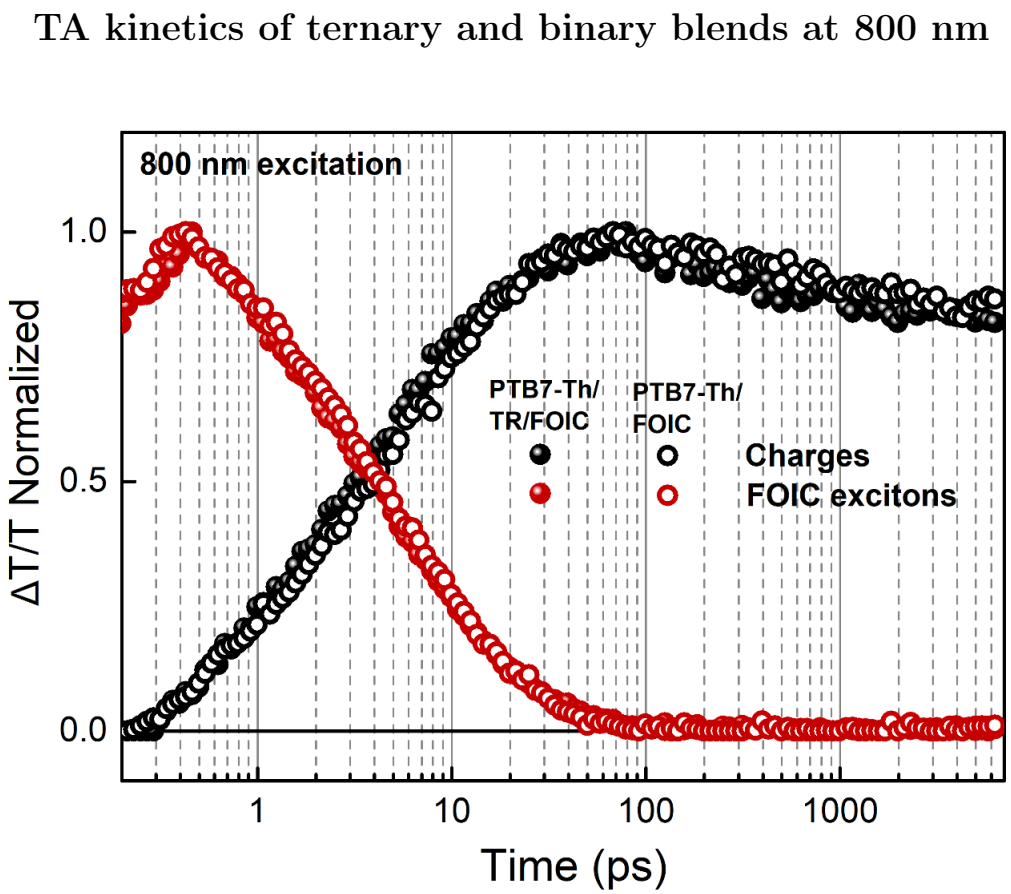

Figure A.23: Transient absorption kinetics of excitons and charges in the ternary (PTB7-Th/TR/FOIC) and the binary (PTBh-Th/FOIC) blends, excited at 800 nm with pump fluences of 0.7 μJ/cm^2 and 0.6 μJ/cm^2, respectively.

Bibliography

[1] V. Abramavic, D. A. Vithanage, and A. Deviz. Visualizing charge separation in bulk heterojunction organic solar cells. *Nature communications*, 4(2334), 2013.

[2] N.-f. Acceptors, J. T. Bloking, T. Giovenzana, A. T. Higgs, A. J. Ponec, and E. T. Hoke. Comparing the Device Physics and Morphology of Polymer Solar Cells Employing Fullerenes and Non-Fullerene Acceptors. *Advanced Energy Materials*, pages 1–12, 2014.

[3] U. Albrecht and B. Heinz. Yield of geminate pair dissociation in an energetically random hopping system. *Chemical Physics Letters*, 4(March), 1995.

[4] K. Anagnostou, M. M. Stylianakis, K. Petridis, and E. Kymakis. Building an organic solar cell: Fundamental procedures for device fabrication. *Energies*, 12(11), 2019.

[5] A. Anctil, C. W. Babbitt, R. P. Raffaelle, and B. J. Landi. Material and energy intensity of fullerene production. *Environmental Science and Technology*, 45(6):2353–2359, 2011.

[6] B. J. E. Anthony, A. Facchetti, M. Heeney, and S. R. Marder. n-Type Organic Semiconductors in Organic Electronics. *Advanced Materials*, pages 3876–3892, 2010.

[7] A. L. Ayzner, C. J. Tassone, S. H. Tolbert, and B. J. Schwartz. Reappraising the need for bulk heterojunctions in polymer-fullerene photovoltaics: The role of carrier transport in all-solution-processed P3HT/PCBM bilayer solar cells. *Journal of Physical Chemistry C*, 113(46):20050–20060, 2009.

[8] H. Bai, Y. Wang, P. Cheng, J. Wang, Y. Wu, J. Hou, and X. Zhan. An electron acceptor based on indacenodithiophene and 1,1-dicyanomethylene-3-indanone for fullerene-free organic solar cells. *Journal of Material Chemistry A*, 3(Scheme 1):1910–1914, 2015.

[9] H. Bai, Y. Wu, Y. Wang, Y. Wu, R. Li, and P. Cheng. Nonfullerene acceptors based on extended fused rings fl anked with benzothiadiazolyl- methylenemalononitrile for polymer solar cells †. *Journal of Materials Chemistry A: Materials for energy and sustainability*, 3:20758–20766, 2015.

[10] N. Banerji. Sub-picosecond delocalization in the excited state of conjugated homopolymers and donor-acceptor copolymers. *Journal of Materials Chemistry C*, 1(18):3052–3066, 2013.

[11] N. Banerji, S. Cowan, E. Vauthey, and A. J. Heeger. Ultrafast relaxation of the poly(3-hexylthiophene) emission spectrum. *Journal of Physical Chemistry C*, 115(19):9726–9739, 2011.

[12] D. Baran, R. S. Ashraf, D. A. Hanifi, M. Abdelsamie, N. Gasparini, J. A. Röhr, S. Holliday, A. Wadsworth, S. Lockett, M. Neophytou, C. J. Emmott, J. Nelson, C. J. Brabec, A. Amassian, A. Salleo, T. Kirchartz, J. R. Durrant, and I. McCulloch. Reducing the efficiency-stability-cost gap of organic photovoltaics with highly efficient and stable small molecule acceptor ternary solar cells. *Nature Materials*, 16(3):363–369, 2017.

[13] D. Baran, T. Kirchartz, S. Wheeler, S. Dimitrov, M. Abdelsamie, J. Gorman, R. S. Ashraf, S. Holliday, A. Wadsworth, N. Gasparini, P. Kaienburg, H. Yan, A. Amassian, C. J. Brabec, J. R. Durrant, and I. Mcculloch. Reduced voltage losses yield 10solar cells with >1 V open circuit voltages. *Energy and Environmental Science*, pages 3783–3793, 2016.

[14] H. Benten, T. Nishida, D. Mori, H. Xu, H. Ohkita, and S. Ito. High-performance ternary blend all-polymer solar cells with complementary absorption bands from visible to near-infrared wavelengths. *Energy and Environmental Science*, 9(1):135–140, 2016.

[15] T. M. Burke and M. D. Mcgehee. How High Local Charge Carrier Mobility and an Energy Cascade in a Three-Phase Bulk Heterojunction Enable > 90% Quantum Efficiency. *Advanced Materials*, pages 1923–1928, 2014.

[16] Y. Cai, L. Huo, X. Sun, D. Wei, M. Tang, and Y. Sun. High performance organic solar cells based on a twisted bay-substituted tetraphenyl functionalized perylenediimide electron acceptor. *Advanced Energy Materials*, 5(11):1–5, 2015.

[17] H. Cha, J. Wu, A. Wadsworth, J. Nagitta, S. Limbu, S. Pont, Z. Li, J. Searle, M. F. Wyatt, D. Baran, J.-s. Kim, I. Mcculloch, and J. R. Durrant. An Efficient , " Burn in " Free Organic Solar Cell Employing a Nonfullerene Electron Acceptor. *Advanced Materials*, 1701156:1–8, 2017.

[18] S. Chandrabose, K. Chen, A. J. Barker, J. J. Sutton, S. K. K. Prasad, J. Zhu, J. Zhou, K. C. Gordon, Z. Xie, X. Zhan, and J. M. Hodgkiss. High Exciton Diffusion Coefficients in Fused Ring Electron Acceptor Films. *Journal of the American Chemical Society*, 2019.

[19] C. A. Chatzidimitriou-Dreismann, T. Abdul-Redah, B. Kolaric, and I. Juranic. Physical review letters. *Physical Review Letters*, 84(22):5237, 2000.

[20] K. Chen, A. J. Barker, M. E. Reish, K. C. Gordon, and J. M. Hodgkiss. Broadband ultrafast photoluminescence spectroscopy resolves charge photogeneration via delocalized hot excitons in polymer:Fullerene photovoltaic blends. *Journal of the American Chemical Society*, 135(49):18502–18512, 2013.

[21] K. Chen, J. K. Gallaher, A. J. Barker, and J. M. Hodgkiss. Transient grating photoluminescence spectroscopy: An ultrafast method of gating broadband spectra. *Journal of Physical Chemistry Letters*, 5(10):1732–1737, 2014.

[22] P. Cheng, J. Hou, Y. Li, and X. Zhan. Layer-by-layer solution-processed low-bandgap polymer-PC61BM solar cells with high efficiency. *Advanced Energy Materials*, 4(9):1–7, 2014.

[23] P. Cheng, G. Li, X. Zhan, and Y. Yang. Next-generation organic photovoltaics based on non-fullerene acceptors. *Nature Photonics*, 12(March), 2018.

[24] D. Chirvase, Z. Chiguvare, M. Knipper, J. Parisi, V. Dyakonov, and J. C. Hummelen. Temperature dependent characteristics of poly(3 hexylthiophene)-fullerene based heterojunction organic solar cells. *Journal of Applied Physics*, 93(6):3376–3383, 2003.

[25] D. Chirvase, Z. Chiguvare, M. Knipper, J. Parisi, V. Dyakonov, and J. C. Hummelen. Temperature dependent characteristics of poly(3 hexylthiophene)-fullerene based heterojunction organic solar cells. *Journal of Applied Physics*, 93(6):3376–3383, 2003.

[26] A. G. Ciriolo, M. Negro, M. Devetta, E. Cinquanta, D. Faccialà, A. Pusala, S. De Silvestri, S. Stagira, and C. Vozzi. Optical parametric amplification techniques for the generation of high-energy few-optical-cycles IR pulses for strong field applications. *Applied Sciences (Switzerland)*, 7(3), 2017.

[27] B. A. Collins, E. Gann, L. Guignard, X. He, C. R. McNeill, and H. Ade. Molecular miscibility of polymer-fullerene blends. *Journal of Physical Chemistry Letters*, 1(21):3160–3166, 2010.

[28] S. Cook, H. Liyuan, A. Furube, and R. Katoh. Singlet Annihilation in Films of Regioregular Poly (3-hexylthiophene): Estimates for Singlet Diffusion Lengths and the Correlation between Singlet Annihilation Rates and Spectral Relaxation. *Journal of Physical Chemistry C*, pages 10962–10968, 2010.

[29] C. Cui, X. Guo, J. Min, B. Guo, X. Cheng, M. Zhang, C. J. Brabec, and Y. Li. High-Performance Organic Solar Cells Based on a Small Molecule with Alkylthio-Thienyl-Conjugated Side Chains without Extra Treatments. *Advanced Materials*, 27(45):7469–7475, 2015.

[30] Y. Cui, S. Zhang, N. Liang, J. Kong, C. Yang, H. Yao, L. Ma, and J. Hou. Toward Efficient Polymer Solar Cells Processed by a Solution-Processed Layer-By-Layer Approach. *Advanced Materials*, 30(34):1802499, 2018.

[31] S. Dai, T. Li, W. Wang, Y. Xiao, T.-k. Lau, Z. Li, K. Liu, X. Lu, and X. Zhan. Enhancing the Performance of Polymer Solar Cells via Core Engineering of NIR-Absorbing Electron Acceptors. *Advanced Materials*, 1706571:1–8, 2018.

[32] S. Dai, F. Zhao, Q. Zhang, T.-k. Lau, T. Li, K. Liu, and Q. Ling. Fused Nonacyclic Electron Acceptors for E ffi cient Polymer Solar Cells. *Journal of the American Chemical Society*, 2017.

[33] G. D'Avino, S. Mothy, L. Muccioli, C. Zannoni, L. Wang, J. Cornil, D. Beljonne, and F. Castet. Energetics of electron-hole separation at P3HT/PCBM heterojunctions. *Journal of Physical Chemistry C*, 117(25):12981–12990, 2013.

[34] A. De Juan, J. Jaumot, and R. Tauler. Multivariate Curve Resolution (MCR). Solving the mixture analysis problem. *Analytical Methods*, 6(14):4964–4976, 2014.

[35] A. De Juan, M. Maeder, M. Martínez, and R. Tauler. Combining hard- and soft-modelling to solve kinetic problems. *Chemometrics and Intelligent Laboratory Systems*, 54(2):123–141, 2000.

[36] J. C. De Mello, H. F. Wittmann, and R. H. Friend. An improved experimental determination of external photoluminescence quantum efficiency. *Advanced Materials*, 9(3):230–232, 1997.

[37] C. Deibe, T. Strobe, and V. Dyakonov. Role of the charge transfer state in organic donor-acceptor solar cells. *Advanced Materials*, 22(37):4097–4111, 2010.

[38] C. Deibel and V. Dyakonov. Polymer – fullerene bulk heterojunction solar cells. *Reports in Progress in Physics*, 2010.

[39] S. Dong, K. Zhang, B. Xie, J. Xiao, H. L. Yip, H. Yan, F. Huang, and Y. Cao. High-Performance Large-Area Organic Solar Cells Enabled by Sequential Bilayer Processing via Nonhalogenated Solvents. *Advanced Energy Materials*, 9(1):1–7, 2019.

[40] T. Drori, C. Sheng, A. Ndobe, S. Singh, J. Holt, and Z. V. Vardeny. Below-Gap Excitation of -Conjugated Polymer-Fullerene Blends : Implications for Bulk Organic Heterojunction Solar Cells. *Phyical Review Letters*, 037401(July):1–4, 2008.

[41] A. Dubietis, G. Tamošauskas, R. Šuminas, V. Jukna, and A. Couairon. Ultrafast supercontinuum generation in bulk condensed media. *Lithuanian Journal of Physics*, 57(3), 2017.

[42] N. D. Eisenmenger, K. T. Delaney, V. Ganesan, G. H. Fredrickson, and M. L. Chabinyc. Energy Transfer Directly to Bilayer Interfaces to Improve Exciton Collection in Organic Photovoltaics. *Journal of Physical Chemistry C*, 2015.

[43] E. Engel, K. Leo, and M. Hoffmann. Ultrafast relaxation and exciton-exciton annihilation in PTCDA thin films at high excitation densities. *Chemical Physics*, 325(October 2005):170–177, 2006.

[44] T. Erb, U. Zhokhavets, G. Gobsch, S. Raleva, B. Stühn, P. Schilinsky, C. Waldauf, and C. J. Brabec. Correlation between structural and optical properties of composite polymer/fullerene films for organic solar cells. *Advanced Functional Materials*, 2005.

[45] B. Fan, D. Zhang, M. Li, W. Zhong, Z. Zeng, L. Ying, F. Huang, and Y. Cao. Achieving over 16% efficiency for single-junction organic solar cells. *Science China Chemistry*, 62(6):746–752, 2019.

[46] B. Fan, W. Zhong, X. F. Jiang, Q. Yin, L. Ying, F. Huang, and Y. Cao. Improved Performance of Ternary Polymer Solar Cells Based on A Nonfullerene Electron Cascade Acceptor. *Advanced Energy Materials*, 7(11), 2017.

[47] R. H. Friend, M. Phillips, A. Rao, M. W. B. Wilson, Z. Li, and C. R. Mcneill. Excitons and charges at organic semiconductor heterojunctions. *Faraday Discuss*, pages 339–348, 2012.

[48] J. K. Gallaher, K. Chen, G. S. Huff, S. K. Prasad, K. C. Gordon, and J. M. Hodgkiss. Evolution of Nonmirror Image Fluorescence Spectra in Conjugated Polymers and Oligomers. *Journal of Physical Chemistry Letters*, 7(17):3307–3312, 2016.

[49] R. Ganesamoorthy, G. Sathiyan, and P. Sakthivel. Solar Energy Materials & Solar Cells Review : Fullerene based acceptors for e ffi cient bulk heterojunction organic solar cell applications. *Solar Energy Materials and Solar Cells*, 161(August 2016):102–148, 2017.

[50] F. Gao and O. Inganäs. Charge generation in polymer-fullerene bulk-heterojunction solar cells. *Physical Chemistry Chemical Physics*, 16(38):20291–20304, 2014.

[51] F. Gao, W. Ma, G. Yang, B. Gautam, O. Inganäs, F. Zhang, H. Yan, S. Chen, J. Liu, H. Ade, K. Gundogdu, J. Bergqvist, J. Zhao, and D. Qian. Fast charge separation in a non-fullerene organic solar cell with a small driving force. *Nature Energy*, 1(7):1–7, 2016.

[52] L. Gao, Z.-g. Zhang, H. Bin, L. Xue, Y. Yang, C. Wang, F. Liu, T. P. Russell, and Y. Li. High-Effi ciency Nonfullerene Polymer Solar Cells with Medium Bandgap Polymer Donor and Narrow Bandgap Organic Semiconductor Acceptor. *Advanced Materials*, pages 8288–8295, 2016.

[53] N. Gasparini. The role of the third component in ternary organic solar cells. *Nature Reviews Materials*, 2019.

[54] N. Gasparini, X. Jiao, T. Heumueller, D. Baran, G. J. Matt, S. Fladischer, E. Spiecker, H. Ade, C. J. Brabec, and T. Ameri. Designing ternary blend bulk heterojunction solar cells with reduced carrier recombination and a fill factor of 77%. *Nature Energy*, 1(9):1–9, 2016.

[55] N. Gasparini, M. Salvador, S. Strohm, T. Heumueller, I. Levchuk, A. Wadsworth, J. H. Bannock, J. C. D. Mello, H.-j. Egelhaaf, D. Baran, I. Mcculloch, and C. J. Brabec. Burn-in Free Nonfullerene-Based Organic Solar Cells. *Advanced energy Materials*, 1700770:1–7, 2017.

[56] B. R. Gautam, R. Younts, J. Carpenter, H. Ade, and K. Gundogdu. The Role of FRET in Non-Fullerene Organic Solar Cells: Implications for Molecular Design. *Journal of Physical Chemistry A*, 122(15):3764–3771, 2018.

[57] H. H. P. Gommans, M. Kemerink, J. M. Kramer, and R. A. J. Janssen. Field and temperature dependence of the photocurrent in polymer / fullerene bulk heterojunction solar cells. *Applied Physics Letters*, 122104(August 2005):1–4, 2012.

[58] G. Grancini, M. Maiuri, D. Fazzi, A. Petrozza, H.-j. Egelhaaf, D. Brida, G. Cerullo, and G. Lanzani. Hot exciton dissociation in polymer solar cells. *Nature Materials*, 12(1):29–33, 2012.

[59] M. Granström, K. Petritsch, A. C. Arias, A. Lux, M. R. Andersson, and R. H. Friend. Laminated fabrication of polymeric photovoltaic diodes. *Nature*, 395(6699):257–260, 1998.

[60] B. A. Gregg, J. Sprague, and M. W. Peterson. Long-Range Singlet Energy Transfer in Perylene Bis(phenethylimide) Films. *Journal of Physical Chemistry B*, 5647(97):5362–5369, 1997.

[61] V. Gulbinas, I. Minevičiūtė, D. Hertel, R. Wellander, A. Yartsev, and V. Sundström. Exciton diffusion and relaxation in methyl-substituted polyparaphenylene polymer films. *The Journal of Chemical Physics*, 144907(2007), 2014.

[62] V. Gupta, V. Bharti, M. Kumar, S. Chand, and A. J. Heeger. Polymer-Polymer Förster Resonance Energy Transfer Significantly Boosts the Power Conversion Efficiency of Bulk-Heterojunction Solar Cells. *Advanced Materials*, 27(30):4398–4404, 2015.

[63] M. Hallermann, S. Haneder, and E. Da Como. Charge-transfer states in conjugated polymer/fullerene blends: Below-gap weakly bound excitons for polymer photovoltaics. *Applied Physics Letters*, 93(5):2006–2009, 2008.

[64] G. Han, Y. Guo, X. Song, Y. Wang, and Y. Yi. Terminal – stacking determines three-dimensional molecular packing and isotropic charge transport in an A—A electron acceptor for non-fullerene organic solar cells. *Journal of Material Chemistry C*, pages 4852–4857, 2017.

[65] A. Haugeneder, M. Neges, C. Kallinger, W. Spirkl, U. Lemmer, and J. Feldmann. Exciton diffusion and dissociation in conjugated polymer / fullerene blends and heterostructures. *Physical Review B*, 59(23):346–351, 1999.

[66] D. R. Haynes, A. Tokmakoff, and S. M. George. Distance dependence of electronic energy transfer between donor and acceptor adlayers: p-terphenyl and 9,10-diphenylanthracene. *The Journal of Chemical Physics*, 100(3):1968–1980, 1994.

[67] G. J. Hedley, A. J. Ward, A. Alekseev, C. T. Howells, E. R. Martins, L. A. Serrano, G. Cooke, A. Ruseckas, and I. D. W. Samuel. Determining the optimum morphology in high-performance polymer-fullerene organic photovoltaic cells. *Nature Communications*, 4:1–10, 2013.

[68] M. Heeney, J. Durrant, I. McCulloch, Z. Fei, C. Nielsen, H. Bronstein, S. Dimitrov, and B. Schroeder. Singlet Exciton Lifetimes in Conjugated Polymer Films for Organic Solar Cells. *Polymers*, 8(1):14, 2016.

[69] A. D. Hendsbee, J. P. Sun, W. K. Law, H. Yan, I. G. Hill, D. M. Spasyuk, and G. C. Welch. Synthesis, self-assembly, and solar cell performance of N-annulated perylene diimide non-fullerene acceptors. *Chemistry of Materials*, 28(19):7098–7109, 2016.

[70] M. Herz, C. Daniel, C. Silva, M. Hoeben, H. J. Schenning, W. Meijer, H. Friend, and T. Phillips. Fast exciton diffusion in chiral stacks of conjugated p-phenylene vinylene oligomers. *Physical Review B - Condensed Matter and Materials Physics*, 68(4):1–7, 2003.

[71] E. T. Hoke, M. T. Lloyd, I. Kauvar, W. R. Mateker, A. M. Nardes, C. H. Peters, N. Kopidakis, and M. D. Mcgehee. The Role of Electron Affi nity in Determining

Whether Fullerenes Catalyze or Inhibit Photooxidation of Polymers for Solar Cells. *Advanced Energy Materials*, pages 1351–1357, 2012.

[72] S. Holliday, R. S. Ashraf, A. Wadsworth, D. Baran, S. A. Yousaf, C. B. Nielsen, C.-h. Tan, S. D. Dimitrov, Z. Shang, N. Gasparini, C. J. Brabec, A. Salleo, J. R. Durrant, I. Mcculloch, and M. Alamoudi. Hi efficiency and air stable p3ht based polymer solar cells with a new non-fullerene acceptor. *Nature communications*, pages 1–11, 2016.

[73] H. Hoppe, M. Niggemann, C. Winder, J. Kraut, R. Hiesgen, A. Hinsch, D. Meissner, and N. S. Sariciftci. Nanoscale morphology of conjugated polymer/fullerene-based bulk-heterojunction solar cells. *Advanced Functional Materials*, 14(10):1005–1011, 2004.

[74] I. A. Howard, H. Mangold, F. Etzold, D. Gehrig, and F. Laquai. Transient absorption data analysis by soft-modelling. *Ultrafast Dynamics in Molecules, Nanostructures and Interfaces*, pages 53–78, 2013.

[75] W. Huang, P. Cheng, Y. M. Yang, G. Li, and Y. Yang. High-Performance Organic Bulk-Heterojunction Solar Cells Based on Multiple-Donor or Multiple-Acceptor Components. *Advanced Materials*, 30(8):1–24, 2018.

[76] S. Inal, M. Schubert, A. Sellinger, and D. Neher. The relationship between the electric field-induced dissociation of charge transfer excitons and the photocurrent in small molecular/polymeric solar cells. *Journal of Physical Chemistry Letters*, 1(6):982–986, 2010.

[77] A. C. Jakowetz, M. L. Böhm, A. Sadhanala, S. Huettner, A. Rao, and R. H. Friend. Visualizing excitations at buried heterojunctions in organic semiconductor blends. *Nature Materials*, 16(5):551–557, 2017.

[78] J. Jaumot, R. Gargallo, A. De Juan, and R. Tauler. A graphical user-friendly interface for MCR-ALS: A new tool for multivariate curve resolution in MATLAB. *Chemometrics and Intelligent Laboratory Systems*, 76(1):101–110, 2005.

[79] J. Kalowekamo and E. Baker. Estimating the manufacturing cost of purely organic solar cells. *Solar Energy*, 83(8):1224–1231, 2009.

[80] V. Kamm, G. Battagliarin, I. A. Howard, W. Pisula, A. Mavrinskiy, and C. Li. Polythiophene : Perylene Diimide Solar Cells – the Impact of Alkyl-Substitution

on the Photovoltaic Performance. *Advanced Energy Materials*, pages 297–302, 2011.

[81] I. Kassal, J. Yuen-zhou, and S. Rahimi-keshari. Does Coherence Enhance Transport in Photosynthesis? *The Journal of Physical Chemistry Letters*, 2013.

[82] E. A. Katz, D. Faiman, S. M. Tuladhar, J. M. Kroon, M. M. Wienk, T. Fromherz, F. Padinger, C. J. Brabec, and N. S. Sariciftci. Temperature dependence for the photovoltaic device parameters of polymer-fullerene solar cells under operating conditions. *Journal of Applied Physics*, 90(10):5343–5350, 2001.

[83] M. Kemerink, J. M. Kramer, H. H. Gommans, and R. A. Janssen. Temperature-dependent built-in potential in organic semiconductor devices. *Applied Physics Letters*, 88(19):86–89, 2006.

[84] I. S. Kim, B. U. Sohn, S. I. Hwang, C. L. Lee, and D. K. Ko. Chirp-independent time-resolved spectroscopy using the self-reference method. *Laser Physics*, 24(4), 2014.

[85] B. Kippelen and J.-L. Brédas. Organic photovoltaics. *Energy and Environmental Science*, 2:241–332, 2009.

[86] Knowledge at FiberOptic.com. Chromatic Dispersion. 9114, 2017.

[87] K. E. Knowles, M. D. Koch, J. L. Shelton, and K. E. Knowles. Three applications of ultrafast transient absorption spectroscopy of semiconductor thin films: spectroelectrochemistry, microscopy, and identification of thermal contributions. *Journal of Material Chemistry C*, pages 11853–11867, 2018.

[88] S. Ko, D. H. Kim, A. L. Ayzner, S. C. Mannsfeld, E. Verploegen, A. M. Nardes, N. Kopidakis, M. F. Toney, and Z. Bao. Thermotropic phase transition of benzodithiophene copolymer thin films and its impact on electrical and photovoltaic characteristics. *Chemistry of Materials*, 27(4):1223–1232, 2015.

[89] A. Köhler. Electronic Processes in Organic Semiconductors. (i), 2015.

[90] L. J. Koster, V. D. Mihailetchi, and P. W. Blom. Bimolecular recombination in polymer/fullerene bulk heterojunction solar cells. *Applied Physics Letters*, 88(5):1–3, 2006.

[91] L. J. Koster, E. C. Smits, V. D. Mihailetchi, and P. W. Blom. Device model for the operation of polymer/fullerene bulk heterojunction solar cells. *Physical Review B - Condensed Matter and Materials Physics*, 72(8):1–9, 2005.

[92] O. K. Kwon, M. A. Uddin, J.-H. Park, S. K. Park, T. L. Nguyen, H. Y. Woo, and S. Y. Park. A High Efficiency Nonfullerene Organic Solar Cell with Optimized Crystalline Organizations. *Advanced Materials*, 28(5):910–916, 2016.

[93] J. R. Lakowicz. *Principles of Fluorescence Spectroscopy*.

[94] K. H. Lee, P. E. Schwenn, A. R. Smith, H. Cavaye, P. E. Shaw, M. James, K. B. Krueger, I. R. Gentle, P. Meredith, and P. L. Burn. Morphology of all-solution-processed "bilayer" organic solar cells. *Advanced Materials*, 2011.

[95] A. J. Lewis, A. Ruseckas, O. P. M. Gaudin, and G. R. Webster. Singlet exciton diffusion in MEH-PPV films studied by exciton – exciton annihilation. *Organic Electronics*, 7:452–456, 2006.

[96] K. Li, Y. Wu, Y. Tang, M.-A. Pan, W. Ma, H. Fu, C. Zhan, and J. Yao. Ternary Blended Fullerene-Free Polymer Solar Cells with 16.5% Efficiency Enabled with a Higher-LUMO-Level Acceptor to Improve Film Morphology. *Advanced Energy Materials*, 0(0):1901728, 2019.

[97] N. Li, J. D. Perea, T. Kassar, M. Richter, T. Heumueller, G. J. Matt, Y. Hou, N. S. Güldal, H. Chen, S. Chen, S. Langner, M. Berlinghof, T. Unruh, and C. J. Brabec. Abnormal strong burn-in degradation of highly efficient polymer solar cells caused by spinodal donor-acceptor demixing. *Nature Communications*, 8:1–9, 2017.

[98] T. Li, K. Chen, J. Xin, J. M. Hodgkiss, W. Ma, S. Chandrabose, P. Xue, S. Dai, K. Zhou, X. Zhan, and K. Liu. High-performance organic solar cells based on polymer donor/small molecule donor/nonfullerene acceptor ternary blends. *Journal of Materials Chemistry A*, 7(5):2268–2274, 2019.

[99] T. Li, S. Dai, Z. Ke, L. Yang, J. Wang, C. Yan, and W. Ma. Fused Tris (thienothiophene) -Based Electron Acceptor with Strong Near-Infrared Absorption for High-Performance As-Cast Solar Cells. *Advanced Materials*, 1705969:1–7, 2018.

[100] N. Liang, W. Jiang, and Z. Wang. New developments in non-fullerene small molecule acceptors for polymer solar cells. *Material Chemistry Frontiers*, pages 1291–1303, 2017.

[101] S. H. Liao, H. J. Jhuo, Y. S. Cheng, and S. A. Chen. Fullerene derivative-doped zinc oxide nanofilm as the cathode of inverted polymer solar cells with low-bandgap polymer (PTB7-Th) for high performance. *Advanced Materials*, 25(34):4766–4771, 2013.

[102] H. Lin, S. Chen, Z. Li, J. Yuk, L. Lai, G. Yang, T. Mcafee, K. Jiang, Y. Li, Y. Liu, H. Hu, J. Zhao, W. Ma, H. Ade, and H. Yan. High-Performance Non-Fullerene Polymer Solar Cells Based on a Pair of Donor – Acceptor Materials with Complementary Absorption Properties. *Advanced Materials*, pages 7299–7304, 2015.

[103] J. D. A. Lin, O. V. Mikhnenko, J. Chen, Z. Masri, A. Ruseckas, A. Mikhailovsky, R. P. Raab, J. Liu, P. W. M. Blom, M. A. Loi, C. J. García-Cervera, I. D. W. Samuel, and T.-Q. Nguyen. Systematic study of exciton diffusion length in organic semiconductors by six experimental methods. *Mater. Horiz.*, 1(2):280–285, 2014.

[104] Y. Lin, Q. He, F. Zhao, L. Huo, J. Mai, X. Lu, C.-j. Su, T. Li, J. Wang, J. Zhu, Y. Sun, C. Wang, and X. Zhan. A Facile Planar Fused-Ring Electron Acceptor for As-Cast Polymer Solar Cells with 8.71 *Journal of the American Chemical Society*, pages 10–13, 2016.

[105] Y. Lin, Q. He, F. Zhao, L. Huo, J. Mai, X. Lu, C. J. Su, T. Li, J. Wang, J. Zhu, Y. Sun, C. Wang, and X. Zhan. A Facile Planar Fused-Ring Electron Acceptor for As-Cast Polymer Solar Cells with 8.71% Efficiency. *Journal of the American Chemical Society*, 138(9):2973–2976, 2016.

[106] Y. Lin, T. Li, F. Zhao, L. Han, Z. Wang, Y. Wu, Q. He, and J. Wang. Structure Evolution of Oligomer Fused-Ring Electron Acceptors toward High Effi ciency of As-Cast Polymer Solar Cells. *Advanced Energy Materials*, pages 1–9, 2016.

[107] Y. Lin, Y. Li, and X. Zhan. Small molecule semiconductors for high-efficiency organic photovoltaics. *Chemical Society Reviews*, 41(11):4245–4272, 2012.

[108] Y. Lin, J. Wang, Z.-g. Zhang, H. Bai, Y. Li, and D. Zhu. An Electron Acceptor Challenging Fullerenes for Effi cient Polymer Solar Cells. *Advanced Materials*, pages 1170–1174, 2015.

[109] Y. Lin, F. Zhao, Q. He, L. Huo, Y. Wu, T. C. Parker, W. Ma, Y. Sun, C. Wang, D. Zhu, A. J. Heeger, S. R. Marder, and X. Zhan. High-Performance Electron Acceptor with Thienyl Side Chains for Organic Photovoltaics. *Journal of the American Chemical Society*, 2016.

[110] Y. Lin, F. Zhao, S. K. Prasad, J. D. Chen, W. Cai, Q. Zhang, K. Chen, Y. Wu, W. Ma, F. Gao, J. X. Tang, C. Wang, W. You, J. M. Hodgkiss, and X. Zhan. Balanced Partnership between Donor and Acceptor Components in Nonfullerene Organic Solar Cells with >12% Efficiency. *Advanced Materials*, 30(16):1–8, 2018.

[111] Y. Lin, F. Zhao, Y. Wu, K. Chen, Y. Xia, G. Li, S. K. K. Prasad, J. Zhu, L. Huo, H. Bin, Z.-g. Zhang, X. Guo, M. Zhang, Y. Sun, F. Gao, Z. Wei, W. Ma, C. Wang, J. Hodgkiss, Z. Bo, O. Inganäs, Y. Li, and X. Zhan. Mapping Polymer Donors toward High-Efficiency Fullerene Free Organic Solar Cells. *Advanced Materials*, pages 1–9, 2016.

[112] Y. C. Lin, Y. W. Su, J. X. Li, B. H. Lin, C. H. Chen, H. C. Chen, K. H. Wu, Y. Yang, and K. H. Wei. Energy transfer within small molecule/conjugated polymer blends enhances photovoltaic efficiency. *Journal of Materials Chemistry A*, 5(34):18053–18063, 2017.

[113] F. Liu, Y. Gu, X. Shen, S. Ferdous, H. W. Wang, and T. P. Russell. Characterization of the morphology of solution-processed bulk heterojunction organic photovoltaics. *Progress in Polymer Science*, 38(12):1990–2052, 2013.

[114] T. Liu, Y. Guo, Y. Yi, L. Huo, X. Xue, X. Sun, H. Fu, W. Xiong, D. Meng, Z. Wang, F. Liu, T. P. Russell, and Y. Sun. Ternary Organic Solar Cells Based on Two Compatible Nonfullerene Acceptors with Power Conversion Efficiency >10%. *Advanced Materials*, 28(45):10008–10015, 2016.

[115] T. Liu, L. Huo, S. Chandrabose, K. Chen, G. Han, F. Qi, X. Meng, D. Xie, W. Ma, Y. Yi, J. M. Hodgkiss, F. Liu, J. Wang, C. Yang, and Y. Sun. Optimized Fibril Network Morphology by Precise Side-Chain Engineering to Achieve High-Performance Bulk-Heterojunction Organic Solar Cells. *Advanced Materials*, 30(26):1–8, 2018.

[116] X. Liu, Y. Yan, A. Honarfar, Y. Yao, K. Zheng, and Z. Liang. Unveiling Excitonic Dynamics in High-Efficiency Nonfullerene Organic Solar Cells to Direct Morphological Optimization for Suppressing Charge Recombination. *Advanced Science*, 6(8), 2019.

[117] Y. Liu, C.-c. Chen, Z. Hong, J. Gao, H. Zhou, L. Dou, G. Li, and Y. Yang. Solution-processed small-molecule solar cells: breaking the 10% power conversion efficiency. *Scientific Reports*, 2013.

[118] M. Lorenc, M. Ziolek, R. Naskrecki, J. Karolczak, J. Kubicki, and A. Maciejewski. Artifacts in femtosecond transient absorption spectroscopy. *Applied Physics B: Lasers and Optics*, 74(1):19–27, 2002.

[119] W. A. Luhman and R. J. Holmes. Investigation of energy transfer in organic photovoltaic cells and impact on exciton diffusion length measurements. *Advanced Functional Materials*, 21(4):764–771, 2011.

[120] R. R. Lunt, J. B. Benziger, and S. R. Forrest. Relationship between crystalline order and exciton diffusion length in molecular organic semiconductors. *Advanced Materials*, 22(11):1233–1236, 2010.

[121] R. R. Lunt, N. C. Giebink, A. A. Belak, J. B. Benziger, and S. R. Forrest. Exciton diffusion lengths of organic semiconductor thin films measured by spectrally resolved photoluminescence quenching. *Journal of Applied Physics*, 105(5):1–7, 2009.

[122] R. Ma, T. Liu, Z. Luo, K. Gao, K. Chen, G. Zhang, W. Gao, T.-k. Lau, Q. Fan, Y. Chen, L.-k. Ma, and H. Sun. Adding a third component with reduced miscibility and higher LUMO level enables efficient ternary organic solar cells. *ACS Energy Letters*, 2020.

[123] J. H. Marburger. Self-focusing: Theory. *IQEC, International Quantum Electronics Conference Proceedings*, 2005:1593, 2005.

[124] H. Marciniak, X.-q. Li, W. Frank, and S. Lochbrunner. One-Dimensional Exciton Diffusion in Perylene Bisimide Aggregates. *Journal of Physical Chemistry A*, pages 648–654, 2011.

[125] C. M. Marian. Spin-orbit coupling and intersystem crossing in molecules. *Wiley Interdisciplinary Reviews: Computational Molecular Science*, 2(2):187–203, 2012.

[126] D. E. Markov, C. Tanase, P. W. M. Blom, and J. Wildeman. Simultaneous enhancement of charge transport and exciton diffusion in poly (p -phenylene vinylene) derivatives. *Physical Review B*, pages 1–6, 2005.

[127] B. R. A. Marsh, J. M. Hodgkiss, and R. H. Friend. Direct Measurement of Electric Field-Assisted Charge Separation in Polymer : Fullerene Photovoltaic Diodes. *Advanced Materials*, 600:3672–3676, 2010.

[128] W. R. Mateker, I. T. Sachs-Quintana, G. F. Burkhard, R. Cheacharoen, and M. D. McGehee. Minimal Long-Term Intrinsic Degradation Observed in a Polymer Solar Cell Illuminated in an Oxygen-Free Environment. *Chemistry of Materials*, 27(2):404–407, 2015.

[129] A. C. Mayer, S. R. Scully, B. E. Hardin, M. W. Rowell, and M. D. McGehee. Polymer-based solar cells. *Materials Today*, 10(11):28–33, 2007.

[130] A. C. Mayer, M. F. Toney, S. R. Scully, J. Rivnay, C. J. Brabec, M. Scharber, M. Koppe, M. Heeney, I. McCulloch, and M. D. McGehee. Bimolecular crystals of fullerenes in conjugated polymers and the implications of molecular mixing for solar cells. *Advanced Functional Materials*, 19(8):1173–1179, 2009.

[131] D. P. Mcmahon, D. L. Cheung, and A. Troisi. Why Holes and Electrons Separate So Well in Polymer / Fullerene photovoltaic cells. *Journal of Physical chemistry Letters*, pages 2737–2741, 2011.

[132] D. Meng, D. Sun, C. Zhong, T. Liu, B. Fan, L. Huo, Y. Li, W. Jiang, H. Choi, T. Kim, J. Y. Kim, Y. Sun, Z. Wang, and A. J. Heeger. High-Performance Solution-Processed Non-Fullerene Organic Solar Cells Based on Selenophene-Containing Perylene Bisimide Acceptor. *Journal of the American Chemical Society*, 138(1):375–380, 2016.

[133] L. Meng, Y. Zhang, X. Wan, C. Li, X. Zhang, Y. Wang, X. Ke, Z. Xiao, L. Ding, R. Xia, H. L. Yip, Y. Cao, and Y. Chen. Organic and solution-processed tandem solar cells with 17.3% efficiency. *Science*, 361(6407):1094–1098, 2018.

[134] S. M. Menke and R. J. Holmes. Exciton diffusion in organic photovoltaic cells. *Energy and Environmental Sciences*, 7(2), 2014.

[135] O. V. Mikhnenko, P. W. M. Blom, and T.-Q. Nguyen. Exciton diffusion in organic semiconductors. *Energy & Environmental Science*, 8(7):1867–1888, 2015.

[136] O. V. Mikhnenko, F. Cordella, A. B. Sieval, J. C. Hummelen, P. W. Blom, and M. A. Loi. Temperature dependence of exciton diffusion in conjugated polymers. *Journal of Physical Chemistry B*, 112(37):11601–11604, 2008.

[137] O. V. Mikhnenko, M. Kuik, J. Lin, N. Van Der Kaap, T. Q. Nguyen, and P. W. Blom. Trap-limited exciton diffusion in organic semiconductors. *Advanced Materials*, 26(12):1912–1917, 2014.

[138] O. V. Mikhnenko, J. Lin, Y. Shu, J. E. Anthony, P. W. Blom, T. Q. Nguyen, and M. A. Loi. Effect of thermal annealing on exciton diffusion in a diketopyrrolopyrrole derivative. *Physical Chemistry Chemical Physics*, 14(41):14196–14201, 2012.

[139] T. D. Nielsen, C. Cruickshank, S. Foged, J. Thorsen, and F. C. Krebs. Solar Energy Materials & Solar Cells Business , market and intellectual property analysis of polymer solar cells. *Solar Energy Materials and Solar Cells*, 94(10):1553–1571, 2010.

[140] H. Ohkita, Y. Tamai, H. Benten, and S. Ito. for Polymer Solar Cells. *IEEE J. Sel. Top. Quantum Electron.*, 22:4100612, 2016.

[141] O. Ostroverkhova. Organic Optoelectronic Materials : Mechanisms and Applications. *Chemical Reviews*, 2016.

[142] Y.-s. Park, J.-j. Kim, and T. Basche. Excitation Energy Transfer in Organic Materials : From Fundamentals to Optoelectronic Devices. *Macromolecular Rapid Communications*, pages 1203–1231, 2009.

[143] C. H. Peters, J. P. Kastrop, S. Beaupre, M. Leclerc, and M. D. Mcgehee. High Efficiency Polymer Solar Cells with Long Operating Lifetimes. *Advanced Energy Materials*, pages 491–494, 2011.

[144] C. H. Peters, W. R. Mateker, T. Heumueller, J. Rivnay, R. Noriega, Z. M. Beiley, E. T. Hoke, A. Salleo, and M. D. Mcgehee. The Mechanism of Burn-in Loss in a High Efficiency Polymer Solar Cell. *Advanced Materials*, pages 663–668, 2012.

[145] R. C. Powell. Singlet exciton energy transfer in organic solids. *Journal of Luminescence*, 11, 1975.

[146] U. M. I. Pugliesi, C. S. C. F. Sailer, and E. Riedle. Sub-50 fs broadband absorption spectroscopy with tunable excitation : putting the analysis of ultrafast molecular dynamics on solid ground. *Applied Physics B*, pages 215–231, 2009.

[147] B. P. Rand, D. P. Burk, and S. R. Forrest. Offset energies at organic semiconductor heterojunctions and their influence on the open-circuit voltage of thin-film solar cells. *Physical Review B - Condensed Matter and Materials Physics*, 75(11):1–11, 2007.

[148] H. W. Ro, J. M. Downing, S. Engmann, A. A. Herzing, D. M. Delongchamp, L. J. Richter, S. Mukherjee, H. Ade, M. Abdelsamie, L. K. Jagadamma, A. Amassian, Y. Liu, and H. Yan. Morphology changes upon scaling a high-efficiency, solution-processed solar cell. *Energy and Environmental Science*, 9(9):2835–2846, 2016.

[149] C. W. Rochester, S. A. Mauger, and A. J. Moulé. Investigating the morphology of polymer/fullerene layers coated using orthogonal solvents. *Journal of Physical Chemistry C*, 116(13):7287–7292, 2012.

[150] C. Ruckebusch, M. Sliwa, P. Pernot, A. de Juan, and R. Tauler. Comprehensive data analysis of femtosecond transient absorption spectra: A review. *Journal of Photochemistry and Photobiology C: Photochemistry Reviews*, 13(1):1–27, 2012.

[151] N. S. Sariciftci, L. Smilowitz, A. J. Heeger, and F. Wudi. Photoinduced Electron Transfer from a Conducting Polymer to Buckminsterfullerene. *Science*, 258(November):27–30, 1992.

[152] M. Scarongella, J. De Jonghe-Risse, E. Buchaca-Domingo, M. Causa, Z. Fei, M. Heeney, J. E. Moser, N. Stingelin, and N. Banerji. A close look at charge generation in polymer: Fullerene blends with microstructure control. *Journal of the American Chemical Society*, 137(8):2908–2918, 2015.

[153] M. C. Scharber and N. S. Sariciftci. Efficiency of bulk-heterojunction organic solar cells. *Progress in Polymer Science*, 38(12):1929–1940, 2013.

[154] S. R. Scully and M. D. McGehee. Effects of optical interference and energy transfer on exciton diffusion length measurements in organic semiconductors. *Journal of Applied Physics*, 100(3), 2006.

[155] P. E. Shaw, A. Ruseckas, J. Peet, G. C. Bazan, and I. D. W. Samuel. Exciton - Exciton annihilation in mixed-phase polyfluorene films. *Advanced Functional Materials*, 20(1):155–161, 2010.

[156] P. E. Shaw, A. Ruseckas, and I. D. W. Samuel. Exciton diffusion measurements in poly(3-hexylthiophene). *Advanced Materials*, 20(18):3516–3520, 2008.

[157] H. Shirakawa, E. J. Louis, A. G. MacDiarmid, C. K. Chiang, and A. J. Heeger. Synthesis of electrically conducting organic polymers: Halogen derivatives of polyacetylene, (CH)x. *Journal of the Chemical Society, Chemical Communications*, (16):578–580, 1977.

[158] C. Silva, D. M. Russell, M. A. Stevens, J. D. Mackenzie, S. Setayesh, K. Mullen, and R. H. Friend. Excited-state absorption in luminescent conjugated polymer thin films : ultrafast studies of processable polyindenofluorene derivatives. *Chemical Physics Letters*, 319(March):494–500, 2000.

[159] M. Sim, J. Shin, C. Shim, M. Kim, S. B. Jo, J.-h. Kim, and K. Cho. Dependence of Exciton Di ff usion Length on Crystalline Order in Conjugated Polymers. *Journal of Physical Chemistry C*, 2014.

[160] M. A. Stevens, C. Silva, D. M. Russell, and R. H. Friend. Exciton dissociation mechanisms in the polymeric semiconductors poly „ 9 , 9-dioctylfluorene ... and poly „ 9 , 9-dioctylfluorene-co-benzothiadiazole .... *Physical Review B*, 63:1–18, 2001.

[161] M. Stolte, F. Wu, and F. Wu. ChemComm Naphthalene and perylene diimides for organic transistors. *Chemical communications*, 47(November 2010):5109–5115, 2011.

[162] Y. Sun, G. C. Welch, W. L. Leong, C. J. Takacs, G. C. Bazan, and A. J. Heeger. Solution-processed small-molecule solar cells with 6.7% efficiency. *Nature Materials*, 11:44, 2011.

[163] S. M. Swick, W. Zhu, M. Matta, T. J. Aldrich, A. Harbuzaru, J. T. L. Navarrete, R. P. Ortiz, K. L. Kohlstedt, G. C. Schatz, A. Facchetti, F. S. Melkonyan, and T. J. Marks. Closely packed, low reorganization energy π-extended postfullerene acceptors for efficient polymer solar cells. *Proceedings of the National Academy of Sciences of the United States of America*, 115(36):E8341–E8348, 2018.

[164] Y. Tamai, Y. Matsuura, H. Ohkita, H. Benten, and S. Ito. One-dimensional singlet exciton diffusion in poly(3-hexylthiophene) crystalline domains. *Journal of Physical Chemistry Letters*, 5(2):399–403, 2014.

[165] Y. Tamai, H. Ohkita, H. Benten, and S. Ito. Exciton Diffusion in Conjugated Polymers: From Fundamental Understanding to Improvement in Photovoltaic Conversion Efficiency. *Journal of Physical Chemistry Letters*, 6(17):3417–3428, 2015.

[166] N. D. Treat, A. Varotto, C. J. Takacs, N. Batara, M. Al-Hashimi, M. J. Heeney, A. J. Heeger, F. Wudl, C. J. Hawker, and M. L. Chabinyc. Polymer-fullerene miscibility: A metric for screening new materials for high-performance organic solar cells. *Journal of the American Chemical Society*, 134(38):15869–15879, 2012.

[167] V. A. Trukhanov and D. Y. Paraschuk. Non-fullerene acceptors for organic solar cells. *Polymer Science - Series C*, 56(1):72–83, 2014.

[168] K. Tvingstedt, K. Vandewal, F. Zhang, and O. Inganäs. On the dissociation efficiency of charge transfer excitons and Frenkel excitons in organic solar cells: A luminescence quenching study. *Journal of Physical Chemistry C*, 114(49):21824–21832, 2010.

[169] D. Veldman, Ö. Ipek, S. C. Meskers, J. Sweelssen, M. M. Koetse, S. C. Veenstra, J. M. Kroon, S. S. Van Bavel, J. Loos, and R. A. Janssen. Compositional and electric field dependence of the dissociation of charge transfer excitons in alternating polyfluorene copolymer/fullerene blends. *Journal of the American Chemical Society*, 130(24):7721–7735, 2008.

[170] T. Virgili, D. Marinotto, C. Manzoni, G. Cerullo, and G. Lanzani. Ultrafast intrachain photoexcitation of polymeric semiconductors. *Physical Review Letters*, 94(11):1–4, 2005.

[171] B. Walker, H. Choi, and J. Y. Kim. Interfacial engineering for highly efficient organic solar cells. *Current Applied Physics*, 17(3):370–391, 2017.

[172] L. Wang, J. Yan, X. Chen, Y. Weng, and S. Zhou. Experimental study on the chirp of the white-light continuum generation in CaF 2 and sapphire. *Nonlinear Optical Phenomena and Applications*, 5646(January 2005):108, 2005.

[173] M. R. Wasielewski. Energy , Charge , and Spin Transport in Molecules and Self-Assembled Nanostructures Inspired by Photosynthesis. *The Journal of Organic Chemistry*, pages 5051–5066, 2006.

[174] L. A. Weinstein, W. C. Hsu, S. Yerci, S. V. Boriskina, and G. Chen. Enhanced absorption of thin-film photovoltaic cells using an optical cavity. *Journal of Optics (United Kingdom)*, 17(5), 2015.

[175] H. Wiesenhofer, D. Beljonne, G. D. Schales, E. Hennebicq, J. L. Brédas, and E. Zojer. Limitations of the förster description of singlet exciton migration: The illustrative example of energy transfer to ketonic defects in ladder-type poly(para-phenylenes). *Advanced Functional Materials*, 15(1):155–160, 2005.

[176] F. Würthner, O. Chemie, U. Würzburg, and A. Hubland. Perylene bisimide dyes as versatile building blocks for functional supramolecular architectures. *Chemical communications*, pages 1564–1579, 2004.

[177] F. Xiao, C. Li, J. Sun, and L. Zhang. Knowledge domain and emerging trends in organic photovoltaic technology: A scientometric review based on citespace analysis. *Frontiers in Chemistry*, 5(Sep):1–12, 2017.

[178] Y. Xiao and X. Lu. Morphology of Organic Photovoltaic Non-Fullerene Acceptors Investigated by Grazing-Incidence X-Ray Scattering Techniques. *Materials Today Nano*, page 100030, 2019.

[179] C. Yan, S. Barlow, Z. Wang, H. Yan, A. K.-Y. Jen, S. R. Marder, and X. Zhan. Non-fullerene acceptors for organic solar cells. *Nature Reviews Materials*, 3(18003), 2018.

[180] C. Yan, S. Dai, L. Yang, W. Ma, X. Zhan, T. Li, J. Wang, and Z. Ke. Fused Tris(thienothiophene)-Based Electron Acceptor with Strong Near-Infrared Absorption for High-Performance As-Cast Solar Cells. *Advanced Materials*, 30(10):1705969, 2018.

[181] C. L. Yang, Z. K. Tang, W. K. Ge, J. N. Wang, Z. L. Zhang, X. Y. Jian, C. L. Yang, Z. K. Tang, W. K. Ge, and J. N. Wang. Exciton diffusion in light-emitting organic thin films studied by photocurrent spectra Exciton diffusion in light-emitting organic thin films studied by photocurrent spectra. *Applied Physics Letters*, 1737(2003), 2009.

[182] L. Yang, L. Yan, and W. You. Organic solar cells beyond one pair of donor-acceptor: Ternary blends and more. *Journal of Physical Chemistry Letters*, 4(11):1802–1810, 2013.

[183] H. Yao, Y. Cui, R. Yu, B. Gao, H. Zhang, and J. Hou. Design, Synthesis, and Photovoltaic Characterization of a Small Molecular Acceptor with an Ultra-Narrow Band Gap. *Angewandte Chemie - International Edition*, 56(11):3045–3049, 2017.

[184] H. Yao, L. Ye, J. Hou, B. Jang, G. Han, Y. Cui, G. M. Su, C. Wang, B. Gao, R. Yu, H. Zhang, Y. Yi, H. Y. Woo, H. Ade, and J. Hou. Achieving Highly Efficient Nonfullerene Organic Solar Cells with Improved Intermolecular Interaction and Open-Circuit Voltage. *Advanced Materials*, 29(21), 2017.

[185] W. You, K. Chen, C. Wang, J.-D. Chen, J.-X. Tang, F. Gao, Y. Wu, Q. Zhang, X. Zhan, W. Cai, S. K. K. Prasad, J. M. Hodgkiss, F. Zhao, Y. Lin, and W. Ma. Balanced Partnership between Donor and Acceptor Components in Nonfullerene Organic Solar Cells with >12% Efficiency. *Advanced Materials*, 30(16):1706363, 2018.

[186] G. Yu, J. Gao, J. C. Hummelen, F. Wudl, and A. J. Heeger. device structure consisted Polymer Photovoltaic Cells : Enhanced Efficiencies via a (Ca The on a g | | g. *Science*, 270:1789–1791, 1995.

[187] R. Yu, H. Yao, and J. Hou. Recent Progress in Ternary Organic Solar Cells Based on Nonfullerene Acceptors. *Advanced Energy Materials*, 8(28):1–9, 2018.

[188] J. Yuan, M. J. Ford, Y. Xu, Y. Zhang, G. C. Bazan, and W. Ma. Improved Tandem All-Polymer Solar Cells Performance by Using Spectrally Matched Subcells. *Advanced Energy Materials*, 8(14):1–8, 2018.

[189] J. Yuan, Y. Zhang, L. Zhou, G. Zhang, H. L. Yip, T. K. Lau, X. Lu, C. Zhu, H. Peng, P. A. Johnson, M. Leclerc, Y. Cao, J. Ulanski, Y. Li, and Y. Zou. Single-Junction Organic Solar Cell with over 15% Efficiency Using Fused-Ring Acceptor with Electron-Deficient Core. *Joule*, 2019.

[190] C. Zhan and A. D. Q. Li. Perylene Diimide : Versatile Building Blocks for Molecular Self-Assemblies , Folding Motifs , and Reaction-Directing Codes. *Current Organic Chemistry*, pages 1314–1339, 2011.

[191] X. Zhan, A. Facchetti, S. Barlow, T. J. Marks, M. A. Ratner, M. R. Wasielewski, and S. R. Marder. Rylene and Related Diimides for Organic Electronics. *Advanced Materials*, pages 268–284, 2011.

[192] X. Zhan, Z. Tan, B. Domercq, Z. An, X. Zhang, S. Barlow, Y. Li, D. Zhu, B. Kippelen, and S. R. Marder. A High-Mobility Electron-Transport Polymer with Broad Absorption and Its Use in Field-Effect Transistors and All-Polymer Solar Cells. *Journal of American Chemical Society*, pages 7246–7247, 2007.

[193] J. Zhang, M. H. Futscher, V. Lami, F. U. Kosasih, C. Cho, Q. Gu, A. Sadhanala, A. J. Pearson, B. Kan, G. Divitini, X. Wan, D. Credgington, N. C. Greenham, Y. Chen, C. Ducati, B. Ehrler, Y. Vaynzof, R. H. Friend, and A. A. Bakulin. Sequentially Deposited versus Conventional Nonfullerene Organic Solar Cells: Interfacial Trap States, Vertical Stratification, and Exciton Dissociation. *Advanced Energy Materials*, 1902145, 2019.

[194] J. Zhang, B. Kan, A. J. Pearson, A. J. Parnell, J. F. Cooper, X. K. Liu, P. J. Conaghan, T. R. Hopper, Y. Wu, X. Wan, F. Gao, N. C. Greenham, A. A. Bakulin, Y. Chen, and R. H. Friend. Efficient non-fullerene organic solar cells employing sequentially deposited donor-acceptor layers. *Journal of Materials Chemistry A*, 6(37):18225–18233, 2018.

[195] J. Zhang, H. S. Tan, X. Guo, A. Facchetti, and H. Yan. Material insights and challenges for non-fullerene organic solar cells based on small molecular acceptors. *Nature Energy*, 3(9):720–731, 2018.

[196] J. Zhang, Y. Zhao, J. Fang, L. Yuan, B. Xia, G. Wang, Z. Wang, Y. Zhang, W. Ma, W. Yan, W. Su, and Z. Wei. Enhancing Performance of Large-Area Organic Solar Cells with Thick Film via Ternary Strategy. *Small*, 13(21):1–8, 2017.

[197] K. Zhang, R. Xia, B. Fan, X. Liu, Z. Wang, S. Dong, H. L. Yip, L. Ying, F. Huang, and Y. Cao. 11.2% All-Polymer Tandem Solar Cells with Simultaneously Improved Efficiency and Stability. *Advanced Materials*, 30(36):1–8, 2018.

[198] Z. Zhang, C. Zhan, X. Zhang, S. Zhang, J. Huang, A. D. Li, and J. Yao. A self-assembly phase diagram from amphiphilic perylene diimides. *Chemistry - A European Journal*, 18(39):12305–12313, 2012.

[199] F. Zhao, S. Dai, Y. Wu, Q. Zhang, J. Wang, L. Jiang, Q. Ling, Z. Wei, W. Ma, W. You, C. Wang, and X. Zhan. Single-Junction Binary-Blend Nonfullerene Polymer Solar Cells with 12.1% Efficiency. *Advanced Materials*, 29(18):1700144, 2017.

[200] L. Zhong, L. Gao, H. Bin, Q. Hu, Z. G. Zhang, F. Liu, T. P. Russell, Z. Zhang, and Y. Li. High Efficiency Ternary Nonfullerene Polymer Solar Cells with Two Polymer Donors and an Organic Semiconductor Acceptor. *Advanced Energy Materials*, 7(14):1–7, 2017.

[201] E. Zhou, J. Cong, Q. Wei, K. Tajima, C. Yang, and K. Hashimoto. All-Polymer Solar Cells from Perylene Diimide Based Copolymers : Material Design and Phase Separation Control. *Angewandte Chemie*, pages 2799–2803, 2011.

[202] Y. Zhou, K. Tvingstedt, F. Zhang, C. Du, W. X. Ni, M. R. Andersson, and O. Inganä. Observation of a charge transfer state in low-bandgap polymer/fullerene blend systems by photoluminescence and electroluminescence studies. *Advanced Functional Materials*, 19(20):3293–3299, 2009.

[203] J. Zhu, Z. Ke, Q. Zhang, J. Wang, S. Dai, Y. Wu, Y. Xu, Y. Lin, W. Ma, W. You, and X. Zhan. Naphthodithiophene-Based Nonfullerene Acceptor for High-Performance Organic Photovoltaics: Effect of Extended Conjugation. *Advanced Materials*, 30(2):1–7, 2018.

[204] J. Zhu, Y. Wu, J. Rech, J. Wang, K. Liu, T. Li, Y. Lin, W. Ma, W. You, and X. Zhan. Enhancing the performance of a fused-ring electron acceptor: Via extending benzene to naphthalene. *Journal of Materials Chemistry C*, 6(1):66–71, 2017.

[205] X. Zhu, Q. Yang, M. Muntwiler, and F. Charge. Charge-Transfer Excitons at Organic semiconductor surfaces and interfaces. *Accounts of Chemical Research*, 42(11):1779–1787, 2009.